An Analysis of Localized Patterns in Some Novel Reaction Diffusion Models

by

Daniel Gomez

B.E., University of Saskatchewan, 2014

B.Sc., University of Saskatchewan, 2014

M.Sc., University of British Columbia, 2016

A THESIS SUBMITTED IN PARTIAL FULFILLMENT
OF THE REQUIREMENTS FOR THE DEGREE OF

Doctor of Philosophy

in

THE FACULTY OF GRADUATE AND POSTDOCTORAL STUDIES

(Mathematics)

The University of British Columbia

(Vancouver)

November 2020

The following individuals certify that they have read, and recommend to the Faculty of Graduate and Postdoctoral Studies for acceptance, the thesis entitled:

An Analysis of Localized Patterns in Some Novel Reaction Diffusion Models

submitted by **Daniel Gomez** in partial fulfillment of the requirements for the degree of **Doctor of Philosophy** in **Mathematics**.

Examining Committee:

Michael J. Ward, Mathematics
Supervisor

Juncheng Wei, Mathematics
Co-supervisor

Neil Balmforth, Mathematics
University Examiner

Jiahua Chen, Statistics
University Examiner

Additional Supervisory Committee Members:

Colin B. Macdonald, Mathematics
Supervisory Committee Member

Wayne Nagata, Mathematics
Supervisory Committee Member

Abstract

In this thesis we investigate strongly localized solutions to systems of singularly perturbed reaction-diffusion equations arising in several new contexts. The first such context is that of bulk-membrane-coupled reaction diffusion systems in which reaction-diffusion systems posed on the boundary and interior of a domain are coupled. In particular we analyze the consequences of introducing bulk-membrane-coupling on the behaviour of strongly localized solutions to the singularly perturbed Gierer-Meinhardt model posed on the one-dimensional boundary of a flat disk and the singularly perturbed Brusselator model posed on the two-dimensional unit sphere. Using formal asymptotic methods we derive hybrid numerical-asymptotic equations governing the structure, linear stability, and slow dynamics of strongly localized solutions consisting of multiple spikes. By numerically calculating stability thresholds we illustrate that bulk-membrane coupling can lead to both the stabilization and the destabilization of strongly localized solutions based on intricate relationships between the bulk-membrane-coupling parameters.

The remainder of the thesis focuses exclusively on the singularly perturbed Gierer-Meinhardt model in two new contexts. First, the introduction of an inhomogeneous activator boundary flux to the classically studied one-dimensional Gierer-Meinhardt model is considered. Using the method of matched asymptotic expansions we determine the emergence of *shifted* boundary-bound spikes. By linearizing about such a shifted boundary-spike solution we derive a class of *shifted* nonlocal eigenvalue problems parametrized by a shift parameter. We rigorously prove partial stability results and by considering explicit examples we illustrate novel phenomena introduced by the inhomogeneous boundary fluxed. In the second and final context we consider the Gierer-Meinhardt model in three-dimensions

for which we use formal asymptotic methods to study the structure, stability, and dynamics of strongly localized solutions. Most importantly we determine two distinguished parameter regimes in which strongly localized solutions exist. This is in contrast to previous studies of strongly localized solutions in three-dimensions where such solutions are found to exist in only one parameter regime. We trace this distinction back to the far-field behaviour of certain core problems and formulate an appropriate conjecture whose resolution will be key in the rigorous study of strongly localized solutions in three-dimensional domains.

Lay Summary

The formation of patterns in biological models is often described by systems of reaction-diffusion equations describing ways in which diffusing chemicals interact with one another. A detailed description of the patterns that emerge in these systems is often unattainable without extensive computer simulations. However, when one of the chemicals is assumed to diffuse very slowly, patterns described by *strongly localized solutions* emerge. Such solutions are characterized by the concentration of chemicals at discrete points and can be accurately described using a variety of mathematical techniques. In this thesis we apply and extend these techniques to analyze the structure and behaviour of localized solutions in several new models.

Preface

The content of this thesis is based on the original research conducted by the author, Daniel Gomez, under the supervision of Dr. Michael J. Ward and Dr. Juncheng Wei. The introduction found in Chapter 1 is original unpublished work of which I am the sole author.

A version of Chapter 2 has been published as a paper titled *The linear stability of symmetric spike patterns for a bulk-membrane coupled Gierer-Meinhardt model* by Michael Ward, Juncheng Wei, and myself in Volume 18, Issue 2 of the SIAM Journal of Applied Dynamical Systems. The project conception is due to Michael Ward and I conducted derivations and numerical computations. Juncheng Wei was involved in technical discussions and provided valuable feedback throughout this project.

The content of Chapter 3 is unpublished original work of which I am the sole author. A version of this chapter is currently in preparation for publication.

Chapter 4 is based on joint work with Juncheng Wei and a version of this chapter has been submitted for publication. The rigorous results of §4.3 are primarily due to Juncheng Wei whereas the derivations, analysis, and numerical simulations are primarily due to myself.

Chapter 5 is based on joint work with Michael Ward and Juncheng Wei. A version of this chapter has been submitted for publication. The conceptualization for this project is in part due previous work by Michael Ward on $D = \mathcal{O}(1)$ regime, and in part due to ongoing research by Juncheng Wei on rigorous existence results for ground states of the core problem. I performed derivations in the $D = \mathcal{O}(\varepsilon^{-1})$ regime, performed a detailed analysis of the resulting quasi-equilibrium solutions and their stability, and performed all numerical simulations.

Table of Contents

List of Tables

List of Figures

Acknowledgements

First and foremost, I want to thank my supervisors Michael Ward and Juncheng Wei for their continued guidance and support throughout the completion of this thesis. Your boundless enthusiasm for research has and always will be a source of inspiration and motivation.

I would also like to thank the people that I am fortunate to call my support system. For their openness and enthusiasm in talking about life and research I want to thank my friends and colleagues at UBC: Aaron, Thomas, Frédéric, Sarafa, and Tony. I want to thank my family for always supporting and encouraging me throughout all of my studies. And last but not least I want to thank Kirin for her love and unwavering support when I needed it most.

My decision to pursue graduate studies was largely influenced by the early mentorship I received from James Brooke, Jacek Szmigielski, and Alexey Shevyakov at the University of Saskatchewan and for this I will always be grateful. Thank you.

Finally I am grateful for the financial support I have received from the Natural Sciences and Engineering Research Council of Canada which first gave me the opportunity to pursue research as an undergraduate student and then allowed me to focus on research as a graduate student.

Chapter 1

Introduction

In 1952, Alan M. Turing's paper *The Chemical Basis of Morphogenesis* [93] laid down the foundations for a rich and insightful direction of biological and mathematical enquiry that continues to this day. Early embryonic development, Turing hypothesized, is guided by *pre-patterns* of biochemical *morphogens* that undergo passive diffusion with prescribed reaction kinetics. Turing's key insight was that, under certain conditions on the morphogens' diffusivities and their reaction kinetics, a spatially homogeneous distribution of morphogens could undergo a symmetry breaking bifurcation resulting in the formation of morphogen patterns. Surprisingly, this insight implies that diffusion, which is typically assumed to have a smoothing and stabilizing effect, could instead have a structured coarsening effect leading to the formation of spatial patterns.

While the biological implications of Turing's original theory of morphogenesis continue to be influential, it is Turing's mathematical approach that is most relevant for this thesis. In particular, to illustrate his insights Turing considered a system involving two morphogens whose concentrations, u and v, satisfy a two-component reaction-diffusion (RD) system of the form

$$u_t = D_u \Delta u + f(u,v), \qquad v_t = D_v \Delta v + g(u,v), \qquad \text{in } \Omega, \tag{1.1}$$

where D_u and D_v denote the morphogens' diffusivities and $f(u,v)$ and $g(u,v)$ their respective kinetics. With a simple choice of reaction-kinetics reflecting a chemi-

cal reaction, Turing determined conditions under which a spatially homogeneous equilibrium of (1.1) that is stable with respect to the reaction-kinetics may bifurcate into a spatially heterogeneous equilibrium. Such a transition to a spatially heterogeneous equilibrium is the result of what is now commonly referred to as a *Turing*, or *diffusion-driven*, *instability*, while the resulting spatially heterogeneous states are often referred to as *Turing patterns*. In addition to discovering this mechanism for pattern formation, it is also important to highlight that by restricting his attention to a system of the form (1.1), Turing distilled the complex and multifaceted problem of pattern formation in biological systems into an analytically tractable *model equation* from which key insights about the pattern-forming potential of two interacting mechanisms, mainly passive diffusion and reaction-kinetics, can be inferred. Such an approach is now ubiquitous in mathematical biology (see [68]) and has led to the ongoing application, extension, and refinement of Turing's original ideas.

Reaction-diffusion systems exhibiting pattern forming behaviour, often times through a Turing, or Turing-like, instability mechanism, have been proposed in a variety of applications including animal coat markings [67], stripe patterns in the marine angelfish *Pomacanthus* [50], sea shell patterns [80], early limb development [64], morphogenesis in the fresh water polyp *hydra* [23, 62], plant growth [35, 36, 69], ecological models [86], and the formation of crime hot spots [8, 87] among many others (see [59] for a review of chemical and biological applications). These models typically prescribe reaction-kinetics that reflect specific chemical reactions, such as in the Gray-Scott [30, 31] and Brusselator [79] models, or other phenomenologically motivated interactions as in the activator-inhibitor model of Gierer and Meinhardt [23]. Originally motivated by the role of lateral inhibition in visual pattern recognition, the Gierer-Meinhardt (GM) model is particularly important in the literature for its recognition of the importance of autocatalytic feedback loops and inhibitory reactions, commonly referred to as local self-activation and long-range inhibition, in biological pattern formation.

While some molecular candidates for morphogens have been identified [42] (see also [62, 88]) the experimental establishment of a Turing mechanism driving pattern formation in biological systems remains an area of ongoing research [61, 88]. Moreover, theoretical shortcomings of the classical Turing mechanism such

as a sensitivity to initial conditions and a lack of robustness have been recognized [61]. Such shortcomings do not repudiate Turing's original ideas however, but instead serve as an opportunity to better understand pattern formation in general. One way this has been done is by incorporating additional mechanisms to reaction-diffusion systems of the form (1.1). For example, studies incorporating growth [10, 14, 25, 52, 78], mechanical feedback [7, 63], and bulk-membrane coupling [54, 58, 81] have shown favourable results. The latter, mainly the introduction of bulk-membrane coupling, serves as the primary motivation for Chapters 2 and 3 of this thesis and is reviewed in more detail in §1.2 below.

In addition to serving as a model equation for pattern forming systems, reaction-diffusion systems of the form (1.1) and its extensions discussed above have also been the focus of the application and development of numerous mathematical ideas. While classical stability analysis predicts parameter thresholds beyond which a spatially homogeneous equilibrium is destabilized, it does not adequately predict the equilibrium, if one exists, to which it settles. Linear stability analysis is therefore often accompanied with full numerical simulations to explore system dynamics beyond the onset of instabilities [77]. Alternatively, techniques from a dynamical systems perspective such as centre manifold reductions [9] and weakly nonlinear analysis [76] can be used to further examine the system dynamics near the onset of linear instabilities. However, for parameter values far from the stability thresholds predicted by the linear theory, diverse techniques need to be employed (see [15, 72]). A particular class of reaction-diffusion systems of the form (1.1) for which substantial progress has been made in understanding pattern formation far from the onset of Turing instabilities occurs when the ratio between the species, D_u/D_v, is asymptotically small. Such reaction-diffusion systems often exhibit localized patterns that are characterized by large amplitude solutions compactly supported in asymptotically small spatial regions [100] (see also [44] for an overview of localization in general dissipative systems). The natural separation of spatial scales exhibited by these solutions makes them particularly amenable to analysis by both asymptotic and rigorous reduction methods, both of which have been highly successful in characterizing the existence, structure, and stability of these solutions. These types of solutions, and especially the asymptotic methods used to analyze them, underlie the bulk of this thesis and are outlined in §1.3.

In the preceding paragraphs we have outlined several of the theoretical and applied aspects as well as recent modelling and mathematical developments of Turing's original theory of biological pattern formation. Two key aspects from this discussion constitute the primary motivation and core technical aspects of this thesis. The first is the incorporation of bulk-membrane coupling into models of intracellular processes. The resulting *bulk-membrane-coupled* (BMC), or *bulk-surface-coupled*, models explicitly incorporate the inherent compartmentalization of cytosolic- and membrane- bound biochemical processes often found in intracellular processes. These models serve as the primary motivation for Chapters 2 and 3 and are therefore reviewed in more detail in §1.2. The second aspect constitutes the core technical component of this thesis and involves the asymptotic analysis of localized patterns in singularly perturbed reaction-diffusion systems and is reviewed in more detail in §1.3 below. To more explicitly place both of these aspects in the context of Turing instability driven pattern formation, we first provide an outline of the calculation of Turing instability thresholds for the two-component reaction-diffusion system (1.1) using classical linear stability analysis.

1.1 Classical Linear Stability Analysis

The starting point for the classical analysis of Turing instabilities is the assumption that (1.1) admits a spatially homogeneous steady state that is stable with respect to the reaction-kinetics. This means that constants $u^\star$ and $v^\star$ can be found such that

$$f(u^\star, v^\star) = g(u^\star, v^\star) = 0, \quad \text{trace}\, J^\star < 0, \quad \det J^\star > 0, \tag{1.2}$$

where $J^\star$ is the Jacobian evaluated at $(u,v) = (u^\star, v^\star)$ and explicitly given by

$$J^\star = \begin{pmatrix} f_u^\star & f_v^\star \\ g_u^\star & g_v^\star \end{pmatrix}.$$

We close (1.1) by imposing homogeneous Neumann boundary conditions so that the spatially homogeneous solution is an equilibrium of the closed system. Next we let $\mu_k \geq 0$ and $\phi_k(x)$ $(k \geq 0)$ denote the eigenvalues and accompanying eigenfunctions of $-\Delta$ in Ω with homogeneous Neumann boundary conditions on $\partial\Omega$. We

recall that $\phi_0 = 1$ while the eigenvalues satisfy the ordering $0 = \mu_0 < \mu_1 \leq \mu_2 \leq \cdots$. Although we are assuming that $(u^\star, v^\star)$ is stable with respect to the spatially homogeneous $k = 0$ mode, it may become unstable with respect to $k \geq 1$ modes and we therefore consider perturbations of the form

$$u = u^\star + \xi e^{\lambda t}\phi_k(x), \qquad v = v^\star + \eta e^{\lambda t}\phi_k(x), \qquad (k \geq 1).$$

Substituting int (1.1) and linearizing yields an eigenvalue problem with characteristic polynomial

$$\lambda^2 - \tau(\mu_k)\lambda + \delta(\mu_k) = 0,$$

where

$$\tau(\mu) = \text{trace } J^\star - (D_u + D_v)\mu, \quad \delta(\mu) = D_u D_v \mu^2 - (D_u g_v^\star + D_v f_u^\star)\mu + \det J^\star,$$

and for which we are interested in conditions under which an unstable root (i.e. with positive real part) can be found. Since $\mu_k > 0$ and trace $J^\star < 0$ we deduce that $\tau(\mu_k) < 0$ for all $k \geq 1$ and Turing instabilities are therefore triggered if $\delta(\mu_k) < 0$ for some $k \geq 1$. From the form of $\delta(\mu)$ we deduce that a Turing instability will be triggered provided that $D_u g_v^\star + D_v f_u^\star$ is sufficiently large. Indeed, by calculating the roots of $\delta(\mu)$ we determine the *necessary* condition for a Turing instability

$$\frac{D_v}{D_u} f_u^\star - 2\sqrt{\frac{D_v}{D_u}\det J^\star} + g_v^\star > 0. \tag{1.3}$$

We emphasize that this inequality is a necessary condition and in practice the requirement that $\delta(\mu_k) < 0$ for some $k \geq 1$ often requires that D_v/D_u exceeds the threshold predicted by (1.3). In some cases the requirement for a large diffusivity ratio needed to trigger Turing instabilities is physically prohibitive which has motivated the exploration of extensions to the classical Turing mechanism. Most pertinent to this thesis, and reviewed in more detail in §1.2 below, is the proposal that bulk membrane coupling can lead to the formation of Turing-like patterns.

Together with the assumption that $(u^\star, v^\star)$ is stable with respect to $k = 0$ modes, (1.3) provides us with insights on the reaction-kinetics for which (1.1) admits Turing instabilities. In particular, trace $J^\star < 0$ implies that at least one of $f_u^\star$ or $g_v^\star$

is negative. Without loss of generality we assume that $g_v^\star < 0$, with which (1.3) implies $f_u^\star > 0$. Furthermore, the condition that $\det J^\star > 0$ implies that $f_v^\star$ and $g_u^\star$ are of opposite sign which characterizes *activator-inhibitor* and *activator-substrate* models depending on whether $f_v > 0$ and $g_u < 0$ or $f_v < 0$ and $g_u > 0$ respectively.

To directly illustrate the above analysis we consider the one-dimensional GM model posed on the unit interval with homogeneous Neumann boundary conditions. Specifically, we consider

$$u_t = D_u u_{xx} - u + \frac{u^p}{v^q}, \quad \tau v_t = D_v v_{xx} - v + \frac{u^m}{v^s}, \quad 0 < x < 1, \tag{1.4}$$

with $u_x(0) = u_x(1) = v_x(0) = v_x(1) = 0$ and for which we impose the constraints $p > 1$, $q > 0$, $m > 0$, and $s \geq 0$ on the GM exponents. The spatially homogeneous steady state is then given by $u^\star = v^\star = 1$ with which the Jacobian is explicitly given by

$$J^\star = \begin{pmatrix} p-1 & -q \\ m\tau^{-1} & -(1+s)\tau^{-1} \end{pmatrix},$$

and from which we deduce that $(u,v) = (u^\star, v^\star)$ is linearly stable with respect to the reaction-kinetics provided that

$$0 < \tau < \frac{1+s}{p-1}, \qquad 0 < \frac{p-1}{q} < \frac{m}{1+s}. \tag{1.5}$$

Calculating

$$\delta(\mu) = D_u D_v \mu^2 - \left((p-1)D_v - \frac{1+s}{\tau} D_u \right) \mu + \frac{mq - (p-1)(1+s)}{\tau}, \tag{1.6}$$

we then determine that (1.3) implies

$$\frac{D_v}{D_u} > \frac{2mq}{(p-1)^2 \tau} \left(1 - \frac{(1+s)(p-1)}{2mq} + \sqrt{1 - \frac{(1+s)(p-1)}{mq}} \right). \tag{1.7}$$

Since $\mu_k = (\pi k)^2$ and $\phi_k(x) = \cos \pi k x$ ($k \geq 0$), the system (1.4) is susceptible to Turing instabilities provided that $\delta(\pi^2 k^2) < 0$ for some $k \geq 1$.

In the commonly studied case where the GM exponents are given by $(p,q,m,s) =$

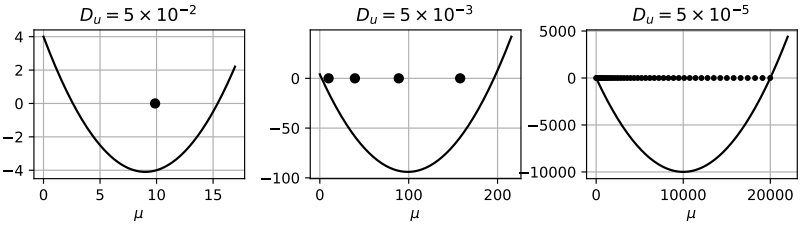

Figure 1.1: Solid lines indicate values of $\delta(\mu)$ versus μ for the GM exponents $(p,q,m,s) = (2,1,2,0)$, with $D_v = 2$, $\tau = 0.25$, and specified values of $D_u > 0$. Markers indicate the values of the modes $\mu_k = \pi^2 k^2$ for which $\delta(\mu_k) < 0$ and the spatially homogeneous pattern becomes susceptible to Turing instabilities.

$(2,1,2,0)$ we calculate that $\tau < 1$ in order for the spatially homogeneous solution to be linearly stable with respect to the reaction kinetics. On the other hand, after fixing $\tau = 0.25$, (1.7) implies that $D_v/D_u > 23.4$ is a necessary condition for Turing instabilities. Fixing $D_v = 2$ we then find that as D_u is decreased the $k = 1$ mode is the first to go unstable at a value of $D_u \approx 0.067$ for which $D_v/D_u \approx 29.8$. In Figure 1.1 we plot $\delta(\mu)$ for values of $D_u = 5 \times 10^{-2}, 5 \times 10^{-3}, 5 \times 10^{-5}$ for which we note that, respectively, the $k = 1$, $1 \leq k \leq 4$, and $1 \leq k \leq 45$ modes are linearly unstable. In Figure 1.2 we plot the solution at discrete times obtained by numerically solving (1.4) when $D_u = 5 \times 10^{-2}$ and $D_u = 5 \times 10^{-5}$. In the former case only the $k = 1$ mode is linearly unstable and this is qualitatively reflected in the solution's time evolution. Using the proximity of the diffusivity ratio D_v/D_u to the Turing instability threshold a weakly nonlinear analysis could be used to track the sole unstable mode and effectively characterize the resulting equilibrium solution. On the other hand, when $D_u = 5 \times 10^{-5}$ our previous calculations indicate that 45 distinct spatial modes are linearly unstable. These modes interact nonlinearly eventually leading to the formation of the spiky solution shown in Figure 1.2. In particular, this illustrates that perturbation techniques using the closeness of the diffusivity ratio to the Turing instability threshold fail to hold when $D_u \ll D_v$, in part due to the emergence of a large band of unstable spatial modes. However, the resulting numerically computed solution illustrates that this large band of unstable modes leads to a localized solution and suggests that perturbation methods that

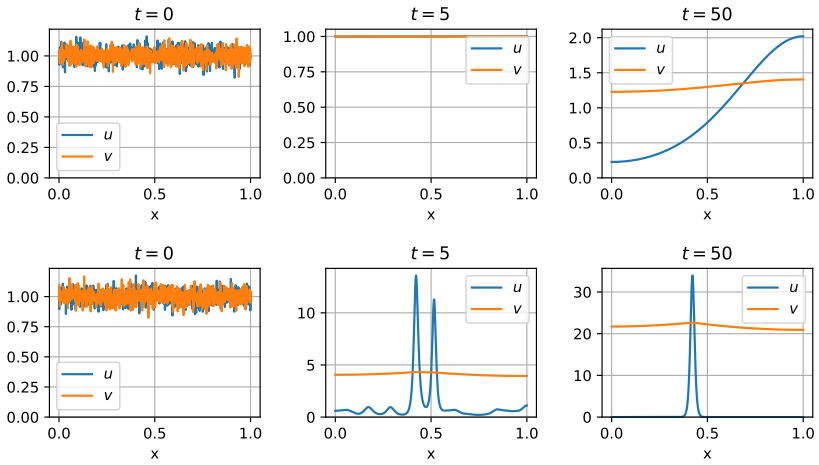

Figure 1.2: Snapshots of numerically computed solutions of the one-dimensional singularly perturbed Gierer-Meinhardt model with exponents $(p,q,m,s) = (2,1,2,0)$ when $\tau = 0.25$, $D_v = 2$ and $D_u = 5 \times 10^{-2}$ (top) and $D_u = 5 \times 10^{-5}$ (bottom).

exploit large disparities between spatial scales can instead be used approximate the resulting solution. Indeed, a combination of both rigorous and formal asymptotic methods have been used to study such localized solutions and we provide an outline of these developments in §1.3 below.

1.2 Bulk-Membrane Coupled Models

One of the key biological motivation for the recent interest in mathematical models incorporating bulk-membrane coupling is the naturally occurring compartmentalization of cytosol- and membrane-bound processes found in complex intracellular self-organizing processes. One classic example of such compartmentalization is the Min System in which the dynamics of cytosol- and membrane-bound MinC, MinD, and MinE are believed to drive the positioning and localization of the contractile Z-ring ultimately leading to cell septation [37]. Another classic example can be found in the establishment of cell polarity by the Rho family of guanosine-triphosphate binding proteins (GTPases) for which GTPases undergo activation and inactivation on the cell membrane in addition to cell membrane attachment

and detachment [65, 81]. While early mathematical models of these intracellular processes recognized the compartmentalization of bulk- and membrane-bound biochemical agents by separately modelling their respective concentrations and reaction kinetics, the resulting mathematical models did not explicit model cell membrane attachment and detachment [37, 38, 65]. However in 2005 Levine and Rappel studied the formation of Turing-like patterns in a bulk-membrane-coupled (BMC) reaction-diffusion (RD) system and found that the details of the membrane attachment and detachment process can have a pronounced effect on pattern formation [54]. This discovery has motivated numerous additional investigations of pattern formation in a new class of BMC RD systems. In particular, the systematic incorporation of bulk-membrane-coupling has been introduced into new models of the Min System [5, 6, 33] and GTPase driven cell polarization [16, 17, 29, 75, 81]. More generally Halatek et. al. [34] have proposed that the key mechanism underlying intracellular pattern formation involves the mass-conserving redistribution of proteins by cytosolic diffusion together with the cycling of proteins between bulk- and membrane-bound states. Such a restriction to mass-conserved BMC RD systems however neglects the synthesis of proteins or other signalling molecules within the cytosol. In this context it remains pertinent to understand pattern formation in more general BMC RD systems incorporating cytosolic synthesis by introducing, for example, cytosol-bound reaction-kinetics [58] or cytosol-bound spatial inhomogeneities (see Chapter 3).

In the remainder of this section we outline several key recent developments in the analysis of Turing-like patterns in BMC RD systems. First however we introduce the general mathematical description of BMC models. Letting Ω be a bounded domain in $\mathbb{R}^N$ ($N \geq 2$) a BMC RD system governing the concentrations $\boldsymbol{U} = (U_1, ..., U_n)^T$ and $\boldsymbol{u} = (u_1, ..., u_m)^T$ of n bulk-bound and m membrane-bound species respectively is given by

$$\tau_B \partial_t \boldsymbol{U} = D_B \Delta \boldsymbol{U} + \boldsymbol{F}(\boldsymbol{U}), \qquad \text{in} \quad \Omega, \tag{1.8a}$$

$$D_B \partial_n \boldsymbol{U} = \gamma q(\boldsymbol{u}, \boldsymbol{U}), \qquad \text{on} \quad \partial\Omega, \tag{1.8b}$$

$$\tau_M \partial_t \boldsymbol{u} = D_M \Delta_{\partial\Omega} \boldsymbol{u} + \boldsymbol{f}(\boldsymbol{u}) - \boldsymbol{q}(\boldsymbol{u}, \boldsymbol{U}), \qquad \text{in} \quad \partial\Omega, \tag{1.8c}$$

where τ_B and D_B are matrices consisting of the time constants and diffusivities of

the bulk-bound species while τ_M and D_M those of the membrane-bound species, $\boldsymbol{F}$ and $\boldsymbol{f}$ reflect the bulk- and membrane-bound kinetics respectively, and $\boldsymbol{q}$ reflects the membrane attachment-detachment process while $\gamma > 0$ accounts for asymmetries in the exchange. With some notable exceptions (see [16, 17]) authors studying BMC-RD models have primarily modelled the membrane attachment-detachment process as a Langmuir process (see §4 of [43]) which is reflected by choosing $\boldsymbol{q}$ as a linear function of the membrane- and bulk-bound concentrations. In particular this leads to Robin boundary conditions and linear terms in the bulk-bound problem and membrane equations respectively. Unless otherwise specified, the models we discuss in the remainder of this section use a Langmuir process to describe membrane attachment-detachment. Finally we note that (1.8) is to be understood as a leading order approximation of a system of two N-dimensional RD systems, one posed inside of the bulk and the other posed on a thin external protrusion, in the limit of the external protrusions thickness going to zero. The systematic derivation of this leading order approximation is presented in Appendix A.

In the two-component BMC-RD system considered by Levine and Rappel [54] the membrane-bound diffusivities were assumed to be identically zero in order to reflect experimental observations that indicate membrane-bound diffusivities are much smaller than bulk-bound diffusivities [55]. In addition the authors assumed that within the bulk the two species only diffuse and decay but do not react, with reactions being instead restricted to the membrane. Under these assumptions the two-component BMC-RD system reduces to a system coupling two bulk-bound linear partial differential equations (PDEs) to two membrane-bound nonlinear ordinary differential equations (ODEs). For this simplified model Levine and Rappel performed a linear stability analysis about an equilibrium that is spatially homogeneous on the boundary and demonstrated that even if the bulk-bound diffusivities of two species are equal, bulk-membrane-coupling can lead to pattern formation on the membrane. Thus, bulk-membrane-coupling provides an attractive extension to classically studied models exhibiting Turing instabilities which otherwise require large differences in diffusivities to initiate pattern formation.

Motivated both by the natural compartmentalization between bulk- and membrane-bound processes and by the weakened restrictions for Turing-like instabilities illustrated by Levine and Rappel [54], numerous additional studies have explored the

effects of bulk-membrane-coupling on pattern formation. In the context of symmetry breaking in cell signalling networks, Rätz and Röger have studied the formation of Turing-like patterns in a two-component BMC-RD system with nonzero membrane-bound diffusion in which only one species detaches into the bulk where it undergoes passive diffusion and bulk-decay [81, 83]. Similarly, Madzvamuse et. al. [57, 58] studied the formation of Turing-like patterns in a general two-component BMC-RD system with diffusion and reactions in both the bulk and the membrane. In both the studies by Rätz and Rögers and those of Madzvamuse et. al., criteria for Turing-like instabilities were derived using an analogue of the classical linear stability analysis reviewed in §1.1 above. Moreover the authors in both studies used numerical methods, a phase-field approach in the former and a BMC finite-element method in the latter, to verify their linear stability predictions and explore the resulting patterns formed beyond the onset of linear instabilities. The effects of cell shape and diffusion barriers for two-dimensional BMC-RD systems were investigated by Giese et. al. [24] through extensive *in silico* experimentation on the cell polarization models of Goryachev et. al. [29], for which a Turing-like instability drives polarization, as well as that of Mori et. al. [65], in which wave-pinning is the central polarizing mechanism. We conclude by noting the studies of Diegmiller et. al.[17], as well as Cussedu et. al. [16], for which the wave-pinning model of Mori et. al. [65] was extended to explicitly model bulk-membrane coupling in three-dimensional domains. These latter models consist of a single-component BMC-RD system for which membrane attachment-detachment is modelled by a nonlinear Hill function. In contrast to the self-activation and lateral inhibition required for Turing instabilities, the wave-pinning mechanism instead relies on the interplay between bi-stability and mass conservation.

With the exception of the analysis of the wave-pinning model found in [16, 17], the analysis of Turing-like patterns in the BMC-RD systems discussed above have been primarily limited to *in silico* experiments and linear stability analysis. While weakly nonlinear analysis and the derivation of amplitude equations have been used to analyze dynamics beyond the onset of linear instabilities [73, 74] there are no studies analyzing of patterns formation far from equilibrium in BMC-RD systems. This gap serves as the primary motivation for the contents of Chapters 2 and 3 for which pattern formation is investigated in two singularly perturbed BMC-RD

systems. In particular, in these chapters we study the effects of incorporating bulk-membrane coupling into two well studied singularly perturbed RD systems: the one-dimensional GM model, and the two-dimensional Brusselator model posed on the unit sphere. These two models are part of a large class of singularly perturbed RD models that exhibit *strongly localized* solutions for which substantial rigorous and asymptotic developments have been made in the past two decades and which we outline in more detail in the next section.

1.3 Strongly Localized Patterns

Although a detailed analysis of far-from-equilibrium solutions to general two-component reaction-diffusion systems of the form (1.1) is typically intractable, substantial progress has been made for a wide class of *singularly perturbed* reaction-diffusion systems of the form

$$u_t = \varepsilon^2 \Delta u + f(u,v), \quad \tau v_t = D\Delta v + g(u,v), \qquad x \in \Omega, \tag{1.9}$$

where $\Omega \subset \mathbb{R}^d$ ($d \geq 1$) and $\varepsilon \ll 1$ is an asymptotically small parameter. Specifically, when the reaction kinetics $f(u,v)$ and $g(u,v;\varepsilon)$ are of *activator-inhibitor* or *activator-substrate* type (see §1.1) the system (1.9) exhibits *strongly localized* solutions in the sense that the activator $u(x,t)$ is of a large amplitude in asymptotically small spatial regions. This separation of spatial scales makes (1.9) particularly well suited to analysis by both formal and rigorous reduction methods. In this section we outline some of the key developments in the analysis of strongly localized solutions to (1.9).

Historically, the Gierer-Meinhardt (GM) model given by

$$u_t = \varepsilon^2 \Delta u - u + \frac{u^p}{v^q}, \quad \tau v_t = D\Delta v - v + \frac{u^m}{v^s}, \qquad x \in \Omega \subset \mathbb{R}^d \tag{1.10}$$

$$\partial_n u = 0, \quad \partial_n v = 0, \qquad x \in \partial\Omega, \tag{1.11}$$

where $d \geq 1$ and the GM exponents (p,q,m,s) satisfy (1.5), has been one of the primary models driving the development of both formal and rigorous techniques in the study of strongly localized solutions. Early work on the GM model focused

on the *shadow-limit* obtained by letting $D \to \infty$ and for which $v(x,t) \to \xi(t)$ is spatially constant. By an appropriate rescaling, steady state solutions to (1.10) in the shadow limit can be found by solving the single equation

$$\varepsilon^2 \Delta u - u + u^p = 0, \quad x \in \Omega, \qquad \partial_n u = 0, \quad x \in \partial\Omega, \tag{1.12}$$

which has a variational structure with energy functional

$$J_\varepsilon[u] \equiv \int_\Omega \left(\frac{\varepsilon^2}{2} |\nabla u|^2 + \frac{1}{2} u^2 - \frac{1}{p+1} u_+^{p+1} \right) dx, \quad u_+ \equiv \max(0,u).$$

In this case both formal asymptotic [39, 40, 102] and rigorous [32, 51, 107] (see also the review articles [71, 108] and book [112]) methods have been used to construct multi-spike equilibrium solutions and study their stability. Interestingly, while many multi-spike equilibrium solutions exist in the shadow limit, only those equilibrium solutions consisting of a single spike concentrating on the boundary at a non-degenerate local maximum of the mean curvature are stable. In contrast, by using the method of matched asymptotic expansions when $D > 0$ is finite Iron et. al. [41] demonstrated that *symmetric* multi-spike equilibrium solutions to (1.10) when $d = 1$ are stable provided that D is sufficiently small. Similar methods were also used by Ward and Wei [104] to construct *asymmetric* multi-spike solutions. In contrast to the shadow limit, the equilibrium system for (1.10) when $D > 0$ is finite does not have a variational structure thereby limiting the availability of rigorous techniques for studying the existence and stability of multi-spike equilibrium solutions. Such rigorous results have nevertheless been established for $d = 1$ [20, 90, 111] and $d = 2$ [45, 110] dimensional domains.

While many of the formal asymptotic studies discussed above were in the context of the singularly perturbed GM model (1.10), the techniques used have been successfully applied to study localized solutions in various $d = 1$, $d = 2$, and $d = 3$ dimensional singularly perturbed RD systems such as the one- and two-dimensional Gray-Scott [12, 47] and Brusselator [96, 97] models, the Brusselator and Schnakenberg model on the surface of a sphere [84, 91] and torus [95] respectively, as well as the three-dimensional Schnakenberg model [98]. In each of these studies the method of matched asymptotic expansions is used to reduce the

problem of calculating an N-spike equilibrium solution to that of calculating the N spike locations as well as N parameters that determine the local spike profiles. In particular, the N spike profile parameters are found by solving a nonlinear algebraic system arising from a leading order matching condition, whereas the N-spike locations are found by calculating equilibrium configurations to an ODE system arising from a higher order solvability condition and describing slow spike dynamics. While the method of matched asymptotic expansions typically proceeds in a similar way for constructing localized spike solutions, differences in the choice of reaction-kinetics and dimension of the domain lead to pronounced technical differences in the details of the analysis. In particular the key role of the dimension of the domain arises through the free-space Green's function satisfying

$$\Delta G_f = -\delta(x-\xi), \quad x \in \mathbb{R}^f, \tag{1.13}$$

and the reduced wave Green's function satisfying

$$\Delta G - \kappa^2 G = -\delta(x-\xi), \quad x \in \Omega \subset \mathbb{R}^d, \tag{1.14}$$

with appropriate boundary conditions if $\partial\Omega \neq \emptyset$, both of which are prominently featured in the method of matched asymptotic expansions with the former determining the far-field behaviour of the inner solution and the latter playing a key role in the construction of outer solutions. Moreover, the choice of reaction kinetics and order of D and τ with respect to $\varepsilon \ll 1$ leads to pronounced qualitative and quantitative differences in the formulation of the appropriate inner problem.

In addition to differences in the details of the method of matched asymptotic expansions, different choices of reaction-kinetics and parameter values also lead to diverse dynamics of multi-spike solutions. In particular multi-spike solutions may undergo *oscillatory*, *competition*, and *splitting* instabilities depending on the choice of parameter values and reaction-kinetics. Moreover, detailed thresholds for both Hopf and competition instabilities can be calculated by using the method of matched asymptotic expansions to derive a *Globally Coupled Eigenvalue Problem* (GCEP) which, for certain reaction-kinetics and parameter regimes, can be further reduced to a *Nonlocal Eigenvalue Problem* (NLEP). While GCEPs are typ-

ically analytically intractable, a substantial collection of rigorous stability results for various NLEPs have been established [99, 107, 112]. In cases where such rigorous results are not applicable, instability thresholds can nevertheless be calculated by using a numerically-aided winding number argument [105] as well as standard root-finding algorithms. Additionally, we remark that under appropriate conditions NLEPs can be *explicitly solvable* whereby they can be reduced to simpler algebraic equations [66, 70]. Finally, due to the fast decay of higher-mode localized perturbations when $d \geq 2$, splitting instabilities are independent of global contributions and instead depend only on the local spike profile. We note that that splitting instabilities when $d = 1$ arise through a different mechanism altogether [46]. While the instability thresholds calculated in these studies predict the onset of linear instabilities, recent progress has been made to determine the criticality of Hopf [26, 28, 101] bifurcations and splitting [113] instabilities.

1.4 Main Contributions and Thesis Outline

As discussed in §1.2, BMC-RD systems provide an attractive extension to classical Turing-instability driven pattern forming models. However, with the exception of studies performing a weakly nonlinear analysis near the onset of Turing-like instabilities, the majority of BMC-RD system studies have focused on the calculation of linear Turing-like instability thresholds predicting the onset of spatial instabilities near analogues to spatially homogeneous steady states. With patterns arising far from the onset of Turing-like instabilities in BMC-RD systems being primarily explored through *in silico* experiments there is a gap in our detailed understanding of such far-from-equilibrium patterns. By using the formal asymptotic methods that have been successfully used to develop a detailed understanding of strongly localized solutions to singularly perturbed RD-systems as outlined in §1.3 we aim to develop an analogous understanding of strongly localized patterns in singularly perturbed BMC-RD systems in the first part of this thesis. Specifically, by introducing bulk-membrane-coupling to two well-studied singularly perturbed RD systems, mainly the one-dimensional GM model and the Brusselator model posed on the unit sphere, we investigate the effects of bulk-membrane-coupling on both the structure of multi-spike equilibrium solutions as well as their linear stability.

The analysis of these two singularly perturbed BMC-RD systems is pursued in Chapters 2 and 3 with our main contributions outlined in more detail below.

In the remainder of the thesis, mainly Chapters 4 and 5, we pursue the analysis of strongly localized solutions for the GM model in two new context: in a one-dimensional domain with an inhomogeneous activator boundary flux, and in a three-dimensional domain. While numerous studies have considered multi-spike solutions for the one-dimensional GM system with homogeneous Neumann [41, 105] and Robin [60] boundary conditions, the effects of an inhomogeneous boundary flux have not yet been investigated. In 2018 Tzou et. al. [96] considered the effects of a non-zero boundary flux for the inhibitor, but a similar investigation for the activator has not been pursued. With a growing interest in bulk-membrane coupling, understanding the effects of non-zero boundary fluxes for both activator and inhibitor is increasingly important. By considering a non-zero activator boundary flux for the one-dimensional GM system in Chapter 4 we initiate this line of investigation as outlined in more detail below. The final context in which we study strongly localized solutions is the three-dimensional GM model. Although our analysis is heavily influenced by the work of Tzou et. al. [98] in which strongly localized solutions of the three-dimensional Schnakenberg model are analyzed, our analysis provides key new insights into the formation of strongly localized solutions in three-dimensional systems in general. Specifically, in contrast to the Schnakenberg model for which localized solutions can only be constructed in the $D = \mathcal{O}(\varepsilon^{-1})$ regime, we find that localized solutions can be constructed in both the $D = \mathcal{O}(\varepsilon^{-1})$ and $D = (1)$ regimes for the three-dimensional GM model. We trace this distinction back to the far-field behaviour of a particular core problem and by calculating this far-field behaviour numerically we formulate several key conjectures. The formulation of these conjectures as well as the detailed asymptotic analysis of localized patterns in the three-dimensional GM model is pursued in Chapter 5 as outlined in more detail below.

The detailed outlines of the remaining chapters of this thesis are as follows.

In Chapter 2 we analyze a BMC PDE model in which a scalar linear two-dimensional bulk diffusion process for the inhibitor is coupled to the classically studied activator-inhibitor GM model posed on the domain boundary. In the singularly perturbed limit of a long-range inhibition and short-range activation for the

membrane-bound species we use formal asymptotic methods to analyze the existence of localized steady-state multi-spike membrane-bound patterns and to derive a nonlocal eigenvalue problem (NLEP) characterizing instabilities of these patterns. A novel feature of this NLEP is that it involves a membrane Green's function that is coupled nonlocally to a bulk Green's function. By considering two special cases, mainly when the domain is a disk or when the bulk-bound inhibitor diffusivity is infinitely large, we can calculate this membrane Green's function explicitly which allows for the use of a hybrid analytical-numerical approach for determining unstable spectra of the NLEP. This analysis reveals how bulk-membrane coupling modifies the well-known linear stability properties of multi-spike equilibrium solutions to the singularly perturbed one-dimensional GM mode in the absence of bulk-membrane-coupling. In particular, bulk-membrane-coupling is shown to exhibit both stabilization and destabilization with respect to either oscillatory instabilities due to Hopf bifurcations or competition instabilities arising due to zero-eigenvalue crossings. Moreover, in the case of oscillatory instabilities our analysis reveals an intricate dependence on the coupling parameters as well as the diffusivity and time-scale constant of the bulk-bound inhibitor. Finally, linear stability predictions from the NLEP analysis are confirmed with full numerical finite element simulations of the coupled PDE system. We remark that our approach is valid in more general settings than the disk or the well-mixed shadow system, with the key hurdle being the computation of the relevant Green's functions. By restricting our detailed analysis to these two specialized cases, we can bypass the computational challenges of calculating the Green's functions and therefore focus instead on the novel effects of coupling on the construction and stability of multi-spike solutions.

In Chapter 3 we incorporate bulk-membrane-coupling to the Brusselator model posed on the unit sphere by coupling it to a passive diffusion process with an inhomogeneous source for the activator within the bulk. Motivated by studies of the Min and GTPase systems, for which proteins and signalling molecules originating in the bulk attach to the membrane, our model proposes a mechanism whereby a bulk-bound activator source term is transported to the membrane by diffusion. The resulting membrane-bound feed term substitutes the external feed term included in the classically studied Brusselator model required for sustaining pattern formation. Our model therefore proposes a mechanism by which pattern sustaining feed terms

can be introduced in a self-contained manner. In the singularly perturbed limit where the membrane-bound activator diffusivity is asymptotically small, we use formal asymptotic methods to construct and study the stability and slow dynamics of localized solutions. In particular we derive a nonlinear algebraic system, globally coupled eigenvalue problem, and system of ODEs that determine, respectively, the structure, stability and slow dynamics of a multi-spot solution. Furthermore we highlight the key differences introduced by bulk-membrane coupling in comparison to previous studies of the uncoupled Brusselator model on the sphere [84, 91] and unit disk [96]. In particular, we find that changes to the linear stability due to bulk-membrane-coupling primarily result from a *recirculation* mechanism for the membrane-bound activator. This recirculation effect also introduces an attractive term to the slow dynamics, but we show that it is weaker than the classically observed coupling-independent repulsive term. Finally, analogously to results obtained for the Brusselator on a two-dimensional disk [96], we find that spots are attracted to local maximum points of the membrane-bound, bulk-originating, feed term.

In Chapter 4 we study the effects of an inhomogeneous activator boundary flux on the existence, linear stability, and slow dynamics of multi-spike solutions to the singularly perturbed GM model on the unit interval in the singularly perturbed limit of an asymptotically small activator diffusivity $\varepsilon^2 \ll 1$. Specifically, we use the method of matched asymptotic expansions to construct multi-spike solutions using two classical methods pioneered in [39, 104]. One of the novel aspects introduced by assuming inhomogeneous Neumann boundary conditions for the activator is that it necessitates the concentration of spikes at the boundaries. Furthermore these spikes are parameterized by a *shift parameters* which plays a central role in the linear stability of these boundary-bound spikes. Proceeding with standard methods previously used for the singularly perturbed one-dimensional GM model we derive a system of NLEPs governing the linear stability on an $\mathcal{O}(1)$ timescale as well as a system of ODEs governing slow spike dynamics on an $\mathcal{O}(\varepsilon^{-2})$ timescale. In the simplest case of a single boundary-bound spike we formulate a scalar *shifted* NLEP for which we establish partial stability results rigorously. Finally, by applying the asymptotically derived structure, linear stability, and slow dynamic results as well as full numerical simulations to examples of two-spike configurations involving

both boundary and interior spike we highlight some of the novel phenomena that arise.

In Chapter 5 we study the existence, linear stability, and slow dynamics of localized multi-spot solutions to the GM model in an arbitrary three-dimensional domain in the singularly perturbed limit of an asymptotically small activator diffusivity $\varepsilon^2 \ll 1$. Using the method of matched asymptotic expansions we determine that in the $D = \mathcal{O}(1)$ only symmetric multi-spike patterns can be constructed and these are always linearly stable on an $\mathcal{O}(1)$ timescale. In contrast, in the $D = \mathcal{O}(\varepsilon^{-1})$ regime we find that both symmetric and asymmetric multi-spike patterns can be constructed. However we show that the asymmetric patterns are always linearly unstable on an $\mathcal{O}(1)$ timescale whereas the symmetric patterns may, upon exceeding certain numerically computed thresholds, undergo oscillatory instabilities through a Hopf bifurcation or competition instabilities through a zero-eigenvalue bifurcation on an $\mathcal{O}(1)$ timescale. Both of these instability predictions are supported by full numerical simulations of the three-dimensional GM model using the finite-element software FlexPDE 6 [1]. Furthermore, the existence of multi-spot solutions in both the $D = \mathcal{O}(1)$ and $D = \mathcal{O}(\varepsilon^{-1})$ regimes is traced back to the far-field behaviour of a certain core problem which we may compute numerically and from which we formulate several key conjectures. Additionally, we derive a system of ODEs governing the slow dynamics of multi-spot solutions over an $\mathcal{O}(\varepsilon^{-3})$ timescale in both the $D = \mathcal{O}(1)$ and $D = \mathcal{O}(\varepsilon^{-1})$ regimes. Finally, by performing a linear stability analysis we determine that multi-spike solutions in the weak-interaction $D = \mathcal{O}(\varepsilon^2)$ regime may undergo peanut-splitting instabilities and we numerically demonstrate that this leads to a cascade of self-replication events.

Chapter 2

The Linear Stability of Symmetric Spike Patterns for a Bulk-Membrane Coupled Gierer-Meinhardt Model

The primary goal of this chapter is to initiate detailed asymptotic studies of strongly localized patterns in coupled bulk-surface RD systems. To this end, we introduce such a PDE model in which a scalar linear 2-D bulk diffusion process is coupled through a linear Robin boundary condition to a two-component 1-D RD system with Gierer-Meinhardt (nonlinear) reaction kinetics defined on the domain boundary or "membrane". Similar, but more complicated, coupled bulk-surface models, some with nonlinear bulk reaction kinetics and in higher space dimensions, have previously been formulated and studied through either full PDE simulations or from a Turing instability analysis around some patternless steady-state (cf. [81], [82], [83], [58], [58], [83], [56]). Our coupled model, formulated below, provides the first analytically tractable PDE system with which to investigate how the bulk diffusion process and the bulk-membrane coupling influences the existence and linear stability of localized "far-from-equilibrium" (cf. [72]) steady-state spike patterns on the membrane. In the limit where the bulk and membrane are

uncoupled, our PDE system reduces to the well-studied 1-D Gierer-Meinhardt RD system on the membrane with periodic boundary conditions. The existence and linear stability of steady-state spike patterns for this limiting uncoupled problem is well understood (cf. [107], [41], [20], [21], [105]).

Our model is formulated as follows: Given some 2-D bounded domain Ω we pose on its boundary an RD system with Gierer-Meinhardt kinetics

$$\partial_t u = \varepsilon^2 \partial_\sigma^2 u - u + u^p/v^q, \qquad 0 < \sigma < L, \quad t > 0, \tag{2.1a}$$

$$\tau_s \partial_t v = D_v \partial_\sigma^2 v - (1+K)v + KV + \varepsilon^{-1} u^m/v^s, \qquad 0 < \sigma < L, \quad t > 0, \tag{2.1b}$$

where σ denotes arc length along the boundary of length L, and where both u and v are L-periodic. In Ω we consider the linear 2-D bulk diffusion process

$$\tau_b \partial_t V = D_b \Delta V - V, \qquad x \in \Omega, \qquad D_b \partial_n V + KV = Kv, \qquad x \in \partial\Omega, \tag{2.1c}$$

where the coupling to the membrane is through a Robin condition. The Gierer-Meinhardt exponent set (p,q,m,s) is assumed to satisfy the usual conditions (cf. [41, 107])

$$p > 1, \qquad q > 0, \qquad m > 0, \qquad s \geq 0, \qquad 0 < \frac{p-1}{q} < \frac{m}{s+1}. \tag{2.2}$$

In this model τ_b and τ_s are time constants associated with the bulk and membrane diffusion process, D_b and D_v are the diffusivities of the bulk and membrane inhibitor fields, and $K > 0$ is the bulk-membrane coupling parameter.

The remainder of this chapter is organized as follows. In §2.2 we use the method of matched asymptotic expansions to derive a nonlinear algebraic system for the spike locations and heights of a multi-spike steady-state pattern for the membrane-bound species. A singular perturbation analysis is then used to derive an NLEP characterizing the linear stability of these localized steady-states to $\mathcal{O}(1)$ time-scale instabilities. A more explicit analysis of both the nonlinear algebraic system and the NLEP requires the calculation of a novel 1-D membrane Green's function that is coupled nonlocally to a 2-D bulk Green's function. Although intractable analytically in general domains, this Green's function problem

is explicitly studied in two special cases: the well-mixed limit, $D_b \gg 1$, for the bulk diffusion field in an arbitrary bounded 2-D domain with C^2 boundary, and when Ω is a disk of radius R with finite D_b.

In §2.3 we restrict our steady-state and NLEP analysis to these two special cases, and consider only symmetric N-spike patterns characterized by equally-spaced spikes on the 1-D membrane, for which the nonlinear algebraic system is readily solved. In this restricted scenario, by using a hybrid analytical-numerical method on the NLEP we are then able to provide linear stability thresholds for either synchronous or asynchronous perturbations of the steady-state spike amplitudes. More specifically, we provide phase diagrams in parameter space characterizing either oscillatory instabilities of the spike amplitudes, due to Hopf bifurcations, or asynchronous (competition) instabilities, due to zero-eigenvalue crossings, that trigger spike annihilation events. These linear stability phase diagrams show that the bulk-membrane coupling can have a diverse effect on the linear stability of symmetric N-spike patterns. In each case we find that stability thresholds are typically increased (making the system more stable) when the bulk-membrane coupling parameter K is relatively small, whereas the stability thresholds are decreased as K continues to increase. This nontrivial effect is further complicated

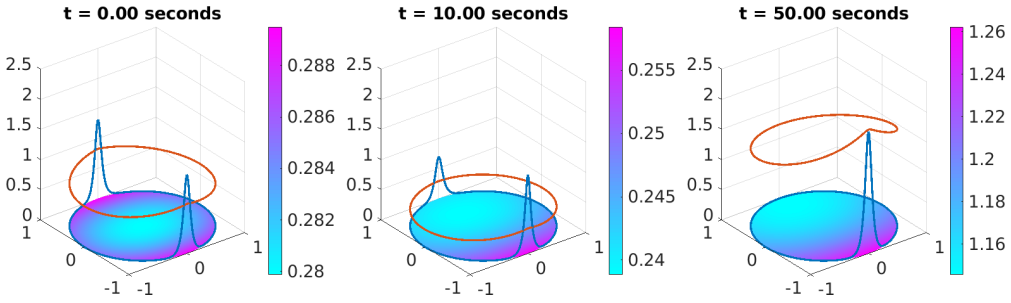

Figure 2.1: Snapshots of the numerically computed solution of (2.1) starting from a 2-spike equilibrium for the unit disk with $\varepsilon = 0.05$, $D_b = 10$, $\tau_s = 0.6$, $\tau_b = 0.1$, $K = 2$, and $D_v = 10$ (this corresponds to point 2 in the left panel of Figure 2.12). The bulk inhibitor is shown as the colour map, whereas the lines along the boundary indicate the activator (blue) and inhibitor (orange) membrane concentrations. The results show a competition instability, leading to the annihilation of a spike.

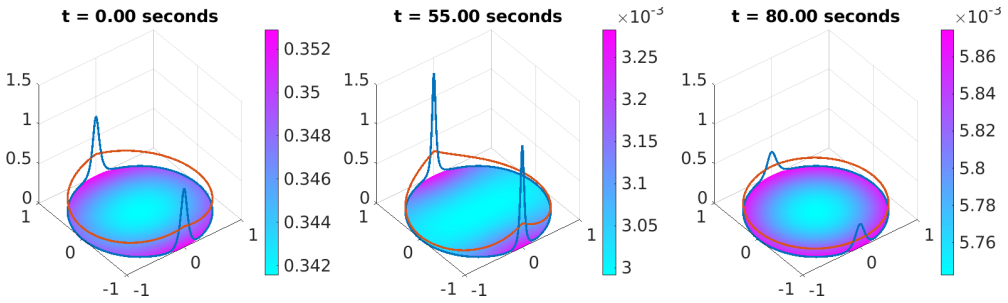

Figure 2.2: Snapshots of the numerically computed solution of (2.1) starting from a 2-spike equilibrium for the unit disk with $\varepsilon = 0.05$, $D_b = 10$, $\tau_s = 0.6$, $\tau_b = 0.1$, $K = 0.025$, and $D_v = 1.8$ (this corresponds to point 5 in the left panel of Figure 2.12). The bulk inhibitor is shown as the colour map, whereas the lines along the boundary indicate the activator (blue) and inhibitor (orange) membrane concentrations. The results show a synchronous oscillatory instability of the spike amplitudes.

when studying synchronous instabilities, for which there appears to be a complex interplay between the membrane and bulk timescales, τ_s and τ_b, as well as with the coupling K. At various specific points in these phase diagrams for both the well-mixed case (with D_b infinite) and the case of the disk (with D_b finite), our linear stability predictions are confirmed with full numerical finite-element simulations of the coupled PDE system (2.1).

As an illustration of spike dynamics resulting from full PDE simulations, in Figures 2.1 and 2.2 we show results computed for the unit disk with $D_b = 10$, showing competition and oscillatory instabilities for a two-spike solution, respectively. The parameter values are given in the figure captions and correspond to specific points in the linear stability phase diagram given in the left panel of Figure 2.12.

In §2.4 we use a regular perturbation analysis to show the effect on the asynchronous instability thresholds of introducing a small smooth perturbation of the boundary of the unit disk. This analysis, which requires a detailed calculation of the perturbed 1-D membrane Green's function, shows that a two-spike pattern can be stabilized by a small outward peanut-shaped deformation of a circular disk. Finally, in §2.5 we briefly summarize our results and highlight some open problems

and directions for future research.

2.2 Spike Equilibrium and its Linear Stability: General Asymptotic Theory

2.2.1 Asymptotic Construction of N-Spike Equilibrium Solution

In this section we provide an asymptotic construction of an N-spike steady-state solution to (2.1). Specifically, we consider the steady-state problem for the membrane species

$$\varepsilon^2\partial_\sigma^2 u_e - u_e + u_e^p/v_e^q = 0, \qquad 0<\sigma<L, \quad u \text{ is } L\text{-periodic}, \tag{2.1a}$$

$$D_v\partial_\sigma^2 v_e - (1+K)v_e + KV_e + \varepsilon^{-1}u_e^m/v_e^s = 0, \qquad 0<\sigma<L, \quad v \text{ is } L\text{-periodic}, \tag{2.1b}$$

which is coupled to the steady-state bulk-diffusion process by

$$D_b\Delta V_e - V_e = 0, \quad x\in\Omega; \qquad D_b\partial_n V_e + KV_e = Kv_e, \quad x\in\partial\Omega. \tag{2.1c}$$

From (2.1c), the bulk-inhibitor evaluated on the membrane is readily expressed in terms of a Green's function as

$$V_e(\sigma) = K\int_0^L G_\Omega(\sigma,\tilde{\sigma})v_e(\tilde{\sigma})\,d\tilde{\sigma}, \tag{2.2}$$

where we have used arc-length to parameterize the boundary. Here, $G_\Omega(\sigma,\tilde{\sigma})$ is the Green's function satisfying

$$\begin{aligned} D_b\Delta_x G_\Omega(x,\tilde{\sigma}) - G_\Omega(x,\tilde{\sigma}) = 0, \quad x\in\Omega \\ D_b\partial_n G_\Omega(\sigma,\tilde{\sigma}) + KG_\Omega(\sigma,\tilde{\sigma}) = \delta(\sigma-\tilde{\sigma}), \quad 0<\sigma<L. \end{aligned} \tag{2.3}$$

We remark that the values of the bulk-inhibitor field within the bulk can likewise be obtained with a Green's function whose source is in the interior. However, for our purposes it is only the restriction to the boundary that is important.

At this stage the steady-state membrane problem takes the form

$$\begin{aligned} \varepsilon^2 \partial_\sigma^2 u_e - u_e + u_e^p / v_e^q &= 0 \\ D_v \partial_\sigma^2 v_e - (1+K) v_e + K^2 \int_0^L G_\Omega(\sigma, \tilde{\sigma}) v_e(\tilde{\sigma})\, d\tilde{\sigma} + \varepsilon^{-1} u_e^m / v_e^s &= 0, \end{aligned} \tag{2.4}$$

for $0 < \sigma < L$ and which differs from the problem studied in [41] for the uncoupled ($K = 0$) case only by the addition of the non-local term. This additional term leads to difficulties in the construction of spike patterns. In particular, it complicates the concept of a "symmetric" pattern since, in general, the non-local term will not be translation invariant. Moreover, in the well-mixed and disk case, the construction of *asymmetric* patterns is more intricate as a result of the non-local term.

We now construct an N-spike steady-state pattern for (2.4) characterized by an activator concentration that is localized at N distinct spike locations $0 \le \sigma_1 < ... < \sigma_N < L$ to be determined. We assume that the spikes are well-separated in the sense that $|\sigma_{\{(i+1) \mod N\}} - \sigma_i \mod L| \gg \varepsilon$ for $i = 1, \ldots, N$. Upon introducing stretched coordinates $y = \varepsilon^{-1}(\sigma - \sigma_j)$, we deduce that the inhibitor field is asymptotically constant near each spike, i. e.

$$v_e \sim v_{ej} \equiv v_e(\sigma_j). \tag{2.5}$$

In addition, the activator concentration is determined in terms of the unique solution $w(y)$ to the core problem

$$\begin{aligned} w'' - w + w^p &= 0, \quad y \in \mathbb{R}, \\ w'(0) = 0, \quad w(0) > 0, \quad w(y) &\to 0 \quad \text{as} \quad |y| \to \infty. \end{aligned} \tag{2.6}$$

Since the solution to the core problem decays exponentially as $y \to \pm\infty$ we deduce that

$$u_e(\sigma) \sim \sum_{j=1}^{N} v_{ej}^{\gamma} w\big(\varepsilon^{-1}[\sigma - \sigma_j]\big), \qquad \text{as} \quad \varepsilon \to 0^+, \tag{2.7}$$

where $\gamma \equiv q/(p-1)$. The solution to (2.6) is given explicitly as

$$w(y) = \left(\frac{p+1}{2}\right)^{\frac{1}{p-1}} \left[\operatorname{sech}\left(\frac{p-1}{2} y\right)\right]^{\frac{2}{p-1}}. \tag{2.8}$$

Next, since u_e is localized, we have in the sense of distributions that

$$\varepsilon^{-1} u_e^m / v_e^s \longrightarrow \omega_m \sum_{j=1}^{N} [v_e(\sigma_j)]^{\gamma m - s} \delta(\sigma - \sigma_j) \qquad \text{as} \quad \varepsilon \to 0^+,$$

where we have defined

$$\omega_m \equiv \int_{-\infty}^{\infty} [w(y)]^m \, dy. \tag{2.9}$$

In this way, for $\varepsilon \to 0^+$, we obtain from (2.4) the following integro-differential equation for the inhibitor field:

$$D_v \partial_\sigma^2 v_e - (1+K) v_e + K^2 \int_0^L G_\Omega(\sigma, \tilde{\sigma}) v_e(\tilde{\sigma}) \, d\tilde{\sigma} = -\omega_m \sum_{j=1}^{N} v_{ej}^{\gamma m - s} \delta(\sigma - \sigma_j).$$

To conveniently represent the solution to this equation we introduce the Green's function $G_{\partial\Omega}(\sigma, \zeta)$ satisfying

$$\begin{aligned} D_v \partial_\sigma^2 G_{\partial\Omega}(\sigma, \zeta) - (1+K) G_{\partial\Omega}(\sigma, \zeta) \\ + K^2 \int_0^L G_\Omega(\sigma, \tilde{\sigma}) G_{\partial\Omega}(\tilde{\sigma}, \zeta) \, d\tilde{\sigma} = -\delta(\sigma - \zeta), \end{aligned} \tag{2.10}$$

for $0 < \sigma, \zeta < L$. In terms of this Green's function, the membrane inhibitor field is given by

$$v_e(\sigma) = \omega_m \sum_{j=1}^{N} v_{ej}^{\gamma m - s} G_{\partial\Omega}(\sigma, \sigma_j). \tag{2.11}$$

Substituting $\sigma = \sigma_i$, and recalling the definition $v_{ei} \equiv v_e(\sigma_i)$, (2.11) yields the N self-consistency conditions

$$v_{ei} - \omega_m \sum_{j=1}^{N} v_{ej}^{\gamma m - s} G_{\partial\Omega}(\sigma_i, \sigma_j) = 0, \qquad i = 1, \ldots, N. \tag{2.12}$$

These conditions provide the first N algebraic equations for our overall system in $2N$ unknowns to be completed below. The remaining N equations arise from solvability conditions when performing a higher-order matched asymptotic expansion analysis of the steady-state solution.

To this end, we again introduce stretched coordinates $y = \varepsilon^{-1}(\sigma - \sigma_j)$, but we

now introduce a two-term inner expansion for the surface bound species for $\varepsilon \to 0$ as

$$\begin{aligned} u_e(y) &\sim v_{ej}^{\gamma} w(y) + \varepsilon u_1(y) + \mathcal{O}(\varepsilon^2), \\ v_e(y) &\sim v_{ej} + \varepsilon v_1(y) + \mathcal{O}(\varepsilon^2), \qquad V_e \sim \mathcal{O}(1). \end{aligned} \tag{2.13}$$

Upon substituting this expansion into (2.1), and collecting the $\mathcal{O}(\varepsilon)$ terms, we get

$$\begin{aligned} \mathcal{L}_0 u_1 \equiv u_1'' - u_1 + p w^{p-1} u_1 &= q v_{ej}^{\gamma-1} w^p v_1, \\ D_v v_1'' + v_{ej}^{\gamma m - s} w^m &= 0. \end{aligned} \tag{2.14}$$

Since $\mathcal{L}_0 w' = 0$, the solvability condition for the first equation yields that

$$q v_{ej}^{\gamma-1} \int_{-\infty}^{\infty} w^p w' v_1 \, dy = 0 \qquad \Longleftrightarrow \qquad \int_{-\infty}^{\infty} (w^{p+1})' v_1 \, dy = 0.$$

Then, we integrate by parts twice, use the exponential decay of $w(y)$ as $|y| \to \infty$, and substitute (2.14) for v_1''. This yields that

$$I_p(y) v_1'(y) \Big|_{-\infty}^{\infty} + \frac{v_{ej}^{\gamma m - s}}{D_v} \int_{-\infty}^{\infty} I_p(y) [w(y)]^m \, dy = 0,$$

where we have defined $I_p(y) \equiv \int_0^y [w(z)]^{p+1} dz$. Since w is even, while I_p is odd, the integral above vanishes, and we get

$$v_1'(+\infty) + v_1'(-\infty) = 0.$$

In this way, a higher order matching process between the inner and outer solutions yields the *balance conditions*,

$$\partial_\sigma v_e(\sigma_i + 0) + \partial_\sigma v_e(\sigma_i - 0) = 0, \qquad i = 1, \ldots, N.$$

By using (2.11) for v_e, we can write these balance equations in terms of the Green's function $G_{\partial\Omega}$ as

$$v_{ei}^{\gamma m - s} \left[\partial_\sigma G_{\partial\Omega}(\sigma_i + 0, \sigma_i) + \partial_\sigma G_{\partial\Omega}(\sigma_i - 0, \sigma_i) \right] + 2 \sum_{j \neq i} v_{ej}^{\gamma m - s} \partial_\sigma G_{\partial\Omega}(\sigma_i, \sigma_j) = 0,$$

for $i = 1,\dots,N$. We summarize the results of this formal asymptotic construction in the following proposition:

Proposition 2.2.1. *As $\varepsilon \to 0^+$ an N-spike steady-state solution to* (2.1) *with spikes centred at $\sigma_1,\dots,\sigma_N$ is asymptotically given by*

$$u_e(\sigma) \sim \sum_{j=1}^{N} v_{ej}^{\gamma} w\big(\varepsilon^{-1}[\sigma-\sigma_j]\big), \qquad v_e(\sigma) \sim \omega_m \sum_{j=1}^{N} v_{ej}^{\gamma m-s} G_{\partial\Omega}(\sigma,\sigma_j), \quad (2.15a)$$

$$V_e(\sigma) \sim \omega_m K \sum_{j=1}^{N} v_{ej}^{\gamma m-s} \int_0^L G_{\Omega}(\sigma,\tilde{\sigma}) G_{\partial\Omega}(\tilde{\sigma},\sigma_j)\, d\tilde{\sigma}, \quad (2.15b)$$

where $\omega_m \equiv \int_{-\infty}^{\infty}[w(y)]^m\, dy$, $\gamma \equiv q/(p-1)$, and G_Ω and $G_{\partial\Omega}$ are the bulk and membrane Green's functions satisfying (2.3) *and* (2.10) *respectively. Here the steady-state spike locations $\sigma_1,\dots,\sigma_N$ and $v_{e1},\dots,v_{eN}$, which determine the heights of the spikes, are to be found from the following non-linear algebraic system:*

$$v_{ei} - \omega_m \sum_{j=1}^{N} v_{ej}^{\gamma m-s} G_{\partial\Omega}(\sigma_i,\sigma_j) = 0, \quad (2.16a)$$

$$v_{ei}^{\gamma m-s}\big[\partial_\sigma G_{\partial\Omega}(\sigma_i+0,\sigma_i) + \partial_\sigma G_{\partial\Omega}(\sigma_i-0,\sigma_i)\big] + 2\sum_{j\neq i} v_{ej}^{\gamma m-s}\partial_\sigma G_{\partial\Omega}(\sigma_i,\sigma_j) = 0, \quad (2.16b)$$

for each $i = 1,\dots,N$.

2.2.2 Linear Stability of N-Spike Equilibrium Solution

In our linear stability analysis, given below, of N-spike equilibrium solutions we make two simplifying assumptions. First, we focus exclusively on the case $s = 0$. Second, we consider only instabilities that arise on an $\mathcal{O}(1)$ timescale. Therefore, we do not consider very weak instabilities, occurring on asymptotically long timescales in ε, that are due to any unstable small eigenvalue that tends to zero as $\varepsilon \to 0$.

Let $u_e(\sigma)$, $v_e(\sigma)$, and $V_e(x)$ denote the the steady-state constructed in §2.2.1. For $\lambda \in \mathbb{C}$, we consider a perturbation of the form

$$u(\sigma) = u_e(\sigma) + e^{\lambda t}\phi(\sigma), \quad v(\sigma) = v_e(\sigma) + e^{\lambda t}\psi(\sigma), \quad V(x) = V_e(x) + e^{\lambda t}\eta(x),$$

where ϕ, ψ, and η are small. Upon substituting into (2.1) and linearizing, we

obtain the eigenvalue problem

$$\varepsilon^2\partial_\sigma^2\phi - \phi + pu_e^{p-1}v_e^{-q}\phi - qu_e^p v_e^{-(q+1)}\psi = \lambda\phi, \qquad 0<\sigma<L, \tag{2.17a}$$

$$D_v\partial_\sigma^2\psi - \mu_{s\lambda}^2\psi + K\eta = -m\varepsilon^{-1}u_e^{m-1}\phi, \qquad 0<\sigma<L, \tag{2.17b}$$

$$D_b\Delta\eta - \mu_{b\lambda}^2\eta = 0, \qquad x\in\Omega, \tag{2.17c}$$

$$D_b\partial_n\eta + K\eta = K\psi, \qquad x\in\partial\Omega, \tag{2.17d}$$

where we have defined $\mu_{s\lambda}$ and $\mu_{b\lambda}$ by

$$\mu_{s\lambda} = \sqrt{1+K+\tau_s\lambda}, \qquad \mu_{b\lambda} = \sqrt{1+\tau_b\lambda}. \tag{2.18}$$

The bulk inhibitor field evaluated on the boundary is represented as

$$\eta(\sigma) = K\int_0^L G_\Omega^\lambda(\sigma,\tilde{\sigma})\psi(\tilde{\sigma})\,d\tilde{\sigma},$$

where G_Ω^λ is the λ-dependent bulk Green's function satisfying

$$\begin{aligned} D_b\Delta_x G_\Omega^\lambda(x,\tilde{\sigma}) - \mu_{b\lambda}^2 G_\Omega^\lambda(x,\tilde{\sigma}) = 0, \quad x\in\Omega, \\ D_b\partial_n G_\Omega^\lambda(\sigma,\tilde{\sigma}) + KG_\Omega^\lambda(\sigma,\tilde{\sigma}) = \delta(\sigma-\tilde{\sigma}), \quad 0<\sigma<L. \end{aligned} \tag{2.19}$$

Next, we seek a localized activator perturbation of the form

$$\phi(\sigma) \sim \sum_{j=1}^N \phi_j\big(\varepsilon^{-1}[\sigma-\sigma_j]\big), \tag{2.20}$$

where we impose that $\phi_j(y)\to 0$ as $|y|\to\infty$. With this form, we evaluate in the sense of distributions that

$$\varepsilon^{-1}mu_e^{m-1}\phi \longrightarrow m\sum_{j=1}^N v_{ej}^{\gamma(m-1)}\left(\int_{-\infty}^{\infty}[w(y)]^{m-1}\phi_j(y)\,dy\right)\delta(\sigma-\sigma_j) \quad \text{as } \varepsilon\to 0^+.$$

By using this limiting result in (2.17b), the problem for ψ becomes

$$D_v\partial_\sigma^2\psi-\mu_{s\lambda}^2\psi+K^2\int_0^L G_\Omega^\lambda(\sigma,\tilde{\sigma})\psi(\tilde{\sigma})\,d\tilde{\sigma} \\ =-m\sum_{j=1}^N v_{ej}^{\gamma(m-1)}\left(\int_{-\infty}^{\infty}[w(y)]^{m-1}\phi_j(y)\,dy\right)\delta(\sigma-\sigma_j).$$

The solution to this problem is represented as

$$\psi(\sigma)=m\sum_{j=1}^N v_{ej}^{\gamma(m-1)}G_{\partial\Omega}^\lambda(\sigma,\sigma_j)\int_{-\infty}^{\infty}[w(y)]^{m-1}\phi_j(y)\,dy, \tag{2.21}$$

where $G_{\partial\Omega}^\lambda$ is the λ-dependent membrane Green's function satisfying

$$D_v\partial_\sigma^2 G_{\partial\Omega}^\lambda(\sigma,\zeta)-\mu_{s\lambda}^2 G_{\partial\Omega}^\lambda(\sigma,\zeta)+K^2\int_0^L G_\Omega^\lambda(\sigma,\tilde{\sigma})G_{\partial\Omega}^\lambda(\tilde{\sigma},\zeta)\,d\tilde{\sigma}=-\delta(\sigma-\zeta), \tag{2.22}$$

for $0<\sigma,\zeta<L$.

Next, it is convenient to re-scale v_e as

$$v_e(\sigma)=\omega_m^{\frac{1}{1-\gamma m}}\hat{v}_e(\sigma),\qquad v_{ej}=\omega_m^{\frac{1}{1-\gamma m}}\hat{v}_{ej}. \tag{2.23}$$

In the stretched coordinates $y=\varepsilon^{-1}(\sigma-\sigma_j)$, we use (2.21) to obtain that (2.17a) becomes

$$\phi_i''-\phi_i+pw^{p-1}\phi_i-mqw^p\sum_{j=1}^N\hat{v}_{ei}^{\gamma-1}G_{\partial\Omega}^\lambda(\sigma_i,\sigma_j)\hat{v}_{ej}^{\gamma(m-1)}\frac{\int_{-\infty}^{\infty}w^{m-1}\phi_j\,dy}{\int_{-\infty}^{\infty}w^m\,dy}=\lambda\phi_i.$$

To recast this spectral problem in vector form we define

$$\boldsymbol{\phi}\equiv\begin{pmatrix}\phi_1\\ \vdots\\ \phi_N\end{pmatrix},\ \hat{\mathscr{V}}_e\equiv\begin{pmatrix}\hat{v}_{e1}&&0\\ &\ddots&\\ 0&&\hat{v}_{eN}\end{pmatrix},\ \mathscr{G}_{\partial\Omega}^\lambda\equiv\begin{pmatrix}G_{\partial\Omega}^\lambda(\sigma_1,\sigma_1)&\cdots&G_{\partial\Omega}^\lambda(\sigma_1,\sigma_N)\\ \cdots&\ddots&\vdots\\ G_{\partial\Omega}^\lambda(\sigma_N,\sigma_1)&\cdots&G_{\partial\Omega}^\lambda(\sigma_N,\sigma_N)\end{pmatrix}, \tag{2.24}$$

and we introduce the matrix $\mathscr{E}$ by

$$\mathscr{E}\equiv\hat{\mathscr{V}}_e^{\gamma-1}\mathscr{G}_{\partial\Omega}^\lambda\hat{\mathscr{V}}_e^{\gamma(m-1)}. \tag{2.25}$$

In this way, we deduce that $\boldsymbol{\phi}$ must solve the vector nonlocal eigenvalue problem (NLEP) given by

$$\boldsymbol{\phi}''(y) - \boldsymbol{\phi}(y) + pw^{p-1}\boldsymbol{\phi}(y) - mqw^p \frac{\int_{-\infty}^{\infty}[w(y)]^{m-1}\mathscr{E}\boldsymbol{\phi}(y)\,dy}{\int_{-\infty}^{\infty}[w(y)]^m\,dy} = \lambda\boldsymbol{\phi}(y). \tag{2.26}$$

We can reduce this vector NLEP to a collection of scalar NLEPs by diagonalizing it. Specifically, we seek perturbations of the form $\boldsymbol{\phi} = \phi\boldsymbol{c}$ where $\boldsymbol{c}$ is an eigenvector of $\mathscr{E}$, that is

$$\mathscr{E}\boldsymbol{c} = \chi(\lambda)\boldsymbol{c}. \tag{2.27}$$

Then, it readily follows that the vector NLEP (2.26) can be recast as the scalar NLEP

$$\mathscr{L}_0\phi - mq\chi(\lambda)w^p \frac{\int_{-\infty}^{\infty}[w(y)]^{m-1}\phi(y)\,dy}{\int_{-\infty}^{\infty}[w(y)]^m\,dy} = \lambda\phi, \tag{2.28}$$

where $\chi(\lambda)$ is any eigenvalue of $\mathscr{E}$. In (2.28), the operator $\mathscr{L}_0$, referred to as the local operator, is defined by

$$\mathscr{L}_0\phi \equiv \phi''(y) - \phi(y) + pw^{p-1}\phi(y). \tag{2.29}$$

Notice that we obtain a (possibly) different NLEP for each eigenvalue $\chi(\lambda)$ of $\mathscr{E}$. Therefore, the spectrum of the matrix $\mathscr{E}$ will be central in the analysis below for classifying the various types of instabilities that can occur.

2.2.3 Reduction of NLEP to an Algebraic Equation and an Explicitly Solvable Case

Next, we show how to reduce the determination of the spectrum of the NLEP (2.28) to a root-finding problem. To this end, we define c_m by

$$c_m \equiv mq\chi(\lambda)\frac{\int_{-\infty}^{\infty}[w(y)]^{m-1}\phi(y)\,dy}{\int_{-\infty}^{\infty}[w(y)]^m\,dy}, \tag{2.30}$$

and write the NLEP as $(\mathscr{L}_0 - \lambda)\phi = c_m w^p$, so that $\phi = c_m(\mathscr{L}_0 - \lambda)^{-1}w^p$. Upon multiplying both sides of this expression by w^{m-1}, we integrate over the real line and substitute the resulting expression back into (2.30). For eigenfunctions for

which $\int_{-\infty}^{\infty} w^{m-1}\phi\, dy \neq 0$, we readily obtain that λ must be a root of $\mathscr{A}(\lambda) = 0$, where

$$\begin{aligned} \mathscr{A}(\lambda) &\equiv \mathscr{C}(\lambda) - \mathscr{F}(\lambda), \quad \mathscr{C}(\lambda) \equiv \frac{1}{\chi(\lambda)}, \\ \mathscr{F}(\lambda) &\equiv mq \frac{\int_{-\infty}^{\infty} [w(y)]^{m-1} (\mathscr{L}_0 - \lambda)^{-1} [w(y)]^p\, dy}{\int_{-\infty}^{\infty} [w(y)]^m\, dy}. \end{aligned} \tag{2.31}$$

Since, it is readily shown that there are no unstable eigenvalues of the NLEP (2.28) for eigenfunctions for which

$$\int_{-\infty}^{\infty} w^{m-1}\phi\, dy = 0,$$

the roots of $\mathscr{A}(\lambda) = 0$ will provide all the unstable eigenvalues of the NLEP (2.28).

For general Gierer-Meinhardt exponents, the spectral theory of the operator $\mathscr{L}_0$ leads to some detailed properties of the term $\mathscr{F}(\lambda)$ for various exponent sets (cf. [105]). In addition, to make further progress on the root-finding problem (2.31), we need some explicit results for the multiplier $\chi(\lambda)$.

For special sets of Gierer-Meinhardt exponents, known as the "explicitly solvable cases" (cf. [70]), the term $\mathscr{F}(\lambda)$ can be evaluated explicitly. We focus specifically on one such set $(p,q,m,0) = (3,1,3,0)$ for which the key identity $\mathscr{L}_0 w^2 = 3w^2$ holds, where $w = \sqrt{2}\,\mathrm{sech} y$ from (2.8). Thus, after integrating by parts we obtain

$$\begin{aligned} \int_{-\infty}^{\infty} w^2 (\mathscr{L}_0 - \lambda)^{-1} w^3 dy &= \frac{\int_{-\infty}^{\infty} (\mathscr{L}_0 - \lambda) w^2 (\mathscr{L}_0 - \lambda)^{-1} w^3 dy}{3 - \lambda} \\ &= \frac{\int_{-\infty}^{\infty} w^2 (\mathscr{L}_0 - \lambda)(\mathscr{L}_0 - \lambda)^{-1} w^3 dy}{3 - \lambda} = \frac{\int_{-\infty}^{\infty} w^5 dy}{3 - \lambda}. \end{aligned}$$

By making use of the identities

$$\int_{-\infty}^{\infty} w^5 dy = \frac{3\pi}{\sqrt{2}}, \qquad \int_{-\infty}^{\infty} w^3 dy = \sqrt{2}\pi,$$

we obtain that $\mathscr{F}(\lambda) = 9/[2(3-\lambda)]$, so that the root-finding problem (2.31) re-

duces to determining λ such that

$$\mathscr{A}(\lambda) \equiv \frac{1}{\chi(\lambda)} - \frac{9/2}{3-\lambda} = 0. \tag{2.32}$$

In addition to the explicitly solvable case $(p,q,m,s) = (3,1,3,0)$, the root-finding problem (2.31) simplifies considerably for a general Gierer-Meinhardt exponent set, when we focus on determining parameter thresholds for zero-eigenvalue crossings (corresponding to asynchronous instabilities). Since $\mathscr{L}_0 w = w'' - w + pw^p = (p-1)w^p$, it follows that $\mathscr{L}_0^{-1} w^p = \frac{1}{p-1} w$, from which we calculate

$$\mathscr{F}(0) = mq \frac{\int_{-\infty}^{\infty} w^{m-1} \mathscr{L}_0^{-1} w^p \, dy}{\int_{-\infty}^{\infty} w^m \, dy} = \frac{mq}{p-1}.$$

Therefore, a zero-eigenvalue crossing for a general Gierer-Meinhardt exponent set occurs when

$$\mathscr{A}(0) = \frac{1}{\chi(0)} - \frac{mq}{p-1} = 0. \tag{2.33}$$

2.3 Symmetric N-Spike Patterns: Equilibrium Solutions and their Stability

For the remainder of this chapter we will focus exclusively on *symmetric* N-spike steady-states that are characterized by equidistant (in arc-length) spikes of equal heights. Due to the bulk-membrane coupling it is unclear whether such symmetric patterns will exist for a general domain. Indeed it may be that a spike pattern with spikes of equal heights may require the equidistant requirement to be dropped. These more general considerations can perhaps be better approached by requiring that the Green's matrix $\mathscr{G}_{\partial\Omega}^{\lambda}$ admit the eigenvector $\mathbf{e} = (1,...,1)^T$. A detailed study of the geometries for which such an eigenvector can be found remains to be done.

Avoiding these additional complications, we focus instead on two distinct cases for which symmetric spike patterns, as we have defined them, can be constructed. The first case is the disk of radius R, denoted by $\Omega = B_R(0)$, and the second case corresponds to the *well-mixed* limit for which $D_b \to \infty$ in an arbitrary bounded domain with C^2 boundary. The membrane and bulk Green's functions in these two

special cases can be found in the Appendices B.1.2 for the well-mixed case, and B.1.3 for the disk. In both cases the Green's function is invariant under translations, satisfying

$$G_{\partial\Omega}(\sigma+\vartheta \mod L, \zeta+\vartheta \mod L) = G_{\partial\Omega}(\sigma,\zeta), \quad \forall\, \sigma,\zeta \in [0,L), \quad \vartheta \in \mathbb{R}.$$

By using this key property in (2.16a), we calculate the common spike height as

$$v_{ej} = v_{e0} = \left[\omega_m \sum_{k=0}^{N-1} G_{\partial\Omega}\left(\frac{kL}{N},0\right)\right]^{\frac{1}{1-\gamma m+s}}. \tag{2.1}$$

With a common spike height, the balance equations (2.16b) then reduce to

$$\left[\partial_\sigma G_{\partial\Omega}(0^+,0) + \partial_\sigma G_{\partial\Omega}(0^-,0)\right] + 2\sum_{k=1}^{N-1} \partial_\sigma G_{\partial\Omega}\left(\frac{kL}{N},0\right) = 0, \tag{2.2}$$

which can be verified either explicitly or by using the symmetry of the Green's function.

For a symmetric N-spike steady-state the NLEP (2.28) can be simplified significantly. First the matrix $\mathscr{E}$, defined in (2.25), simplifies to

$$\mathscr{E} = \hat{v}_{e0}^{\gamma m-1}\mathscr{G}^{\lambda}_{\partial\Omega}.$$

Therefore, from (2.27) it follows that $\chi(\lambda) = \hat{v}_{e0}^{\gamma m-1}\mu(\lambda)$, where $\mu(\lambda)$ is an eigenvalue of the Green's matrix $\mathscr{G}^{\lambda}_{\partial\Omega}$ defined in (2.24). Furthermore, by using the bi-translation invariance and symmetry of $G^{\lambda}_{\partial\Omega}$, we can define

$$H^{\lambda}_{|j-i|} \equiv G^{\lambda}_{\partial\Omega}(|\sigma_i-\sigma_j|,0) = G^{\lambda}_{\partial\Omega}(|i-j|L/N,0), \tag{2.3}$$

which allows us to write the Green's matrix as

$$\mathscr{G}^{\lambda}_{\partial\Omega} = \begin{pmatrix} H^{\lambda}_0 & H^{\lambda}_1 & H^{\lambda}_2 & \cdots & H^{\lambda}_{N-1} \\ H^{\lambda}_{N-1} & H^{\lambda}_0 & H^{\lambda}_1 & \cdots & H^{\lambda}_{N-2} \\ \vdots & \vdots & \vdots & \ddots & \vdots \\ H^{\lambda}_1 & H^{\lambda}_2 & H^{\lambda}_3 & \cdots & H^{\lambda}_0 \end{pmatrix},$$

which we recognize as a *circulant matrix*. As a result, the matrix spectrum of $\mathscr{G}^{\lambda}_{\partial\Omega}$ is readily available as

$$\mu_k(\lambda) = \sum_{j=0}^{N-1} H_j^{\lambda} e^{i\frac{2\pi jk}{N}}, \qquad \boldsymbol{c}_k(\lambda) = \left(1, e^{i\frac{2\pi k}{N}}, \cdots, e^{i\frac{2\pi(N-2)k}{N}}, e^{i\frac{2\pi(N-1)k}{N}}\right)^T, \quad (2.4)$$

for all $k = 0, \ldots, N-1$.

For each value of $k = 0, \ldots, N-1$ we obtain a corresponding NLEP problem from (2.28). Since $\boldsymbol{c}_0 = (1, \ldots, 1)^T$ we can interpret this "mode" as a *synchronous* perturbation. In contrast, the values $k = 1, \ldots, N-1$ for $N \geq 2$ correspond to *asynchronous* perturbations, since the corresponding eigenvectors $\boldsymbol{c}_k(\lambda)$ are all orthogonal to $(1, \ldots, 1)^T$. Any unstable asynchronous "mode" of this type is referred to as a *competition* instability, in the sense that the linear stability theory predicts that the heights of individual spikes may grow or decay, but that the overall sum of all the spike heights remains fixed. For each value of k, the NLEP (2.28) becomes

$$\mathscr{L}_0\phi - mq\chi_k(\lambda) w^p \frac{\int_{-\infty}^{\infty} [w(y)]^{m-1}\phi(y)\,dy}{\int_{-\infty}^{\infty}[w(y)]^m\,dy} = \lambda\phi, \quad (2.5a)$$

where

$$\chi_k(\lambda) \equiv \frac{\mu_k(\lambda)}{\sum_{j=1}^{N-1} G_{\partial\Omega}(jL/N, 0)} = \frac{\mu_k(\lambda)}{\mu_0(0)}. \quad (2.5b)$$

Thus, each NLEP leads to a distinct algebraic system of the form (2.31) corresponding to $\chi_k(\lambda)$ for $k = 0, ..., N$. In particular, for the explicitly solvable case (2.32) becomes

$$\mathscr{A}_k(\lambda) = \frac{1}{\chi_k(\lambda)} - \frac{9/2}{3-\lambda}.$$

In addition, note that when $K = 0$ the bulk dependent term in (2.22) vanishes and $G^{\lambda}_{\partial\Omega}$ reduces to the uncoupled periodic Green's function (see Appendix B.1.1). In such a case the expression for $\chi_k(\lambda)$ in (2.5) reduces to that of the classical uncoupled case. When $K > 0$ further analysis of the NLEP (2.5) requires details of the Green's function $G^{\lambda}_{\partial\Omega}$, which are available in our two special cases.

2.3.1 NLEP Multipliers for the Well-Mixed Limit

In the well-mixed limit, $D_b \to \infty$, the membrane Green's function, satisfying (2.22), is given by (see (B.5) of Appendix B.1)

$$G^{\lambda}_{\partial\Omega}(\sigma,\zeta) = \Gamma^{\lambda}(|\sigma-\zeta|) + \frac{\gamma_\lambda}{\mu^2_{s\lambda}}, \quad \gamma_\lambda \equiv \frac{K^2/A}{\mu^2_{s\lambda}(\mu^2_{b\lambda}+\beta) - K\beta}, \tag{2.6}$$

where $\beta \equiv KL/A$. Here Γ^{λ} is the periodic Green's function for the uncoupled ($K=0$) problem, which is given explicitly by (B.2) of Appendix B.1 as

$$\Gamma^{\lambda}(x) = \frac{1}{2\sqrt{D_v}\mu_{s\lambda}} \coth\left(\frac{\mu_{s\lambda}L}{2\sqrt{D_v}}\right)\cosh\left(\frac{\mu_{s\lambda}}{\sqrt{D_v}}|x|\right) - \frac{1}{2\sqrt{D_v}\mu_{s\lambda}}\sinh\left(\frac{\mu_{s\lambda}}{\sqrt{D_v}}|x|\right).$$

After some algebra we use (2.4) to calculate the eigenvalues $\mu_k(\lambda)$ of the Green's matrix as

$$\begin{aligned}\mu_k(\lambda) &= \sum_{j=0}^{N-1}\Gamma^{\lambda}(jL/n)e^{i\frac{2\pi jk}{N}} + \delta_{k0}\frac{N\gamma_\lambda}{\mu^2_{s\lambda}} \\ &= \frac{1}{2\sqrt{D_v}\mu_{s\lambda}}\frac{\cosh\left(\frac{\mu_{s\lambda}L}{2N\sqrt{D_v}}\right)\sinh\left(\frac{\mu_{s\lambda}L}{2N\sqrt{D_v}}\right)}{\sinh\left(\frac{\mu_{s\lambda}L}{2N\sqrt{D_v}}+\frac{i\pi k}{N}\right)\sinh\left(\frac{\mu_{s\lambda}L}{2N\sqrt{D_v}}-\frac{i\pi k}{N}\right)} + \delta_{k0}\frac{N\gamma_\lambda}{\mu^2_{s\lambda}},\end{aligned}$$

where δ_{k0} is the Kronecker symbol. In this way, we obtain from (2.5) that the NLEP multipliers are given by

$$\chi_0(\lambda) = \frac{\frac{1}{2\sqrt{D_v}\mu_{s\lambda}}\coth\left(\frac{\mu_{s\lambda}L}{2N\sqrt{D_v}}\right) + \frac{N\gamma_\lambda}{\mu^2_{s\lambda}}}{\frac{1}{2\sqrt{D_v}\mu_{s0}}\coth\left(\frac{\mu_{s0}L}{2N\sqrt{D_v}}\right) + \frac{N\gamma_0}{\mu^2_{s0}}}, \tag{2.7a}$$

$$\chi_k(\lambda) = \frac{\frac{1}{2\sqrt{D_v}\mu_{s\lambda}}\frac{\cosh\left(\frac{\mu_{s\lambda}L}{2N\sqrt{D_v}}\right)\sinh\left(\frac{\mu_{s\lambda}L}{2N\sqrt{D_v}}\right)}{\sinh\left(\frac{\mu_{s\lambda}L}{2N\sqrt{D_v}}+\frac{i\pi k}{N}\right)\sinh\left(\frac{\mu_{s\lambda}L}{2N\sqrt{D_v}}-\frac{i\pi k}{N}\right)}}{\frac{1}{2\sqrt{D_v}\mu_{s0}}\coth\left(\frac{\mu_{s0}L}{2N\sqrt{D_v}}\right) + \frac{N\gamma_0}{\mu^2_{s0}}}, \tag{2.7b}$$

for $k = 1,...,N-1$. We observe from the $\chi_0(\lambda)$ term in (2.7), that any synchronous instability will depend on the membrane diffusivity D_v only in the form N^2D_v. This shows that a synchronous instability parameter threshold will be fully determined

by the one-spike case upon rescaling by $1/N^2$. We remark here that the numerator for $\chi_k(\lambda)$ can be simplified by using the identity $\sinh(z+ia)\sinh(z-ia) = \frac{1}{2}[\cosh(2z)-\cos(2a)]$ so that $\chi_k(\lambda)$ is real valued whenever $\mathrm{Im}\lambda = 0$.

2.3.2 NLEP Multipliers for the Disk

In the disk we can calculate the membrane Green's function as a Fourier series (see (B.7) of Appendix B.1)

$$G^{\lambda}_{\partial\Omega}(\sigma,\zeta) = \frac{1}{2\pi R}\sum_{n=-\infty}^{\infty} g^{\lambda}_n e^{i\frac{n}{R}(\sigma-\zeta)}, \tag{2.8}$$

where g^{λ}_n is given explicitly by

$$g^{\lambda}_n = \frac{1}{D_v\left(\frac{n}{R}\right)^2 + \mu^2_{s\lambda} - K^2 a^{\lambda}_n} \tag{2.9a}$$

and where

$$a^{\lambda}_n = \frac{1}{D_b P_n'(R) + K}, \quad P_n(r) \equiv \frac{I_{|n|}(\omega_{b\lambda} r)}{I_{|n|}(\omega_{b\lambda} R)}, \quad \omega_{b\lambda} \equiv \frac{\mu_{b\lambda}}{\sqrt{D_b}}. \tag{2.9b}$$

Here $I_n(z)$ is the n^{th} modified Bessel function of the first kind. From (2.4) the eigenvalues of the Green's matrix become

$$\mu_k(\lambda) = \frac{1}{2\pi R}\sum_{n=1}^{\infty} g^{\lambda}_n \sum_{j=0}^{N-1} e^{i\frac{2\pi(k+n)j}{N}}.$$

By using the identities

$$\sum_{j=0}^{N-1} e^{i\frac{2\pi(k+n)j}{N}} = \begin{cases} N & n \in N\mathbb{Z}-k, \\ 0 & \text{otherwise} \end{cases}, \qquad \text{and} \qquad g^{\lambda}_{-n} = g^{\lambda}_n,$$

the eigenvalues are given explicitly by

$$\mu_k(\lambda) = \frac{N}{2\pi R} g^{\lambda}_k + \frac{N}{2\pi R}\sum_{n=1}^{\infty}\left(g^{\lambda}_{nN+k} + g^{\lambda}_{nN-k}\right).$$

Therefore, since $\chi_k(\lambda) = \mu_k(\lambda)/\mu_0(0)$, the NLEP multipliers are given by

$$\chi_k(\lambda) = \frac{g_k^\lambda + \sum_{n=1}^{\infty}\left(g_{nN+k}^\lambda + g_{nN-k}^\lambda\right)}{g_0^0 + 2\sum_{n=1}^{\infty} g_{nN}^0}, \qquad k = 0,\ldots,N-1. \tag{2.10}$$

2.3.3 Synchronous Instabilities

From (2.33), and the special form of $\chi_k(\lambda)$ given in (2.5), we deduce that

$$\mathscr{A}_0(0) = 1 - \frac{mq}{p-1} < 0,$$

where the strict inequality follows from the the usual assumption (2.2) on the Gierer-Meinhardt exponents. As a result, synchronous instabilities do not occur through a zero-eigenvalue crossing, and can only arise through a Hopf bifurcation. To examine whether such a Hopf bifurcation for the synchronous mode can occur, we now seek purely imaginary zeros of $\mathscr{A}_0(\lambda)$. Classically, in the uncoupled case $K = 0$, such a threshold occurs along a Hopf bifurcation curve $D_v = D_v^\star(\tau_s)$ (cf. [105]). We have an oscillatory instability if τ_s is sufficiently large, and no such instability when τ_s is small (cf. [105], [106]). Bulk-membrane coupling introduces two additional parameters, τ_b and K, in addition to the quantities L and A for the well-mixed case, or R and D_b for the case of the disk. Thus, it is no longer clear how the existence of a synchronous instability threshold $D_v = D_v^\star(\tau_s)$ will be modified by the additional parameters. Indeed, the analysis below reveals a variety of new phenomenon such as the existence of synchronous instabilities for $\tau_s = 0$ and islands of stability for large values of τ_s. These are two behaviours that do not occur for the classical uncoupled case $K = 0$.

We begin by addressing the question of the existence of synchronous instability thresholds. The key assumption (supported below by numerical simulations) underlying this analysis is that synchronous instabilities persist as either the bulk and/or membrane diffusivities increase. While this assumption is heuristically reasonable (large diffusivities make it easier for neighbouring spikes to communicate) an open problem is to demonstrate it analytically. With this assumption it suffices to seek parameter values of τ_b, τ_s, and K for which no Hopf bifurcations exist when $D_v \to \infty$ in the well-mixed limit $D_b \to \infty$.

As a first step, we remark that in [105] it was shown that $\mathrm{Re}\mathscr{F}(i\lambda_I)$ is monotone decreasing when $\lambda_I > 0$ for special choices of the Gierer-Meinhardt exponents (see also [106]). The monotonicity of this function for general Gierer-Meinhardt exponents is supported by numerical calculations. Thus we expect that $\mathrm{Re}\mathscr{F}(i\lambda_I)$ decreases monotonically from $\mathrm{Re}\mathscr{F}(0) = \frac{mq}{p-1} > 1$ as $\lambda_I > 0$ increases. Furthermore, numerical evidence suggests that $\mathrm{Re}\mathscr{C}_0(i\lambda_I)$ is monotone increasing in λ_I. Since $\mathscr{C}_0(0) = 1$ there must exist a unique root $\lambda_I = \lambda_I^\star > 0$ to $\mathrm{Re}\mathscr{A}_0(i\lambda_I) = 0$ bounded above by λ_I^F, the unique solution to $\mathrm{Re}\mathscr{F}(i\lambda_I^F) = 1$, which depends solely on the exponents $(p,q,m,0)$. Therefore in the limit $D_v \to \infty$ the well-mixed NLEP multiplier, as given in (2.7), becomes

$$\chi_0(\lambda) \sim \frac{\mu_{s0}^2(\mu_{b0}^2+\beta) - K\beta}{\mu_{s\lambda}^2(\mu_{b\lambda}^2+\beta) - K\beta}\left(\frac{\mu_{b\lambda}^2+\beta}{\mu_{b0}^2+\beta}\right).$$

Seeking a purely imaginary root of $\mathscr{A}_0(\lambda) = 0$ we focus first on the real part. We calculate

$$\mathrm{Re}\mathscr{A}_0(i\lambda_I) = \frac{1+\beta}{1+\beta+K}\left(1+K - \frac{K\beta}{1+\beta}\frac{1}{1+\left(\frac{\tau_b\lambda_I}{1+\beta}\right)^2}\right) - \mathrm{Re}\mathscr{F}(i\lambda_I),$$

and note that the root $\lambda_I = \lambda_I^\star(\tau_b, K)$ to $\mathrm{Re}\mathscr{A}_0(i\lambda_I) = 0$ is independent of τ_s. Next, for the imaginary part we calculate

$$\mathrm{Im}\mathscr{A}_0(i\lambda_I^\star) = \frac{1+\beta}{1+\beta+K}\left(\tau_s + \frac{K\beta}{1+\beta}\frac{\frac{\tau_b}{1+\beta}}{1+\left(\frac{\tau_b\lambda_I^\star}{1+\beta}\right)^2}\right)\lambda_I^\star - \mathrm{Im}\mathscr{F}(i\lambda_I^\star).$$

Fortunately, at each fixed value of τ_s the threshold $K = K(\tau_b)$ can be calculated as the τ_s-level-set of a function depending only on K and τ_b. Indeed the condition $\mathrm{Im}\mathscr{A}_0(i\lambda_I^\star) = 0$ can equivalently be written as

$$\mathrm{Im}\mathscr{A}_0(i\lambda_I^\star) = \frac{1+\beta}{1+\beta+K}\Big(\tau_s - \mathscr{M}(\tau_b, K)\Big)\lambda_I^\star = 0, \tag{2.11}$$

where we have defined

$$\mathscr{M}(\tau_b, K) \equiv \left(\frac{1+\beta+K}{1+\beta}\right)\frac{\mathrm{Im}\mathscr{F}(i\lambda_I^\star)}{\lambda_I^\star} - \frac{K\beta}{1+\beta}\left(\frac{\frac{\tau_b}{1+\beta}}{1+\left(\frac{\tau_b\lambda_I^\star}{1+\beta}\right)^2}\right). \tag{2.12}$$

In the $(p,q,m,s) = (3,1,3,0)$ explicitly solvable case we find that $\mathrm{Im}\mathscr{F}(i\lambda_I^\star) = \frac{1}{3}\lambda_I^\star \mathrm{Re}\mathscr{F}(i\lambda_I^\star)$, so that by solving $\mathrm{Re}\mathscr{A}_0(i\lambda_I) = 0$ for $\mathrm{Re}\mathscr{F}(i\lambda_I^\star)$, (2.12) becomes

$$\mathscr{M}(\tau_b, K) = \frac{1+K}{3} - \frac{K\beta}{1+\beta}\left(\frac{\frac{\tau_b}{1+\beta}+\frac{1}{3}}{1+\left(\frac{\tau_b\lambda_I^\star}{1+\beta}\right)^2}\right).$$

By substituting this expression into (2.11), we deduce the existence of two distinct threshold branches obtained by considering the limits $K \gg 1$ and $K \ll 1$. In this way, we derive

$$\begin{aligned}
&\tau_s - \mathscr{M}(\tau_b, K) \sim \tau_s - \frac{1}{3} + \frac{1}{\beta_0}\left(\tau_b - \frac{1}{3}\right) + \mathscr{O}(K^{-1}) \qquad \text{for} \quad K \gg 1, \\
&\tau_s - \mathscr{M}(\tau_b, K) \sim \tau_s - \frac{1}{3} - \frac{1}{3}K + \mathscr{O}(K^2) \qquad \text{for} \qquad K \ll 1,
\end{aligned}$$

where $\beta_0 \equiv L/A$. Notice that in ordering both of these asymptotic expansions we have used that $0 < \lambda_I^\star \leq \lambda_I^F$, where the upper bound is independent of K. In the $K \gg 1$ regime we deduce that if $\tau_b = \frac{1}{3} - \beta_0\left(\tau_s - \frac{1}{3}\right)$, then $\mathrm{Im}\mathscr{A}_0(i\lambda_I^\star) = 0$ forces $K \to \infty$, implying the existence of a threshold branch emerging from $K = \infty$ at these parameter values. We remark here that in the $K = \infty$ limit we have $V = v$ on the boundary and therefore the contribution of V to the membrane equation is just the Dirichlet to Neumann map of v. Furthermore, since τ_b approaches 0 when τ_s tends to $\frac{1}{3}\left(\frac{1}{\beta_0}+1\right)$, we deduce that this branch will disappear for sufficiently large values of τ_s. In addition, in the $K \ll 1$ regime we find that a new branch given by $K \approx 3\tau_s - 1$ emerges when $\tau_s > \frac{1}{3}$. The left panel of Figure 2.3 shows the numerically-computed contours of $\mathscr{M}(\tau_b, K)$ for the explicitly solvable case $(p,q,m,s) = (3,1,3,0)$. The right panel of Figure 2.3 shows a qualitatively similar behaviour that occurs for the prototypical Gierer-Meinhardt parameter set $(p,q,m,s) = (2,1,2,0)$.

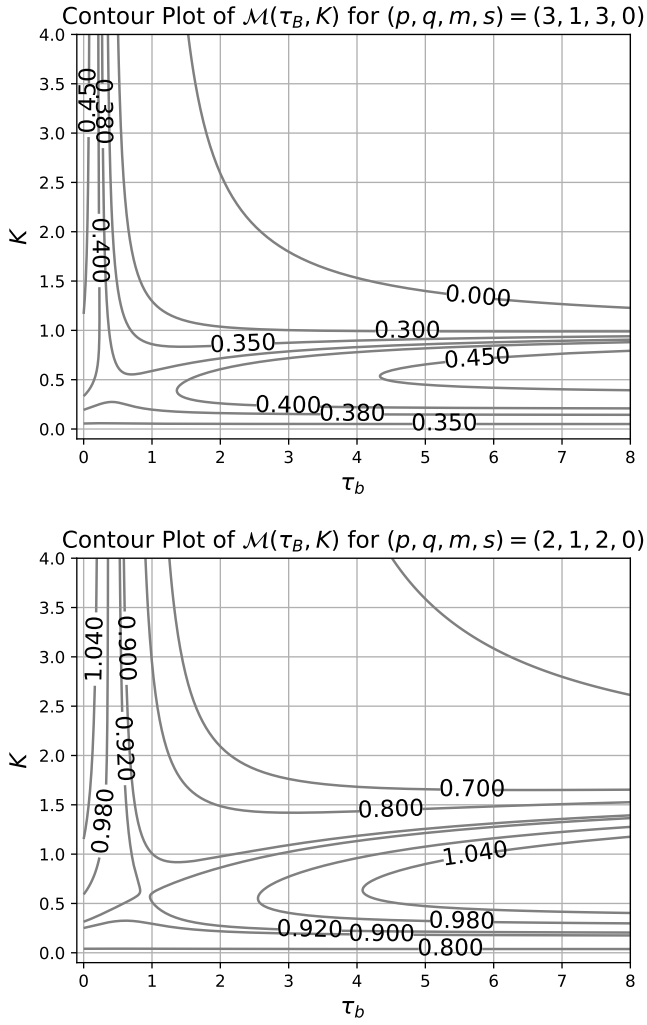

Figure 2.3: Level sets of $\mathscr{M}(\tau_b, K)$ for Gierer-Meinhardt exponents $(p,q,m,s) = (3,1,3,0)$ (left) and $(p,q,m,s) = (2,1,2,0)$ (right). In both cases the level set value corresponds to a value of $\tau_s = \mathscr{M}(\tau_b, K)$. Note also the contours tending to a vertical asymptote, and the emergence of a horizontal asymptote as τ_s exceeds some threshold. Geometric parameters are $L = 2\pi$ and $A = \pi$.

The preceding analysis does not directly predict in which regions synchronous instabilities exist, as it only provides the boundaries of these regions. We now

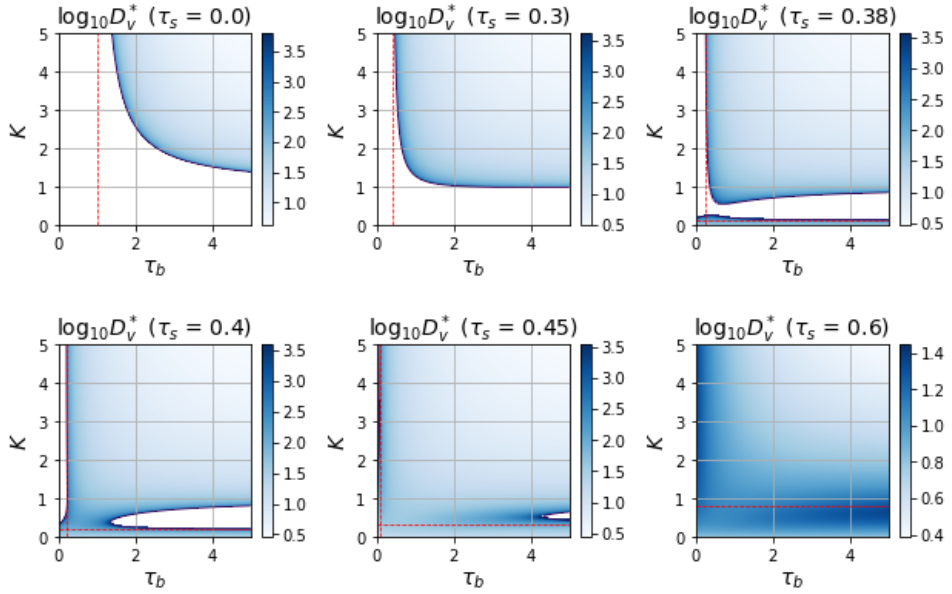

Figure 2.4: Colour map of the synchronous instability threshold $D_v^\star$ in the K versus τ_b parameter plane for the well-mixed explicitly solvable case for various values of τ_s with $L = 2\pi$ and $A = \pi$. The dashed vertical lines indicate the asymptotic predictions for the large K threshold branch, while the dashed horizontal lines indicate the asymptotic predictions for the small K threshold branch. The unshaded regions correspond to those parameter values for which synchronous instabilities are absent.

outline a winding-number argument, related to that used in [106], that provides a hybrid analytical-numerical algorithm for calculating the synchronous instability threshold $D_v = D_v^\star(K, \tau_b, \tau_s)$. Furthermore, as we show below, this algorithm indicates that synchronous instabilities exist whenever $\mathscr{M}(\tau_b, K) < \tau_s$.

Synchronous instabilities are identified with the zeros to (2.31) having a positive real-part when $\chi(\lambda)$ in (2.31) is replaced by $\chi_0(\lambda)$. By using a winding number argument, the search for such zeros can be reduced from one over the entire right-half plane $\mathrm{Re}(\lambda) > 0$ to one along only the positive imaginary axis. Indeed, if we consider a counterclockwise contour composed of a segment of the imaginary axis, $-\rho \leq \mathrm{Im}\lambda \leq \rho$, together with the semi-circle defined by $|\lambda| = \rho$ and

$-\pi/2 < \arg\lambda < \pi/2$, then in the limit $\rho \to \infty$ the change in the argument as the contour is traversed is

$$\Delta\arg \mathscr{A}_0(\lambda) = 2\pi(Z-1), \tag{2.13}$$

where Z is the number of zeros of $\mathscr{A}_0$ with positive real-part. Here we have used that $\chi_0(\lambda) \neq 0$ when $\mathrm{Re}(\lambda) \geq 0$, while $\mathscr{F}(\lambda)$ has exactly one simple (and real) pole in the right-half plane corresponding to the only positive eigenvalue of the self-adjoint local operator $\mathscr{L}_0$ (cf. [107]). We immediately note that $\mathscr{F}(\lambda) = \mathscr{O}(\lambda^{-1})$ for $|\lambda| \gg 1$, $|\arg\lambda| < \pi/2$, whereas for $|\lambda| \gg 1$ and $|\arg\lambda| < \pi/2$

$$\mathscr{C}_0(\lambda) \sim 2\mu_0(0)\sqrt{\tau_s D_v}\lambda^{1/2}, \quad \mathscr{C}_0(\lambda) \sim \mu_0(0)\frac{N\sqrt{D_v\tau_s}}{\pi R}\lambda^{1/2}, \tag{2.14}$$

for the well-mixed limit and the disk cases, respectively. Therefore, in both cases we have $\mathscr{A}_0(\lambda) \sim \mathscr{O}(\lambda^{1/2})$ for $|\lambda| \gg 1$ with $|\arg\lambda| < \pi/2$, so that the change in argument over the large semi-circle is $\pi/2$. Furthermore, since the parameters in $\mathscr{A}_0(\lambda)$ are real-valued, the change in argument over the segment of the imaginary axis can be reduced to that over the positive imaginary axis. In this way, we deduce that

$$Z = \frac{5}{4} + \frac{1}{\pi}\Delta\arg\mathscr{A}_0(i\lambda_I)\big|_{\lambda_I\in(\infty,0]}. \tag{2.15}$$

We readily evaluate the limiting behaviour $\lim_{\lambda_I\to\infty}\arg\mathscr{A}_0(i\lambda_I) = \pi/4$. Moreover since $\chi_0(0) = 1$ we evaluate $\mathscr{A}_0(0) = 1 - \frac{mq}{p-1} < 0$ by the assumption (2.2) on the Gierer-Meinhardt exponents. Numerical evidence suggests that $\mathrm{Re}\mathscr{A}_0(i\lambda_I)$ increases monotonically with λ_I and there should therefore be a unique $\lambda_I^\star$ for which $\mathrm{Re}\mathscr{A}_0(i\lambda_I^\star) = 0$. We conclude that there are two positive values for the change in argument, and hence the number of zeros of $\mathscr{A}_0(\lambda)$ in $\mathrm{Re}(\lambda) > 0$ is dictated by the sign of $\mathrm{Im}\mathscr{A}_0(i\lambda_I^\star)$ as follows:

$$Z = 2 \quad \text{if} \quad \mathrm{Im}\mathscr{A}_0(i\lambda_I^\star) > 0, \qquad \text{or} \qquad Z = 0 \quad \text{if} \quad \mathrm{Im}\mathscr{A}_0(i\lambda_I^\star) < 0. \tag{2.16}$$

Note in particular that, in view of the expression (2.11) for $\mathrm{Im}\mathscr{A}_0(i\lambda_I)$, this criterion implies that synchronous instabilities will exist whenever $M(\tau_b, K) < \tau_s$ in the previous analysis. Within this region, the criterion (2.16) suggests a simple numerical algorithm for iteratively computing the threshold value of $D_v = D_v^\star(K, \tau_b, \tau_s)$.

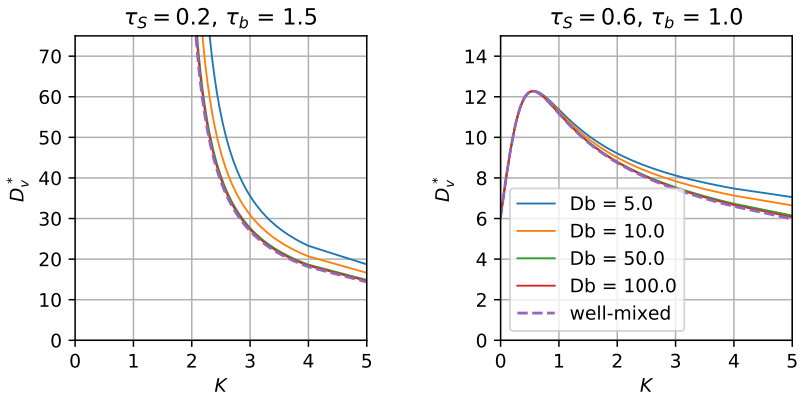

Figure 2.5: Synchronous instability threshold $D_v^\star$ versus K for two pairs of (τ_s, τ_b) for a one-spike steady-state ($N = 1$) in the unit disk ($R = 1$). The quality of the well-mixed approximation rapidly improves as D_b is increased. The labels for D_b in the right panel also apply to the left and middle panels.

Specifically, with all parameters fixed, we first solve $\mathrm{Re}\mathscr{A}_0(i\lambda_I) = 0$ for λ_I^0. Then, we calculate $\mathrm{Im}\mathscr{A}_0(i\lambda_I^0)$ and increase (resp. decrease) D_v if $\mathrm{Im}\mathscr{A}_0(i\lambda_I^0) < 0$ (resp. $\mathrm{Im}\mathscr{A}_0(i\lambda_I^0) > 0$ until $\mathrm{Im}\mathscr{A}_0(i\lambda_I^0) = 0$. This procedure is repeated until $|\mathscr{A}_0(i\lambda_I^0)|$ is sufficiently small.

Using the algorithm described above, the results in Figure 2.4 illustrate how the synchronous instability threshold $D_v^\star$ depends on parameters τ_s, τ_b, and K for the explicitly solvable case in the well-mixed limit. From these figures we observe that coupling can have both a stabilizing and a destabilizing effect with respect to synchronous instabilities. Indeed, on the $K = 0$ axis we see, as expected from the classical theory, that synchronous instabilities exist beyond some τ_s value. However, well before this threshold of τ_s is even reached it is possible for synchronous instabilities to exist when both τ_b and K are sufficiently large. In contrast, we also see from the panels in Fig. 2.4 with $\tau_s = 0.36$, $\tau_s = 0.38$, and $\tau_s = 0.4$ that when τ_b is sufficiently small, there are no synchronous instabilities when the coupling K is large enough. Perhaps the most perplexing feature of this bulk-membrane interaction is the island of stability that arises around $\tau_s = 0.4$ and appears to per-

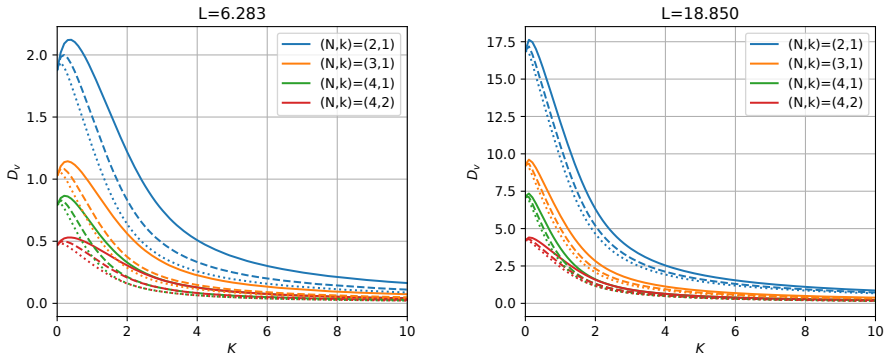

Figure 2.6: Asynchronous instability thresholds D_v versus the coupling K in the well-mixed limit for different values of L, different (N,k) pairs, and for domain areas $A = 3.142$ (solid), 1.571 (dashed), and 0.785 (dotted).

sist, propagating to larger values of τ_b as τ_s increases (only shown up to $\tau_s = 0.6$). Finally in Figure 2.5 we demonstrate how the synchronous instability threshold behaves for finite bulk-diffusivity. A key observation from these plots is that that the instability threshold increases with decreasing value of D_b, which further supports our earlier monotonicity assumption.

2.3.4 Asynchronous Instabilities

Since asynchronous instabilities emerge from a zero-eigenvalue crossing there are two significant simplifications. Firstly, the thresholds are determined by the nonlinear algebraic problem $\mathscr{A}_k(0) = 0$, for each mode $k = 1,\ldots,N-1$, as given by (2.31) in which $\chi(\lambda)$ is replaced by $\chi_k(\lambda)$ as defined in (2.5). Secondly, by setting $\lambda = 0$, it follows that all τ_s and τ_b dependent terms in $\chi_k(\lambda)$ vanish. Therefore, asynchronous instability thresholds are independent of these two parameters. The resulting nonlinear algebraic equations are readily solved with an appropriate root finding algorithm (e.g. the brentq routine in the Python library SciPy). Furthermore, in the uncoupled case ($K = 0$) the threshold can be determined explicitly (notice that when $K = 0$ the well-mixed and disk cases coincide). Indeed, defining $z = \frac{L}{2N\sqrt{D_v}}$ and $y = \pi k/N$, the algebraic problem $\mathscr{A}_k(0) = 0$ becomes

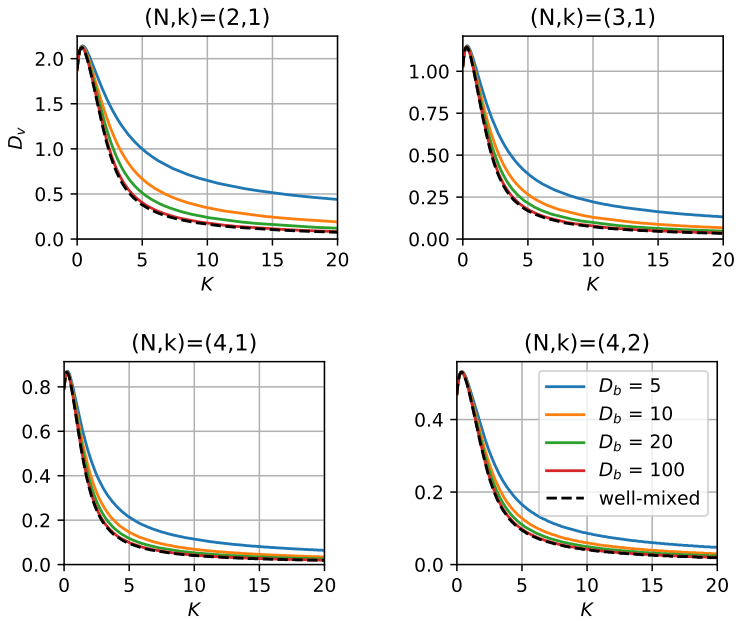

Figure 2.7: Asynchronous instability thresholds D_v versus the coupling K for the unit disk with Gierer-Meinhardt exponents $(3,1,3,0)$, and for different D_b. The dashed lines show the corresponding thresholds for the well-mixed limit. The legend in the bottom right plot applies to each plot.

$\left(\frac{mq}{p-1}-1\right)\sinh^2(z)=\sin^2(y)$. From this relation it readily follows that the competition stability threshold for $K=0$ is

$$D_v=\left[\frac{2N}{L}\log\left(\sqrt{\tfrac{p-1}{mq-p+1}}\left|\sin\left(\frac{\pi k}{N}\right)\right|+\sqrt{\tfrac{p-1}{mq-p+1}\sin^2\left(\frac{\pi k}{N}\right)+1}\right)\right]^{-2}. \quad (2.17)$$

Figure 2.6 illustrates the dependence of the asynchronous threshold on the geometric parameters L and A for the well-mixed limit. In Figure 2.7 the effect of finite bulk diffusivity D_b is explored for the unit disk. This figure also illustrates that while the asynchronous threshold tends to zero as $K\to\infty$ for sufficiently large values of D_b the same is not true for small values of D_b. It is however worth remembering that for large K, where the competition threshold value of D_v appears to approach zero in these figures, the result is not uniformly valid since the NLEP

derivation required that $D_v \gg \varepsilon^2$.

2.3.5 Numerical Support of the Asymptotic Theory

In this subsection we verify some of the predictions of the steady-state and linear stability theory by performing full numerical PDE simulations of the coupled bulk-membrane system (2.1). In particular we first give an outline of the numerical method used for solving (2.1). We then use full numerical simulations to quantitatively support our predicted synchronous instability threshold. Finally we consider a gallery of numerical simulations that qualitatively support the asymptotic theory developed above.

Outline of Numerical Methods

The spatial discretization of (2.1) in the well-mixed limit is simplified by observing that equation (2.1c) reduces to an ODE. In particular, to leading order V must be spatially homogeneous so that by integrating (2.1c) and using the divergence theorem we obtain that $V(t)$ must satisfy the ODE

$$\tau_b V_t = -(\beta - 1)V + \frac{\beta}{L}\int_0^L v\, d\sigma. \tag{2.18}$$

The remaining equations (2.1a) and (2.1b) can be discretized using a finite-difference method on a uniform discretization of the interval $[0, L]$. Using this same discretization we can numerically evaluate the integral appearing in (2.18) using the trapezoidal rule.

When the bulk diffusivity D_b is finite we use the finite-element method with linear basis functions for the bulk equation (2.1c). Using the nodes on the boundary of the bulk triangulation we can use the finite difference method to discretize the boundary equations (2.1a) and (2.1b). This aspect of the computation is simplified by enforcing the bulk-triangulation to have boundary nodes that are uniformly distributed with respect to the arc-length. In addition, we remark that the relevant integral contribution of $v(x,t)$ to the bulk finite-element discretization requires only the values of $v(x,t)$ at the boundary nodes as can be seen by expanding $v(x,t)$ in terms of the restriction of the linear basis functions to the boundary.

For both the well-mixed case and the disk problem, the spatial discretization ultimately leads to a large system of ODEs

$$\frac{dW}{dt} = \mathbb{A}W + F(W). \tag{2.19}$$

Here the matrix $\mathbb{A}$ arises from the spatially discretized differential operators, while $F(W)$ denotes the reaction kinetics and the bulk-membrane coupling terms.

The choice of a time-stepping scheme for reaction diffusion systems is generally non-trivial. Since the operator $\mathbb{A}$ is stiff, it is best handled using an implicit time-stepping method. On the other hand, the kinetics $F(W)$ are typically non-linear so explicit time-stepping is favourable. Using a purely implicit or explicit time-stepping algorithm therefore leads to substantial computation time, either by requiring the use of a non-linear solver to handle the kinetics in the first case, or by requiring a prohibitively small time-step to handle the stiff linear operator in the second case. This difficulty can be circumvented by using so-called mixed methods, specifically the implicit-explicit methods described in [2]. We will use a second order semi-implicit backwards difference scheme (2-SBDF), which employs a second-order backwards difference to handle the diffusive term together with an explicit time-stepping strategy for the nonlinear term (cf. [85]). This time-stepping strategy is given by

$$(3\mathbb{I} - 2\Delta t\mathbb{A})W^{n+1} = 4W^n + 4\Delta t F(W^n) - W^{n-1} - 2\Delta t F(W^{n-1}). \tag{2.20}$$

To initialize this second-order method we bootstrap with a first order semi-implicit backwards difference scheme (1-SBDF) as follows:

$$(\mathbb{I} - \Delta t\mathbb{A})W^{n+1} = W^n + \Delta t F(W^n). \tag{2.21}$$

We will use the numerical method outlined above in the two proceeding sections.

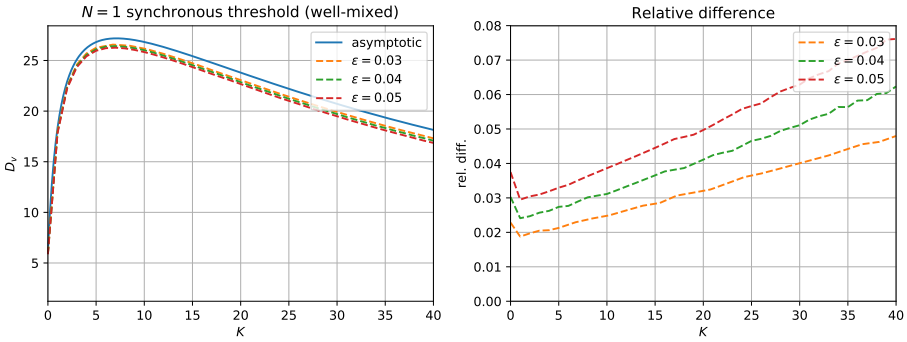

Figure 2.8: Comparison between numerical and asymptotic synchronous instability threshold for $N = 1$ with $L = 2\pi, A = \pi$, $\tau_s = 0.6$, and $\tau_b = 0.01$. Notice that, as expected, the agreement improves as ε decreases.

Quantitative Numerical Validation: Numerically Computed Synchronous Threshold

We begin by describing a method for numerically calculating the synchronous instability threshold for a one (or more) spike pattern. Given an equilibrium solution (u_0, v_0, V_0), for sufficiently small times the numerical solution will evolve approximately as the linearization

$$u(\sigma,t) = u_0(\sigma) + e^{\lambda t}\phi(\sigma), \quad v(\sigma,t) = v_0(\sigma) + e^{\lambda t}\psi(\sigma), \quad V(\sigma,t) = V_0(\sigma) + e^{\lambda t}\eta(\sigma).$$

For $\varepsilon > 0$ fixed and sufficiently small the steady-state will be very close to that predicted by the asymptotic theory. By initializing the numerical solver with one of the steady-state solutions predicted by the asymptotic theory, and then tracking its time evolution, we will thus be able to approximate the value of $\mathrm{Re}(\lambda)$. If we fix a location on the boundary $\sigma^\star$ (e.g. one of the spike locations) and let $t_1^\star < t_2^\star < \ldots$ denote the sequence of times at which $u(\sigma^\star, t)$ attains a local maximum or minimum in t, then the sequence $u_j^\star = u(\sigma^\star, t_j^\star)$ $(j = 1, ..,)$ will approximate the envelope of $u(\sigma^\star, t)$. If this sequence is diverging from its average then $\mathrm{Re}\lambda \geq 0$, whereas if it is converging then $\mathrm{Re}\lambda < 0$. Furthermore, by writing

$$|u_n^\star - u_0(\sigma^\star)| \approx e^{t_n \mathrm{Re}(\lambda)} |\phi(\sigma^\star)|,$$

we can solve for $\mathrm{Re}(\lambda)$ by taking two values $t_n^\star > t_m^\star$ sufficiently far apart to get

$$\mathrm{Re}(\lambda) \approx \frac{\log\left|u_n^\star - u_0(\sigma^\star)\right| - \log\left|u_m^\star - u_0(\sigma^\star)\right|}{t_n^\star - t_m^\star}.$$

This motivates a simple method for estimating the synchronous instability threshold numerically. Starting with some point in parameter space (chosen close to the threshold predicted by the asymptotic theory) we approximate $\mathrm{Re}(\lambda)$ and then increase or decrease one of the parameters to drive $\mathrm{Re}(\lambda)$ toward zero. Once $\mathrm{Re}(\lambda)$ is sufficiently close to zero we designate the resulting point in parameter space as a numerically-computed synchronous instability threshold point.

In the well-mixed limit, we fix values of K and vary D_v using the numerical approach described above until $\mathrm{Re}(\lambda)$ is sufficiently small. The results in Figure 2.8 compare the synchronous instability threshold for $N = 1$ in the well-mixed limit as predicted by the asymptotic theory and by our full numerical approach for $\varepsilon = 0.3, 0.4, 0.5$. We observe, as expected, that the asymptotic prediction improves with decreasing values of ε, but that the agreement is non-uniform in the coupling parameter K.

Qualitative Numerical Support: A Gallery of Numerical Simulations

We conclude this section by first showcasing the dynamics of multiple spike patterns for several choices of the parameters K, D_v, τ_s, and τ_b in the well-mixed limit. We will focus exclusively on the explicitly solvable Gierer-Meinhardt exponent set $(p,q,m,s) = (3,1,3,0)$ with $\varepsilon = 0.05$ and the geometric parameters $L = 2\pi$ and $A = \pi$. For the numerical computation we discretized the domain boundary with 1200 uniformly distributed points ($\Delta\sigma \approx 0.00524$) and used trapezoidal integration for the bulk-inhibitor equation (2.18). Furthermore, we used 2-SBDF time-stepping initialized by 1-SBDF with a time-step size of $\Delta t = 2.5(\Delta\sigma)^2 \approx 6.854 \times 10^{-4}$. In Figure 2.9 we plot the asymptotically predicted synchronous and asynchronous instability thresholds for two pairs of time-scale parameters: $(\tau_s, \tau_b) = (0.2, 2), (0.6, 2)$. Each plot also contains several sample points whose K and D_v values are given in Table 2.1 below. The corresponding full PDE numerical simulations, tracking the heights of the spikes versus time, at these sample

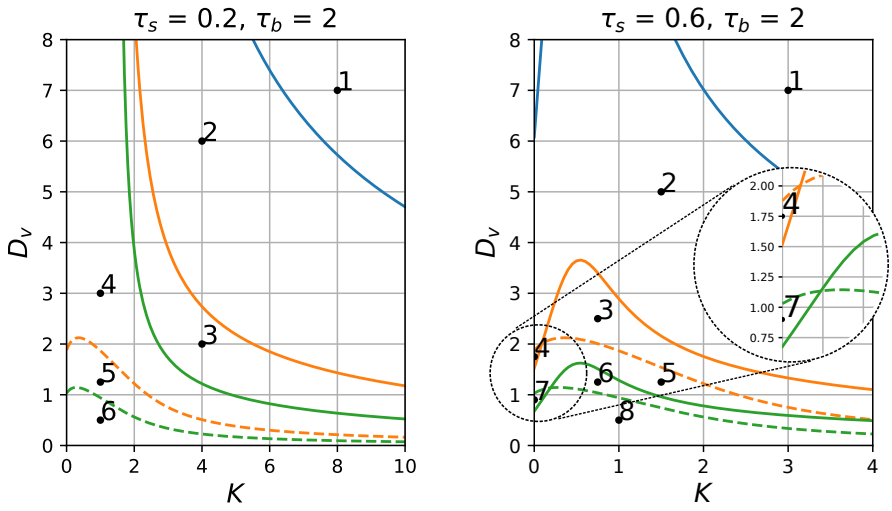

Figure 2.9: Synchronous (solid) and asynchronous (dashed) instability thresholds in the D_v versus K parameter plane in the well-mixed limit for $N = 1$ (blue), $N = 2$ (orange), and $N = 3$ (green). At the top of each of the three panels a different pair (τ_s, τ_b) is specified. See Table 2.1 for D_v and K values at the numbered points in each panel. Figures 2.10 and 2.11 show the corresponding spike dynamics from full PDE simulations of (2.1) at the indicated points.

points are shown in Figures 2.10 and 2.11. We observe that the initial instability onset in these figures is in agreement with that predicted by the linear stability theory. For example, when $\tau_s = 0.6$ and $\tau_b = 2$ an $N = 3$ spike pattern at point six should be stable with respect to an $N = 3$ synchronous instability but unstable with respect to the $N = 3$ asynchronous instabilities. Indeed the initial instability onset depicted in the "point 6, $N = 3$" plot of Figure 2.11 showcases the non-oscillatory growth of two spikes and decay of one as expected. In addition the plots in Figures 2.10 and 2.11 support two previously stated conjectures. First, pure Hopf bifurcations for $N \geq 2$ should be supercritical (see "Point 4, $N = 2$" and "Point 7, $N = 3$" in Figure 2.11). Secondly, we observe that asynchronous instabilities lead to the eventual annihilation of some spikes and the growth of others. As a result, our PDE

Point	K	D_v
1	8	7
2	4	6
3	4	2
4	1	3
5	1	1.25
6	1	0.5

(a)

Point	K	D_v
1	3	7
2	1.5	5
3	0.75	2.5
4	0	1.75
5	1.5	1.25
6	0.75	1.25
7	0	0.9
8	1	0.5

(b)

Point	K	D_v
1	0.5	18
2	2	10
3	2	3.5
4	1	0.5
5	0.025	1.8

(c)

Table 2.1: K and D_v values at the sampled points in the two panels of Fig. 2.9: (a) Left panel: $(\tau_s, \tau_b) = (0.2, 2)$, and (b) Right panel: $(\tau_s, \tau_b) = (0.6, 2)$. Table (d) shows the K and D_v values at the sampled points for the disk appearing in the left panel of Fig. 2.12.

simulations suggest that these instabilities are subcritical.

We now show that this agreement between predictions of our linear stability theory and results from full PDE simulations continues to hold for the case of a finite bulk diffusivity. To illustrate this agreement, we consider the unit disk with $D_b = 10$ for $(\tau_s, \tau_b) = (0.6, 0.1)$. For this parameter set, in the left panel of Figure 2.12 we show the asymptotically predicted synchronous and asynchronous instability thresholds in the D_v versus K parameter plane for $N = 1$ and $N = 2$. The faint grey dotted lines in this figure indicate the corresponding well-mixed thresholds. In the right panel of Figure 2.12 we plot the spike heights versus time, as computed numerically from (2.1), at the sample points indicated in the left panel. In each case, the numerically computed solution uses a 2% perturbation away from the asymptotically computed N-spike equilibrium. As in the well-mixed case, the full numerical simulations confirm the predictions of the linear stability theory. Furthermore, Figures 2.1 and 2.2 depict both the bulk-inhibitor and the two membrane-bound species at certain times for an $N = 2$ spike pattern at points 2 and 5 in the left panel of Figure 2.12, respectively. From this figure, we observe that the bulk-inhibitor field is largely constant except within a small near region near

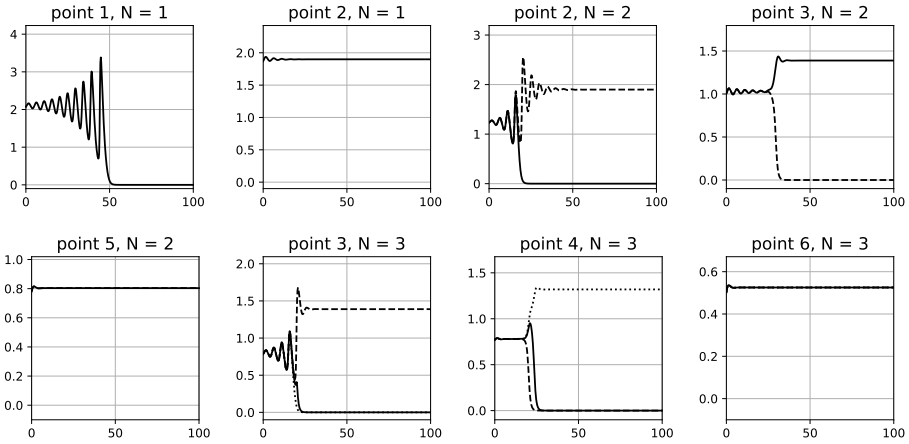

Figure 2.10: Numerically computed spike heights (vertical axis) versus time (horizontal axis) from full PDE simulations of (2.1) for $\tau_s = 0.2$ and $\tau_b = 2$ at the points indicated in the left panel of Figure 2.9. Distinct spike heights are distinguished by line types (solid, dashed, and dotted).

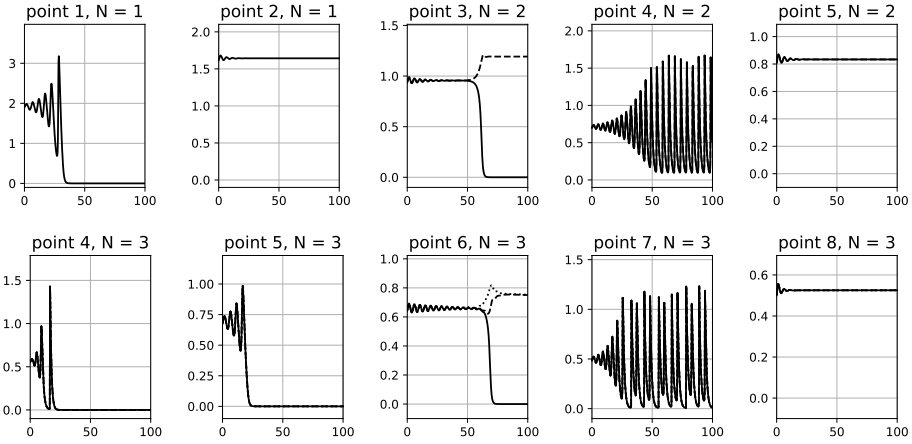

Figure 2.11: Numerically computed spike heights (vertical axis) versus time (horizontal axis) from full PDE simulations of (2.1) for $\tau_s = 0.6$ and $\tau_b = 2$ at the points indicated in the middle panel of Figure 2.9. Distinct spike heights are distinguished by line types (solid, dashed, and dotted).

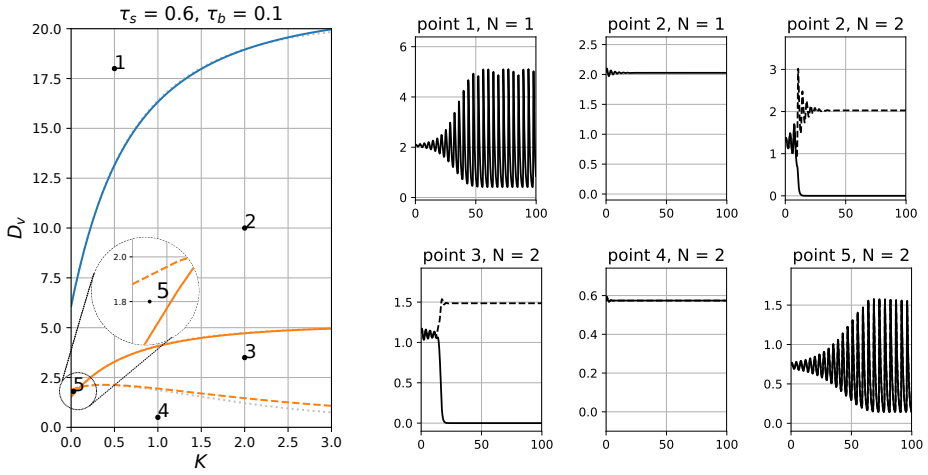

Figure 2.12: Left panel (a): Synchronous (solid) and asynchronous (dashed) instability thresholds in the D_v versus K parameter plane for the unit disk with $D_b = 10$ and $(\tau_s, \tau_b) = (0.6, 0.1)$. $N = 1$ spike and $N = 2$ spikes correspond to the (blue) and (orange) curves, respectively. The faint grey dotted lines are the corresponding well-mixed thresholds. Right panel (b): Numerically computed spike heights (vertical axis) versus time (horizontal axis) from full PDE simulations of (2.1) at the points indicated in the left panel for $N = 1$ and $N = 2$ spikes. For videos of the PDE simulations please see the supplementary materials.

the spike locations.

2.4 The Effect of Boundary Perturbations on Asynchronous Instabilities

The goal of this section is to calculate the leading order correction to the asynchronous instability thresholds for a perturbed disk. Specifically we consider the domain

$$\Omega_\delta \equiv \{(r,\theta)\,|\,0 \le r < R + \delta h(\theta), \quad 0 \le \theta < 2\pi\},$$

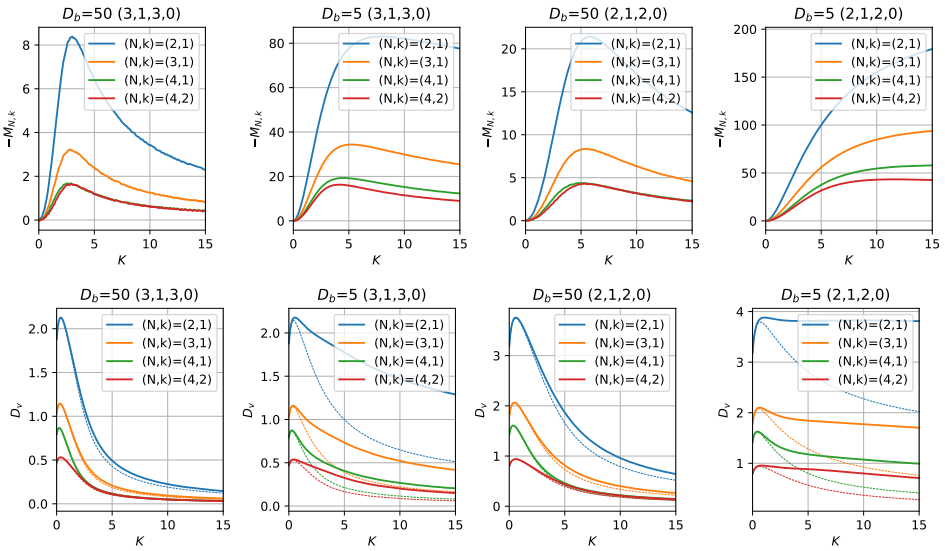

Figure 2.13: The effect of boundary perturbations on the asynchronous stability of symmetric N-spike patterns for the unit disk. The top row shows the multiplier $M_{N,k}$, defined in (2.7), as a function of K while the bottom row shows the leading order correction to the asynchronous instability threshold, with the dashed line indicating the unperturbed threshold. Each column correspond to a choice of $D_b = 50$ or $D_b = 5$ with Gierer-Meinhardt exponents of $(p,q,m,s) = (3,1,3,0)$ or $(p,q,m,s) = (2,1,2,0)$. In the second row the boundary perturbation has parameters $\xi = 1$ (indicating an outward bulge at the spike locations), and $\delta = 0.01$.

where $h(\theta)$ is a smooth $\mathcal{O}(1)$ function with a Fourier series $h(\theta) = \sum_{n=-\infty}^{\infty} h_n e^{in\theta}$. Although our final results will be restricted to the specific form

$$h(\theta) = 2R\xi\cos(N\theta) = R\xi e^{iN\theta} + R\xi e^{-iN\theta}, \tag{2.1}$$

where ξ is a parameter, there is no additional difficulty in considering a general Fourier series in the analysis below. However, we remark that in using the general Fourier series given above we must impose appropriate symmetry conditions on $h(\theta)$ so that the symmetric N-spike pattern construction, and in particular the resulting NLEP (2.5), remain valid. Our main goal is to determine a two-term

asymptotic expansion in powers of δ for each asynchronous instability threshold in the form

$$D_v \sim D^\star_{vk0}(D_b,K,R) + D^\star_{vk1}(D_b,K,R)\delta + \mathscr{O}(\delta^2),$$

such that a zero-eigenvalue crossing is maintained to at least second order, i.e. for which $\lambda = \mathscr{O}(\delta^2)$.

Recall that the only component of the asynchronous NLEP (2.5) that depends on the problem geometry is the NLEP multiplier $\chi_k(\lambda)$. To study the effect of boundary perturbations, it therefore suffices to calculate the leading order corrections to the corresponding membrane Green's function satisfying (2.22). Furthermore, we note that since we are only interested in a first order expansion, whereas $\lambda = \mathscr{O}(\delta^2)$, there is no loss in validity assuming that λ is an independent parameter that we ultimately set to zero. Upon expanding $D_v = D_{v0}\big(1 + \frac{D_{v1}}{D_{v0}}\delta\big)$, a two-term expansion for the perturbed membrane Green's function is given by (see Appendix B.2)

$$G^\lambda_{\partial\Omega}(\theta,\theta_0) \sim G^\lambda_{\partial\Omega 0}(\theta,\theta_0) + G^\lambda_{\partial\Omega 1}(\theta,\theta_0)\delta + \mathscr{O}(\delta^2),$$

where $G^\lambda_{\partial\Omega 0}$ is the membrane Green's function for the unperturbed disk calculated previously in (B.7) and the leading-order correction is

$$\begin{aligned} G^\lambda_{\partial\Omega 1}(\theta,\theta_0) = -\tfrac{h(\theta_0)}{R} G^\lambda_{\partial\Omega 0}(\theta,\theta_0) + \tfrac{1}{2\pi R}\sum_{n=-\infty}^{\infty}\sum_{k=-\infty}^{\infty} \hat{g}^\lambda_{n,k} h_{n-k} g^\lambda_k g^\lambda_n e^{in\theta - ik\theta_0} \\ - \tfrac{D_{v1}}{2\pi R^3}\sum_{n=-\infty}^{\infty} n^2 (g^\lambda_n)^2 e^{in(\theta-\theta_0)}. \end{aligned} \tag{2.2}$$

In this expression the coefficients $\hat{g}^\lambda_{n,k}$ are given by

$$\hat{g}^\lambda_{n,k} = \tfrac{D_{v0}}{R^3} k(n+k) + K^2 a^\lambda_k \left(\hat{a}^\lambda_{n,k} + P'_k(R)\right), \tag{2.3}$$

where g^λ_k, a^λ_k, and $\hat{a}^\lambda_{n,k}$ are defined in (2.9), (B.6), and (B.14), respectively.

Restricting our attention to perturbations of the form (2.1), and considering a symmetric N-spike pattern with spikes centred at $\theta_j = \frac{2\pi(j-1)}{N}$ for $j = 1,\ldots,N$, we

deduce from (2.2) that

$$G^{\lambda}_{\partial\Omega 1}(\theta,\theta_j) = -2\xi G^{\lambda}_{\partial\Omega 0}(\theta,\theta_j) - \tfrac{D_{v1}}{2\pi R^3}\sum_{n=-\infty}^{\infty} n^2 (g^{\lambda}_{0n})^2 e^{in(\theta-\theta_j)} \\ +\frac{\xi}{2\pi}\sum_{n=-\infty}^{\infty}\{\hat{g}^{\lambda}_{n,n+N}g^{\lambda}_{0,n+N} + \hat{g}^{\lambda}_{n,n-N}g^{\lambda}_{0,n-N}\}g^{\lambda}_{0n}e^{in(\theta-\theta_j)}. \tag{2.4}$$

Note that by symmetry the consistency and balance equations continue to hold for a symmetric N spike pattern. Furthermore the perturbed Green's matrix remains circulant, and therefore its eigenvalues can be read off as

$$\mu_k(\lambda) = \sum_{j=0}^{N-1} G^{\lambda}_{\partial\Omega}\big(\tfrac{2\pi}{N}j,0\big)e^{\frac{2\pi ijk}{N}} \sim \mu_{k0}(\lambda) + \delta\Big\{-2\xi\mu_{k0}(\lambda) + \xi\mu_{k11}(\lambda) + D_{v1}\mu_{k12}(\lambda)\Big\}$$

where

$$\mu_{k0}(\lambda) = \tfrac{N}{2\pi R}\sum_{n=-\infty}^{\infty} g^{\lambda}_{nN-k}, \tag{2.5a}$$

$$\mu_{k11}(\lambda) = \tfrac{N}{2\pi}\sum_{n=-\infty}^{\infty}\{\hat{g}^{\lambda}_{nN-k,(n+1)N-k}g^{\lambda}_{(n+1)N-k} + \hat{g}^{\lambda}_{nN-k,(n-1)N-k}g^{\lambda}_{(n-1)N-k}\}g^{\lambda}_{nN-k}, \tag{2.5b}$$

$$\mu_{k12}(\lambda) = -\tfrac{N}{2\pi R^3}\sum_{n=-\infty}^{\infty}(nN-k)^2(g^{\lambda}_{nN-k})^2. \tag{2.5c}$$

Finally, upon setting $\lambda = 0$ in the zero-eigenvalue crossing condition $\mathscr{A}_k(0) = [\chi_k(0)]^{-1} - mq/(p-1)$ for the asynchronous modes $k = 1,\ldots,N-1$ (see (2.33)), and noting $\chi_k(0) = \mu_k(0)/\mu_0(0)$ from (2.5), we obtain that

$$\frac{\mu_{00}(0) + \delta\left[-2\xi\mu_{00}(0) + \xi\mu_{011}(0) + D_{v1}\mu_{012}(0)\right]}{\mu_{k0}(\lambda) + \delta\left[-2\xi\mu_{k0}(\lambda) + \xi\mu_{k11}(\lambda) + D_{v1}\mu_{k12}(\lambda)\right]} - \frac{mq}{p-1} = 0, \tag{2.6}$$

for each $k = 1,\ldots,N-1$. The leading-order problem is satisfied by the previously determined threshold $D_{v0} = D^{\star}_{vk0}(K,D_b,R)$. On the other hand, by expanding (2.6) in powers of δ, we obtain from equating $\mathscr{O}(\delta)$ terms in this expansion that

$$\xi\big(\mu_{011}(0) - \tfrac{mq}{p-1}\mu_{k11}(0)\big) + D_{v1}\big(\mu_{012}(0) - \tfrac{mq}{p-1}\mu_{k12}(0)\big) = 0.$$

Upon solving for $D_{v1} = D^{\star}_{vk1}(K, D_b, R)$ in this expression, we conclude that

$$D^{\star}_{vk1} = -M_{N,k}\xi, \qquad \text{where} \quad M_{N,k} \equiv \frac{\mu_{011}(0) - \frac{mq}{p-1}\mu_{k11}(0)}{\mu_{012}(0) - \frac{mq}{p-1}\mu_{k12}(0)}. \tag{2.7}$$

Therefore, the sign and magnitude of the multiplier $M_{N,k}$ determines how the asynchronous instability threshold changes when the boundary is perturbed by a single Fourier mode of the form (2.1).

Figure 2.13 illustrates the effect of boundary perturbations of the form (2.1) by plotting the multiplier $-M_{N,k}$ in the top row, and the leading order corrected asynchronous threshold $D_v \sim D^{\star}_{vk0} + D^{\star}_{vk1}\delta$ in the bottom row. Note that the (positive) maximums of $h(\theta)$ correspond with the quasi-equilibrium spike locations θ_j for each $j = 1, ..., N$. From (2.7) we therefore conclude that positive values of $-M_{N,k}$ indicate an increase in stability when spike locations bulge out ($\xi > 0$), and a decrease in stability otherwise. The results of Figure 2.13 thus indicate that an outward bulge at the location of each spike in a symmetric N-spike pattern leads to an improvement in stability of the pattern with respect to asynchronous instabilities. In addition, the magnitude of $-M_{N,k}$ shows that this stabilizing effect is most pronounced at some finite value of K corresponding to a maximum of $-M_{N,k}$. Furthermore, comparing the $D_b = 50$ and $D_b = 5$ plots we see that decreasing the bulk diffusivity further accentuates the effect of boundary perturbations as is clear from the relative magnitude of $-M_{N,k}$ in these two cases. These numerical observations lead us to propose the following numerically supported proposition.

Proposition 2.4.1. *Consider a symmetric N-spike pattern for the Gierer-Meinhardt system* (2.1) *on the unit disk. Then a domain perturbation of the form* (2.1)*, which creates an outward bulge at each spike location, will increase the asynchronous instability threshold of the symmetric N-spike pattern.*

2.5 Discussion

We have introduced a coupled bulk-membrane PDE model in which a scalar linear 2-D bulk diffusion process is coupled through a linear Robin boundary condition to a two-component 1-D RD system with Gierer-Meinhardt (nonlinear) reaction kinetics defined on the domain boundary. For this coupled bulk-membrane

PDE model, in the singularly perturbed limit of a long-range inhibition and short-range activation for the membrane-bound species, we have studied the existence and linear stability of localized steady-state multi-spike patterns defined on the membrane. Our primary goal was to study how the bulk diffusion process and the bulk-membrane coupling modifies the well-known linear stability properties of steady-state spike patterns for the 1-D Gierer-Meinhardt model in the absence of coupling.

By using a singular perturbation analysis on our coupled model (2.1) we first derived a nonlinear algebraic system (2.16) characterizing the locations and heights of steady-state multi-spike patterns on the membrane. Then we derived a new class of NLEPs (nonlocal eigenvalue problems) characterizing the linear stability on $\mathcal{O}(1)$ time-scales of these steady-state patterns. In this NLEP, the multiplier of the nonlocal term is determined in terms of the model parameters together with a new coupled nonlocal Green's function problem. More specifically, a novel feature of our steady-state and linear stability analysis is the appearance of a nonlocal 1-D membrane Green's function $G^{\lambda}_{\partial\Omega}(\sigma,\zeta)$ (see (2.22)), satisfying

$$D_v\partial^2_\sigma G^{\lambda}_{\partial\Omega}(\sigma,\zeta)-(1+K+\tau_s\lambda)G^{\lambda}_{\partial\Omega}(\sigma,\zeta)+K^2\int_0^L G^{\lambda}_{\Omega}(\sigma,\tilde{\sigma})G^{\lambda}_{\partial\Omega}(\tilde{\sigma},\zeta)\,d\tilde{\sigma}=-\delta(\sigma-\zeta),$$

for $0<\sigma,\zeta<L$ which is coupled to a 2-D bulk Green's function G^{λ}_{Ω} satisfying (see (2.19))

$$D_b\Delta G^{\lambda}_{\Omega}-(1+\tau_b\lambda)G^{\lambda}_{\Omega}=0,\quad \text{in } \Omega;\qquad D_b\partial_n G^{\lambda}_{\Omega}+KG^{\lambda}_{\Omega}=\delta_{\partial\Omega}(x-x_0),\quad \text{on } \partial\Omega.$$

Recall (2.1) for the description of all the model parameters including, the time constants τ_s and τ_b, the diffusivities D_v and D_b, and the coupling constant K.

To proceed with a more explicit linear stability theory we restricted our analysis to symmetric multi-spike patterns, which are characterized by equidistantly (in arc-length) separated spikes of equal height, for two analytically tractable cases. The first case is when Ω is a disk of radius R, while the second case is when the bulk is well mixed (i.e. $D_b\gg 1$). While our formulation is equally valid for more general settings there are two significant hurdles toward a more detailed stability analysis. First, the global coupling introduced by the nonlocal membrane Green's function makes it unclear how to define symmetric multi-spike patterns. Although we re-

marked earlier that such a classification can be associated with the condition that $\mathcal{G}^{\lambda}_{\partial\Omega}$ has the eigenvector $\mathbf{e}$, apart from domains with certain rotational symmetries it is not clear how the geometry is related to this condition. Secondly, the numerical computation of the bulk Green's function for more general domains remains a topic of ongoing research. For the two specific cases, we obtained analytical expressions for the relevant Green's function, and consequently the NLEP multipliers, in the form of infinite series for the disk and explicit formulae for the well-mixed limit. Parameter thresholds for two distinct forms of linear instabilities, corresponding to either synchronous or asynchronous perturbations of the heights of the steady-state spikes, were then computed from the NLEP. Our results indicate a non-monotonic dependence on the bulk-membrane coupling strength K for both modes of instability, together with an intricate relationship between the time-scale and coupling parameters for the synchronous instabilities. Specifically, for the asynchronous instability modes the coupling has the effect of improving stability for smaller values of K by raising the instability threshold for D_v, but reducing the range of stability for larger values of K. This effect is amplified in the synchronous case where for certain choices of τ_s a small region in the K versus τ_b parameter space can be found for which no instabilities exist (see Figure 2.4). Finally, by using a Finite Element / Finite Difference mixed IMEX scheme, we confirmed our linear stability thresholds with full numerical PDE simulations.

We conclude the discussion by highlighting some open problems and directions for future research. Firstly, for our coupled model, additional work is required to calculate and study the linear stability of asymmetric spike patterns. Secondly, we have neglected the role of small $\mathcal{O}(\varepsilon^2)$ eigenvalues corresponding to weak drift instabilities, which can be studied either through a more detailed asymptotic analysis or by deriving and analyzing a corresponding slow spike-dynamics ODE system. Thirdly, the numerical evidence provided by our PDE simulations suggests that, when $N \geq 2$ in the absence of competition instabilities, the Hopf bifurcation is supercritical, and leads to the emergence of a small amplitude time-periodic solution near the bifurcation point. The numerical evidence also suggests that competition instabilities are subcritical, and result in the annihilation of one or more spikes in a multi-spike pattern. It would be worthwhile to analytically establish these conjectured branching behaviours from a weakly nonlinear analysis that is valid either

near a Hopf bifurcation point or near a zero-eigenvalue crossing. In particular, it would be interesting to perform a more detailed analysis of the observed time-periodic solution near the Hopf bifurcation threshold to determine whether it has some regularity or is otherwise chaotic.

Finally, there are several directions for extending our model and applying a similar methodology. One direction would be to analyze similar problems in higher space dimensions, such as a 3-D linear bulk diffusion process coupled to a nonlinear RD system on a 2-D surface. A common feature in the matched asymptotics calculation for higher-dimensional problems is that the inhibitor and activator no longer decouple in the inner problem. This leads to a nonlinear algebraic system and globally coupled eigenvalue problem markedly different from those in one-dimensional problems. An analytical treatment of the effect of coupling on these systems has, as of yet, been unexplored. A further direction would be to consider a two-component bulk diffusion process, with nonlinear bulk kinetics. For this more complicated model it would be interesting to study the interplay between 1-D membrane-bound and 2-D bulk-bound localized patterns. Additionally it would be instructive to asymptotically construct and analyze the localized patterns observed in the numerical study of Madzvamuse et. al. [57, 58] as well those of Rätz et. al. [81–83].

Chapter 3

Localized Spot Patterns in a Bulk-Membrane Coupled Brusselator Model

The classical Brusselator model [79] is characterized by the reaction kinetics

$$E \to U, \quad B+U \to V+D, \quad 2U+V \to 3U, \quad U \to A, \tag{3.1}$$

for the activator U, inhibitor V, fuel E, and catalyst B. In most studies of the Brusselator model the fuel and catalyst are typically assumed to be of constant concentration while the activator and inhibitor concentrations are assumed to depend on both space and time. In particular, the spatiotemporal evolution of the activator and inhibitor concentrations is determined by a two-component reaction diffusion system which is obtained by applying the Law of Mass Action and assuming that both chemical components have a finite diffusivity.

In this chapter we analyze the structure and stability of localized spot patterns in a model which incorporates bulk-membrane coupling into a reaction-diffusion-system with Brusselator-like reaction kinetics. In particular we consider a model in which the activator U and inhibitor V are bound to the membrane $\partial\Omega_0$ of a

three-dimensional domain Ω_0 where they passively diffuse with reaction kinetics

$$B + U \to V + D, \quad 2U + V \xrightarrow{k_a} 3U, \tag{3.2}$$

where B is a catalyst component and D a passive product. Bulk-membrane coupling is incorporated by assuming that the activator shuttles between membrane- and bulk-bound states through a Langmuir process of membrane attachment and detachment [43]. Moreover we assume that the fuel necessary to sustain pattern formation originates within the bulk and passively diffuses to the membrane. The resulting bulk-membrane coupled reaction diffusion system for the membrane-bound inhibitor concentration $\mathscr{V}$ and membrane- and bulk-bound activator concentrations $\mathscr{U}$ and $\mathscr{W}$ respectively is then given by the bulk-membrane coupled reaction-diffusion system

$$\partial_T \mathscr{U} = \mathscr{D}_{\mathscr{U}} \Delta_{\partial\Omega_0} \mathscr{U} - (\mathscr{B} + k_d + \mathscr{K}_1)\mathscr{U} + k_a \mathscr{U}^2 \mathscr{V} + \mathscr{K}_2 \mathscr{W}, \quad \boldsymbol{X} \in \partial\Omega_0, \tag{3.3a}$$

$$\partial_T \mathscr{V} = \mathscr{D}_{\mathscr{V}} \Delta_{\partial\Omega_0} \mathscr{V} + \mathscr{B}\mathscr{U} - k_a \mathscr{U}^2 \mathscr{V}, \quad \boldsymbol{X} \in \partial\Omega_0, \tag{3.3b}$$

$$\partial_T \mathscr{W} = \mathscr{D}_{\mathscr{W}} \Delta \mathscr{W} + \mathscr{E}(\boldsymbol{X}), \quad \boldsymbol{X} \in \Omega_0, \tag{3.3c}$$

$$\mathscr{D}_{\mathscr{W}} \partial_N \mathscr{W} = \mathscr{K}_1 \mathscr{U} - \mathscr{K}_2 \mathscr{W}, \quad \boldsymbol{X} \in \partial\Omega_0. \tag{3.3d}$$

where ∂_T is the time derivative, ∂_N is the derivative in the direction of the outward unit normal to $\partial\Omega_0$, $\Delta_{\partial\Omega_0}$ is the Laplace-Beltrami operator on $\partial\Omega_0$ which describes lateral diffusion on the membrane, $\mathscr{D}_{\mathscr{U}}$, $\mathscr{D}_{\mathscr{V}}$, and $\mathscr{D}_{\mathscr{W}}$ are the diffusivities of $\mathscr{U}, \mathscr{V}$, and $\mathscr{W}$ respectively, $\mathscr{B}$ is the conversion rate of U to V through the reaction $B + U \to V + D$, $\mathscr{K}_1$ and $\mathscr{K}_2$ are the rates of activator membrane detachment and attachment respectively, k_a is the rate of the autocatalytic reaction $2U + V \xrightarrow{k_a} 3U$, k_d is the activator membrane-degradation rate, and $\mathscr{E}(\boldsymbol{X})$ is the bulk-bound activator fuel source which we assume is compactly supported in the interior of Ω_0.

While the bulk-membrane coupled model (3.3) explicitly includes only two of the reactions from the Brusselator reaction-kinetics (3.1), the remaining two reactions are incorporated primarily through bulk-membrane coupling. In particular the reaction $U \to A$ in (3.1) is replaced by a membrane-to-bulk detachment process characterized by the $-\mathscr{K}_1 \mathscr{U}$ term in (3.3a) in addition to a generic membrane

degradation term characterized by the $-k_d\mathscr{U}$ term. Similarly, the reaction $E \to U$ in (3.1) required for sustaining pattern formation is replaced by the transport of a localized fuel-term in the bulk to the membrane through passive diffusion. Note that if $\mathscr{K}_1 = 0$ then the two-component system (3.3a)-(3.3b) is indistinguishable from the classically studied Brusselator system, albeit with a possibly spatially heterogeneous fuel term given by $\mathscr{K}_2\mathscr{W}$. However, the introduction of bulk-membrane coupling provides a systematic way of choosing the fuel term appearing in the classical Brusselator reaction kinetics (3.1). In our model the fuel term $\mathscr{E}(\boldsymbol{X})$ can encompass a wide variety of bulk-originating fuel terms that closely describe biological processes being modelled. Such a modelling paradigm may be particularly fruitful in the context of conifer growth models previously based on the Brusselator reaction kinetics (see for example [35, 36] and the references therein). In addition bulk-membrane coupling introduces a nonlocal mechanism of chemical transport on the membrane characterized by a cycle of membrane detachment, bulk-bound diffusion, and membrane reattachment. One of the key goals of this chapter is to explore the effects of this nonlocal mechanism on the structure, stability, and dynamics of localized patterns.

To simplify our analysis and isolate key parameters we first perform a nondimensionalization of the model (3.3). Letting L be a characteristic length scale for the domain Ω_0 and its boundary $\partial\Omega_0$ we introduce non-dimensional spatial variables $\boldsymbol{x} = L^{-1}\boldsymbol{X}$ so and define $\Omega = L^{-1}\Omega$ and $\partial\Omega = L^{-1}\partial\Omega_0$. We further let $\mathscr{D}_U \equiv L^{-2}\mathscr{D}_{\mathscr{U}}$, $\mathscr{D}_V \equiv L^{-2}\mathscr{D}_{\mathscr{V}}$, and $\mathscr{D}_W \equiv L^{-2}\mathscr{D}_{\mathscr{W}}$. In the limit of an asymptotically small activator diffusivity $\mathscr{D}_U = \varepsilon_0^2 \ll 1$ the resulting two-dimensional singularly perturbed Brusselator system is known to support localized spot patterns when the fuel is $\mathscr{O}(\varepsilon_0)$ [84, 91]. It follows that $\mathscr{W} = \mathscr{O}(\varepsilon_0)$ is needed to sustain patterns so we assume that $\mathscr{E}(\boldsymbol{X}) = \varepsilon_0 E_0 E(\boldsymbol{x})$ where $E(\boldsymbol{x}) = \mathscr{O}(1)$ in Ω and by introducing the non-dimensional variables

$$\mathscr{U} = \varepsilon_0^{-1} E_0 L u, \quad \mathscr{V} = \varepsilon_0 \frac{\mathscr{B}}{k_a L E_0} v, \quad \mathscr{W} = \varepsilon_0 \frac{E_0 L}{\mathscr{K}_2} w, \quad T = \frac{t}{\mathscr{B} + k_d + \mathscr{K}_1}, \tag{3.4}$$

we obtain the nondimensionalized bulk-membrane coupled system

$$\partial_t u = \varepsilon^2 \Delta_{\partial\Omega} u - u + f u^2 v + \varepsilon^2 w, \qquad \boldsymbol{x} \in \partial\Omega, \quad t > 0 \tag{3.5a}$$

$$\tau_v \partial_t v = D_v \Delta_{\partial\Omega} v + \varepsilon^{-2}(u - u^2 v) \qquad \boldsymbol{x} \in \partial\Omega, \quad t > 0, \tag{3.5b}$$

$$\tau_w \partial_t w = D_w \Delta w + E(\boldsymbol{x}), \qquad \boldsymbol{x} \in \Omega, \quad t > 0, \tag{3.5c}$$

$$D_w \partial_n w + w = \varepsilon^{-2} K u, \qquad \boldsymbol{x} \in \partial\Omega, \quad t > 0, \tag{3.5d}$$

where $\Delta_{\partial\Omega}$ is the Laplace-Beltrami operator on $\partial\Omega$, ∂_n denotes the derivative in the direction of the outer unit normal, the time-constants and diffusivities are given by

$$\tau_v \equiv (\mathscr{B} + k_d + \mathscr{K}_1)^2 \frac{1}{k_a E_0^2 L^2}, \quad D_v \equiv \frac{\tau_v \mathscr{D}_V}{\mathscr{B} + k_d + \mathscr{K}_1},$$
$$\tau_w \equiv \frac{(\mathscr{B} + k_d + \mathscr{K}_1) L}{\mathscr{K}_2}, \quad D_w \equiv \frac{\mathscr{D}_W L}{\mathscr{K}_2},$$

and the remaining parameter are given by

$$\varepsilon \equiv \frac{\varepsilon_0}{\sqrt{\mathscr{B} + k_d + \mathscr{K}_1}} \ll 1, \quad K \equiv \frac{\mathscr{K}_1}{\mathscr{B} + k_d + \mathscr{K}_1}, \quad f \equiv \frac{\mathscr{B}}{\mathscr{B} + k_d + \mathscr{K}_1}. \tag{3.6}$$

Recall that the membrane-bound activator is reduced by three processes: conversion to V through the reaction $B + U \to V + D$, membrane detachment at a rate of $\mathscr{K}_1$, and degradation at a rate of k_d. Therefore $0 \leq K < 1$ and $0 < f < 1$ correspond to the proportion of the rate of membrane-bound activator lost due to membrane detachment and conversion to membrane-bound inhibitor respectively. An additional constraint on the two parameters f and K is obtained from (3.3) by using the divergence theorem to calculate

$$\frac{d}{dT} \int_{\partial\Omega_0} (\mathscr{U} + \mathscr{V}) dS = -k_d \int_{\partial\Omega} U dS + \mathscr{E}_0,$$

from which it is clear that $k_d > 0$ is needed to sustain stationary patterns and we deduce the constraint

$$0 < f + K < 1. \tag{3.7}$$

In the absence of bulk-membrane coupling (e.g. with $K = 0$), several studies have investigated the resulting singularly perturbed reaction diffusion system con-

sisting of (3.5a) and (3.5b). In particular when $\partial\Omega$ is the unit sphere in $\mathbb{R}^3$ the quasi-equilibrium structure, linear stability, and slow dynamics of multi-spot patterns in the presence of a spatially homogeneous and time-independent fuel have been analyzed using the method of matched asymptotic expansions in [84, 91]. Assuming henceforth that Ω is the unit ball in $\mathbb{R}^3$ our aim is to extend the results obtained in these previous studies to the bulk-membrane coupled model (3.5). The novel features of this extension are twofold. First, the bulk originating fuel term will in general lead to a spatially heterogeneous fuel source for the membrane activator equation. Presently, the effects of such a spatially heterogeneous fuel term have been considered only in the context of the unit disk in $\mathbb{R}^2$ [96]. Secondly, membrane-detachment and reattachment leads to a nonlocal mechanism of membrane-bound activator transport which has no yet been explored in the context of localized patterns on two-dimensional surfaces.

The remainder of this chapter is organized as follows. In §3.1 we use the method of matched asymptotic expansions to construct quasi-equilibrium multi-spot patterns that are stationary on an $\mathcal{O}(1)$ time scale and in §3.2 we study their linear stability on an $\mathcal{O}(1)$ timescale. In §3.3 we derive a differential algebraic system of equations governing the slow evolution of multi-spot solutions on an $\mathcal{O}(\varepsilon^{-2})$ timescale. In §3.4 we explicitly construct and consider the stability and dynamics of one-, two-, and three-spot patterns. Finally, in §3.5 we provide a brief conclusion.

3.1 Asymptotic Construction of N-Spot Quasi-Equilibrium

The method of matched asymptotic expansions has been extensively used to analyze localized solutions to singularly perturbed reaction diffusion systems in one-, two-, and three-dimensional domains [41, 48, 97, 98]. It has likewise been used to study localized multi-spot patterns on the unit sphere [84, 91], and more recently on the torus [95]. Applying these techniques we now construct a quasi-equilibrium solution consisting of N spots concentrating on $\partial\Omega$ at

$$\boldsymbol{x}_i = (\sin\theta_i\cos\varphi_i, \sin\theta_i\sin\varphi_i, \cos\theta_i)^T, \qquad \text{for } i = 1,...,N, \tag{3.8}$$

where $0 < \theta_i < \pi$ and $0 \leq \varphi_i < 2\pi$ ($i = 1, ..., N$) are the typical spherical coordinates and for which we assume that the spots are well separated in the sense that $|\boldsymbol{x}_i - \boldsymbol{x}_j| \gg \varepsilon$ for all $i \neq j$. This solution is to be understood only as a *quasi*-equilibrium because, unless additional constraints are imposed on $\boldsymbol{x}_1, ..., \boldsymbol{x}_N$, the spots will drift on an $\mathcal{O}(\varepsilon^{-2})$ timescale according to prescribed dynamics developed in §3.3. With these assumptions a local expansion of (3.5a) and (3.5b) near each $\boldsymbol{x}_i$ ($i = 1, ..., N$) yields a system of core-problems which are coupled only through the prescription of far-field constants for the local inhibitor concentrations. An appropriate choice of local coordinates greatly simplifies the resulting analysis. Motivated by the use of geodesic normal coordinates in [92] and more recently in [95] we first construct local normal coordinates near each spot.

3.1.1 Geometric Preliminaries: Local Geodesic Normal Coordinates on the Unit Sphere

In terms of spherical coordinates $r > 0$ and $(\theta, \varphi) \in (0, \pi) \times [0, 2\pi)$ the Laplace operator and Laplace-Beltrami operator on the unit sphere are respectively given by

$$\Delta = \frac{1}{r^2}\frac{\partial}{\partial r} r^2 \frac{\partial}{\partial r} + \frac{1}{r^2}\Delta_{\partial\Omega}, \qquad \Delta_{\partial\Omega} = \frac{1}{\sin\theta}\frac{\partial}{\partial\theta}\sin\theta\frac{\partial}{\partial\theta} + \frac{1}{\sin^2\theta}\frac{\partial^2}{\partial\varphi^2}. \tag{3.9}$$

Previous studies of multi-spot patterns on the unit sphere have used the local coordinates $s_2 = \varepsilon^{-1}(\theta - \theta_i)$ and $s_2 = \varepsilon^{-1}\sin\theta_i(\varphi - \varphi_i)$ to parameterize points on $\partial\Omega$ within a $\mathcal{O}(\varepsilon)$ neighbourhood of each spot location $\boldsymbol{x}_i$ [84, 91] (see also [13] for a similar approach in the context of narrow escape problems). In terms of these local coordinates it is then straightforward to calculate the two term expansion

$$\Delta_{\partial\Omega} = \varepsilon^{-2}(\partial_{s_1}^2 + \partial_{s_2}^2) + \varepsilon^{-1}\cot\theta_i(\partial_{s_1} - 2s_1\partial_{s_2}^2) + \mathcal{O}(1).$$

The factor of $\cot\theta_i$ in the $\mathcal{O}(\varepsilon^{-1})$ correction implies that the local behaviour of spots depends on their location on the unit sphere which suggests this correction is an artifact of the choice of local coordinates. Indeed this term was recognized as a correction to the leading order tangent plane approximation by Trinh and Ward [91]. The accompanying analysis in the study of slow spot dynamics that arises due

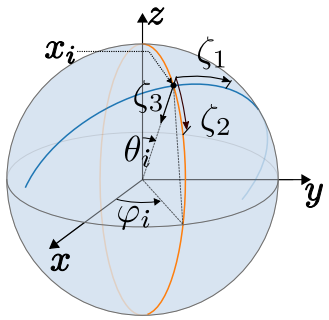

Figure 3.1: Example of geodesic normal coordinates $(\zeta_1, \zeta_2, \zeta_3)$ at $\boldsymbol{x}_i \in \partial\Omega$. The blue (resp. orange) curves indicate geodesics obtained by varying $-\pi/2 < \zeta_1 < \pi/2$ (resp. $-\pi < \zeta_2 < \pi$) and fixing $\zeta_3 = 0$ and $\zeta_2 = 0$ (resp. $\zeta_1 = 0$).

to such an $\mathscr{O}(\varepsilon^{-1})$ correction can be bypassed through the use of local geodesic normal coordinates in terms of which it can be shown that the $\mathscr{O}(\varepsilon^{-1})$ correction in the local expansion of the Laplace-Beltrami operator vanishes identically [92]. For the remainder of this section we explicitly construct such a coordinate system for the unit ball.

We begin by defining new coordinates $\boldsymbol{\zeta} = (\zeta_1, \zeta_2, \zeta_3)^T \in (-\pi/2, \pi/2) \times (-\pi, \pi) \times [0, 1]$ in $\Omega \cup \partial\Omega$ such that $\boldsymbol{\zeta} = \mathbf{0}$ corresponds to $\boldsymbol{x}_i \in \partial\Omega$, $\xi_3 > 0$ corresponds to the interior of Ω, and the curves obtained by setting $\zeta_3 = 0$ and fixing either $\zeta_1 = 0$ or $\zeta_2 = 0$ are geodesics on $\partial\Omega$. Specifically we first calculate the orthonormal vectors

$$\boldsymbol{x}_i = \begin{pmatrix} \sin\theta_i \cos\varphi_i \\ \sin\theta_i \sin\varphi_i \\ \cos\theta_i \end{pmatrix}, \partial_\theta \boldsymbol{x}_i = \begin{pmatrix} \cos\theta_i \cos\varphi_i \\ \cos\theta_i \sin\varphi_i \\ -\sin\theta_i \end{pmatrix}, \boldsymbol{x}_i \times \partial_\theta \boldsymbol{x}_i = \begin{pmatrix} -\sin\varphi_i \\ \cos\varphi_i \\ 0 \end{pmatrix}, \quad (3.10a)$$

and define $\boldsymbol{\zeta}$ by

$$\boldsymbol{x}^i(\boldsymbol{\zeta}) = (1-\zeta_3)\big(\cos\zeta_1 \cos\zeta_2 \boldsymbol{x}_i + \cos\zeta_1 \sin\zeta_2 \partial_\theta \boldsymbol{x}_i + \sin\zeta_1 \boldsymbol{x}_i \times \partial_\theta \boldsymbol{x}_i\big). \quad (3.10b)$$

Thus ζ_1 and ζ_2 are the standard spherical coordinates in the reference frame with orthonormal basis $\{\boldsymbol{x}_i, \partial_\theta \boldsymbol{x}_i, \boldsymbol{x}_i \times \partial_\theta \boldsymbol{x}_i\}$, while ζ_3 measures the distance from $\partial\Omega$.

It is easy to verify that setting $\boldsymbol{\zeta} = \mathbf{0}$ corresponds to $\boldsymbol{x} = \boldsymbol{x}_i$. Additionally the coordinate curves obtained by setting $\zeta_3 = 0$ and fixing either $\zeta_2 = 0$ or $\zeta_1 = 0$ are respectively given by

$$\boldsymbol{x}^i(\zeta_1,0,0) = \cos\zeta_1\boldsymbol{x}_i + \sin\zeta_1\boldsymbol{x}_i \times \partial_\theta \boldsymbol{x}_i, \quad \boldsymbol{x}^i(0,\zeta_2,0) = \cos\zeta_2\boldsymbol{x}_i + \sin\zeta_1\partial_\theta\boldsymbol{x}_i,$$

which correspond to intersections of $\partial\Omega$ with the planes spanned by $\{\boldsymbol{x}_i, \boldsymbol{x}_i \times \partial_\theta \boldsymbol{x}_i\}$ and $\{\boldsymbol{x}_i, \partial_\theta \boldsymbol{x}_i\}$ respectively. In particular, these coordinates curves are geodesics on $\partial\Omega$ so that in terms of

$$\boldsymbol{\zeta} = \varepsilon \boldsymbol{Y} = \varepsilon(Y_1, Y_2, Y_3)^T, \qquad \boldsymbol{Y} = \mathscr{O}(1) \tag{3.11a}$$

we obtain the local expansions (see Appendix A of [92])

$$\Delta = \varepsilon^{-2}\partial_{Y_3}^2 + \varepsilon^{-2}\Delta_{(Y_1,Y_2)} + \mathscr{O}(\varepsilon^{-1}), \quad \Delta_{\partial\Omega} = \varepsilon^{-2}\Delta_{(Y_1,Y_2)} + \mathscr{O}(1), \tag{3.11b}$$

where

$$\Delta_{(Y_1,Y_2)} \equiv \partial_{Y_1}^2 + \partial_{Y_2}^2. \tag{3.11c}$$

Moreover, by letting $\boldsymbol{Y}' \equiv (Y_1, Y_2)^T$, $\rho \equiv |\boldsymbol{Y}'| = \sqrt{Y_1^2 + Y_2^2}$, and

$$\mathscr{J}_i \equiv \big(\boldsymbol{x}_i \times \partial_\theta \boldsymbol{x}_i \,\big|\, \partial_\theta \boldsymbol{x}_i\big) = \begin{pmatrix} -\sin\varphi_i & \cos\theta_i\cos\varphi_i \\ \cos\varphi_i & \cos\theta_i\sin\varphi_i \\ 0 & -\sin\theta_i \end{pmatrix},$$

we readily calculate

$$\boldsymbol{x}^i(\varepsilon\boldsymbol{Y}) = \boldsymbol{x}_i + \varepsilon\big(\mathscr{J}_i\boldsymbol{Y}' - Y_3\boldsymbol{x}_i\big) - \varepsilon^2\big(\frac{\rho^2\boldsymbol{x}_i}{2} + Y_3\big(Y_2\partial_\theta\boldsymbol{x}_i + Y_1\boldsymbol{x}_i\times\partial_\theta\boldsymbol{x}_i\big)\big) + \mathscr{O}(\varepsilon^3), \tag{3.12}$$

from which it follows that for all $\boldsymbol{Y}' = \mathscr{O}(1)$

$$|\boldsymbol{x}^i(\varepsilon(\boldsymbol{Y}',0)) - \boldsymbol{\xi}|^2 = |\boldsymbol{x}_i - \boldsymbol{\xi}|^2 + 2\varepsilon\boldsymbol{Y}'^T\mathscr{J}_i^T(\boldsymbol{x}_i - \boldsymbol{\xi}) + \mathscr{O}(\varepsilon^2) \tag{3.13a}$$

when $|\boldsymbol{\xi} - \boldsymbol{x}_i| = \mathscr{O}(1)$, and

$$|\boldsymbol{x}^i(\varepsilon(\boldsymbol{Y}',0)) - \boldsymbol{\xi}|^2 = \varepsilon^2|\boldsymbol{Y}' - \boldsymbol{Z}'|^2 + \mathscr{O}(\varepsilon^4), \tag{3.13b}$$

when $\boldsymbol{\xi} = \boldsymbol{x}^i(\varepsilon(\boldsymbol{Z}',0))$ and $\boldsymbol{Z}' = \mathscr{O}(1)$. In the second case we have used $\mathscr{J}_i^T\mathscr{J}_i = \mathscr{I}_2$ (the 2×2 identity matrix) as well as $\mathscr{J}_i^T\boldsymbol{x}_i = \boldsymbol{0}$ to cancel the $\mathscr{O}(\varepsilon^3)$ contribution. On the other hand, writing any $\boldsymbol{v}\in\mathbb{R}^3$ as $\boldsymbol{v} = v_1\boldsymbol{x}_i + v_2\partial_\theta\boldsymbol{x}_i + v_3\boldsymbol{x}_i\times\partial_\theta\boldsymbol{x}_i$ we obtain

$$\mathscr{J}_i\mathscr{J}_i^T\boldsymbol{v} = \mathscr{J}_i\begin{pmatrix} v_3 \\ v_2\end{pmatrix} = v_2\partial_\theta\boldsymbol{x}_i + v_3\boldsymbol{x}_i\times\partial_\theta\boldsymbol{x}_i,$$

from which we obtain

$$\mathscr{J}_i\mathscr{J}_i^T = \mathscr{I}_3 - \boldsymbol{x}_i\boldsymbol{x}_i^T, \tag{3.14}$$

and deduce that $\mathscr{J}_i\mathscr{J}_i^T$ is the projection onto the tangent plane of $\partial\Omega$ at $\boldsymbol{x}_i$.

3.1.2 Matched Asymptotic Expansions and the Nonlinear Algebraic System

We seek a quasi-equilibrium solution to (3.5) which is stationary on an $\mathscr{O}(1)$ time scale. First we construct the inner solution by letting $\boldsymbol{Y}$ be the local coordinates near $\boldsymbol{x}_i$ given by (3.11a). From (3.5c) we see that $w(\boldsymbol{x}^i(\varepsilon\boldsymbol{Y})) = \mathscr{O}(\varepsilon^{-1})$ and therefore the leading order core problem for the membrane-bound activator and inhibitor are identical to those previously considered in [84] and [91]. In particular the leading order inner solution is completely determined by an unknown constant *spot strength* S_i and is explicitly given by

$$u(\boldsymbol{x}^i(\varepsilon\boldsymbol{Y}',0)) = \sqrt{D_v}U_{i0}(\rho) + \mathscr{O}(\varepsilon), \quad v(\boldsymbol{x}^i(\varepsilon\boldsymbol{Y}',0)) = \frac{1}{\sqrt{D_v}}V_{i0}(\rho) + \mathscr{O}(\varepsilon), \tag{3.15}$$

where

$$U_{i0}(\rho) \equiv U_c(\rho;S_i,f), \qquad V_{i0}(\rho) \equiv V_c(\rho;S_i,f), \tag{3.16}$$

and $(U_c(\rho;S,f),V_c(\rho;S,f))$ is the radially symmetric solution to the core problem

$$\partial_\rho^2 U_c + \rho^{-1}\partial_\rho U_c - U_c + fU_c^2 V_c = 0, \qquad \rho > 0, \tag{3.17a}$$
$$\partial_\rho^2 V_c + \rho^{-1}\partial_\rho V_c + U_c - U_c^2 V_c = 0, \qquad \rho > 0, \tag{3.17b}$$
$$\partial_\rho U_c = \partial_\rho V_c = 0, \qquad \text{at } \rho = 0, \tag{3.17c}$$
$$U_c \to 0, \quad V_c \sim S\log\rho + \chi(S,f) + o(1), \qquad \text{as } \rho \to \infty. \tag{3.17d}$$

The function $\chi(S,f)$ indicates the far-field constant behaviour of the inner inhibitor solution and can be numerically calculated by solving (3.17) on a truncated domain (see §2 of [84]). In Figure 3.2a we plot the numerically calculated $\chi(S,f)$ versus $S > 0$ for select values of $0 < f < 1$. By integrating (3.17b) over $0 < \rho < \infty$ we obtain the useful identity

$$S_i = \frac{1-f}{f}\int_0^\infty U_{i0}(\rho)\rho d\rho = -\int_0^\infty \big(U_{i0}(\rho) - U_{i0}(\rho)^2 V_{i0}(\rho)\big)\rho d\rho. \tag{3.18}$$

The leading order behaviour of the bulk-bound activator near $\boldsymbol{x}_i$ is then readily computed by letting

$$w(\boldsymbol{x}^i(\varepsilon\boldsymbol{Y})) = \varepsilon^{-1}W_{i0}(\boldsymbol{Y}) + \mathscr{O}(1), \tag{3.19}$$

so from (3.11b) we obtain

$$\partial_{Y_3}^2 W_{i0} + \Delta_{(Y_1,Y_2)} W_{i0} = 0, \qquad (\boldsymbol{Y}', Y_3) \in \mathbb{R}^2 \times (0,\infty),$$
$$D_w \partial_{Y_3} W_{i0} = K\sqrt{D_v}U_{i0}(\rho), \qquad (\boldsymbol{Y}', Y_3) \in \mathbb{R}^2 \times \{0\}.$$

This in turn can be explicitly solved using the Neumann Green's function on the upper half-space which yields

$$W_{i0}(\boldsymbol{Y}) = \frac{K\sqrt{D}_v}{2\pi D_w}\int_0^\infty\int_0^\infty \frac{U_c(\sqrt{\xi_1^2+\xi_2^2})}{\sqrt{(\xi_1-Y_1)^2+(\xi_2-Y_2)^2+Y_3^2}}d\xi_1 d\xi_2 + \overline{W}_{i0}, \tag{3.20}$$

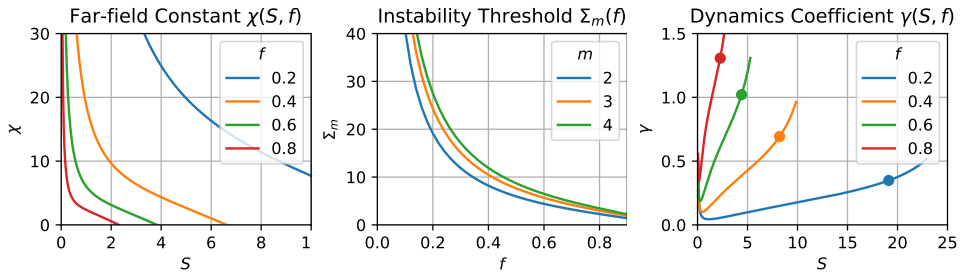

Figure 3.2: Numerically calculated (a) far-field constant $\chi(S,f)$, (b) m-mode instability threshold $\Sigma_m(f)$ for $2 \leq m \leq 4$, and (c) slow dynamics multiplier $\gamma(S,f)$. The solid circles in (c) indicate values of $\gamma(S,f)$ at the splitting instability thresholds $\Sigma_2(f)$. These functions depend only on the local structure of each spot and are therefore independent of bulk-membrane coupling.

where $\overline{W}_{i0}$ is an undetermined constant. Note that W_{i0} is bounded for all $Y_3 \geq 0$, and is radially symmetric when $Y_3 = 0$.

When $\boldsymbol{x} \in \partial\Omega$ and $|\boldsymbol{x}-\boldsymbol{x}_i| \gg \varepsilon$ for all $i = 1,\ldots,N$ the exponential decay of each $U_{i0}(\rho)$ as $\rho \to \infty$, together with (3.13) implies that the membrane-bound activator is, to leading order, given by

$$u(\boldsymbol{x}) \sim \varepsilon^2 w(\boldsymbol{x}) + \sqrt{D_v}\sum_{i=1}^{N} U_{i0}(\varepsilon^{-1}|\boldsymbol{x}-\boldsymbol{x}_i|), \tag{3.21}$$

which in turn implies the distributional limits

$$\frac{u-u^2v}{\varepsilon^2} \to w(\boldsymbol{x}) - 2\pi\sqrt{D_v}\sum_{i=1}^{N} S_i \delta_{\partial\Omega}(\boldsymbol{x}-\boldsymbol{x}_i), \qquad \varepsilon \to 0^+,$$

$$\frac{u}{\varepsilon^2} \to w(\boldsymbol{x}) + \frac{2\pi\sqrt{D_v}f}{1-f}\sum_{i=1}^{N} S_i \delta_{\partial\Omega}(\boldsymbol{x}-\boldsymbol{x}_i), \qquad \varepsilon \to 0^+.$$

The leading order outer problems for the membrane-bound inhibitor and bulk-

bound activator are then respectively given by

$$D_v \Delta_{\partial\Omega} v = -w(\boldsymbol{x}) + 2\pi\sqrt{D_v}\sum_{i=1}^{N} S_i \delta_{\partial\Omega}(\boldsymbol{x}-\boldsymbol{x}_i), \qquad \boldsymbol{x}\in\partial\Omega, \tag{3.22}$$

and

$$D_w \Delta w = -E(\boldsymbol{x}), \qquad \boldsymbol{x}\in\Omega, \tag{3.23a}$$

$$D_w \partial_n w + (1-K)w = 2\pi\sqrt{D_v}\frac{Kf}{1-f}\sum_{i=1}^{N} S_i \delta_{\partial\Omega}(\boldsymbol{x}-\boldsymbol{x}_i), \qquad \boldsymbol{x}\in\partial\Omega. \tag{3.23b}$$

By first integrating (3.22) over $\partial\Omega$ and then applying the divergence theorem to (3.23) we deduce the solvability condition

$$\sum_{i=1}^{N} S_i = \frac{1}{2\pi\sqrt{D_v}(1-K)}\int_{\Omega} E(\boldsymbol{x})d^3\boldsymbol{x} + \frac{Kf}{(1-f)(1-K)}\sum_{i=1}^{N} S_i,$$

which can be further rearranged into the form

$$\sum_{i=1}^{N} S_i = \frac{1}{2\pi\sqrt{D_v}}\left(1-\frac{K}{1-f}\right)^{-1}\int_{\Omega} E(\boldsymbol{x})d^3\boldsymbol{x}. \tag{3.24}$$

The dependence of the spot strengths on the total membrane-bound fuel is similar to that obtained for spot patterns to the Brusselator model in the unit disk with an inhomogeneous fuel source [96], whereas the coupling-dependence reflects a feedback mechanism introduced by the cycle of membrane detachment and reattachment. Moreover, using (3.6) we obtain that in terms of the original problem parameters $(1-K/(1-f))^{-1} = \mathscr{K}_1/k_d$ which indicates that the coupling-dependent multiplier reflects the ratio between the rate of membrane-detachment to that of degradation.

Next we solve for the membrane-bound inhibitor and bulk-bound activator in the outer region where $|\boldsymbol{x}-\boldsymbol{x}_i| \gg \mathscr{O}(\varepsilon)$ for all $i = 1,...,N$. First we note that (3.23) is solved by

$$w(\boldsymbol{x}) \sim \frac{1}{D_w} w_E(\boldsymbol{x}) + \frac{2\pi\sqrt{D_v}}{D_w}\frac{Kf}{1-f}\sum_{i=1}^{N} S_i G_{mr}(\boldsymbol{x},\boldsymbol{x}_i), \tag{3.25}$$

where $w_E(\boldsymbol{x})$ is the unique solution to

$$\Delta w_E = -E(x), \qquad \boldsymbol{x} \in \Omega; \qquad \partial_n w_E + \frac{1-K}{D_w} w_E = 0, \qquad \boldsymbol{x} \in \partial\Omega, \tag{3.26}$$

and $G_{mr}(\boldsymbol{x},\boldsymbol{x}_i)$ is the membrane Robin Green's function satisfying

$$\Delta G_{mr} = 0, \qquad \boldsymbol{x} \in \Omega; \qquad \partial_n G_{mr} + \frac{1-K}{D_w} G_{mr} = \delta_{\partial\Omega}(\boldsymbol{x}-\boldsymbol{x}_i), \qquad \boldsymbol{x} \in \partial\Omega, \tag{3.27a}$$

for which we note the explicit series expansion

$$G_{mr}(\boldsymbol{x},\boldsymbol{\xi}) = \frac{1}{4\pi} \sum_{l=0}^{\infty} g_l P_l(\boldsymbol{\xi}^T \boldsymbol{x}), \qquad g_l \equiv \frac{2l+1}{l + \frac{1-K}{D_w}}, \tag{3.27b}$$

where $P_l(x)$ is the Legendre polynomial of degree l. Assuming the solvability condition (3.24) is satisfied, substituting (3.25) into (3.22) we explicitly calculate the outer solution for the membrane-bound inhibitor

$$\begin{aligned} v \sim &- \frac{2\pi}{\sqrt{D_v}} \sum_{i=1}^{N} \left(G_s(\boldsymbol{x},\boldsymbol{x}_i) - \frac{1}{D_w} \frac{Kf}{1-f} \int_{\partial\Omega} G_s(\boldsymbol{x},\boldsymbol{\xi}) G_{mr}(\boldsymbol{\xi},\boldsymbol{x}_i) dA_{\boldsymbol{\xi}} \right) S_i \\ &+ \frac{1}{\sqrt{D_v}} \bar{v} + \frac{1}{D_w D_v} v_E(\boldsymbol{x}), \end{aligned} \tag{3.28}$$

where $\bar{v}$ is an undetermined constant, $v_E(\boldsymbol{x})$ is given by

$$v_E(\boldsymbol{x}) \equiv \int_{\partial\Omega} G_s(\boldsymbol{x},\boldsymbol{\xi}) w_E(\boldsymbol{\xi}) dA_{\boldsymbol{\xi}}, \tag{3.29}$$

and $G_s(\boldsymbol{x},\boldsymbol{\xi})$ is the membrane Green's function satisfying

$$\Delta_{\partial\Omega} G_m(\boldsymbol{x},\boldsymbol{\xi}) = \frac{1}{4\pi} - \delta_{\partial\Omega}(\boldsymbol{x}-\boldsymbol{\xi}), \qquad \boldsymbol{x} \in \partial\Omega, \tag{3.30a}$$

$$\int_{\partial\Omega} G_s(\boldsymbol{x},\boldsymbol{\xi}) dA_{\boldsymbol{x}} = 0, \qquad \boldsymbol{\xi} \in \partial\Omega, \tag{3.30b}$$

and given explicitly given by [84]

$$G_s(\boldsymbol{x},\boldsymbol{\xi}) = -\frac{1}{2\pi} \log|\boldsymbol{x}-\boldsymbol{\xi}| + R_0, \qquad R_0 \equiv \frac{\log 4 - 1}{4\pi}. \tag{3.30c}$$

In addition we note that this membrane Green's function has the series expansion

$$G_s(\boldsymbol{x},\boldsymbol{\xi}) = \frac{1}{4\pi}\sum_{l=1}^{\infty}\frac{2l+1}{l(l+1)}P_l(\boldsymbol{\xi}^T\boldsymbol{x}), \tag{3.31}$$

so that by using the well known product formula

$$\int_{\partial\Omega} P_l(\boldsymbol{x}_i^T\boldsymbol{x})P_k(\boldsymbol{x}^T\boldsymbol{x}_j)dA_x = \delta_{kl}\frac{4\pi}{2l+1}P_l(\boldsymbol{x}_i^T\boldsymbol{x}_j), \tag{3.32}$$

and expansion (3.27b) we obtain

$$\int_{\partial\Omega} G_s(\boldsymbol{x},\boldsymbol{\xi})G_{mr}(\boldsymbol{\xi},\boldsymbol{x}_i)dA_{\boldsymbol{\xi}} = \frac{1}{4\pi}\sum_{l=1}^{\infty}\frac{g_l}{l(l+1)}P_l(\boldsymbol{x}_i^T\boldsymbol{x}), \qquad \boldsymbol{x}\in\partial\Omega. \tag{3.33}$$

To determine the unknown spot strengths $S_1,\cdots,S_N$ we match the behaviour of the inner solution (3.15) as $\rho\to\infty$ with the limiting behaviour of the outer solution (3.28) as $|\boldsymbol{x}-\boldsymbol{x}_i|\to 0$ for each $i=1,...,N$. Recalling the local expansion (3.13) and using (3.30c) we calculate

$$G_s(\boldsymbol{x}^i(\varepsilon(\boldsymbol{Y}',0)),\boldsymbol{\xi}) \sim G_s(\boldsymbol{x}_i,\boldsymbol{\xi}) - \frac{\varepsilon}{2\pi}\boldsymbol{Y}'^T\mathscr{J}_i^T\frac{\boldsymbol{x}-\boldsymbol{\xi}}{|\boldsymbol{x}-\boldsymbol{\xi}|^2} + \mathscr{O}(\varepsilon^2), \tag{3.34a}$$

when $|\boldsymbol{\xi}-\boldsymbol{x}_i|\gg\varepsilon$, and

$$G_s(\boldsymbol{x}^i(\varepsilon(\boldsymbol{Y}',0)),\boldsymbol{\xi}) \sim -\frac{1}{2\pi}\log|\boldsymbol{Y}'-\boldsymbol{Z}'| + \frac{1}{2\pi\nu} + R_0 + \mathscr{O}(\varepsilon^2), \tag{3.34b}$$

when $\boldsymbol{\xi}=\boldsymbol{x}^i(\varepsilon(\boldsymbol{Z}',0))$ and $\boldsymbol{Z}'=\mathscr{O}(1)$ and where we identify

$$\nu \equiv -\frac{1}{\log\varepsilon} \ll 1. \tag{3.35}$$

Evaluating (3.28) at $\boldsymbol{x}=\boldsymbol{x}^i(\varepsilon(\boldsymbol{Y}',0))$ we therefore obtain

$$\begin{aligned}\sqrt{D_v}v(\boldsymbol{x}^i(\varepsilon(\boldsymbol{Y}',0))) \sim &\left(\log\rho-\frac{1}{\nu}\right)S_i - 2\pi\sum_{j=1}^{N}\mathscr{G}_{ij}S_j + \frac{v_E(\boldsymbol{x}_i)}{D_w\sqrt{D_v}} + \bar{v}\\ &+\varepsilon\boldsymbol{Y}'^T\mathscr{J}_i^T\left(\sum_{j\neq i}S_j\boldsymbol{\alpha}_{ij} + \frac{\nabla_{\boldsymbol{x}}v_E(\boldsymbol{x}_i)}{D_w\sqrt{D_v}}\right) + \mathscr{O}(\varepsilon^2).\end{aligned} \tag{3.36}$$

where for all $i, j = 1, ..., N$ we define

$$\mathscr{G}_{ij} \equiv -\frac{1}{D_w}\frac{Kf}{1-f}\int_{\partial\Omega} G_s(\boldsymbol{x}_i, \boldsymbol{\xi}) G_{mr}(\boldsymbol{\xi}, \boldsymbol{x}_j) dA_{\boldsymbol{\xi}} + \begin{cases} R_0, & i = j, \\ G_s(\boldsymbol{x}_i, \boldsymbol{x}_j), & i \neq j, \end{cases} \tag{3.37}$$

and

$$\boldsymbol{\alpha}_{ij} \equiv \frac{\boldsymbol{x}_i - \boldsymbol{x}_j}{|\boldsymbol{x}_i - \boldsymbol{x}_j|^2} - \frac{f}{1-f}\frac{K}{D_w}\int_{\partial\Omega} \frac{\boldsymbol{x}_i - \boldsymbol{\xi}}{|\boldsymbol{x}_i - \boldsymbol{\xi}|^2} G_{mr}(\boldsymbol{\xi}, \boldsymbol{x}_j) dA_{\boldsymbol{\xi}}. \tag{3.38}$$

We also note that by using (3.29) and (3.30c) we explicitly calculate

$$\nabla_{\boldsymbol{x}} v_E(\boldsymbol{x}_i) \equiv -\frac{1}{2\pi}\int_{\partial\Omega} \frac{\boldsymbol{x}_i - \boldsymbol{\xi}}{|\boldsymbol{x}_i - \boldsymbol{\xi}|^2} w_E(\boldsymbol{\xi}) dA_{\boldsymbol{\xi}}. \tag{3.39}$$

While the $\mathscr{O}(\varepsilon)$ correction in (3.36) does not play a role in either the quasi-equilibrium construction or the leading-order linear stability theory on an $\mathscr{O}(1)$ timescale, it does play a crucial role in deriving the slow dynamics taking place on an $\mathscr{O}(\varepsilon^{-2})$ timescale as detailed in §3.3 below.

Comparing the behaviour of the outer solution (3.36) in the limit $|x - x_i| \to 0$ with the limiting behaviour of the inner solution (3.15) as $\rho \to \infty$ yields, to leading order, the nonlinear system

$$\nu^{-1}\boldsymbol{S} + 2\pi\mathscr{G}\boldsymbol{S} + \boldsymbol{\chi}(\boldsymbol{S}, f) = \bar{v}\boldsymbol{e} + \frac{1}{D_w\sqrt{D_v}}\boldsymbol{v}_E, \tag{3.40}$$

where

$$\boldsymbol{S} \equiv \begin{pmatrix} S_1 \\ \vdots \\ S_N \end{pmatrix}, \boldsymbol{e} \equiv \begin{pmatrix} 1 \\ \vdots \\ 1 \end{pmatrix}, \boldsymbol{v}_E \equiv \begin{pmatrix} v_E(\boldsymbol{x}_1) \\ \vdots \\ v_E(\boldsymbol{x}_N) \end{pmatrix}, \boldsymbol{\chi}(\boldsymbol{S}; f) \equiv \begin{pmatrix} \chi(S_1, f) \\ \vdots \\ \chi(S_N, f) \end{pmatrix}, \tag{3.41}$$

and $\mathscr{G}$ is the $N \times N$ matrix with entries $\mathscr{G}_{ij}$ given by (3.37). The nonlinear system (3.40) must be solved subject to the solvability condition (3.24) which we can rewrite as $\boldsymbol{e}^T\boldsymbol{S} = NS_c$ where the common spot strength S_c is defined by

$$S_c \equiv \frac{1}{2\pi N\sqrt{D_v}}\left(1 - \frac{K}{1-f}\right)^{-1}\int_{\Omega} E(\boldsymbol{x}) d^3\boldsymbol{x}. \tag{3.42}$$

Left-multiplying (3.40) by $\boldsymbol{e}^T$ and using the solvability condition we calculate

$$\bar{v} = \frac{1}{\nu} S_c + \frac{1}{N} \boldsymbol{e}^T \left(2\pi \mathscr{G} + \boldsymbol{\chi}(\boldsymbol{S}, f) \right) - \frac{1}{D_w \sqrt{D_v} N} \boldsymbol{e}^T \boldsymbol{v}_E, \tag{3.43a}$$

from which we find that the unknown spot strengths $\boldsymbol{S}$ must solve the nonlinear algebraic system (NAS)

$$\boldsymbol{S} + 2\pi\nu(\mathscr{I}_N - \mathscr{E}_N)\mathscr{G}\boldsymbol{S} + \nu(\mathscr{I}_N - \mathscr{E}_N)\boldsymbol{\chi}(\boldsymbol{S}, f) = S_c \boldsymbol{e} + \frac{\nu}{D_w \sqrt{D_v}} (\mathscr{I}_N - \mathscr{E}_N) \boldsymbol{v}_E \tag{3.43b}$$

where $\mathscr{I}_N$ is the $N \times N$ identity matrix and $\mathscr{E}_N \equiv N^{-1} \boldsymbol{e}\boldsymbol{e}^T$. Summarizing, we have the following proposition.

Proposition 3.1.1. *Let $\varepsilon \ll 1$ and assume that $\boldsymbol{x}_1, ..., \boldsymbol{x}_N \in \partial\Omega$ are well separated in the sense that $|\boldsymbol{x}_i - \boldsymbol{x}_j| \gg \varepsilon$ for all $i \neq j$. Then, a quasi-equilibrium solution to* (3.5) *consisting of N-spots concentrating at $\boldsymbol{x}_1, ..., \boldsymbol{x}_N$ is asymptotically given by* (3.15) *and* (3.19) *when $|\boldsymbol{x} - \boldsymbol{x}_i| \ll \varepsilon$ for each $i = 1, ..., N$, and by* (3.21)*,* (3.28)*, and* (3.25) *when $|\boldsymbol{x} - \boldsymbol{x}_i| \gg \varepsilon$ for all $i = 1, ..., N$, where $\bar{v}$ is given by* (3.43a) *and the spot strengths $S_1, ..., S_N$ are found by solving the NAS* (3.43b)*.*

Although the NAS (3.43b) must in general be solved numerically, it provides an asymptotic approximation that is accurate to all orders of $\nu = -1/\log\varepsilon \ll 1$. Indeed, assuming that all problem parameters are $\mathscr{O}(1)$ with respect to $\varepsilon \ll 1$, we can easily calculate a two-term asymptotic expansion in powers of ν as

$$\boldsymbol{S} \sim S_c \boldsymbol{e} + \nu(\mathscr{I}_N - \mathscr{E}_N) \left(\frac{1}{D_w \sqrt{D_v}} \boldsymbol{v}_E - 2\pi S_c \mathscr{G} \boldsymbol{e} \right) + \mathscr{O}(\nu^2),$$

for which we highlight that the logarithmic dependence of ν on ε may render the correction term ν^2 impractically large. On the other hand, under certain conditions on the spot configuration $\boldsymbol{x}_1, ..., \boldsymbol{x}_N$ and bulk-bound fuel source $E(\boldsymbol{x})$ the NAS (3.43b) may be explicitly solved. In fact, since the range of $\mathscr{I}_N - \mathscr{E}_N$ is orthogonal to $\boldsymbol{e}$ we find that $\boldsymbol{S} = S_c \boldsymbol{e}$ is an exact solution of (3.43b) provided that

$$(\mathscr{I}_N - \mathscr{E}_N) \left(\frac{1}{D_w \sqrt{D_v}} \boldsymbol{v}_E - 2\pi S_c \mathscr{G} \boldsymbol{e} \right) = \boldsymbol{0}.$$

One such example occurs when the bulk-bound fuel has azimuthal symmetry about

an axis spanned by $\boldsymbol{z} \neq \boldsymbol{0}$. In such a case $v_E = v_E(\boldsymbol{z}^T\boldsymbol{x})$ and $\boldsymbol{S} = S_c\boldsymbol{e}$ exactly solves (3.43b) provided that $\boldsymbol{x}_1, ..., \boldsymbol{x}_N$ are uniformly distributed on a ring making a common angle with $\boldsymbol{z}$. Indeed for such a configuration $\boldsymbol{v}_E$ is proportional to $\boldsymbol{e}$ while $\mathscr{G}$ is a circulant matrix and therefore has a constant row-sum. Finally, we remark that distinct asymptotic approximations to (3.43b) can be calculated when the remaining problem parameters are in different ε-dependent regimes [91].

3.2 Linear Stability on an $\mathscr{O}(1)$ Timescale

In this section we consider the linear stability on an $\mathscr{O}(1)$ timescale of the quasi-equilibrium solution (u_e, v_e, w_e) constructed in §3.1 above. We begin by first considering perturbations of the form

$$u(\boldsymbol{x}) = u_e(\boldsymbol{x}) + e^{\lambda t}\varphi(\boldsymbol{x}),\ v(\boldsymbol{x}) = v_e(\boldsymbol{x}) + e^{\lambda t}\psi(\boldsymbol{x}),\ w(\boldsymbol{x}) = w_e(\boldsymbol{x}) + e^{\lambda t}\eta(\boldsymbol{x}),$$

where we assume that $\lambda = \mathscr{O}(1)$ to reflect our restriction to instabilities arising on an $\mathscr{O}(1)$ timescale. Substituting into (3.5) and retaining only the linear terms in φ, ψ, and η then yields the linearized eigenvalue problem

$$\varepsilon^2\Delta_{\partial\Omega}\phi - \phi + 2fu_ev_e\phi + fu_e^2\psi + \varepsilon^2\eta = \lambda\phi, \qquad \boldsymbol{x} \in \partial\Omega, \tag{3.44a}$$

$$D_v\Delta_{\partial\Omega}\psi + \varepsilon^{-2}(\phi - 2u_ev_e\phi - u_e^2\psi) = \tau_v\lambda\psi \qquad \boldsymbol{x} \in \partial\Omega, \tag{3.44b}$$

$$D_w\Delta\eta = \tau_w\lambda\eta, \qquad \boldsymbol{x} \in \Omega, \tag{3.44c}$$

$$D_w\partial_n\eta + \eta = \varepsilon^{-2}K\phi, \qquad \boldsymbol{x} \in \partial\Omega,, \tag{3.44d}$$

Comparing this system with (3.5) we deduce that, as in §3.1, ϕ is localized at the N spot locations $\boldsymbol{x}_1, ..., \boldsymbol{x}_N$, while ϕ, ψ, and η retain the same relative scalings in the inner-region near each spot location as in §3.1, mainly ϕ and ψ are $\mathscr{O}(1)$ and η is $\mathscr{O}(\varepsilon^{-1})$ near each $\boldsymbol{x}_j$ $(j = 1, ..., N)$. In terms of polar coordinates $\boldsymbol{Y}' = (\rho\cos\Theta, \rho\sin\Theta)$ near the j^{th} spot, we seek an inner expansion of the form

$$\phi(\boldsymbol{x}^j(\varepsilon\boldsymbol{Y}', 0)) = \Phi_j(\rho)e^{im\Theta} + \mathscr{O}(\varepsilon),\ \psi(\boldsymbol{x}^j(\varepsilon\boldsymbol{Y}', 0)) = D_v^{-1}\Psi_j(\rho)e^{im\Theta} + \mathscr{O}(\varepsilon), \tag{3.45}$$

where $m = 0, 2, 3...$ and we omit the neutrally stable translational $m = 1$ mode. Assuming that both $\tau_v\lambda\varepsilon^2 \ll 1$ and $\tau_w\lambda\varepsilon^2 \ll 1$ the leading order inner problem

near the j^{th} spot is then given by

$$\Delta_\rho \boldsymbol{M}_j - \frac{m^2}{\rho^2}\boldsymbol{M}_j + \mathscr{Q}(\rho;S_j,f)\boldsymbol{M}_j = \lambda \mathscr{E}_{11}\boldsymbol{M}_j, \qquad \rho > 0, \tag{3.46a}$$

where $\boldsymbol{M}_j \equiv (\Phi_j(\rho),\Psi_j(\rho))^T$ and

$$\mathscr{Q}(\rho;S,f) \equiv \begin{pmatrix} 2fU_c(\rho;S,f)V_c(\rho;S,f)-1 & fU_c(\rho;S,f)^2 \\ -2U_c(\rho;S,f)V_c(\rho;S,f)+1 & -U_c(\rho;S,f)^2 \end{pmatrix}, \mathscr{E}_{11} = \begin{pmatrix} 1 & 0 \\ 0 & 0 \end{pmatrix}.$$

At the origin we impose the boundary condition $\boldsymbol{M}_j'(0) = 0$ while the limiting behaviour as $\rho \to \infty$ is found by first noting that

$$\mathscr{Q}(\rho;S,f) \to \begin{pmatrix} -1 & 0 \\ 1 & 0 \end{pmatrix} \qquad \text{as } \rho \to \infty,$$

for all $S \geq 0$ and hence

$$\Phi_j \to 0, \qquad \Psi_j \sim \begin{cases} \mathscr{O}(\log\rho) & m = 0 \\ \mathscr{O}(\rho^{-m}) & m \geq 1, \end{cases} \qquad \rho \to \infty. \tag{3.46b}$$

Instabilities due to the $m = 0$ and $m \geq 2$ modes arise through distinct mechanisms due to the logarithmic growth of the former and the algebraic decay of the latter. Indeed, proceeding with the method of matched asymptotic expansions as in §3.1 we determine that the limiting behaviour of ψ as $|\boldsymbol{x} - \boldsymbol{x}_j| \to 0$ for each $j = 1,...,N$ is $\mathscr{O}(1)$ and $\mathscr{O}(\varepsilon^m)$ when $m = 0$ and $m \geq 2$ respectively. Consequently global contributions are, to leading order in $\varepsilon \ll 1$, absent in the calculation of instabilities to due $m \geq 2$ perturbations, whereas they may arise when $m = 0$. In the proceeding sections we discuss these two cases separately.

3.2.1 The $m \geq 2$ Mode Instabilities

Due to the algebraic decay of $\Psi_j(\rho)$ as $\rho \to \infty$ for each $j = 1,...,N$ when $m \geq 2$ the inner problems are interact through the outer solution only weakly. Therefore, each spot may undergo an $m \geq 2$ mode instability individually with the relevant instability threshold being determined solely by the spot strength S_j ($j = 1,...,N$).

In particular, it suffices to consider the spectrum of

$$\Delta_\rho \boldsymbol{M} - \frac{m^2}{\rho^2}\boldsymbol{M} + \mathscr{Q}(\rho; S, f)\boldsymbol{M} = \lambda \mathscr{E}_{11}\boldsymbol{M}, \quad \rho > 0, \tag{3.47a}$$

$$\boldsymbol{M}'(0) = 0, \qquad \boldsymbol{M} \to \begin{pmatrix} 0 \\ M_\infty \rho^{-m} \end{pmatrix} \quad \text{as } \rho \to \infty, \tag{3.47b}$$

as a function of $0 < f < 1$, $m \geq 2$, and $S > 0$. The eigenvalue problem (3.47) is identical to that found in the study of multi-spot solutions for the Brusselator system on the unit sphere [84, 91] and the unit disk [96], and it also shares qualitative similarities with analogous problems derived for the two- and three-dimensional Schnakenberg models [48, 98]. In particular, for a fixed value of $m \geq 2$ it is known that there exists a threshold $\Sigma_m(f) > 0$ such that (3.47) admits an eigenvalue with positive real part if and only if $S > \Sigma_m(f)$. Each threshold $\Sigma_m(f)$ must be calculated numerically and this is easily accomplished by studying the spectrum of the matrix obtained by an appropriate discretization of (3.47) on a truncated domain (see §3.1 of [84] for details).

The plots of $\Sigma_2(f)$, $\Sigma_3(f)$, and $\Sigma_4(f)$ versus $0 < f < 1$ shown in Figure 3.2b indicate that $\Sigma_2(f) < \Sigma_3(f) < \Sigma_4(f)$ while further numerical evidence suggests that in fact $\Sigma_2(f) < \Sigma_m(f)$ for all $m \geq 2$ so that $\Sigma_2(f)$ is the appropriate instability threshold. It follows that a multi-spot pattern with spot strengths $S_1, ..., S_N$ is unstable with respect to the $m \geq 2$ modes if $S_i > \Sigma_2(f)$ for any $i = 1, .., N$. Moreover, numerical simulations of (3.5) have shown that $m = 2$ instabilities lead to nonlinear splitting and self-replicating events [84]. This numerically observed behaviour has more recently been analytically justified by a weakly nonlinear analysis and derivation of normal form amplitude equations for the two-dimensional Schnakenberg and Brusselator models for which it was demonstrated that $m = 2$ mode instabilities are *subcritical* [113].

3.2.2 The $m = 0$ Mode Instabilities

For each $j = 1, ..., N$ we use the homogeneity of the eigenvalue problem (3.46a) and corresponding boundary conditions (3.46b) to let

$$\boldsymbol{M}_j(\rho) = c_j \boldsymbol{M}(\rho; S_j, f), \tag{3.48}$$

where c_j is an undetermined constant and $\boldsymbol{M}$ satisfies

$$\Delta_\rho \boldsymbol{M} + \mathscr{Q}(\rho; S, f)\boldsymbol{M} = \lambda \mathscr{E}_{11} \boldsymbol{M}, \quad \rho > 0, \tag{3.49a}$$

$$\boldsymbol{M}'(0) = 0, \quad \boldsymbol{M} \to \begin{pmatrix} 0 \\ \log\rho + B_\lambda(S, f) \end{pmatrix}, \quad \text{as } \rho \to \infty. \tag{3.49b}$$

The constant far-field constant $B_\lambda(S, f)$ must in general be calculated numerically for $\lambda \neq 0$. On the other hand, differentiating the core problem (3.17) with respect to S we find that $\boldsymbol{M} = \partial_S(U_c(\rho; S, f), V_c(\rho; S, f))^T$ satisfies (3.49) with $\lambda = 0$ and in particular we obtain the important identity

$$B_0(S, f) = \chi'(S, f), \qquad \chi'(S, f) \equiv \frac{\partial \chi(S, f)}{\partial S}. \tag{3.50}$$

We can therefore use the numerically calculated function $\chi(S, f)$ to approximate the derivative $\chi'(S, f)$ to calculate zero eigenvalue crossing instability thresholds. For the remainder of this section we assume that $\lambda = 0$ and hence determine the effect of bulk-membrane couping on zero-eigenvalue crossing instabilities.

Integrating (3.46a) and using the divergence theorem together with (3.48) and (3.49) we calculate

$$\int_0^\infty \left[(1 - 2U_{j0}(\rho)V_{j0}(\rho))\Phi_j(\rho) - U_{j0}(\rho)^2 \Psi_j(\rho)\right] \rho d\rho = -c_j,$$

$$\int_0^\infty \Phi_j(\rho)\rho d\rho = \frac{f}{1-f} c_j,$$

from which we then calculate the distributional limits

$$\frac{(1-2u_e v_e)\phi - u_e^2\psi}{\varepsilon^2} \to \eta(\boldsymbol{x}) - 2\pi \sum_{j=1}^{N} c_j \delta_{\partial\Omega}(\boldsymbol{x}-\boldsymbol{x}_j), \qquad \varepsilon \to 0^+,$$

$$\frac{\phi}{\varepsilon^2} \to \eta(\boldsymbol{x}) + \frac{2\pi f}{1-f} \sum_{j=1}^{N} c_j \delta_{\partial\Omega}(\boldsymbol{x}-\boldsymbol{x}_j), \qquad \varepsilon \to 0^+,$$

In the outer region for which $|\boldsymbol{x}-\boldsymbol{x}_j| \gg \mathcal{O}(\varepsilon)$ for all $j = 1,...,N$ we then find that (3.44c) and (3.44d) become

$$D_w \Delta\eta = 0, \qquad \boldsymbol{x} \in \Omega, \tag{3.51a}$$

$$D_w \partial_n \eta + (1-K)\eta = \frac{2\pi K f}{1-f} \sum_{j=1}^{N} c_j \delta_{\partial\Omega}(\boldsymbol{x}-\boldsymbol{x}_j), \qquad \boldsymbol{x} \in \partial\Omega, \tag{3.51b}$$

for which we calculate the leading order outer solution

$$\eta(\boldsymbol{x}) \sim \frac{2\pi f}{1-f} \frac{K}{D_w} \sum_{j=1}^{N} c_j G_{mr}(\boldsymbol{x}, \boldsymbol{x}_j).$$

Similarly, in the outer region (3.44b) becomes

$$D_v \Delta_{\partial\Omega} \psi = 2\pi \sum_{j=1}^{N} c_j \left(\delta_{\partial\Omega}(\boldsymbol{x}-\boldsymbol{x}_j) - \frac{f}{1-f} \frac{K}{D_w} G_{mr}(\boldsymbol{x}, \boldsymbol{x}_j) \right), \qquad \boldsymbol{x} \in \partial\Omega,$$

for which integration over $\partial\Omega$ leads to the solvability condition

$$\sum_{j=1}^{N} c_j = 0, \tag{3.52}$$

where we have used both the identity $\int_{\partial\Omega} G_{mr}(\boldsymbol{x}, \boldsymbol{\xi}) dA_{\boldsymbol{x}} = (1-K)^{-1} D_w$ as well as the constraint (3.7). Assuming the solvability condition (3.52) holds, then we calculate the following leading order asymptotic expansion in the outer region

$$\psi(\boldsymbol{x}) \sim \frac{1}{D_v}\bar{\psi} - \frac{2\pi}{D_v} \sum_{j=1}^{N} c_j \left(G_m(\boldsymbol{x}, \boldsymbol{x}_j) - \frac{f}{1-f} \frac{K}{D_w} \int_{\partial\Omega} G_m(\boldsymbol{x}, \boldsymbol{\xi}) G_{mr}(\boldsymbol{\xi}, \boldsymbol{x}_j) dA_{\boldsymbol{\xi}} \right).$$

Comparing the limiting behaviour of the inner solution $\Psi_i(\rho)$ as $\rho \to \infty$ with that of the outer solution given above as $|\boldsymbol{x}-\boldsymbol{x}_i| \to 0$ for each $i = 1,...,N$ yields algebraic system

$$\nu^{-1}\boldsymbol{c} + 2\pi\mathscr{G}\boldsymbol{c} + \mathscr{B}_0\boldsymbol{c} = \bar{\psi}\boldsymbol{e}.$$

Left-multiplying by $\boldsymbol{e}^T$ and using the solvability condition (3.52) then gives

$$\mathscr{M}_0\boldsymbol{c} = 0, \qquad \mathscr{M}_0 \equiv \nu^{-1}\mathscr{I}_N + 2\pi\big(\mathscr{I}_N - \mathscr{E}_N\big)\mathscr{G} + \big(\mathscr{I}_N - \mathscr{E}_N\big)\mathscr{B}_0, \tag{3.53a}$$

where

$$\mathscr{B}_0 \equiv \mathrm{diag}(\chi'(S_1,f),...,\chi'(S_N,f)). \tag{3.53b}$$

In particular, a zero-eigenvalue crossing instability threshold can be calculated by seeking parameter values for which $\mathscr{M}_0$ admits a zero eigenvalue or equivalently $\det\mathscr{M} = 0$. For appropriate choices of the multi-spot configuration $\boldsymbol{x}_1,...,\boldsymbol{x}_N$ symmetry properties of the Green's matrix $\mathscr{G}$ can be leveraged to further characterize the modes of instabilities as described below.

3.2.3 Instability Thresholds for Symmetric N-Spot Patterns

When the spot configuration and bulk-bound fuel source are chosen such that the Green's matrix $\mathscr{G}$ is of constant row sum and the common spot strength solution $\boldsymbol{S} = S_c\boldsymbol{e}$ satisfies the NAS (3.43b) exactly then we can derive an explicit criteria for zero-eigenvalue crossing instabilities in terms of the spectrum of $\mathscr{G}$ and the $S \ll 1$ behaviour of $\chi'(S,f)$. In particular, since the Green's matrix $\mathscr{G}$ is symmetric the eigenpairs $\{\mu_j, \boldsymbol{p}_j\}_{j=1}^N$ satisfy

$$\mathscr{G}\boldsymbol{p}_j = \mu_j\boldsymbol{p}_j, \qquad \boldsymbol{p}_1 = \boldsymbol{e}, \qquad \boldsymbol{e}^T\boldsymbol{p}_j = 0 \qquad j = 2,...,N.$$

Additionally, since $\mathscr{B}_0 = \chi'(S_c,f)\mathscr{I}_N$ we find that the spectrum of $\mathscr{M}_0$ consists of the eigenpairs $\{\mathscr{A}_j, \boldsymbol{p}_j\}_{j=1}^N$ where

$$\mathscr{A}_j \equiv \begin{cases} \nu^{-1}, & j = 1, \\ \nu^{-1} + 2\pi\mu_j + \chi'(S_c,f), & 2 \le j \le N, \end{cases} \tag{3.54}$$

Since $\mathscr{A}_1 > 0$ for all parameter values, the $\boldsymbol{p}_1$ mode does not lead to any zero eigenvalue crossing instabilities. Therefore any zero eigenvalue instabilities that arise must be the result of one of the p_j modes for $2 \leq j \leq N$ and since $\boldsymbol{e}^T \boldsymbol{p}_j = 0$ for all such modes the resulting instabilities are typically referred to as *competition instabilities*. Seeking parameter values such that $\mathscr{A}_j = 0$ for some $j = 2, ..., N$ and noting that $\mu_j = \mathscr{O}(1)$ we deduce that the ν^{-1} and $\chi'(S_c, f)$ terms must balance. From the small $S \ll 1$ asymptotics (see Equation (4.20) in [84])

$$\begin{gathered} \chi(S,f) \sim \frac{d_0}{S} + d_1 S + \mathscr{O}(S^3), \\ d_0 = \frac{b(1-f)}{f^2}, \quad d_1 = \frac{0.4893}{1-f} - 0.4698, \quad b \equiv \int_0^\infty w^2 \rho d\rho \approx 4.934, \end{gathered} \tag{3.55}$$

we further deduce $S_c = \mathscr{O}(\nu^{1/2})$ is needed for $\mathscr{A}_j = 0$ to hold for some $2 \leq j \leq N$. Previous studies of the Brusselator system on the unit sphere indicate that competition instabilities arise as S is decreased below a critical threshold [84] and we therefore seek the largest value of S_c for which $\mathscr{A}_j = 0$ for some $j = 2, ..., N$. In particular, noting the $S \ll 1$ asymptotics (3.55), the competition instability threshold is determined by solving the algebraic equation

$$\mathscr{A}_\star(S_{\text{comp}}) \equiv \nu^{-1} + 2\pi\mu_\star + \chi'(S_{\text{comp}}, f) = 0, \qquad \mu_\star \equiv \min_{j=2,...,N} \mu_j, \tag{3.56}$$

for the critical spot strength S_{comp}. The resulting critical spot strength S_{comp} depends on both the spot configuration as well as the problem parameters f, K, and D_w. The resulting competition instability threshold is then found by letting $S_c = S_{\text{comp}}$ and recalling the definition of S_c given by (3.42). Finally, since $\chi'(S, f)$ is monotone increasing for $S \ll 1$ we also remark that $\mathscr{A}_\star(S) \lesseqgtr 0$ if $S \lesseqgtr S_{\text{comp}}$, and in particular, based on the past observations of [84, 91], we expect a common spot strength pattern to be stable (resp. unstable) with respect to competition instabilities when $\mathscr{A}_\star(S_c) > 0$ (resp. $\mathscr{A}_\star(S_c) < 0$).

3.3 Slow-Spot Dynamics

In the previous section we considered the stability of multi-spot quasi-equilibrium solutions on an $\mathscr{O}(1)$ timescale by studying the $\mathscr{O}(1)$ eigenvalues of the eigen-

value problem (3.44). In the inner region we neglected the neutrally stable $m = 1$ mode which results from local translational invariance and is closely related to the slow dynamics of the spots on an $\mathcal{O}(\varepsilon^{-2})$ timescale. The particular timescale of the slow-dynamics arises from a dominant balance in (3.5) and will become clearer in the proceeding derivation. Specifically we begin by introducing the slow timescale $\sigma = \varepsilon^2 t$ and assuming that $\boldsymbol{x}_i = \boldsymbol{x}_i(\sigma)$ for each $i = 1, ..., N$. In the remainder of this section we seek a higher order asymptotic expansion for a multi-spot quasi-equilibrium solution to (3.5) for which the leading order term is given by the quasi-equilibrium solution calculated in §3.1 while a solvability condition arising from the higher order corrections yields a system of ordinary differential equations (ODEs) for the spot locations. The proceeding calculations follow closely those for the sphere in the absence of bulk-membrane coupling in [91] as well as the more recent computations on the torus in [95]. We remark that an analogous procedure is used for deriving the slow dynamics of localized multi-spot solutions in one-, two-, and three-dimensional domains [41, 96, 98].

We begin by left-multiplying (3.12) by $\mathcal{J}_i^T$ and using $\mathcal{J}_i^T \mathcal{J}_i = \mathcal{I}_2$ to calculate

$$\frac{d\boldsymbol{Y}'}{d\sigma} = -\frac{1}{\varepsilon}\boldsymbol{T}_i + \mathcal{O}(1), \quad \frac{\partial}{\partial t} = -\varepsilon \boldsymbol{T}_i \cdot \nabla_{\boldsymbol{Y}'} + \mathcal{O}(\varepsilon^2), \tag{3.57a}$$

$$\boldsymbol{T}_i \equiv \mathcal{J}_i^T \frac{d\boldsymbol{x}_i}{d\sigma}, \quad \nabla_{\boldsymbol{Y}'} \equiv (\partial_{Y_1}, \partial_{Y_2})^T. \tag{3.57b}$$

We then consider the higher order inner expansions

$$u(\boldsymbol{x}^i(\varepsilon \boldsymbol{Y}', 0)) = \sqrt{D_v}\big(U_{i0}(\rho) + \varepsilon U_{i1}(\boldsymbol{Y}')\big) + \mathcal{O}(\varepsilon^2), \tag{3.58a}$$

$$v(\boldsymbol{x}^i(\varepsilon \boldsymbol{Y}', 0)) = \frac{1}{\sqrt{D_v}}\big(V_{i0}(\rho) + \varepsilon V_{i1}(\boldsymbol{Y}')\big) + \mathcal{O}(\varepsilon^2), \tag{3.58b}$$

and recall the leading order inner region expansion of $w(\boldsymbol{x})$ given by (3.19) near $\boldsymbol{x}_i$ for each $i = 1, ..., N$. The leading order inner problem is satisfied identically while the first order correction problem is given by

$$\Delta_{\boldsymbol{Y}'} \boldsymbol{q}_{i1}(\boldsymbol{Y}') + \mathcal{Q}(\rho; S_i, f)\boldsymbol{q}_{i1}(\boldsymbol{Y}') = -\boldsymbol{f}_i, \qquad \boldsymbol{Y}' \in \mathbb{R}^, \tag{3.59a}$$

$$\boldsymbol{q}_{i1}(\boldsymbol{Y}') \to \boldsymbol{q}_{i1}^{\infty}(\boldsymbol{Y}') \qquad \text{as} \quad |\boldsymbol{Y}'| \to \infty. \tag{3.59b}$$

where $\boldsymbol{q}_{i1}(y) \equiv (U_{i1}(\boldsymbol{Y}'), V_{i1}(\boldsymbol{Y}'))^T$ and

$$\boldsymbol{f}_i \equiv \begin{pmatrix} \boldsymbol{T}_i \cdot \nabla_{\boldsymbol{Y}'} U_{i0}(\boldsymbol{Y}') + D_v^{-1/2} W_{i0}((\boldsymbol{Y}', 0)) \\ 0 \end{pmatrix}, \tag{3.59c}$$

$$\boldsymbol{q}_{i1}^{\infty}(\boldsymbol{Y}') \equiv \begin{pmatrix} 0 \\ \boldsymbol{Y}'^T \mathscr{J}_i^T \left(\sum_{j \neq i} S_j \boldsymbol{\alpha}_{ij} + \frac{1}{D_w \sqrt{D_v}} \nabla_{\boldsymbol{x}} v_E(\boldsymbol{x}_i) \right) \end{pmatrix}. \tag{3.59d}$$

for each $i = 1, ..., N$. The expression for $\boldsymbol{f}_i$ is obtained by using (3.57a) as well as the inner region expansion of $w(\boldsymbol{x})$ given by (3.19). On the other hand the expression for $\boldsymbol{q}_{i1}^{\infty}(\boldsymbol{Y}')$ is obtained by matching with the $\mathscr{O}(\varepsilon)$ term in (3.36).

To determine an appropriate solvability condition for (3.59a) we first note that $\Delta_{\boldsymbol{Y}'} + \mathscr{Q}(\rho; S_i, f)$ has a null-space of dimension at least two and is spanned in part by $\partial_{Y_k}(U_{i0}(\rho), V_{i0}(\rho))^T$ for $k = 1, 2$. We assume that the corresponding adjoint homogeneous operator has a null-space of dimension exactly two. We then write solutions to the homogeneous adjoint problem

$$\Delta_{\boldsymbol{Y}'} \boldsymbol{\Psi}(\boldsymbol{Y}') + \mathscr{Q}(\rho; S_i, f)^T \boldsymbol{\Psi}(\boldsymbol{Y}') = 0, \qquad \boldsymbol{Y}' \in \mathbb{R}^2,$$
$$\boldsymbol{\Psi} \to \begin{pmatrix} 0 \\ 0 \end{pmatrix} \qquad \text{as} \quad |\boldsymbol{Y}'| \to \infty,$$

in terms of the polar coordinates introduced in §3.2 as

$$\boldsymbol{\Psi}_c(\rho, \Theta) = \boldsymbol{P}(\rho) \cos\Theta, \qquad \boldsymbol{\Psi}_s(\rho, \Theta) = \boldsymbol{P}(\rho) \sin\Theta.$$

where $\boldsymbol{P}(\rho) = (P_1(\rho), P_2(\rho))^T$ is the unique solution to

$$\Delta_\rho \boldsymbol{P}'(\rho) - \rho^{-2} \boldsymbol{P}(\rho) + \mathscr{Q}_i^T \boldsymbol{P}(\rho) = 0, \quad \text{in } \rho > 0, \tag{3.60}$$
$$\boldsymbol{P} \sim (\rho^{-1}, \rho^{-1})^T \qquad \text{as } \rho \to \infty, \tag{3.61}$$

in which the normalized limiting behaviour as $\rho \to \infty$ is obtained by noting that

$$\mathscr{Q}_i^T \to \begin{pmatrix} -1 & 1 \\ 0 & 0 \end{pmatrix}, \qquad \text{as } \rho \to \infty.$$

Left-multiplying (3.59a) by $\boldsymbol{\Psi}_c^T$ and integrating over a disk of radius $R > 0$ gives

$$\int_0^{2\pi} \left(\boldsymbol{P}^T \frac{\partial \boldsymbol{q}_{i1}}{\partial \rho} - \boldsymbol{q}_{i1}^T \frac{\partial \boldsymbol{P}}{\partial \rho} \right) \Big|_{\rho=R} \cos(\Theta) R d\Theta = - \int_0^R \int_0^{2\pi} \boldsymbol{P}^T \boldsymbol{f}_i \cos(\Theta) \rho d\rho d\Theta. \tag{3.62}$$

Using (3.59b) and (3.61) we obtain the limiting behaviour

$$\left(\boldsymbol{P}^T \frac{\partial \boldsymbol{q}_{i1}}{\partial \rho} - \boldsymbol{q}_{i1}^T \frac{\partial \boldsymbol{P}}{\partial \rho} \right) \Big|_{\rho=R} \sim \frac{2}{R} (\cos\Theta, \sin\Theta)^T \mathscr{J}_i^T \left(\sum_{j \neq i} S_j \boldsymbol{\alpha}_{ij} + \frac{\nabla_{\boldsymbol{x}} v_E(\boldsymbol{x}_i)}{D_w \sqrt{D_v}} \right),$$

as $R \to \infty$ and therefore

$$\lim_{R\to\infty} \int_0^{2\pi} \left(\boldsymbol{P}^T \frac{\partial \boldsymbol{q}_{i1}}{\partial \rho} - \boldsymbol{q}_{i1}^T \frac{\partial \boldsymbol{P}}{\partial \rho} \right) \Big|_{\rho=R} \cos(\Theta) R d\Theta = 2\pi \boldsymbol{e}_1^T \mathscr{J}_i^T \left(\sum_{j \neq i} S_j \boldsymbol{\alpha}_{ij} + \frac{\nabla_{\boldsymbol{x}} v_E(\boldsymbol{x}_i)}{D_w \sqrt{D_v}} \right),$$

where $\boldsymbol{e}_1 = (1,0)^T$. On the other hand the right side of (3.62) is evaluated by first recalling that $W_{i0}((\boldsymbol{Y}', 0))$ is radially symmetric so that its contribution vanishes whereas $\nabla_{\boldsymbol{Y}'} U_{i0} = U_{i0}'(\rho)(\cos\Theta, \sin\Theta)^T$. In particular we obtain the following limit for the right hand side of (3.62)

$$- \lim_{R\to\infty} \int_0^R \int_0^{2\pi} \boldsymbol{P}^T \boldsymbol{f}_i \cos(\Theta) \rho d\rho d\Theta = -\pi \boldsymbol{e}_1^T \boldsymbol{T}_i \int_0^\infty P_1(\rho) U_{i0}'(\rho) \rho d\rho,$$

from which we obtain

$$\boldsymbol{e}_1^T \boldsymbol{T}_i = \frac{-2}{\int_0^\infty P_1(\rho) U_{i0}'(\rho) \rho d\rho} \boldsymbol{e}_1^T \mathscr{J}_i^T \left(\sum_{j \neq i} S_j \boldsymbol{\alpha}_{ij} + \frac{\nabla_{\boldsymbol{x}} v_E(\boldsymbol{x}_i)}{D_w \sqrt{D_v}} \right).$$

Proceeding similarly after left-multiplying (3.59a) by $\boldsymbol{\Psi}_s^T$ we therefore obtain

$$\boldsymbol{T}_i = \gamma(S_i, f) \mathscr{J}_i^T \left(\sum_{j \neq i} S_j \boldsymbol{\alpha}_{ij} + \frac{1}{D_w \sqrt{D_v}} \nabla_{\boldsymbol{x}} v_E(\boldsymbol{x}_i) \right), \tag{3.63a}$$

where

$$\gamma(S, f) \equiv - \frac{2}{\int_0^\infty P_1(\rho) U_c'(\rho; S, f) \rho d\rho}. \tag{3.63b}$$

The multiplier $\gamma(S, f)$ is computed by numerically solving (3.60) for $P_1(\rho)$ using standard techniques. This multiplier depends only on the inner problem and is

identical to that found in studies of the Brusselator system on the unit sphere [91] and the unit disk [96]. For completeness we include a plot of $\gamma(S,f)$ for $S>0$ and select values of $0<f<1$ from which we observe that $\gamma(S,f)>0$. Since $\boldsymbol{x}_i(\sigma)\in\partial\Omega$ for all $\sigma\geq 0$ we find

$$\left(\mathscr{I}_3-\boldsymbol{x}_i\boldsymbol{x}_i^T\right)\frac{d\boldsymbol{x}_i}{d\sigma}=\frac{d\boldsymbol{x}_i}{d\sigma},$$

so that left-multiplying (3.63a) by $\mathscr{J}_i$ and using (3.14) we obtain the system of ODEs

$$\frac{d\boldsymbol{x}_i}{d\sigma}=\gamma(S_i,f)\left(\mathscr{I}_3-\boldsymbol{x}_i\boldsymbol{x}_i^T\right)\left(\sum_{j\neq i}S_j\boldsymbol{\alpha}_{ij}+\frac{1}{D_w\sqrt{D_v}}\nabla_{\boldsymbol{x}}v_E(\boldsymbol{x}_i)\right),\tag{3.64}$$

for each $i=1,...,N$.

The effect of the bulk originating fuel source is analogous to that of a heterogeneous fuel source for the Brusselator model on the unit disk [96]. Specifically, spots are drawn toward regions where the membrane-bound fuel is locally maximized. On the other hand, the first term appearing in the definition of $\boldsymbol{\alpha}_{ij}$ given in (3.38) leads to mutual *repulsion* between spots whereas the second term introduces the effects of bulk-membrane recirculation, though in its current form it is not clear whether it leads to mutual repulsion or attraction between spots. To better understand its effect on the slow dynamics we state the following Lemma for which a proof is given in Appendix C.1.

Lemma 3.3.1. *Let $\boldsymbol{z}\in\Omega\cup\partial\Omega\setminus\{\boldsymbol{0}\}$ and suppose that $f(\boldsymbol{x},\boldsymbol{z})$ is defined on $\partial\Omega$ and has the series expansion*

$$f(\boldsymbol{x},\boldsymbol{z})=\frac{1}{4\pi}\sum_{l=0}^{\infty}f_lP_l\left(\frac{\boldsymbol{z}^T\boldsymbol{x}}{|\boldsymbol{z}|}\right),\qquad f_l=f_l(|\boldsymbol{z}|),\qquad \boldsymbol{x}\in\partial\Omega.\tag{3.65}$$

Then, for any $\boldsymbol{y}\in\partial\Omega$ that is not collinear with $\boldsymbol{z}$ we have the identity

$$\begin{aligned}\int_{\partial\Omega}\frac{\boldsymbol{y}-\boldsymbol{x}}{|\boldsymbol{y}-\boldsymbol{x}|^2}f(\boldsymbol{x},\boldsymbol{z})dA_{\boldsymbol{x}}&=\frac{1}{2}f_0(|\boldsymbol{z}|)\boldsymbol{y}\\&\quad+\frac{1}{2}\sum_{l=1}^{\infty}\frac{f_l(|\boldsymbol{z}|)}{l(l+1)}P_l^1\left(\frac{\boldsymbol{z}^T\boldsymbol{y}}{|\boldsymbol{z}|}\right)\frac{\mathscr{I}_3-\boldsymbol{y}\boldsymbol{y}^T}{\sqrt{1-(\boldsymbol{z}^T\boldsymbol{y}/|\boldsymbol{z}|)^2}}\frac{\boldsymbol{z}}{|\boldsymbol{z}|},\end{aligned}\tag{3.66}$$

where $P_l^1(x)$ is the associated Legendre polynomial of first order and l^{th} degree. If instead $\boldsymbol{y}$ and $\boldsymbol{z}$ are collinear or $f_l = 0$ for all $l \geq 1$, then the second term on the right-hand-side of (3.66) *vanishes identically.*

Using the series expansion (3.27b) and the above Lemma we calculate

$$\begin{aligned} -(\mathscr{I}_3 - \boldsymbol{x}_i\boldsymbol{x}_i^T)\int_{\partial\Omega} \frac{\boldsymbol{x}_i - \boldsymbol{\xi}}{|\boldsymbol{x}_i - \boldsymbol{\xi}|^2} G_{mr}(\boldsymbol{\xi}, \boldsymbol{x}_j) dA_{\boldsymbol{\xi}} \\ = \frac{1}{2}\sum_{l=1}^{\infty} \frac{g_l}{l(l+1)} P_l^1(\boldsymbol{x}_i^T\boldsymbol{x}_j) \frac{\mathscr{I}_3 - \boldsymbol{x}_i^T\boldsymbol{x}_i}{\sqrt{1-(\boldsymbol{x}_i^T\boldsymbol{x}_j)^2}}(\boldsymbol{x}_i - \boldsymbol{x}_j). \end{aligned} \tag{3.67}$$

for which in Appendix C.2 we show that

$$\sum_{l=1}^{\infty} \frac{g_l}{l(l+1)} P_l^1(z) < 0, \qquad \text{for all} \quad -1 < z < 1. \tag{3.68}$$

This implies that bulk-membrane coupling induces a mutual *attraction* between spots. However, as the next proposition shows, the mutual attraction induced by bulk-membrane coupling is not enough to overcome the mutual repulsion between spots given by the first term of $\boldsymbol{\alpha}_{ij}$.

Proposition 3.3.1. *Let $\varepsilon \to 0$ and suppose that the N-spot pattern constructed in §3.1 is linearly stable on an $\mathscr{O}(1)$ timescale. Then, the spot locations vary on an $\mathscr{O}(\varepsilon^{-2})$ time-scale $\sigma = \varepsilon^2 t$ according to the differential algebraic system consisting of the NAS* (3.43b) *and the system of ODEs*

$$\frac{d\boldsymbol{x}_i}{d\sigma} = \gamma(S_i, f)\big(\mathscr{I}_3 - \boldsymbol{x}_i\boldsymbol{x}_i^T\big)\left(\frac{1}{2}\sum_{j\neq i} S_j \frac{C(\boldsymbol{x}_i^T\boldsymbol{x}_j)(\boldsymbol{x}_i - \boldsymbol{x}_j)}{\sqrt{1-(\boldsymbol{x}_i^T\boldsymbol{x}_j)^2}} + \frac{\nabla_{\boldsymbol{x}} v_E(\boldsymbol{x}_i)}{D_w\sqrt{D_v}}\right), \tag{3.69a}$$

for each $i = 1, ..., N$ where $v_E(\boldsymbol{x})$ is given by (3.29) *and*

$$C(z) \equiv \sqrt{\frac{1+z}{1-z}} + \frac{f}{1-f}\frac{K}{D_w}\sum_{l=1}^{\infty} \frac{g_l}{l(l+1)} P_l^1(z) > 0, \qquad -1 < z \leq 1, \tag{3.69b}$$

and $C(-1) = 0$.

The right-hand-side of (3.69a) is obtained by using (3.38) and (3.67) to get

$$(\mathscr{I}_3 - \boldsymbol{x}_i\boldsymbol{x}_i^T)\boldsymbol{\alpha}_{ij} = \tfrac{1}{2}C(\boldsymbol{x}_i^T\boldsymbol{x}_j)(\mathscr{I}_3 - \boldsymbol{x}_i\boldsymbol{x}_i^T)(\boldsymbol{x}_i - \boldsymbol{x}_j),$$

and the sign of $C(z) > 0$ is derived in Appendix C.2.

We conclude this section by deriving a system of ODEs for the spherical coordinates $\theta_i(\sigma)$ and $\varphi_i(\sigma)$ for each $i = 1, ..., N$. First we calculate

$$\boldsymbol{T}_i = \mathscr{J}_i^T\left(\frac{\partial \boldsymbol{x}_i}{\partial \theta_i}\frac{d\theta_i}{d\sigma} + \frac{\partial \boldsymbol{x}_i}{\partial \varphi_i}\frac{d\varphi_i}{d\sigma}\right) = \begin{pmatrix} \sin\theta_i \frac{d\varphi_i}{d\sigma} \\ \frac{d\theta_i}{d\sigma} \end{pmatrix},$$
$$\mathscr{J}_i^T\boldsymbol{x}_j = \begin{pmatrix} -\sin\theta_j \sin(\varphi_i - \varphi_j) \\ \sin\theta_j\cos\theta_i\cos(\varphi_i - \varphi_j) - \sin\theta_i\cos\theta_j. \end{pmatrix}$$

Left-multiplying (3.69a) by $\mathscr{J}_i^T$ and using (3.14) we obtain for each $i = 1, ..., N$

$$\begin{pmatrix} \sin\theta_i \frac{d\varphi_i}{d\sigma} \\ \frac{d\theta_i}{d\sigma} \end{pmatrix} = \gamma(S_i, f)\left(\frac{1}{2}\sum_{j\neq i} S_j \frac{C(\boldsymbol{x}_i^T\boldsymbol{x}_j)\boldsymbol{\beta}_{ij}}{\sqrt{1-(\boldsymbol{x}_i^T\boldsymbol{x}_j)^2}} + \frac{\mathscr{J}_i^T\nabla_{\boldsymbol{x}}v_E(\boldsymbol{x}_i)}{D_w\sqrt{D_v}}\right), \tag{3.70a}$$

where

$$\boldsymbol{\beta}_{ij} = \begin{pmatrix} \sin\theta_j\sin(\varphi_i - \varphi_j) \\ \sin\theta_i\cos\theta_j - \sin\theta_j\cos\theta_i\cos(\varphi_i - \varphi_j) \end{pmatrix} \quad (i, j = 1, ..., N). \tag{3.70b}$$

3.4 Examples

To illustrate the asymptotic theory developed in the previous sections we now consider examples of symmetric N-spot patterns for which we assume that the bulk-bound fuel source is of the form

$$E(\boldsymbol{x}) = E_0\delta(\boldsymbol{x} - \boldsymbol{x}_{\text{source}}), \qquad \boldsymbol{x}_{\text{source}} = \eta\boldsymbol{e}_z, \tag{3.71}$$

where $E_0 > 0$, $0 \le \eta < 1$, and $\boldsymbol{e}_z = (0, 0, 1)^T$. Such a fuel source may represent, for example, a localized site of protein generation within the cell. In the following section we will analyze the effects of the source location parametrized by $\eta \ge 0$. First

we note that the diffusion transported fuel is given by $w_E(\boldsymbol{x}) = E_0 G_{br}(\boldsymbol{x}, \boldsymbol{x}_{\text{source}})$ where G_{br} is the bulk Robin Green's function satisfying

$$\Delta G_{br} = -\delta(\boldsymbol{x} - \boldsymbol{x}_{\text{source}}), \qquad \boldsymbol{x} \in \Omega, \tag{3.72a}$$

$$\partial_n G_{br} + \frac{1-K}{D_w} G_{br} = 0, \qquad \boldsymbol{x} \in \partial\Omega. \tag{3.72b}$$

When $\boldsymbol{x} \in \partial\Omega$ the bulk Robin Green's function has the series expansion

$$G_{br}(\boldsymbol{x}, \boldsymbol{x}_{\text{source}}) = \frac{1}{4\pi} \sum_{l=0}^{\infty} g_l \eta^l P_l(\boldsymbol{e}_z^T \boldsymbol{x}), \qquad \boldsymbol{x} \in \partial\Omega, \tag{3.72c}$$

and by using the series (3.31) and product formula (3.32) as well as Lemma 3.3.1 we calculate

$$v_E(\boldsymbol{x}) = \frac{E_0}{4\pi} \sum_{l=1}^{\infty} \frac{g_l \eta^l}{l(l+1)} P_l(\boldsymbol{e}_z^T \boldsymbol{x}), \tag{3.73a}$$

$$\left(\mathscr{I}_3 - \boldsymbol{x}\boldsymbol{x}^T\right) \nabla_{\boldsymbol{x}} v_E(\boldsymbol{x}) = \frac{E_0}{4\pi} \frac{C_E(\boldsymbol{e}_z^T \boldsymbol{x})}{\sqrt{1 - (\boldsymbol{e}_z^T \boldsymbol{x})^2}} \left(\mathscr{I}_3 - \boldsymbol{x}\boldsymbol{x}^T\right)(\boldsymbol{x} - \boldsymbol{e}_z), \tag{3.73b}$$

$$\mathscr{I}_i^T \nabla_{\boldsymbol{x}} v_E(\boldsymbol{x}_i) = \frac{E_0}{4\pi} C_E(\cos\theta_i) \begin{pmatrix} 0 \\ 1 \end{pmatrix}, \tag{3.73c}$$

where

$$C_E(z) \equiv \sum_{l=1}^{\infty} \frac{g_l \eta^l}{l(l+1)} P_l^1(z). \tag{3.73d}$$

Note that $C_E(z) \equiv 0$ for $\eta = 0$ and proceeding as in the derivation of (3.68) in Appendix C.2 we can similarly establish that $C_E(z) < 0$ for all $-1 < z < 1$ and $\eta > 0$. Note in addition that $C_E(\pm 1 = 0$ since $P_l^1(\pm 1) = 0$ (see (C.7)).

Since $v_E(\boldsymbol{x})$ is constant along lines of constant latitude (i.e. depends only on $\boldsymbol{e}_z^T \boldsymbol{x}$) the common spot strength solution $\boldsymbol{S} = S_c \boldsymbol{e}$ exactly solves the NAS (3.43b) when the spots are uniformly distributed along a ring of fixed latitude, i.e.

$$\theta_i = \theta_c, \quad \varphi_i = \frac{2\pi(i-1)}{N}, \qquad i = 1, ..., N. \tag{3.74}$$

where θ_c is a common polar angle. The common spot strength is then explicitly

given by

$$S_c = \frac{E_0}{2\pi N\sqrt{D_v}}\left(1-\frac{K}{1-f}\right)^{-1}. \tag{3.75}$$

Applying the linear stability results of §3.2 we deduce that the N-spot pattern is linearly stable on an $\mathscr{O}(1)$ timescale provided that

$$S_{\text{comp}} < \frac{E_0}{2\pi N\sqrt{D_v}}\left(1-\frac{K}{1-f}\right)^{-1} < \Sigma_2(f), \tag{3.76}$$

where S_{comp} is the numerically computed solution to (3.56) and $\Sigma_2(f)$ the splitting instability threshold calculated in §3.2.1. The effects of E_0 and N on the competition and splitting instability thresholds for D_v are seen to be identical to those calculated in [84], mainly increasing (resp. decreasing) E_0 may lead to splitting (resp. competition) instabilities while increasing (resp. decreasing) N may lead to competition (resp. splitting) instabilities. On the other hand, increasing the bulk-membrane coupling parameter K increases the value of S_c and may therefore lead to splitting instabilities.

Before proceeding with explicit examples of a one- and two-spot pattern, we use (3.73) to rewrite (3.70) as

$$\begin{pmatrix} \sin\theta_i \frac{d\varphi_i}{d\sigma} \\ \frac{d\theta_i}{d\sigma} \end{pmatrix} = \gamma(S_i, f)\begin{pmatrix} F_i \\ G_i \end{pmatrix}. \tag{3.77}$$

where

$$F_i(\boldsymbol{\varphi},\boldsymbol{\theta}) \equiv \frac{1}{2}\sum_{j\neq i}\frac{S_j C(\boldsymbol{x}_i^T\boldsymbol{x}_j)}{\sqrt{1-(\boldsymbol{x}_i^T\boldsymbol{x}_j)^2}}\sin\theta_j\sin(\varphi_i-\varphi_j),$$

$$G_i(\boldsymbol{\varphi},\boldsymbol{\theta}) \equiv \frac{1}{2}\sum_{j\neq i}\frac{S_j C(\boldsymbol{x}_i^T\boldsymbol{x}_j)}{\sqrt{1-(\boldsymbol{x}_i^T\boldsymbol{x}_j)^2}}(\sin\theta_i\cos\theta_j-\sin\theta_j\cos\theta_i\cos(\varphi_i-\varphi_j)) + \frac{E_0 C_E(\cos\theta_i)}{4\pi D_w\sqrt{D_v}}$$

for each $i = 1,...,N$ and where $\boldsymbol{\varphi} = (\varphi_1,...,\varphi_N)^T$ and $\boldsymbol{\theta} = (\theta_1,...,\theta_N)^T$.

3.4.1 One-Spot Pattern

In the case of a one-spot pattern with an arbitrary fuel source $E(\boldsymbol{x})$ the slow dynamics (3.69a) are explicitly given by

$$\frac{d\boldsymbol{x}_1}{d\sigma} = \frac{\gamma(S_1, f)}{D_w\sqrt{D_v}}(\mathscr{I}_3 - \boldsymbol{x}_1\boldsymbol{x}_1^T)\nabla_{\boldsymbol{x}} v_E(\boldsymbol{x}_1), \tag{3.78}$$

from which we deduce the equilibrium points $\boldsymbol{x}_1 \in \partial\Omega$ occur at both the critical points of $v_E(\boldsymbol{x})$ and the points for which $\nabla_{\boldsymbol{x}} v_E(\boldsymbol{x})$ is parallel to $\boldsymbol{x}$. When the fuel source is given by (3.71) the slow dynamics in spherical coordinates (3.77) are explicitly given by (3.77) where

$$F_1(\varphi_1, \theta_1) = 0, \qquad G_1(\varphi_1, \theta_1) = \frac{E_0 C_E(\cos\theta_1)}{4\pi D_w\sqrt{D_v}}. \tag{3.79}$$

When $\eta = 0$ we calculate $C_E \equiv 0$ and therefore any point $\boldsymbol{x}_1 \in \partial\Omega$ is an equilibrium with respect to the slow dynamics. On the other hand when $0 < \eta < 1$ we calculate $C_E(\pm 1) = 0$ and $C_E(z) < 0$ for all $-1 < z < 1$. As a consequence $\boldsymbol{x}_1 = \pm\boldsymbol{e}_z$ are equilibrium points, but only $\boldsymbol{x}_1 = \boldsymbol{e}_z$ is linearly stable. In addition $\boldsymbol{x}_1 = \boldsymbol{e}_z$ is globally attracting so that any spot concentrated at $\boldsymbol{x}_1 \in \partial\Omega$ tends to $\boldsymbol{e}_z$ along a geodesic on an $\mathscr{O}(\varepsilon^{-2})$ timescale. Note that the remaining problem parameters E_0, D_w, K, f, and D_v only change the speed of the dynamics.

3.4.2 Two-Spot Patterns

Next we consider the case of a two-spot pattern. We begin by considering the case $\eta = 0$ for which $\nabla_{\boldsymbol{x}} v_E(\boldsymbol{x}) = 0$ on $\partial\Omega$. Since the 2×2 matrix $\mathscr{G}$ is symmetric we immediately deduce that $\boldsymbol{S} = S_c\boldsymbol{e}$ exactly solves the NAS (3.43b) for all values of $\boldsymbol{x}_1, \boldsymbol{x}_2 \in \partial\Omega$. Substituting into (3.69a) we find that the slow dynamics are governed by

$$\frac{d\boldsymbol{x}_1}{d\sigma} = \frac{S_c\gamma(S_c, f)}{2}\frac{C(\boldsymbol{x}_1^T\boldsymbol{x}_2)}{\sqrt{1-(\boldsymbol{x}_1^T\boldsymbol{x}_2)^2}}\left(\mathscr{I}_3 - \boldsymbol{x}_1\boldsymbol{x}_1^T\right)(\boldsymbol{x}_1 - \boldsymbol{x}_2),$$
$$\frac{d\boldsymbol{x}_2}{d\sigma} = \frac{S_c\gamma(S_c, f)}{2}\frac{C(\boldsymbol{x}_2^T\boldsymbol{x}_1)}{\sqrt{1-(\boldsymbol{x}_2^T\boldsymbol{x}_1)^2}}\left(\mathscr{I}_3 - \boldsymbol{x}_2\boldsymbol{x}_2^T\right)(\boldsymbol{x}_2 - \boldsymbol{x}_1).$$

Letting $\boldsymbol{x}_1^T\boldsymbol{x}_2 = \cos\beta$ we then calculate

$$\frac{d\beta}{d\sigma} = -\frac{1}{\sin\beta}\frac{d(\boldsymbol{x}_1^T\boldsymbol{x}_2)}{d\sigma} = S_c\gamma(S_c,f)C(\cos\beta). \tag{3.80}$$

Since $C(z) > 0$ for all $-1 < z \leq 1$ and $C(-1) = 0$ we deduce that $\beta = \pi$ is the only equilibrium and it is globally attracting. Therefore any antipodal configuration, in the sense that $\boldsymbol{x}_1 = -\boldsymbol{x}_2$, is a stable equilibrium of the slow dynamics. In particular, the slow dynamics when $K > 0$ are qualitatively identical to those previously investigated when $K = 0$ in [91].

When $\eta > 0$ both spots are mutually repelled while simultaneously being attracted to $\boldsymbol{e}_z$. From (3.73) ad (3.69a) we immediately deduce that a North-South (NS) configuration for which $\boldsymbol{x}_1 = \pm\boldsymbol{e}_z$ and $\boldsymbol{x}_2 = \mp\boldsymbol{e}_z$ is an equilibrium of the slow dynamics. Moreover, any equilibrium configuration in which a spot concentrates at $\pm\boldsymbol{e}_z$ must be a NS-configuration as can be deduced by noting that if $\boldsymbol{x}_1 = \pm\boldsymbol{e}_z$ then $\nabla_{\boldsymbol{x}} v_E(\boldsymbol{x}_1) = \boldsymbol{0}$ and (3.69a) then implies $\boldsymbol{x}_2 = \mp\boldsymbol{e}_z$. Note that the spot strengths are not equal for the NS-configuration. In particular, if $\boldsymbol{x}_1 = \boldsymbol{e}_z$ and $\boldsymbol{x}_2 = -\boldsymbol{e}_z$ then $S_1 > S_2$.

Next we consider non NS-configurations by parameterizing each spot in terms of spherical coordinates $\boldsymbol{\varphi} = (\varphi_1, \varphi_2)^T$ and $\boldsymbol{\theta} = (\theta_1, \theta_2)^T$ and assuming without loss of generality that $0 < \theta_1 \leq \theta_2 < \pi$. The dynamic are then given by (3.77) with

$$F_1(\boldsymbol{\varphi},\boldsymbol{\theta}) = \frac{S_2}{2}\frac{C(\xi)}{\sqrt{1-\xi^2}}f_{12}, \quad G_1(\boldsymbol{\varphi},\boldsymbol{\theta}) \equiv \frac{S_2}{2}\frac{C(\xi)}{\sqrt{1-\xi^2}}g_{12} + \frac{E_0 C_E(\cos\theta_1)}{4\pi D_w\sqrt{D_v}}, \tag{3.81a}$$

$$F_2(\boldsymbol{\varphi},\boldsymbol{\theta}) = \frac{S_1}{2}\frac{C(\xi)}{\sqrt{1-\xi^2}}f_{21}, \quad G_2(\boldsymbol{\varphi},\boldsymbol{\theta}) \equiv \frac{S_1}{2}\frac{C(\xi)}{\sqrt{1-\xi^2}}g_{21} + \frac{E_0 C_E(\cos\theta_2)}{4\pi D_w\sqrt{D_v}} \tag{3.81b}$$

where

$$f_{ij} \equiv \sin\theta_j\sin(\varphi_i - \varphi_j), \quad g_{ij} \equiv \sin\theta_i\cos\theta_j - \cos\theta_i\sin\theta_j\cos(\varphi_i - \varphi_j), \tag{3.82}$$

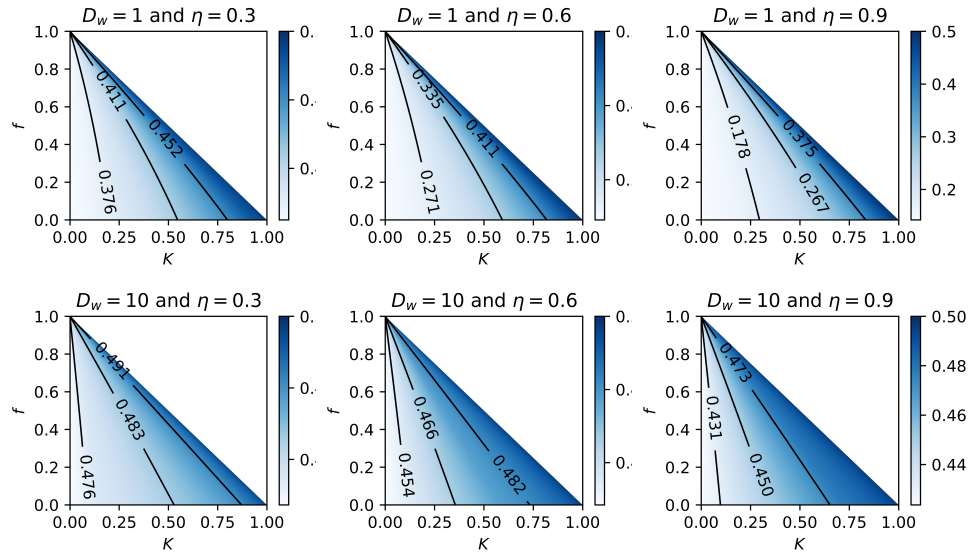

Figure 3.3: Plots of θ_c/π versus K and f for fixed values of $D_w = 1$ (top row) and $D_w = 10$ (bottom row) and $\eta = 0.3, 0.6, 0.9$ from left to right. The solid lines with in-line text are contours indicating fixed values of θ_c/π.

for each $i, j \in \{1,2\}$ and

$$\xi \equiv \boldsymbol{x}_1^T \boldsymbol{x}_2 = \sin\theta_1 \sin\theta_2 \cos(\varphi_1 - \varphi_2) + \cos\theta_1 \cos\theta_2. \tag{3.83}$$

Since two-spot configurations are at equilibrium when $\eta = 0$ if and only if they are antipodal, the upward drift toward $\boldsymbol{e}_z$ implies that there are no non-NS antipodal solutions when $\eta > 0$ and therefore $\xi > -1$. As an immediate consequence $(1 - \xi^2)^{-1/2} C(\xi) > 0$ so that $F_1 = F_2 = 0$ implies that $f_{12} = f_{21} = 0$ and therefore $\varphi_1 - \varphi_2 = 0$ or $|\varphi_1 - \varphi_2| = \pi$. In the former case the assumption $\theta_1 \leq \theta_2$ immediately implies that $G_1 < 0$ since $\boldsymbol{x}_1$ is propagated toward $\boldsymbol{e}_z$ both by the repulsion from $\boldsymbol{x}_2$ and attraction to $\boldsymbol{e}_z$ due to $\nabla_{\boldsymbol{x}} v_E(\boldsymbol{x}_1)$. Therefore any non NS-configuration must have $|\varphi_1 - \varphi_2| = \pi$ and without loss of generality we assume $\varphi_1 = 0$ and $\varphi_2 = \pi$. It follows that $g_{ij} = \sin(\theta_1 + \theta_2) > 0$ where the sign follows from noting that $\xi > -1$ implies $\theta_1 + \theta_2 < \pi$. As a consequence, non-NS equilibrium configurations are

determined by solving

$$G_1(\theta_1,\theta_2) = \frac{S_2}{2}C(\cos(\theta_1+\theta_2)) + \frac{E_0 C_E(\cos\theta_1)}{4\pi D_w\sqrt{D_v}} = 0, \tag{3.84}$$

$$G_2(\theta_1,\theta_2) = \frac{S_1}{2}C(\cos(\theta_1+\theta_2)) + \frac{E_0 C_E(\cos\theta_2)}{4\pi D_w\sqrt{D_v}} = 0, \tag{3.85}$$

for $0 < \theta_1 \leq \theta_2$ with $\theta_1 + \theta_2 < \pi$.

As a special case, when $\theta_1 = \theta_2 = \theta_c$ we find that $S_1 = S_2 = S_c$ and it suffices to determine the common angle θ_c satisfying

$$C(\cos 2\theta_c) + \frac{2}{D_w}\left(1 - \frac{K}{1-f}\right)C_E(\cos\theta_c) = 0, \qquad 0 < \theta_c < \frac{\pi}{2}. \tag{3.86}$$

Since $C(z) \to +\infty$ as $z \to 1$ and $C(-1) = 0$ whereas $C_E(z)$ remains bounded and strictly negative on $0 < z < 1$ the intermediate value theorem implies the existence of a $0 < \theta_c < \pi/2$ satisfying (3.86). Numerical calculations further suggest that the common angle solution is unique and $G_i(\theta,\theta) \lesseqgtr 0$ for $\theta \gtreqless \theta_c$. In addition we note that θ_c is a function only of $\theta_c = \theta_c(K, f, D_w, \eta)$. In Figure 3.3 we plot θ_c/π versus K and f with $K + f < 1$ and for select values of $D_w = 1, 10$ and $\eta = 0.3, 0.6, 0.9$ from which we make the following observations. As $0 < K < 1 - f$ increases, the mutual repulsion reflected by $C(\cos 2\theta_c)$ dominates the attraction toward $\boldsymbol{e}_z$ reflected by $C_E(\cos\theta_c)$ and therefore θ_c increases, tending to the limit $\theta_c \to \pi/2$ as $K \to 1 - f$. On the other hand, increasing η (resp. decreasing D_w) leads to an increase of $|\nabla_{\boldsymbol{x}} v_E(\boldsymbol{x})|$ and therefore decreases θ_c.

Next we analyze in more detail the stability of the common angle and NS solutions by considering the nullclines of (3.84). First note that

$$G_i(\theta,\theta) > 0, \quad G_i(\theta,\pi-\theta) < 0, \qquad \text{for all } 0 < \theta < \theta_c,$$

so that the intermediate value implies the existence of values $\theta_i^\star(\theta)$ such that $G_i(\theta,\theta_i^\star(\theta)) = 0$ for all $0 < \theta < \theta_c$ $(i = 1,2)$. Numerical calculations further suggest that both of these values are unique and monotone decreasing in θ. Clearly $\theta_i^\star(\theta_c) = \theta_c$ for each $i = 1,2$ and we can further deduce that $\lim_{\theta\to 0^+}\theta_1^\star(\theta) = \pi$ and $\lim_{\theta\to 0^+}\theta_2^\star(\theta) < \pi$. Moreover, numerical calculations given below suggest

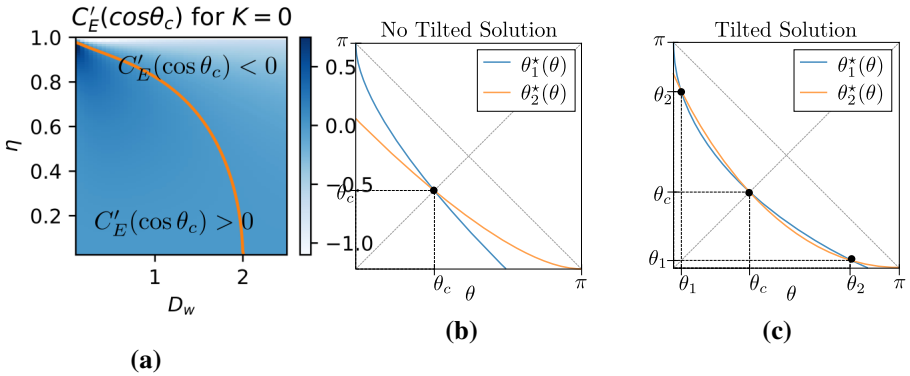

Figure 3.4: (a) Plot of $C_E'(\cos\theta_c)$ at $K=0$ versus $0<\eta<1$ and $D_w>0$ with the solid orange line indicating values where $C_E'(\cos\theta_c)=0$ and demarcating regions where $C_E'(\cos\theta_c)>0$ and $C_E'(\cos\theta_c)<0$. (b)-(c) Schematics showing the functions $\theta_1^\star(\theta)$ and $\theta_2^\star(\theta)$ in the absence and presence of a tilted solution. In the latter case $\theta_1=\theta_t$ and $\theta_2=\theta_1^\star(\theta_t)$ are the polar angles of the tilted solution.

that depending on the choice of problem parameters either $\theta_2^\star(\theta)<\theta_1^\star(\theta)$ for all $0<\theta<\theta_c$, or else there exists a unique value $0<\theta_t<\theta_c$ such that $\theta_2^\star(\theta_t)=\theta_1^\star(\theta_t)$ in which case we define $\theta_t^\star\equiv\theta_i(\theta_t)$ $(i=1,2)$ (see Figures 3.4b and 3.4c for a schematic demonstration of the emergence of $0<\theta_t<\theta_c$). In particular this implies the existence of a *tilted* two spot solution with $\theta_1=\theta_t<\theta_t^\star=\theta_2$. Finally, since $G_i(\theta_1,\theta_2)\lessgtr 0$ if $\theta_2\gtrless\theta_i^\star(\theta_1)$ we deduce that the NS configuration is linearly unstable, the common angle solution is linearly stable only in the absence of a tilted solution, and the tilted solution, if it exists, is linearly stable.

A criteria for the emergence of a tilted solution can be derived by two equivalent approaches: analyzing the stability of the common angle solution, or analyzing the behaviour of $\theta_1^\star(\theta)$ and $\theta_2^\star(\theta)$ at $\theta=\theta_c$. We pursue the latter approach below while the former is pursued in Appendix C.3. Specifically, the criteria for the emergence of a tilted solution is equivalent to the tangency condition

$$\left.\frac{d\theta_1^\star}{d\theta}\right|_{\theta=\theta_c}=\left.\frac{d\theta_2^\star}{d\theta}\right|_{\theta=\theta_c}. \tag{3.87}$$

Indeed, in the absence of a tilted solution $\theta_1^\star(\theta) > \theta_2^\star(\theta)$ for all $0 < \theta < \theta_c$, whereas when a tilted solution emerges $\theta_1^\star(\theta) < \theta_2^\star(\theta)$ for $\theta_t < \theta < \theta_c$. By symmetry it is easy to see that $G_2(\theta_1^\star(\theta), \theta) = 0$ for all $0 < \theta < \theta_c$ so that $\theta_2^\star(\theta) = (\theta_1^\star)^{-1}(\theta)$. In particular $d\theta_2^\star/d\theta = [d\theta_1^\star/d\theta]^{-1}$ and the tangency condition (3.87) therefore becomes $d\theta_1^\star/d\theta|_{\theta=\theta_c} = -1$ where the sign is due to the, numerically observed, monotonicity of $\theta_1^\star(\theta)$. Implicitly differentiating $G_1(\theta, \theta_1^\star(\theta) = 0$ with respect to θ and using (see Appendix C.3 for details)

$$\left.\frac{\partial S_2}{\partial \theta_1}\right|_{(\theta_1,\theta)=(\theta_c,\theta_c)} = -\left.\frac{\partial S_2}{\partial \theta_2}\right|_{(\theta_1,\theta)=(\theta_c,\theta_c)} = -\frac{E_0 C_E(\cos\theta_c)}{8\pi D_w \sqrt{D_v}\mathscr{A}_\star(S_c)},$$

where $\mathscr{A}_\star(S_c)$ is given by (3.56), we deduce that the tangency condition (3.87) is equivalent to

$$C(\cos 2\theta_c) C_E(\cos\theta_c) + 2\mathscr{A}_\star(S_c) C_E'(\cos\theta_c)\sin\theta_c = 0. \tag{3.88}$$

In Appendix C.3 we show that the sign of the left-hand-side of (3.88), which we denote by $(3.88)_{\text{LHS}}$, determines the stability of the common angle solution (see (C.23b)). In particular, if $(3.88)_{\text{LHS}} < 0$ (resp. $(3.88)_{\text{LHS}} > 0$) then the common angle solution is unstable (resp. stable). Assuming that $S_{\text{comp}} < S_c < \Sigma_2(f)$ so that the common angle solution is linearly stable with respect to competition and splitting instabilities, we seek parameter values for which (3.88) is satisfied. From $\mathscr{A}_\star(S_c) > 0$ for $S_c > S_{\text{comp}}$ and $C(\cos 2\theta_c) C_E(\cos\theta_c) < 0$ for all $0 < \theta_c < \pi/2$ we deduce that $C_E'(\cos\theta_c) > 0$ is a necessary condition for (3.88) to hold. Numerical evidence indicates that $C_E'(\cos\theta)$ has a unique zero $0 < \theta_e < \pi/2$ with $C_E'(\cos\theta) \lessgtr 0$ for $\theta \gtrless \theta_e$, and furthermore this zero is monotone increasing in K though at a slower rate than the common angle θ_c. As a consequence if $C_E'(\cos\theta_c) \leq 0$ for $K = 0$ then $C_E'(\cos\theta_c) < 0$ for all $0 < K < 1 - f$ and the common angle solution is linearly unstable. Noting that $C_E'(\cos\theta_c)|_{K=0}$ is a function only of η and D_w we obtain the plot of $C_E'(\cos\theta_c)$ shown in Figure 3.4a. Only within the indicated region of η and D_w values where $C_E'(\cos\theta_c) > 0|_{K=0}$ can the common angle solution be linearly stable for appropriate choices of the remaining problem parameters when

$K \geq 0$. In fact, when $C_E'(\cos\theta_c) > 0$ we may solve

$$C(\cos 2\theta_c)C_E(\cos\theta_c) + 2\mathscr{A}_\star(S_{\text{tilt}})C_E'(\cos\theta_c)\sin\theta_c = 0, \tag{3.89}$$

for the *tilt instability* threshold $S_{\text{tilt}} > S_{\text{comp}}$. Since $(3.88)_{\text{LHS}} < 0$ when $S_c = S_{\text{comp}}$ we deduce that the common angle solution is unstable with respect to tilt instabilities for $S_c < S_{\text{tilt}}$.

We summarize the above discussion as follows. If $C_E'(\cos\theta_c) \leq 0$ then the common angle solution is linearly unstable with respect to a *tilt instability* over an $\mathscr{O}(\varepsilon^{-2})$ timescale. Otherwise, if $C_E'(\cos\theta_c) > 0$ then the common angle solution is linearly stable if and only if $S_{\text{tilt}} < S_c < \Sigma_2(f)$ where $\Sigma_2(f)$ is the splitting instability threshold and S_{tilt} is the tilt instability threshold satisfying (3.89). The NS configuration, for which $\boldsymbol{x}_1 = \pm\boldsymbol{e}_z$ and $\boldsymbol{x}_2 = -\boldsymbol{x}_1$ is always an equilibrium but it is linearly unstable. Finally, if the common angle solution is linearly stable with respect to competition and splitting instabilities, i.e. $S_{\text{comp}} < S_c < \Sigma_2(f)$, but unstable with respect to tilt instabilities then it bifurcates to a *tilted* solution with polar angles satisfying $\theta_1 < \theta_c < \theta_2$. The tilted solution is linearly stable with respect to tilt instabilities and its stability with respect to competition and splitting instabilities depends on the proximity of S_c to S_{comp} and $\Sigma_2(f)$. In particular recalling that $\boldsymbol{S} = S_c\boldsymbol{e} + \mathscr{O}(\nu)$ (see §3.1) it suffices that S_c satisfy $S_{\text{comp}} < S_c < \Sigma_2(f)$ and be an $\mathscr{O}(1)$ distance from these thresholds for the tilted solution to be linearly stable.

To illustrate the above discussion, in Figures 3.5(a)-(c) we plot the competition (blue), splitting (orange), and tilt (green) instability thresholds in the form D_v/E_0^2 versus K for select values of $D_w > 0$ with $\eta = 0.4$, $f = 0.6$, and $\nu = 5 \times 10^{-3}$. Recalling (3.75) and the stability criteria $S_{\text{tilt}} < S_c < \Sigma_2(f)$, the common angle solution is linearly stable in the region bounded by the split (orange) and tilt (green) instability threshold curves provided that the latter exists. If the latter threshold does not exist then $C_E'(\cos\theta_c) \leq 0$ for all $K \geq 0$ and the common angle solution is therefore always unstable with respect to tilt instabilities. In Figures 3.5(d)-(f) we plot the common angle, θ_c, and tilted solution angles, θ_1 and θ_2, as $0 \leq K < 1 - f$ is varied for $D_v/E_0^2 = 0.1$ with the remaining parameters equal to those used in Figures 3.5(a)-(c) respectively. Note that the tilted solution provides a connec-

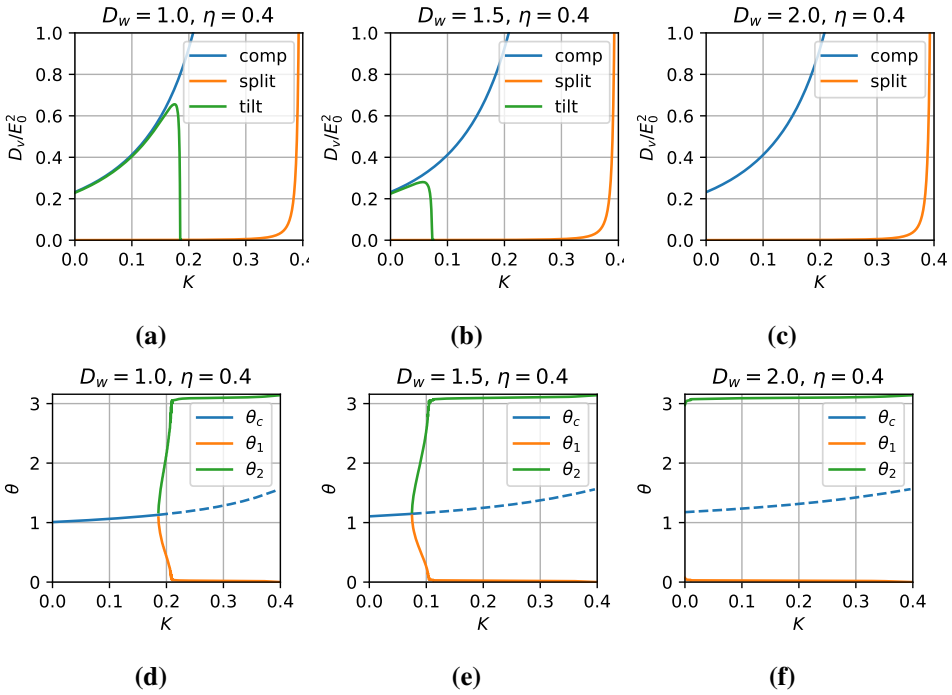

Figure 3.5: (a)-(c) Plots of competition, splitting, and tilt instability thresholds as D_v/E_0^2 versus K for select of $D_w > 0$ with $\eta = 0.4$, $f = 0.6$, and $\nu = 5 \times 10^{-3}$. (d)-(f) Plots of the common angle θ_c, and tilted angles $\theta_1 < \theta_c < \theta_2$ versus K at $D_v/E_0^2 = 0.1$ and with remaining parameters equal to those from (a)-(c) respectively. The solid (resp. dashed) line indicates the stability (resp. instability) of the common angle solution with respect to tilt instabilities.

tion between the common angle and NS two-spot configurations. Furthermore, as $K \to 1 - f$ the tilted solution approaches the NS configuration, but it is destabilized by a splitting instability before reaching this new configuration. Additionally, as K increases the tilted solution rapidly approaches the NS configuration indicating a preference of the system to align the two spots with the two local extrema (maximum at $\boldsymbol{e}_z$ and minimum at $-\boldsymbol{e}_z$) of $\nabla_{\boldsymbol{x}} v_E(\boldsymbol{x})$ on $\partial\Omega$. Interestingly, the above analysis indicates that while the existence of tilted solutions is closely tied to the heterogeneity of the fuel source in the absence of membrane-detachment, the latter mechanism nevertheless plays an important role in the destabilization of the

common angle solution and resulting bifurcation to the stable tilted solution.

3.5 Discussion

In this chapter we have used the method of matched asymptotic expansions to derive hybrid asymptotic-numerical equations which determine the structure, stability, and slow dynamics of strongly localized multi-spot solutions to a bulk-membrane-coupled Brusselator model posed on the unit sphere. Our particular choice of bulk-membrane coupling was made to reflect a process in which the fuel necessary to sustain pattern formation for the Brusselator model originates within the bulk and is transported to the membrane by passive diffusion. In addition, we introduced a membrane-detachment mechanism controlled by the non-dimensional parameter K which satisfies $0 < K < 1 - f$. Our analysis therefore focused on the effects of the bulk-originating fuel source as well as the membrane detachment mechanism on the structure, stability, and slow dynamics of the multi-spot patterns.

To leading order in the small parameter $\nu = -1/\log\varepsilon$, we determined that the total bulk-bound fuel and the membrane-bound activator detachment rate have a direct effect on the strength of the membrane bound spot strengths, with one of the key parameters being the common spot strength which is explicitly given by

$$S_c = \frac{1}{2\pi N\sqrt{D_v}}\left(1 - \frac{K}{1-f}\right)^{-1}\int_\Omega E(\boldsymbol{x})d^3\boldsymbol{x}.$$

The dependence on the total bulk-bound fuel source is analogous to results previously obtained for the Brusselator model on the flat disk with a heterogeneous fuel source [96]. The analysis of the structure of multi-spot solutions and their linear stability on an $\mathcal{O}(1)$ timescale with respect to competition and splitting instabilities is qualitatively similar to that in previous studies of the Brusselator model on the unit sphere without bulk-membrane coupling [84]. However two key differences are the introduction of the membrane Robin Green's function $G_{mr}(\boldsymbol{x},\boldsymbol{\xi})$ satisfying (3.27a) and playing a key role in modelling membrane-detachment, as well as the related quantity

$$\int_{\partial\Omega} G_s(\boldsymbol{x},\boldsymbol{\xi})G_{mr}(\boldsymbol{\xi},\boldsymbol{x}_i)dA_{\boldsymbol{\xi}},$$

which reflects a recirculation mechanism of membrane-detachment and reattachment.

The effects of the recirculation mechanism and the bulk-originating fuel source are perhaps most prominent in the slow dynamics of multi-spot patterns occurring over an $\mathcal{O}(\varepsilon^{-2})$ timescale. Although our derivation of the slow dynamics closely follows that found in [91], our use of local geodesic normal coordinates streamlines this derivation. In particular geodesic normal coordinates lead to local expansions of the Laplace-Beltrami operator that are free of artificial first order correction terms [92, 95]. The resulting system of ODEs governing the slow spot dynamics consists of three terms of which the first reflects mutual repulsion between spots and is independent of bulk-membrane coupling. The second term reflects mutual attraction and is a consequence of the recirculation mechanism. However we show that this term is weaker than the mutual repulsion due to the first term. The final term is a consequence of the bulk-originating fuel source and leads to the attraction of spots toward local extrema of the resulting membrane-bound fuel term. To more closely investigate the consequences of each of these three terms we considered an explicit example in which the bulk-bound fuel source is given by a Dirac delta function concentrating at $\boldsymbol{x}_{\text{source}} = (0,0,\eta)$ for $0 \leq \eta < 1$. We then performed a detailed analysis of the dynamics of one- and two-spot configurations. In particular we illustrated that a one-spot pattern is globally attracted to the only stable equilibrium located at $\boldsymbol{x}_1 = \boldsymbol{e}_z$. On the other hand our analysis of two-spot patterns revealed the existence of a common angle solution given by $\boldsymbol{x}_1 = (\sin\theta_c, 0, \cos\theta_c)$ and $\boldsymbol{x}_2 = (-\sin\theta_c, 0, \cos\theta_c)$, a North-South (NS) solution for which $\boldsymbol{x}_1 = \pm e_z$ and $\boldsymbol{x}_2 = -\boldsymbol{x}_1$, and a tilted solution for which $\boldsymbol{x}_1 = (\sin\theta_t, 0, \cos\theta_t)$ and $\boldsymbol{x}_2 = (-\sin\theta_t^\star, 0, \cos\theta_t^\star)$ with $\theta_t < \theta_c < \theta_t^\star$. By numerically calculating stability thresholds for the common angle solution we the demonstrated an intricate bifurcation structure connecting the common angle solution to the tilted and NS configurations.

Chapter 4

The Singularly Perturbed One-Dimensional Gierer-Meinhardt Model with Non-Zero Activator Boundary Flux

In this chapter we consider the classically studied one-dimensional Gierer-Meinhardt (GM) model

$$u_t = D_u u_{xx} - u + u^2 v^{-1}, \quad v_t = D_v v_{xx} - v + u^2, \qquad 0 < x < 1. \tag{4.1a}$$

In the singularly perturbed limit for which $D_u = \varepsilon^2 \ll 1$ this GM model is known to exhibit multi-spike solutions. While boundary conditions have been identified as playing an important role in pattern formation [18, 59], relatively few studies have investigated the role of boundary conditions on the structure and stability of multi-spike solutions to singularly perturbed reaction diffusion systems. Instead most such studies have assumed either homogeneous Neumann or homogeneous Dirichlet boundary conditions. Notable exceptions include the investigation

of homogeneous Robin boundary conditions for the activator in the GM model [4, 60] and inhomogeneous Robin boundary conditions for the inhibitor in the two-dimensional Brusselator model [96]. These two studies and their illustration of the effect of boundary conditions on the structure and stability of multi-spike patterns serve as the primary motivation for the present chapter in which we consider inhomogeneous Neumann boundary conditions for the activator in the one-dimensional singularly perturbed GM model (4.1a). Additionally, this chapter aims to address some of the technical issues that arise in bulk-surface coupled reaction diffusion systems for which inhomogeneous boundary conditions naturally arise [27, 54, 58, 83].

We assume that that $D_u = \varepsilon^2$ while $D_v = \mathcal{O}(1)$ where $\varepsilon \ll 1$ is an asymptotically small parameter. The activator in an equilibrium solution will then concentrate in intervals of $\mathcal{O}(\varepsilon)$ length and by integrating the inhibitor equation in (4.1a) it is easy to see that if $v = \mathcal{O}(1)$ then we must have $u = \mathcal{O}(\varepsilon^{-1/2})$ in each interval on which it is concentrated. This motivates our choice of rescaling $u = \varepsilon^{-1}\tilde{u}$ and $v = \varepsilon^{-1}\tilde{v}$ which when substituted into (4.1a) and dropping the tildes gives

$$u_t = \varepsilon^2 u_{xx} - u + u^2 v^{-1}, \qquad 0 < x < 1, \tag{4.2a}$$

$$\tau v_t = D v_{xx} - v + \varepsilon^{-1} u^2, \qquad 0 < x < 1, \tag{4.2b}$$

and for which we observe both u and v will be $\mathcal{O}(1)$ in each interval where u is concentrated. In addition we impose inhomogeneous and homogeneous Neumann boundary conditions for the activator and inhibitor respectively which are given by

$$-\varepsilon u_x(0) = A, \quad \varepsilon u_x(1) = B, \quad v_x(0) = 0, \quad v_x(1) = 0, \tag{4.2c}$$

where we assume that $A, B \geq 0$ and for which we note that the scaling for the activator boundary conditions arises naturally from the scaling argument.

In contrast to systems with homogeneous Neumann boundary conditions, we note that (4.2) does *not* have a spatially homogeneous steady state when $A > 0$ and/or $B > 0$ and therefore traditional Turing stability analysis methods no longer apply. In particular the inhomogeneous Neumann boundary conditions for the activator in (4.2c) necessitate that the activator forms a boundary layer near each

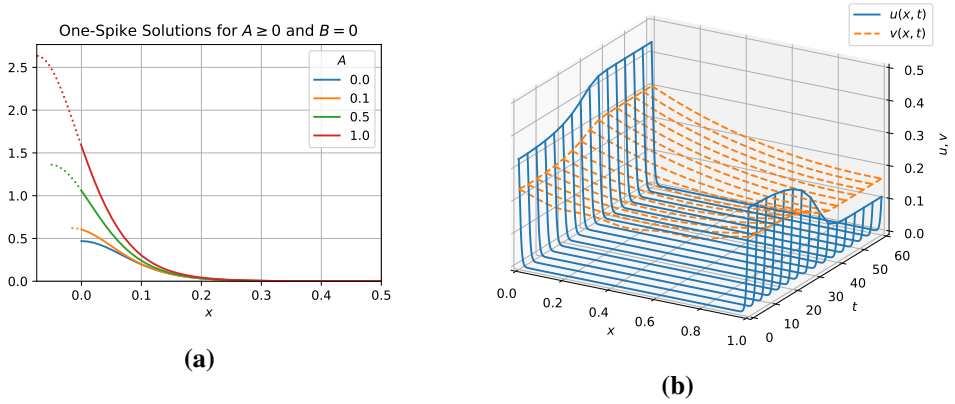

(a) **(b)**

Figure 4.1: (a) Examples of shifted one-spike solution concentrated at $x = 0$ for various values of $A \geq 0$ and with $\varepsilon = 0.05$ and $D = 5$. (b) Evolution of solution to GM problem with $D = 0.6$, $\varepsilon = .005$, $\tau = 0.1$, and $A = B = 0.08$. The initial condition is an unstable two-spike equilibrium where both spikes concentrate at the boundaries. A competition instability predicted by our asymptotic results in Figure 4.5a is triggered and leads to the solution settling at an asymmetric pattern.

boundary when $A > 0$ and/or $B = 0$. As we demonstrate in §4.1 the appropriate boundary layer solution takes the form of a *shifted* spike (see Figure 4.1a) that is analogous to the near-boundary spike solution of [4, 60] though it has different stability properties which we investigate in §4.3. Furthermore, by considering examples of one- and two-spike patterns in §4.4 we investigate the role of non-zero boundary fluxes on the structure of symmetric and asymmetric patterns, as well as their stability with respect to oscillatory (example 1), competition (examples 2-4), and drift (example 4) instabilities. In Figure 4.1b we plot the time-evolution of a linearly unstable equilibrium consisting of two boundary spikes of equal height. We see that the solution undergoes a competition instability, but rather than being subcritical as is the case when $A = B = 0$ [104], the non-zero boundary fluxes force the solution to settle to an asymmetric pattern. This illustrates that one of the key features of introducing non-zero boundary fluxes is that it leads to a kind of robustness of asymmetric solutions similar to that observed in the presence of an inhomogeneous precursor gradient [49].

The remainder of this chapter is organized as follows. In §4.1 we use the

method of matched asymptotic expansions to construct multi-spike equilibrium solutions. The key idea of the construction is to leverage the localized of the spike solution to reduce their construction to a problem of finding the spike heights and their locations. In §4.2 we derive a nonlocal eigenvalue problem which determines the linear stability of the multi-spike solutions on an $\mathcal{O}(1)$ time scale. Then, in §4.3 we rigorously prove partial stability results for an equilibrium consisting of a single boundary spike. This is done by analyzing a class of *shifted* nonlocal eigenvalue problems analogous to those studied in [60]. In §4.4 we consider four examples for which we construct one- and two-spike equilibrium patterns and study their linear stability and dynamics. Finally in §4.5 we conclude with a summary of our results and highlight several open problems and suggestions for future research.

4.1 Quasi-Equilibrium Multi-Spike Solutions and their Slow Dynamics

In this section we use the method of matched asymptotic expansions to derive an algebraic system and an ordinary differential equation that determine the profile and slow dynamics of a multi-spike quasi-equilibrium solution to (4.2). The derivation uses techniques that are now common in the study of localized patterns in one dimension. Our presentation will therefore be brief, highlighting only the novel aspects introduced by the inhomogeneous Neumann boundary conditions for the activator. We begin by supposing that there are two spikes concentrated at the boundaries $x_L = 0$ and $x_R = 1$ as well as N spikes concentrated in the interior at $0 < x_1 < ... < x_N < 1$. In addition we assume that the spikes are well separated in the sense that $|x_i - x_j| = \mathcal{O}(1)$ as $\varepsilon \to 0^+$ for all $i \neq j \in \{L, 1, ..., N, R\}$. This last assumption is key for effectively applying the method of matched asymptotic expansions.

We first construct an asymptotic approximation for the solution near $x = 0$ by letting $x = \varepsilon y$ where $y = \mathcal{O}(1)$ and expanding

$$u \sim u_{L,0}(y) + \mathcal{O}(\varepsilon), \qquad v \sim v_{L,0}(y) + \varepsilon v_{L,1}(y) + \mathcal{O}(\varepsilon^2). \tag{4.3}$$

It is easy to see that $v_L = \xi_L$ where ξ_L is is an undetermined constant, and $u_{L,0}(y) =$

$\xi_L w_c(y+y_L)$ where $w_c(y)$ is the unique *homoclinic* solution to

$$w_c'' - w_c + w_c^2 = 0, \quad 0 < y < \infty, \qquad w_c'(0) = 0, \qquad w_c(y) \to 0 \quad \text{as } y \to \infty, \tag{4.4a}$$

given explicitly by

$$w_c(y) = \frac{3}{2}\text{sech}^2\frac{y}{2}. \tag{4.4b}$$

Moreover, the undetermined *shift* parameter y_L is chosen to satisfy the inhomogeneous Neumann boundary condition

$$w_c'(y_L) = -A/\xi_L. \tag{4.5}$$

The unknown constants ξ_L and y_L are found by matching with the outer solution. To determine the appropriate *Neumann* boundary conditions for the outer problem we must first calculate $v_{L,1}'(y)$ as $y \to \infty$. This is done by integrating the $\mathscr{O}(\varepsilon)$ equation

$$Dv_{L,1}'' = -\xi_L^2 w_c(y+y_L)^2, \quad 0 < y < \infty; \qquad v_{L,1}'(0) = 0. \tag{4.6}$$

over $0 < y < \infty$ to obtain the limit

$$\lim_{y\to+\infty} v_{L,1}'(y) = -\frac{\xi_L^2}{D}\eta(y_L), \tag{4.7}$$

where

$$\eta(y_0) \equiv \int_0^\infty w_c(y+y_0)^2 dy = \frac{6e^{-2y_0}(3+e^{-y_0})}{(1+e^{-y_0})^3} \tag{4.8}$$

Note that $\eta(0) = 3$ and $\eta \to 0^+$ monotonically as $z \to \infty$. In a similar way we obtain the inner solution near $x = 1$ by letting $x = 1 - \varepsilon y$ and finding that

$$u \sim \xi_R w_c(y+y_R) + \mathscr{O}(\varepsilon), \qquad v \sim \xi_R + \varepsilon v_{R,1}(y) + \mathscr{O}(\varepsilon^2),$$

where y_R is determined by solving

$$w_c'(y_R) = -B/\xi_R, \tag{4.9}$$

and for which we calculate the limit

$$\lim_{y\to+\infty} v'_{R,1}(y) = -\frac{\xi_R^2}{D}\eta(y_R). \tag{4.10}$$

We now consider the inner solution at each interior spike location. By balancing dominant terms in a higher order asymptotic expansion, it can be shown that the interior spike locations var on an $\mathscr{O}(\varepsilon^{-2})$ timescale. Therefore we let $x_i = x_i(\varepsilon^2 t)$ for each $i = 1,...,N$ and with $x = x_i(\varepsilon^2 t) + y$ we calculate the inner asymptotic expansions

$$u \sim \xi_i w_c(y) + \mathscr{O}(\varepsilon), \qquad v \sim \xi_i + \varepsilon v_{i1}(y) + \mathscr{O}(\varepsilon^2), \qquad i = 1,...,N. \tag{4.11}$$

Furthermore, we must impose a solvability condition on the v_{i1} problem which gives

$$\frac{1}{\varepsilon^2}\frac{dx_i}{dt} = -\frac{1}{\xi_i}\left(\lim_{y\to+\infty} v'_{i1}(y) + \lim_{y\to-\infty} v'_{i1}(y)\right). \tag{4.12}$$

To determine the $2(N+2)$ undetermined constants ξ_i and y_i where $i \in \{L,1,...,N,R\}$ we must now calculate the outer solution, defined for $|x - x_i| = \mathscr{O}(1)$ for each boundary and interior spike location, and match it with each of the inner solutions. Since w_c decays to zero exponentially as $y \to \pm\infty$ we determine that the activator is asymptotically small in the outer region. On the other hand (4.7) and (4.10) imply the boundary conditions

$$v_x(0) \sim -\frac{\xi_L^2}{D}\eta(y_L), \qquad v_x(1) \sim \frac{\xi_R^2}{D}\eta(y_R),$$

while the exponential decay of w_c implies that the following limits hold (in the sense of distributions)

$$\varepsilon^{-1}u^2 \longrightarrow 6\sum_{j=1}^{N} \xi_j^2 \delta(x - x_j), \qquad\qquad (\varepsilon \to 0^+),$$

Thus, to leading order in $\varepsilon \ll 1$, the outer problem for the inhibitor is given by

$$Dv_{xx} - v = -6\sum_{j=1}^{N} \xi_j^2 \delta(x - x_j), \qquad 0 < x < 1, \tag{4.13}$$

$$Dv_x(0) = -\xi_0^2 \eta(y_L), \qquad Dv_x(1) = \xi_{N+1}^2 \eta(y_R). \tag{4.14}$$

This boundary value problem can be solved explicitly by letting G_ω be the Green's function satisfying

$$\begin{aligned} &G_{\omega,xx} - \omega^2 G_\omega = -\delta(x-\xi), \quad 0 < x < 1; \\ &G_{\omega,x}(0,\xi) = 0, \quad G_{\omega,x}(1,\xi) = 0, \qquad \omega > 0 \end{aligned} \tag{4.15a}$$

and given explicitly by

$$G_\omega(x,\xi) = \frac{1}{\omega \sinh \omega} \begin{cases} \cosh \omega x \cosh \omega(1-\xi), & 0 < x < \xi, \\ \cosh \omega(1-x) \cosh \omega \xi, & \xi < x < 1. \end{cases} \tag{4.15b}$$

Formally substituting $\xi = 0$ or $\xi = 1$ into the above expression gives

$$G_\omega(x,0) = \frac{\cosh \omega(1-x)}{\omega \sinh \omega}, \qquad G_\omega(x,1) = \frac{\cosh \omega x}{\omega \sinh \omega}, \tag{4.15c}$$

which is readily seen to satisfy

$$G_{\omega,xx} - \omega^2 G_\omega = 0, \qquad 0 < x < 1,$$

with boundary conditions

$$G_{\omega,x}(0,0) = -1, \qquad G_{\omega,x}(1,0) = 0, \qquad G_{\omega,x}(0,1) = 0, \qquad G_{\omega,x}(1,1) = 1.$$

Letting $\omega_0 \equiv D^{-1/2}$ we obtain the following leading order asymptotic expansion

for the quasi-equilibrium solution to (4.2)

$$u_e(x) \sim \xi_L w_c\big(\tfrac{x}{\varepsilon}+y_L\big)+\xi_R w_c\big(\tfrac{1-x}{\varepsilon}+y_R\big)+\sum_{j=1}^{N}\xi_j w_c\big(\tfrac{x-x_j}{\varepsilon}\big), \tag{4.16a}$$

$$v_e(x) \sim \omega_0^2\bigg(\xi_L^2\eta(y_L)G_{\omega_0}(x,0)+\xi_R^2\eta(y_R)G_{\omega_0}(x,1)+6\sum_{j=1}^{N}\xi_j^2 G_{\omega_0}(x,x_j)\bigg). \tag{4.16b}$$

Furthermore, by imposing the *consistency* condition $v_e(x_i)=\xi_i$ for each $i\in\{L,1,...,N,R\}$ we obtain the system of $N+2$ nonlinear equations

$$\boldsymbol{B}\equiv\boldsymbol{\xi}-\omega_0^2\mathcal{G}_{\omega_0}\mathcal{N}\boldsymbol{\xi}^2=0, \tag{4.17a}$$

where $\mathcal{G}_{\omega_0}$ and $\mathcal{N}$ are the $(N+2)\times(N+2)$ matrices given by

$$(\mathcal{G}_{\omega_0})_{ij}=G_{\omega_0}(x_i,x_j)\quad i,j=L,R,1,...,N,$$
$$\mathcal{N}\equiv\mathrm{diag}(\eta(y_L),\eta(y_R),6,...,6),$$

and

$$\boldsymbol{\xi}\equiv(\xi_L,\xi_R,\xi_1,...,\xi_N)^T,\qquad \boldsymbol{\xi}^2=(\xi_L^2,\xi_R^2,\xi_1^2,...,\xi_N^2)^T. \tag{4.17b}$$

Thus, for given spike configuration $0<x_1<...<x_N<1$, the system (4.17a) together with (4.5) and (4.9) can be solved for the unknown spike heights $\xi_L,\xi_1,...,\xi_N,\xi_R$ and boundary *shifts* y_L and y_R. Summarizing, we have the following proposition.

Proposition 4.1.1. *In the limit $\varepsilon\to 0^+$ and for $t\ll\mathcal{O}(\varepsilon^{-2})$ an $N+2$ spike quasi-equilibrium solution to* (4.2) *consisting of two boundary spikes and N well separated interior spikes concentrated at specified locations $0<x_1<...<x_N<1$ is given asymptotically by* (4.16) *where $G_{\omega_0}(x,\xi)$ is given explicitly by* (4.15b) *and $\omega_0=D^{-1/2}$. The boundary shifts, y_L and y_R, and spike heights, $\xi_L,\xi_1,...,\xi_N,\xi_R$, are found by solving the system of $N+4$ equations* (4.5), (4.9), *and* (4.17a).

The asymptotic solution constructed in the above proposition will not generally be an equilibrium of (4.2) due to the slow, $\mathcal{O}(\varepsilon^{-2})$, drift motion of the interior spikes described by (4.12). However, this solution can be made into an equilibrium by choosing the interior spike locations $x_1,...,x_N$ appropriately.

Proposition 4.1.2. *The interior spike locations of a multi-spike pattern consisting of two boundary spikes and N interior spikes vary on an $\mathcal{O}(\varepsilon^{-2})$ time scale according to the differential equation*

$$\begin{aligned}\frac{1}{\varepsilon^2}\frac{dx_i}{dt} = &-\frac{6\xi_i}{D}\left\langle \partial_x G_{\omega_0}(x,x_i)\right\rangle_{x=x_i} - \frac{12}{\xi_i D}\sum_{j\neq i}\xi_j^2 G_x(\xi_i,\xi_j)\\ &-\frac{2}{\xi_i D}\left[\xi_L^2\eta(y_R)G_x(x_i,0)+\xi_R^2\eta(y_R)G_x(x_i,1)\right],\end{aligned} \tag{4.18}$$

for each $i = 1,...,N$ where

$$\left\langle f(x)\right\rangle_{x_0} = \lim_{x\to x_0^+} f(x) + \lim_{x\to x_0^-} f(x), \tag{4.19}$$

which is to be solved together with (4.17a)*,* (4.5)*, and* (4.9) *for the spike heights $\xi_L,\xi_1,...,\xi_N,\xi_R$ and shifts y_L and y_R. In particular, if the configuration $x_1,...,x_N$ is stationary with respect to the ODE* (4.18)*, then to leading order the quasi-equilibrium solution of Proposition 4.1.1 is an equilibrium for all $t \geq 0$.*

4.1.1 Equilibrium Multi-Spike Solutions by the Gluing Method

We now use an alternative method for constructing *asymmetric* multi-spike equilibrium solutions to (4.2). This method extends that of Ward and Wei [104] to account for inhomogeneous Neumann boundary conditions. The key idea is to construct a single boundary spike solution in an interval of variable length and use this solution to *glue* together a multi-spike solution. In particular, we begin considering the problem

$$\varepsilon^2 u_{xx} - u + v^{-1}u^2 = 0, \quad Dv_{xx} - v + \varepsilon^{-1}u^2 = 0, \qquad 0 < x < l, \tag{4.20a}$$

$$\varepsilon u_x(0) = -A, \quad \varepsilon u_x(l) = 0, \quad Dv_x(0) = 0, \quad Dv_x(l) = 0, \tag{4.20b}$$

where $l > 0$ is fixed and for which we will use the method of matched asymptotic expansions to construct a single spike solution concentrated at $x = 0$. Proceeding as in §4.1 we readily find that the equilibrium solution in the outer region (i.e. for

$x = \mathcal{O}(1)$) is given by

$$u(x;l,A) \sim \xi_0 w_c\big(\varepsilon^{-1}x + y_0\big), \qquad v(x;l,A) \sim \xi_0 \frac{\cosh\omega_0(l-x)}{\cosh\omega_0 l}, \tag{4.21}$$

where $\omega_0 \equiv D^{-1/2}$ while the shift parameter y_0 and spike height ξ_0 satisfy

$$w_c'(y_0) = -\frac{A}{\xi_0}, \tag{4.22}$$

and for which, using (4.4b) and (4.8), we explicitly calculate

$$\xi_0 = \frac{\tanh\omega_0 l}{\omega_0\eta(y_0)}, \quad y_0 = \log\left(\frac{1+3q+\sqrt{9q^2+10q+1}}{2}\right), \quad q \equiv \frac{\omega_0 A}{\tanh\omega_0 l}, \tag{4.23}$$

for which we remark that $y_0 \sim 4q$ as $q \to 0$ and therefore $\xi_0 \sim (3\omega_0)^{-1}\tanh\omega_0 l$ as $A \to 0^+$. Finally, we note that y_0 is monotone increasing in A and monotone decreasing in D and l when $A > 0$ is fixed.

A multi-spike pattern is constructed by first partitioning the unit interval $0 < x < 1$ into $N+2$ subintervals defined by

$$\begin{aligned} &x_L = 0, && x_i = l_L + 2\sum_{j=1}^{i-1} l_j + l_i \quad (i = 1,...,N), && x_R = 1, \\ &I_L = [0, l_L), && I_i = [x_i - l_i, x_i + l_i) \quad (i = 1,...,N), && I_R = [1-l_R, 1], \end{aligned}$$

where $l_L, l_1, ..., l_N, l_R$ are chosen to satisfy the $N+2$ constraints

$$l_L + 2l_1 + \cdots 2l_N + l_R = 1. \tag{4.24a}$$

$$v(l_L;l_L,A) = v(l_1;l_1,0) = \cdots = v(l_N;l_N,0) = v(l_R;l_R,B),. \tag{4.24b}$$

The first constraint guarantees that the intervals are mutually disjoint, while the second set of $N+1$ constraints guarantees the continuity of the multi-spike equilibrium solution

$$u_e(x) = \begin{cases} u(x;l_L,A), & x \in I_L \\ u(|x-x_i|;l_i,0), & x \in I_i \\ u(1-x,l_R,B), & x \in I_R \end{cases}, \quad v_e(x) = \begin{cases} v(x;l_L,A), & x \in I_L \\ v(|x-x_i|;l_i,0), & x \in I_i \\ v(1-x,l_R,B), & x \in I_R \end{cases}. \tag{4.24c}$$

We remark that the local symmetry of each interior spike implies that the interior spikes are stationary with respect to the slow dynamics found in (4.12), and therefore the multi-spike solution constructed above is an equilibrium of (4.2).

4.2 Linear Stability of Multi-Spike Pattern

In this section we derive a nonlocal eigenvalue problem (NLEP) that, to leading order in $\varepsilon \ll 1$, determines the linear stability of the quasi-equilibrium solution given in Proposition 4.1.1 on an $\mathcal{O}(1)$ timescale. Letting u_e and v_e be the quasi-equilibrium solution from Proposition 4.1.1, we consider the perturbations $u = u_e + e^{\lambda t}\Phi$ and $v = v_e + e^{\lambda t}\Psi$ with which (4.2) becomes

$$\varepsilon^2\Phi_{xx} - \Phi + 2\frac{u_e}{v_e}\Phi - \frac{u_e^2}{v_e^2}\Psi = \lambda\Phi, \qquad 0 < x < 1, \tag{4.25a}$$

$$D\Psi_{xx} - \Psi + 2\varepsilon^{-1}u_e\Phi = \tau\lambda\Psi, \qquad 0 < x < 1. \tag{4.25b}$$

This problem admits both *large* and *small* eigenvalues characterized by $\lambda = \mathcal{O}(1)$ and $\mathcal{O}(\varepsilon^2)$ respectively. The small eigenvalues are closely related to the linearization of the slow-dynamics (4.18) and the resulting instabilities therefore take place over a $\mathcal{O}(\varepsilon^{-2})$ timescale [111]. In contrast, the large eigenvalues lead to amplitude instabilities over a $\mathcal{O}(1)$ timescale. In this section we focus exclusively on the large eigenvalues and limit our discussion of the small eigenvalues to the specific example given in §4.4.4 in which a two-spike solution consisting of one spike on the boundary and one interior spike is considered.

Using the method of matched asymptotic expansions as in §4.1 we readily find that, to leading order in $\varepsilon \ll 1$, the inhibitor perturbation Ψ satisfies

$$D\Psi_{xx} - (1+\tau\lambda)\Psi = -2\sum_{j=1}^{N}\xi_j\int_{-\infty}^{\infty} w_c(y)\phi_j(y)dy\delta(x-x_j), \qquad 0 < x < 1, \tag{4.26a}$$

$$D\Psi_x(0) = -2\xi_L\int_0^{\infty} w_c(y+y_L)\phi_L(y)dy, \tag{4.26b}$$

$$D\Psi_x(1) = 2\xi_R\int_0^{\infty} w_c(y+y_R)\phi_R(y)dy, \tag{4.26c}$$

where ϕ_L and ϕ_R are the leading order inner expansions of the activator perturba-

tion Φ at the boundaries satisfying

$$\begin{gathered}\mathscr{L}_{y_i}\phi_i - w_c(y+y_i)^2\Psi(x_i) = \lambda\phi_i, \quad 0 < y < \infty, \\ \phi_i'(0) = 0, \quad \phi_i \to 0 \quad \text{as } y \to \infty,\end{gathered} \tag{4.27a}$$

for $i = L,R$ respectively, while $\phi_1,...,\phi_N$ are the leading order inner expansions of Φ at each of the interior spike locations $x_1,..,x_N$ satisfying

$$\mathscr{L}_0\phi_i - w_c(y)^2\Psi(x_i) = \lambda\phi_i, \quad -\infty < y < \infty, \quad \phi \to 0 \quad \text{as } y \to \pm\infty, \tag{4.27b}$$

for each $i = 1,...,N$ respectively. The linear differential operator $\mathscr{L}_{y_0}$ parametrized by $y_0 \geq 0$ appearing in each equation is explicitly given by

$$\mathscr{L}_{y_0}\phi \equiv \phi'' - \phi + 2w_c(y+y_0)\phi. \tag{4.28}$$

Note that by decomposing each $\phi_i = \phi_i^{\text{even}} + \phi_i^{\text{odd}}$ $(i = 1,...,N)$ where ϕ_i^{even} and ϕ_i^{odd} are even and odd about $y = 0$ respectively, we find that either $\phi_i^{\text{odd}} = 0$ or else $\lambda \leq 0$. In particular, the odd components of each ϕ_i $(i = 1,...,N)$ do not contribute to any instabilities and without loss of generality we may therefore assume that each ϕ_i is even about $y = 0$. Hence it suffices to pose (4.27b) on the half line with the same homogeneous Neumann boundary conditions used in (4.27a).

Letting $\omega_\lambda \equiv \sqrt{(1+\tau\lambda)/D}$ and recalling the definition of G_ω in (4.15) we readily find that the solution to (4.26) is explicitly given by

$$\Psi(x) = 2\omega_0^2 \sum_{j=L,R,1}^{N} \hat{\xi}_j G_{\omega_\lambda}(x,x_j) \int_0^\infty w_c(y+y_j)\phi_j(y)dy.$$

where we let

$$y_1 = ... = y_N = 0, \qquad \hat{\xi}_i \equiv \begin{cases} \xi_i, & i = L,R, \\ 2\xi_i, & i = 1,...,N, \end{cases}. \tag{4.29}$$

Evaluating $\Psi(x)$ at each $x = x_i$ and substituting into (4.27) yields the system of

NLEPs

$$\mathscr{L}_{y_i}\phi_i - 2\omega_0^2 w_c(y+y_i)^2 \sum_{j=L,R,1}^{N} \hat{\xi}_j G_{\omega_\lambda}(x_i,x_j)\int_0^\infty w_c(y+y_j)\phi_j(y)\,dy = \lambda\phi_i \qquad (4.30a)$$

for $y > 0$ with boundary conditions

$$\phi_i'(0) = 0, \qquad \phi_i \to 0 \qquad \text{as } y \to +\infty. \qquad (4.30b)$$

for each $i = L,R,1,...,N$ where $\mathscr{L}_{y_i}$ is defined by (4.28).

The NLEP system (4.30) has two key features that distinguish it from analogous NLEPs in singularly perturbed reaction diffusion systems [41, 104, 107, 111] and are explored in the rigorous stability results of §4.3 as well as in the specific examples of §4.4. First, it considers both boundary-bound and interior-bound spikes. As explored in Examples 2 to 4 this has immediate consequences for both the existence and stability of asymmetric patterns even in the zero-flux case where $A = B = 0$. The second distinguishing feature of (4.30) is the introduction of the shift parameters $y_L \geq 0$ and $y_R \geq 0$. We remark that an analogous *negative* shift parameter has been examined in the context of near-boundary spike solutions for *homogeneous* Robin boundary conditions [4, 60]. However, as highlighted in the stability results of §4.3, the positive shift parameter plays a key role in the stability properties of boundary-bound spikes. An important critical value of the shift parameter is the unique value $y_{0c} > 0$ such that $w_c''(y_{0c}) = 0$ and which is explicitly given by

$$y_{0c} = \log(2+\sqrt{3}). \qquad (4.31)$$

In particular, it can be shown that if $y_0 \lesseqgtr y_{0c}$ then $\mathscr{L}_{y_0}$ has an unstable and stable spectrum respectively (see Lemma 4.3.1 below). Moreover the operator $\mathscr{L}_{y_{0c}}$ has a one-dimensional kernel spanned by $w_c'(y+y_{0c})$.

4.2.1 Reduction of NLEP to an Algebraic System

It is particularly useful to rewrite (4.30) as an algebraic system as follows. Assuming that λ is not an eigenvalue of $\mathscr{L}_{y_i}$ for all $i = L,R,1,...,N$ we let

$$\phi_i = c_i(\mathscr{L}_{y_i} - \lambda)^{-1} w_c(y+y_i)^2, \qquad i \in \{L,R,1,...,N\}, \qquad (4.32)$$

where the coefficients $c_L, c_R, c_1, ..., c_N$ are undetermined. Note that in (4.32) the homogeneous Neumann boundary condition $\phi_i'(0) = 0$ is assumed. In addition, note that if $\lambda = 0$ then (4.32) is only valid if $y_L, y_R \neq y_{0c}$.

Substituting into (4.30) then yields the linear homogeneous system for $\boldsymbol{c} \equiv (c_L, c_R, c_1, ..., c_N)^T$

$$\mathscr{G}_{\omega_\lambda} \mathscr{D}_\lambda \boldsymbol{c} = (2\omega_0^2)^{-1} \boldsymbol{c}, \tag{4.33}$$

where $\mathscr{G}_{\omega_\lambda}$ is the $(N+2) \times (N+2)$ matrix with entries

$$(\mathscr{G}_{\omega_\lambda})_{ij} = G_{\omega_\lambda}(x_i, x_j), \qquad (i, j = L, R, 1, ..., N), \tag{4.34}$$

while $\mathscr{D}_\lambda$ is the diagonal $(N+2) \times (N+2)$ matrix given by

$$(\mathscr{D}_\lambda)_{ij} = \frac{1}{\omega_0} \begin{cases} \eta(y_i)\xi_i \mathscr{F}_{y_L}(\lambda), & i = j = L, R, \\ 6\xi_i \mathscr{F}_0(\lambda), & i = j = 1, ..., N, \\ 0, & i \neq j, \end{cases} \tag{4.35}$$

where

$$\mathscr{F}_{y_0}(\lambda) \equiv \frac{\int_0^\infty w_c(y+y_0)(\mathscr{L}_{y_0} - \lambda)^{-1} w_c(y+y_0)^2 dy}{\int_0^\infty w_c(y+y_0)^2 dy}, \tag{4.36}$$

and for which (4.46) and (4.47) below imply that for all $y_0 \neq y_{0c}$

$$\mathscr{F}_{y_0}(0) = 1 + \frac{w_c'(y_0) w_c(y_0)^2}{2 w_c''(y_0) \eta(y_0)}. \tag{4.37}$$

Comparing (4.33) and (4.30), it follows that λ is an eigenvalue of (4.30) if and only if $(2\omega_0^2)^{-1}$ is an eigenvalue of $\mathscr{G}_{\omega_\lambda} \mathscr{D}_\lambda$. In particular, when λ is not an eigenvalue of $\mathscr{L}_{y_L}$, $\mathscr{L}_{y_R}$, and $\mathscr{L}_0$ then it is an eigenvalue of the NLEP (4.30) if and only if it satisfies the algebraic equation

$$\det\left(\mathbb{I}_{N+2} - 2\omega_0^2 \mathscr{G}_{\omega_\lambda} \mathscr{D}_\lambda\right) = 0, \tag{4.38}$$

where $\mathbb{I}_{N+2}$ is the $(N+2) \times (N+2)$ identity matrix.

We conclude by noting that if either $y_L = y_{0c}$ and/or $y_R = y_{0c}$ then the algebraic reduction fails when searching for a zero eigenvalue $\lambda = 0$ since $\mathscr{L}_{y_{0c}}$ is not in-

vertible. However, in this case we can deduce an analogous system. In particular letting $\lambda = 0$ and assuming that $y_L = y_{0c}$ and $y_R \neq y_{0c}$, we multiply the $i = L$ NLEP in (4.30) by $w_c'(y + y_{0c})$ and integrate over $0 < y < \infty$ to get

$$\xi_L \int_0^\infty w_c(y+y_L)\phi_L dy = -\sum_{j=R,1}^{N} \tilde{\xi}_j \frac{G_{\omega_0}(0,x_j)}{G_{\omega_0}(0,0)} \int_0^\infty w_c(y+y_j)\phi_j dy. \tag{4.39}$$

Proceeding as above we then deduce that the NLEP (4.30) with $\lambda = 0$ is then equivalent to the algebraic equation

$$\det(\mathbb{I}_{N+1} - 2\omega_0^2 \tilde{\mathscr{G}}_{\omega_0} \tilde{\mathscr{D}}) = 0, \tag{4.40}$$

where $\tilde{\mathscr{G}}_{\omega_0}$ and $\tilde{\mathscr{D}}$ are the $(N+1)\times(N+1)$ matrices with entries

$$(\tilde{\mathscr{G}}_{\omega_0})_{ij} = \mathscr{G}_{ij} - \frac{1}{G_{\omega_0}(0,0)} G_{\omega_0}(x_i,0) G_{\omega_0}(0,x_j), \qquad (\tilde{\mathscr{D}})_{ij} = \mathscr{D}_{ij}, \tag{4.41}$$

for $i, j = R, 1, ..., N$. The same approach can likewise be used if $y_L = y_R = y_{0c}$.

4.2.2 Zero-Eigenvalues of the NLEP and the Consistency Condition

The conditions under which $\lambda = 0$ is an eigenvalue of the NLEP (4.30) can be directly linked to the system (4.17a) as highlighted in [111]. Specifically, assume that $x_1, ..., x_N$ are fixed (not necessarily at an equilibrium configuration of the slow dynamics ODE (4.18)) and let $\xi_L, \xi_R, \xi_1, ..., \xi_N$ together with y_L and y_R solve (4.17a), (4.5), and (4.9) with the additional assumption that $y_L, y_R \neq y_{0c}$. From the definition of η in (4.8) and from (4.5) and (4.9) we calculate

$$\frac{\partial \eta(y_i)}{\partial \xi_i} = \frac{w_c(y_i)^2 w_c'(y_i)}{\xi_i w_c''(y_i)}, \tag{4.42}$$

for $i = L, R$. Taking the Jacobian of the quasi-equilibrium system (4.17a) and recalling the definition of $\mathscr{D}_\lambda$ given in (4.35) we deduce that

$$\nabla_{\boldsymbol{\xi}} \boldsymbol{B} = \mathbb{I} - 2\omega_0^2 \mathscr{G}_{\omega_0} \mathscr{D}_0. \tag{4.43}$$

Together with the discussion of §4.2.1 we deduce that if $y_L, y_R \neq 0$ and each $x_1, ..., x_N$ is independent of $\xi_L, \xi_R, \xi_1, ..., \xi_N$, then $\lambda = 0$ is an eigenvalue of the NLEP (4.30) if and only if the Jacobian $\nabla_{\boldsymbol{\xi}} \boldsymbol{B}$ is singular.

4.3 Rigorous Stability and Instability Results for the Shifted NLEP

In this section we rigorously prove instability and stability results for the *shifted* NLEP

$$\begin{aligned} \mathscr{L}_{y_0}\phi - \mu \frac{\int_0^\infty w\phi}{\int_0^\infty w^2} w^2 = \lambda\phi, \quad 0 < y < \infty, \\ \phi'(0) = 0; \qquad \phi \to 0 \quad \text{as } y \to \infty, \end{aligned} \tag{4.44}$$

where μ is a real constant and for a fixed value of $y_0 \geq 0$ we define

$$\mathscr{L}_{y_0}\phi \equiv \phi'' - \phi + 2w\phi, \qquad w(y) \equiv w_c(y + y_0), \tag{4.45}$$

and where w_c is the unique solution to (4.4a). When $y_0 = 0$ the NLEP (4.44) is stable if $\mu > 1$ and unstable if $\mu < 1$ [107]. We begin by collecting a few facts about the operator $\mathscr{L}_{y_0}$ and its spectrum. First, we calculate

$$\mathscr{L}_{y_0}^{-1} w^2 = w - \frac{w'(0)}{w''(0)} w', \qquad \mathscr{L}_{y_0}^{-1} w = w + \frac{1}{2} y w' - \frac{3w'(0)}{2w''(0)} w' \tag{4.46}$$

where the additional terms are chosen so that homogeneous Neumann boundary conditions at $y = 0$ are satisfied and which we use to compute

$$\int_0^\infty w \mathscr{L}_{y_0}^{-1} w^2 = \int_0^\infty w^2 + \frac{w'(0) w(0)^2}{2w''(0)}, \tag{4.47a}$$

$$\int_0^\infty w \mathscr{L}_{y_0}^{-1} w = \frac{3}{4} \int_0^\infty w^2 + \frac{3w'(0) w(0)^2}{4w''(0)}, \tag{4.47b}$$

$$\int_0^\infty w^2 \mathscr{L}_{y_0}^{-1} w^2 = \int_0^\infty w^3 + \frac{w'(0) w(0)^3}{3w''(0)}, \tag{4.47c}$$

$$\int_0^\infty w^3 = \frac{6}{5} \int_0^\infty w^2 + \frac{3w(0) w'(0)}{5}. \tag{4.47d}$$

In the next two lemmas, we describe some key properties of the eigenvalue problem

$$\mathscr{L}_{y_0}\Phi = \Lambda\Phi, \qquad 0 < y < \infty; \qquad \Phi'(0) = 0; \qquad \Phi \to 0, \quad \text{as } y \to +\infty. \tag{4.48}$$

Lemma 4.3.1. *Let $y_0 \geq 0$ an let Λ_0 be the principal eigenvalue of* (4.48)*. Then $\Lambda_0 = 0$ if $y_0 = y_{0c}$ and $\Lambda_0 \lesseqgtr 0$ if $y_0 \gtreqless y_{0c}$. Furthermore, the eigenfunction corresponding to the principal eigenvalue is of one sign.*

Proof. Since $\mathscr{L}_{y_0}$ is self-adjoint, the variational characterization

$$-\Lambda_0 = \inf_{\Phi \in H^2([0,\infty))} \frac{\int_0^\infty |\Phi'|^2 + |\Phi|^2 - 2w|\Phi|^2}{\int_0^\infty |\Phi|^2}, \tag{4.49}$$

implies that the principal eigenfunction Φ_0 is of one sign. Since $\Phi_0(0) \neq 0$ we may, without loss of generality, assume that $\Phi_0(0) = 1$ and $\Phi_0 > 0$. Now we multiply (4.48) by w' and integrate by parts to get

$$\Lambda_0 = \frac{w''(0)}{\int_0^\infty w'\Phi_0 dy}, \tag{4.50}$$

where we remark that the denominator is negative since $w' \leq 0$ for all $y \geq 0$. The claim follows by noting that $w''(0) = 0$ when $y_0 = 0$ and $w''(0) \gtreqless 0$ for $y_0 \gtreqless y_{0c}$. □

Lemma 4.3.2. *Let Λ_1 be the second eigenvalue of $\mathscr{L}_{y_0}$. Then $\Lambda_1 < 0$ for all $y_0 \geq 0$.*

Proof. First note that the second eigenfunction Φ_1 must cross zero at least once since $\int_0^\infty \Phi_0\Phi_1 dy = 0$ and Φ_0 is of one sign. Next we assume toward a contradiction that $\Lambda_1 \geq 0$. We begin by showing that Φ_1 has exactly one zero in $0 < y < \infty$. Assume that Φ_1 has more than one zero and choose $0 < a < b < \infty$ such that $\Phi_1(a) = \Phi_1(b) = 0$ and $\Phi_1 > 0$ in $a < y < b$. Then $\Phi_1'(a) > 0$ and $\Phi_1'(b) < 0$ so we obtain the contradiction

$$0 \geq \Lambda_1 \int_a^b w'\Phi_1 dy = \int_a^b w'\mathscr{L}_{y_0}\Phi_1 dy = w'(b)\Phi_1'(b) - w'(a)\Phi_1'(a) > 0, \tag{4.51}$$

where we have used $\mathscr{L}_{y_0}w' = 0$ and $w' < 0$ for all $y > 0$. Thus Φ_1 has a unique zero $0 < a < \infty$ and we may assume that $\Phi_1 \lesseqgtr 0$ for $y \lesseqgtr a$. Setting $b = \infty$ in (4.51) we get a contradiction. □

In Figure 4.2a we plot the principal and second eigenvalues of the operator $\mathscr{L}_{y_0}$ which we calculated numerically (see Appendix D.2 for details on the numerical method).

Lemma 4.3.1 implies that the NLEP will have different stability properties depending on whether y_0 is greater than or smaller than y_{0c}. We will henceforth refer to $0 \leq y_0 < y_{0c}$ and $y_0 > y_{0c}$ as the *small-shift* and *large-shift* cases respectively. When $y_0 = 0$ it is known that for $\mu > 0$ sufficiently large, the NLEP (4.44) is stable. In this sense the nonlocal term appearing in (4.44) can stabilize the spectrum of the linearized operator $\mathscr{L}_{y_0}$. Since all the eigenvalues of $\mathscr{L}_{y_0}$ are negative in the large-shift case we expect the spectrum of the NLEP (4.44) to remain stable for all $\mu \geq 0$. Restricting our attention to *real* eigenvalues, we have the following stability result for the large-shift case.

Theorem 4.3.1. *All real eigenvalues of the NLEP* (4.44) *are negative when* $y_0 > y_{0c}$.

To prove this, we first prove the following lemma.

Lemma 4.3.3. *Let* $y_0 > y_{0c}$ *and suppose that* ϕ *satisfies*

$$\mathscr{L}_{y_0}\phi - \lambda\phi \geq 0, \quad 0 < y < \infty; \qquad \phi'(0) \geq 0; \qquad \phi \to 0, \quad \text{as } y \to +\infty, \tag{4.52}$$

where $\lambda \geq 0$. *Then* $\phi < 0$ *for all* $y \geq 0$.

Proof. Assume toward a contradiction that $\phi > 0$ in $0 \leq a < y < b \leq \infty$. Without loss of generality we may assume that $\phi(a) = 0$ if $a > 0$ and $\phi(0) > 0$ if $a = 0$. Then, for any such $0 \leq a < b \leq \infty$ we have

$$\phi(a) \geq 0, \quad \phi'(a) \geq 0, \quad \phi(b) = 0, \quad \phi'(b) \leq 0. \tag{4.53}$$

Let $g(y) \equiv w''(y) - \beta w'(y)$ where $\beta \equiv \frac{\max_{y\geq 0}|w'''(y)|}{w''(a)}$ is well-defined and positive. Then $g > 0$ for all $y \geq 0$, $g'(a) \leq 0$, and moreover $(\mathscr{L}_{y_0} - \lambda)g = \mathscr{L}_{y_0}w'' - \lambda g = -(w')^2 - \lambda g < 0$. Integrating by parts we obtain the contradiction

$$\begin{aligned} 0 &< \int_a^b g(\mathscr{L}_{y_0} - \lambda)\phi dy - \int_a^b \phi(\mathscr{L}_{y_0} - \lambda)g dy \\ &= g(b)\phi'(b) - g(a)\phi'(a) - g'(b)\phi(b) + g'(a)\phi(a) \leq 0. \end{aligned}$$

□

Proof [Theorem 4.3.1.] Suppose that $\lambda \geq 0$ is an eigenvalue of (4.44) so that by Lemma 4.3.1 the operator $\mathscr{L}_{y_0} - \lambda$ is invertible and from (4.44) we calculate

$$\phi = \mu \frac{\int_0^\infty w\phi}{\int_0^\infty w^2} (\mathscr{L}_{y_0} - \lambda)^{-1} w^2.$$

But $w^2 > 0$ so by Lemma 4.3.3 we obtain the contradiction

$$1 = \mu \frac{\int_0^\infty w(\mathscr{L}_{y_0} - \lambda)^{-1} w^2}{\int_0^\infty w^2} < 0. \tag{4.54}$$

□

From Theorem 4.3.1 we immediately deduce that the NLEP does not admit a zero eigenvalue for any $\mu \geq 0$ when $y_0 > y_{0c}$. On the other hand, when $0 \leq y_0 \leq y_{0c}$ we suspect that the NLEP admits a zero eigenvalue for an appropriate choice of $\mu \geq 0$. When $y_0 = y_{0c}$ this is the case for $\mu = 0$. When $0 \leq y_0 < y_{0c}$ we set $\lambda = 0$ in (4.44) and obtain

$$\mathscr{L}_{y_0} \phi = \mu \frac{\int_0^\infty w\phi}{\int_0^\infty w^2} w^2. \tag{4.55}$$

Using (4.46) we calculate $\phi = \mathscr{L}_{y_0}^{-1} w^2$ and substitute back into (4.55) to deduce that $\lambda = 0$ is an eigenvalue if and only if

$$\mu = \mu_c(y_0) \equiv \frac{\int_0^\infty w^2}{\int_0^\infty w \mathscr{L}_{y_0}^{-1} w^2} = \frac{\int_0^\infty w^2}{\int_0^\infty w^2 + \frac{w'(0)w(0)^2}{2w''(0)}}. \tag{4.56}$$

Note that $\mu_c(y_0) \lesseqgtr 0$ if $y_0 \gtreqless y_{0c}$. In terms of the critical value μ_c we have the following instability result for the small-shift case.

Theorem 4.3.2. *Let $0 \leq y_0 < y_{0c}$ and $0 \leq \mu < \mu_c$ where critical value μ_c is defined in* (4.56)*. Then the NLEP* (4.44) *admits a positive real eigenvalue.*

Proof. Let Λ_0 be the principal eigenvalue of $\mathscr{L}_{y_0}$. First note that by Lemma 4.3.1 and 4.3.2 the principal and second eigenvalues of $\mathscr{L}_{y_0}$ satisfy $\Lambda_1 < 0 < \Lambda_0$. Moreover the corresponding eigenfunction Φ_0 is of one sign and we may assume that

$\Phi_0 > 0$ and $\int_0^\infty \Phi_0^2 = 1$. Observe that if $\lambda_0 \neq \Lambda_0$ is a positive eigenvalue of the NLEP (4.44) then

$$\phi = \mu \frac{\int_0^\infty w\phi}{\int_0^\infty w^2} (\mathscr{L}_{y_0} - \lambda_0)^{-1} w^2,$$

and since $\int_0^\infty w\phi \neq 0$ the above equation is equivalent to $h(\lambda_0) = 0$ where

$$h(\lambda) \equiv \int_0^\infty w(\mathscr{L}_{y_0} - \lambda)^{-1} w^2 - \frac{\int_0^\infty w^2}{\mu}. \tag{4.57}$$

We now show that such a λ_0 can always be found in $0 < \lambda_0 < \Lambda_0$ for $0 \leq \mu < \mu_c$.

First we calculate $h(0) = \int_0^\infty w^2(\mu_c^{-1} - \mu^{-1}) < 0$. Next we we let ψ be the unique solution to

$$(\mathscr{L}_{y_0} - \lambda)\psi = w^2, \quad 0 < y < \infty; \qquad \psi'(0) = 0.$$

Decomposing $\psi = c_0\Phi_0 + \psi^\perp$ where $\int_0^\infty \Phi_0 \psi^\perp = 0$ we find that $\psi^\perp$ satisfies

$$(\mathscr{L}_{y_0} - \lambda)\psi^\perp = w^2 - c_0(\Lambda_0 - \lambda)\Phi_0, \quad 0 < y < \infty; \qquad (\psi^\perp)'(0) = 0. \tag{4.58}$$

Multiplying by Φ_0 and integrating by parts we obtain $c_0 = (\Lambda_0 - \lambda)^{-1} \int_0^\infty w^2\Phi_0$ and therefore

$$h(\lambda) = \frac{\int_0^\infty w^2\Phi_0 \int_0^\infty w\Phi_0}{\Lambda_0 - \lambda} + \int_0^\infty w\psi^\perp - \frac{\int_0^\infty w^2}{\mu}. \tag{4.59}$$

On the other hand, if we multiply (4.58) by $\psi^\perp$ and integrate then we obtain

$$-\int_0^\infty |\psi^\perp|^2 \left(\lambda + \frac{-\int_0^\infty \psi^\perp \mathscr{L}_{y_0} \psi^\perp}{\int_0^\infty |\psi^\perp|^2} \right) = \int_0^\infty w^2\psi^\perp. \tag{4.60}$$

By Lemma 4.3.2 and the variational characterization of the second eigenvalue of $\mathscr{L}_{y_0}$ we obtain

$$0 < -\Lambda_1 = \inf_{\substack{\Phi \in H^2([0,\infty)) \\ \int_0^\infty \Phi\Phi_0 = 0}} \frac{\int_0^\infty |\Phi'|^2 + |\Phi|^2 - 2w|\Phi|^2}{|\Phi|^2} \leq \frac{-\int_0^\infty \psi^\perp \mathscr{L}_{y_0} \psi^\perp}{\int_0^\infty |\psi^\perp|^2}.$$

Substituting into (4.60) we calculate $||\psi^{\perp}||^2_{L^2([0,\infty))} \leq \lambda^{-1}||w^2||_{L^2([0,\infty))}||\psi^{\perp}||_{L^2([0,\infty))}$ so that $||\psi^{\perp}||_{L^2([0,\infty))}$ and hence also $\int_0^{\infty} w\psi^{\perp}$ are bounded as $\lambda \to \Lambda_0 > 0$. Therefore, from (4.59) we deduce $h(\lambda) \to +\infty$ as $\lambda \to \Lambda_0^-$. By a continuity argument we deduce the existence of a $\lambda_0 \in (0, \Lambda_1)$ such that $h(\lambda_0) = 0$. □

We conclude this section by establishing sufficient conditions for the stability of the NLEP (4.44) in both the small- and large-shift cases. Suppose that $\phi = \phi_R + i\phi_I$ and $\lambda = \lambda_R + i\lambda_I$ satisfies the NLEP. Separating real and imaginary parts in (4.44) then yields the system

$$\mathscr{L}_{y_0}\phi_R - \mu\frac{\int_0^{\infty} w\phi_R}{\int_0^{\infty} w^2}w^2 = \lambda_R\phi_R - \lambda_I\phi_I,$$
$$\mathscr{L}_{y_0}\phi_I - \mu\frac{\int_0^{\infty} w\phi_I}{\int_0^{\infty} w^2}w^2 = \lambda_R\phi_I + \lambda_I\phi_R.$$

Multiplying the first and second equations by ϕ_R and ϕ_I respectively, integrating, and then adding them together gives

$$\lambda_R\int_0^{\infty}|\phi|^2 = -L_1(\phi_R,\phi_R) - L_1(\phi_I,\phi_I), \tag{4.62}$$

where we define

$$L_1(\Phi,\Phi) \equiv \int_0^{\infty}|\Phi'|^2 + \Phi^2 - 2w\Phi^2 + \mu\frac{\int_0^{\infty} w\Phi\int_0^{\infty} w^2\Phi}{\int_0^{\infty} w^2}. \tag{4.63}$$

It is clear that if $L_1(\Phi,\Phi) > 0$ for all $\Phi \in H^2([0,\infty))$ then the NLEP (4.44) will be linearly stable. In the next theorem we determine sufficient conditions on $\mu \geq 0$ and $y_0 \geq 0$ for which the NLEP is linearly stable.

Theorem 4.3.3. *If* $0 \leq y_0 < y_{0c}$ *and* $\mu_1(y_0) < \mu < \mu_2(y_0)$, *or* $y_0 > y_{0c}$ *and* $0 \leq \mu <$

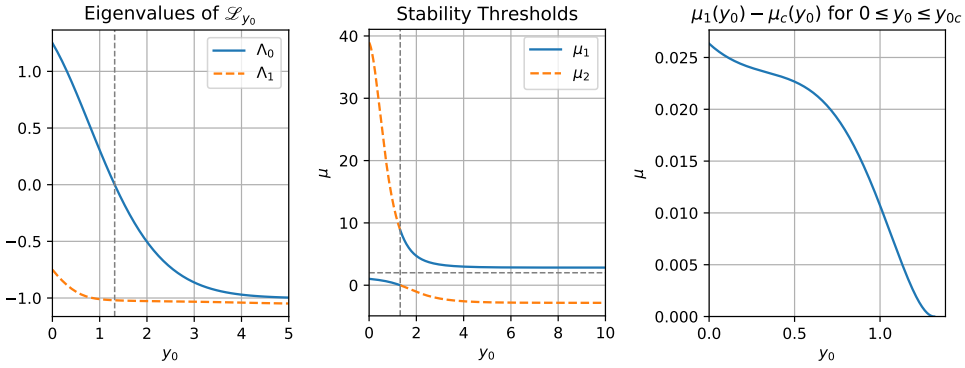

(a) **(b)** **(c)**

Figure 4.2: (a) Plot of the numerically computed principal and second eigenvalues of the operator $\mathscr{L}_{y_0}$. The dashed vertical line corresponds to $y_0 = y_{0c}$. (b) Plot of the stability thresholds μ_1 and μ_2 as functions of y_0. The dashed vertical and horizontal lines correspond to $y_0 = y_{0c}$ and $\mu = 2$ respectively. The NLEP (4.44) has been rigorously demonstrated to be stable in the region bounded by the curves μ_1 and μ_2. Note that μ_1 and μ_2 are interchanged as y_0 passes through y_{0c}. (c) Plot of $\mu_1(y_0) - \mu_c(y_0)$ for $0 \le y_0 < y_{0c}$. The NLEP is unstable for $\mu < \mu_c$ and stable for $\mu_1 < \mu < \mu_2$ when $0 \le y_0 < y_{0c}$. It is conjectured that the NLEP is stable for $\mu > \mu_c$.

$\mu_1(y_0)$ *where*

$$\mu_1(y_0) \equiv \frac{2\int_0^\infty w^2}{\int_0^\infty w\mathscr{L}_{y_0}^{-1}w^2 + \sqrt{\int_0^\infty w\mathscr{L}_{y_0}^{-1}w\int_0^\infty w^2\mathscr{L}_{y_0}^{-1}w^2}}, \tag{4.64}$$

$$\mu_2(y_0) \equiv \frac{2\int_0^\infty w^2}{\int_0^\infty w\mathscr{L}_{y_0}^{-1}w^2 - \sqrt{\int_0^\infty w\mathscr{L}_{y_0}^{-1}w\int_0^\infty w^2\mathscr{L}_{y_0}^{-1}w^2}}, \tag{4.65}$$

then $Re\lambda < 0$ *for all eigenvalues of the NLEP* (4.44).

Proof. We first prove the result for $0 \le y_0 < y_{0c}$. When $\mu = 2$ and $y_0 = 0$, Lemma 5.1 (2) in [107] implies that $L_1(\Phi,\Phi) > 0$ for all $\Phi \in H^2((\infty,\infty))$ and hence, by restricting to even functions, also for all $\Phi \in H^2([0,\infty))$. In particular, by the variational characterization of the principal eigenvalue, this implies that the principal

eigenvalue of the self-adjoint operator

$$L_1\Phi \equiv \mathscr{L}_{y_0}\Phi - \frac{\mu}{2}\frac{\int_0^\infty w\Phi}{\int_0^\infty w^2}w^2 - \frac{\mu}{2}\frac{\int_0^\infty w^2\Phi}{\int_0^\infty w^2}w, \tag{4.66}$$

must be negative. We then perturb $y_0 \geq 0$ and μ until L_1 has a zero eigenvalue and for which we may solve

$$\Phi = c_0\mathscr{L}_{y_0}^{-1}w^2 + c_1\mathscr{L}_{y_0}^{-1}w. \tag{4.67}$$

Substituting back into $L_1\Phi = 0$ we obtain the system

$$\begin{aligned}
&\left(\frac{\mu}{2}\frac{\int_0^\infty w\mathscr{L}_{y_0}^{-1}w^2}{\int_0^\infty w^2} - 1\right)c_0 + \frac{\mu}{2}\frac{\int_0^\infty w\mathscr{L}_{y_0}^{-1}w}{\int_0^\infty w^2}c_1 = 0,\\
&\frac{\mu}{2}\frac{\int_0^\infty w^2\mathscr{L}_{y_0}^{-1}w^2}{\int_0^\infty w^2}c_0 + \left(\frac{\mu}{2}\frac{\int_0^\infty w^2\mathscr{L}_{y_0}^{-1}w}{\int_0^\infty w^2} - 1\right)c_1 = 0.\text{`}
\end{aligned}$$

Since $\int_0^\infty w^2\mathscr{L}_{y_0}^{-1}w = \int_0^\infty w\mathscr{L}_{y_0}^{-1}w^2$ a nontrivial solutions exists if and only if

$$\left(\frac{\mu}{2}\frac{\int_0^\infty w\mathscr{L}_{y_0}^{-1}w^2}{\int_0^\infty w^2} - 1\right)^2 - \frac{\mu^2}{4}\frac{\int_0^\infty w\mathscr{L}_{y_0}^{-1}w\int_0^\infty w^2\mathscr{L}_{y_0}^{-1}w^2}{\left(\int_0^\infty w^2\right)^2} = 0, \tag{4.68}$$

where explicit formulae for each integral can be found in (4.47). When $\mu = 2$ and $y_0 = 0$ the left hand side of (4.68) equals $-9/10 < 0$ and therefore we have stability for $0 \leq y_0 < y_{0c}$ if

$$\left(\frac{\mu}{2}\frac{\int_0^\infty w\mathscr{L}_{y_0}^{-1}w^2}{\int_0^\infty w^2} - 1\right)^2 - \frac{\mu^2}{4}\frac{\int_0^\infty w\mathscr{L}_{y_0}^{-1}w\int_0^\infty w^2\mathscr{L}_{y_0}^{-1}w^2}{\left(\int_0^\infty w^2\right)^2} < 0, \tag{4.69}$$

which is easily seen to be equivalent to $\mu_1 < \mu < \mu_2$.

The thresholds μ_1 and μ_2 are singular as $y_0 \to y_{0c}$ and therefore the continuity argument from above does not extend to $y_0 > y_{0c}$. However $L_1(\Phi,\Phi) > 0$ by Lemma 4.3.1 if $y_0 > y_{0c}$ and $\mu = 0$. Therefore we proceed with the same continuity argument as above, but starting from $\mu = 0$. This yields the same criteria, but since $\mathscr{L}_{y_0}^{-1}w^2 < 0$ by Lemma 4.3.3 the sufficient condition is now $\mu_2(y_0) < 0 \leq \mu < \mu_1(y_0)$.

□

Both of the stability thresholds μ_1 and μ_2 defined in (4.64) as well as the instability threshold μ_c defined in (4.56) are easily computed using (4.47). In Figures 4.2b and 4.2c we plot the stability thresholds and the difference $\mu_1 - \mu_c$ respectively. In particular, from the plot in 4.2c we see that $\mu_1 > \mu_c$. We conjecture, that as in the $y_0 = 0$ case, the NLEP is stable for all $\mu > \mu_c$. In Appendix D.2 we provide numerical support for this conjecture by plotting $\mathrm{Re}\lambda_0$ versus μ and y_0 in Figure D.2a. In addition, we plot $\Lambda_0 - \mathrm{Re}(\lambda_0)$ in Figure D.2b which suggest that $\mathrm{Re}(\lambda_0) \leq \Lambda_0$.

4.4 Examples

In this section we illustrate the effect of introducing a nonzero boundary flux for the activator by considering three distinct examples. Specifically, we first study the stability of a single boundary spike concentrated at $x = 0$ when $A \geq 0$ and $B = 0$. Using a winding number argument we illustrate that the stability of the single spike is improved by increasing the boundary flux A. Moreover, we illustrate that if A exceed a threshold, then the spike is stable independently of the parameters $\tau \geq 0$ and $D > 0$. We then consider the structure and stability of a two-boundary-spike pattern when the boundary fluxes are equal, $A = B \geq 0$. One of the key findings is that if $A > 0$ then the range of $D > 0$ values for which asymmetric patterns exist is extended. Additionally, by assuming that $\tau \ll 1$ we study the stability of both symmetric and asymmetric two-boundary-spike patterns to competition (zero eigenvalue crossing) instabilities. We demonstrate that one branch of asymmetric patterns is always stable. Similarly, in our final example we consider a two-boundary-spike pattern with a one-sided boundary flux $A \geq 0$ and $B = 0$. We demonstrate the existence of several asymmetric patterns, with a certain branch of these patterns always being stable. For each example we include full numerical simulations of the GM system (4.2) using the finite element software FlexPDE [1].

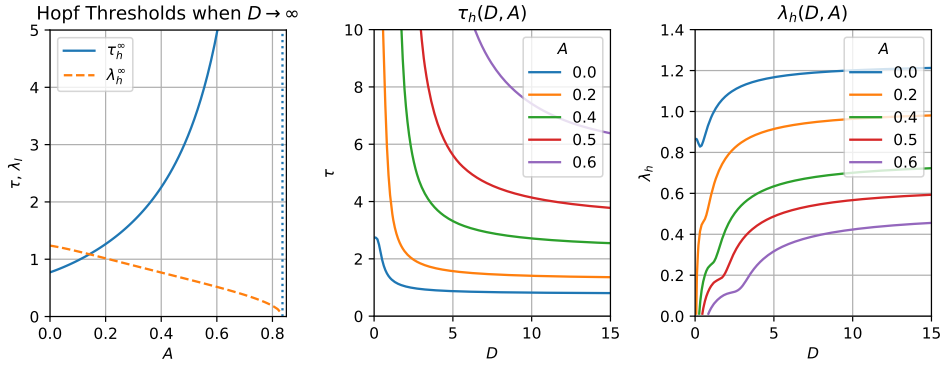

(a) **(b)** **(c)**

Figure 4.3: Hopf bifurcation threshold and accompanying eigenvalue for a single boundary-spike solution with one-sided boundary flux $A \geq 0$ in (a) the shadow limit, $D \to \infty$, and (b and c) for finite $D > 0$ at select values of $0 \leq A < q_{0c}$. In (a) the dashed vertical line corresponds to the threshold $A = q_{0c}$ beyond which no Hopf bifurcations occur.

4.4.1 Example 1: One Boundary Spike at $x = 0$ with $A > 0$ and $B = 0$

In this example we assume that $B = 0$ and investigate the role of a non-negative flux, $A \geq 0$, on the stability of a single boundary spike concentrated at $x = 0$. We denote the left boundary shift parameter by $y_0 = y_L$ so that using (4.15b) and (4.23) we reduce (4.30) to (4.44) where

$$\mu(\lambda) = 2\frac{\omega_0 \tanh \omega_0}{\omega_\lambda \tanh \omega_\lambda}. \tag{4.70}$$

Recalling that $\omega_\lambda = \sqrt{(1+\tau\lambda)/D}$ we first observe that $0 < \mu(\lambda) \leq 2$ for all real-valued $\lambda \geq 0$ so that by Theorem 4.3.3 and Figure 4.2b the NLEP has no non-negative real eigenvalues. Next we determine whether the NLEP has any unstable complex-valued eigenvalues by using a winding number argument. Assuming that λ is not in the spectrum of $\mathscr{L}_{y_0}$ we let $\phi = (\mathscr{L}_{y_0} - \lambda)^{-1} w_c (y + y_0)^2$ so that as in §4.2.1 the NLEP reduces to the algebraic equation

$$\mathscr{A}_{y_0}(\lambda) \equiv \frac{1}{\mu(\lambda)} - \mathscr{F}_{y_0}(\lambda) = 0, \tag{4.71}$$

where $\mathscr{F}_{y_0}(\lambda)$ is defined in (4.36). In Figure D.1 we plot $\mathscr{F}_{y_0}(0)$ versus y_0, as well as the real and imaginary parts of $\mathscr{F}_{y_0}(i\lambda_I)$ versus λ_I for select values of y_0. We integrate in λ over a closed counter-clockwise contour consisting of the imaginary axis and a large semicircle in the right half-plane. Since

$$\mathscr{F}_{y_0}(\lambda) = \mathscr{O}(|\lambda|^{-1}) \quad \text{and} \quad \mu(\lambda) = \mathscr{O}(\lambda^{-1/2}) \quad \text{as } |\lambda| \to \infty, \text{Re}\lambda > 0, \quad (4.72)$$

the change in argument of $\mathscr{A}_{y_0}(\lambda)$ over the large semicircle is $\frac{\pi}{2}$. Moreover, in $\text{Re}\lambda > 0$, $\mu(\lambda) \neq 0$ whereas by Lemmas 4.3.1 and 4.3.2 we deduce that $\mathscr{F}_{y_0}(\lambda)$ has one (resp. zero) pole(s) if $y_0 < y_{0c}$ (resp. $y_0 \geq y_{0c}$). Letting Z denote the number of zeros of $\mathscr{A}_{y_0}(\lambda)$ in $\text{Re}\lambda > 0$ it follows from the argument principle that

$$Z = \frac{1}{\pi}\Delta\arg\mathscr{A}_{y_0}(i\lambda_I)\big|_{+\infty}^{0} + \begin{cases} 5/4, & y_0 < y_{0c}, \\ 1/4, & y_0 \geq y_{0c}, \end{cases} \quad (4.73)$$

where the first term on the right hand side denotes the change in argument of $\mathscr{A}_{y_0}(\lambda)$ as λ follows the imaginary axis from $\lambda = +i\infty$ to $\lambda = 0$. Note in addition that we have used $\mathscr{A}_{y_0}(\bar{\lambda}) = \overline{\mathscr{A}_{y_0}(\lambda)}$ to obtain $\Delta\arg\mathscr{A}_{y_0}(i\lambda_I)\big|_{+\infty}^{-\infty} = 2\Delta\arg\mathscr{A}_{y_0}(i\lambda_I)\big|_{+\infty}^{0}$. From (4.72) we immediately deduce that $\arg\mathscr{A}_{y_0}(+i\infty) = \pi/4$. On the other hand, using (4.47), we evaluate $\mathscr{A}_{y_0}(0) = \frac{1}{2} - \mathscr{F}_{y_0}(0) \lessgtr 0$ for $y_0 \lessgtr y_{0c}$ (see also Figure D.1a). We will consider the cases $y_0 \geq y_{0c}$ and $y_0 < y_{0c}$ separately below.

If $y_0 \geq y_{0c}$ then $\text{Re}\mathscr{F}_{y_0}(i\lambda_I) < 0$ for all $\lambda_I > 0$ (see Figure D.1b) so $\mathscr{A}_{y_0}(i\lambda_I)$ never crosses the imaginary axis for all $\lambda_I > 0$. As a result $\Delta\arg\mathscr{A}_{y_0}(i\lambda_I)|_{\infty}^{0} = -\pi/4$ and therefore $Z = 0$ if $y_0 > y_{0c}$. Since y_0 is monotone decreasing in D when $A > 0$, we deduce that there is a threshold $D_c(A)$ such that the single spike pattern is stable for all $\tau \geq 0$ if $D \geq D_c(A)$. Substituting $y_0 = y_{0c}$ and using (4.23) and (4.31) yields the threshold parameter

$$q_{0c} = \frac{4+3\sqrt{3}}{11} \approx 0.83601, \quad (4.74)$$

with which $D_c(A)$ is found by solving the transcendental equation

$$\tanh D_c^{-1/2} = q_{0c}^{-1} A D_c^{-1/2}. \quad (4.75)$$

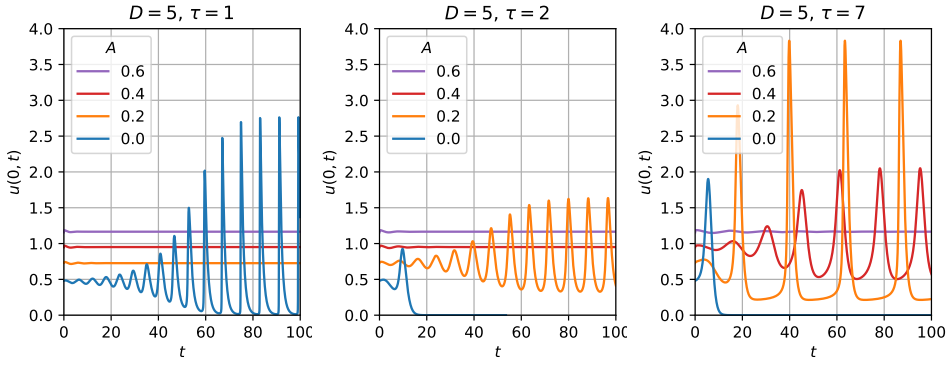

(a) **(b)** **(c)**

Figure 4.4: Plots of $u(0,t)$ for a one boundary-spike solution with one-sided boundary flux $x = 0$ (i.e. $A \geq 0$ and $B = 0$) with $\varepsilon = 0.005$. Note that increasing the boundary flux A stabilizes the single boundary-spike solution for fixed values of D and τ.

It is easy to see that if $A \geq q_{0c}$ then $D_c = \infty$ is the only positive solution. On the other hand, if $0 < A < q_{0c}$ then this equation has a unique positive solution that is monotone increasing in A and satisfies $D_c \to 0^+$ as $A \to 0^+$ and $D_c \to \infty$ as $A \to q_{0c}^-$. In summary we deduce that the single spike pattern is stable for all $D > 0$ and $\tau \geq 0$ if $A \geq q_{0c}$, or for all $\tau \geq 0$ if $0 < D \leq D_c(A)$ and $0 < A < q_{0c}$. To determine the stability when $0 \leq A < q_{0c}$ and $D > D_c(A)$ we must consider the case $0 \leq y < y_{0c}$.

Next we assume that $0 \leq y_0 < y_{0c}$. We begin by considering the *shadow limit*, defined by $D \to \infty$, for which $\mu(i\lambda_I) \sim 2(1 + i\tau\lambda_I)^{-1}$ and hence also

$$\mathrm{Re}\mathscr{A}_{y_0}(i\lambda_I) \sim \frac{1}{2} - \mathrm{Re}\mathscr{F}_{y_0}(i\lambda_I), \qquad \mathrm{Im}\mathscr{A}_{y_0}(i\lambda_I) \sim \frac{\tau\lambda_I}{2} - \mathrm{Im}\mathscr{F}_{y_0}(i\lambda_I), \qquad D \to \infty.$$

Since $\mathscr{F}_{y_0}(0) > 1/2$ and $\mathrm{Re}\mathscr{F}_{y_0}(i\lambda_I) \to 0$ as $\lambda_I \to \infty$ (see Appendix D.1 and accompanying Figure D.1) we deduce that there exists a solution to $\mathrm{Re}\mathscr{A}_{y_0}(i\lambda_I) = 0$. Moreover, in Figure D.1b we observe that when $\mathrm{Re}F_{y_0}(i\lambda_I)$ is positive it is also monotone decreasing in λ_I. Therefore there exists a unique eigenvalue λ_h^∞ and time constant $\tau_h^\infty = 2\mathrm{Im}\mathscr{F}_{y_0}(i\lambda_I)/\lambda_h^\infty$ such that $\mathscr{A}_{y_0}(i\lambda_h^\infty) = 0$. Furthermore, since

$\mathrm{Im}\mathscr{A}_{y_0}(i\lambda_h^\infty) \lessgtr 0$ if $\tau \lessgtr \tau_h^\infty$ we get

$$\Delta \arg \mathscr{A}_{y_0}(i\lambda_I)|_\infty^0 = \begin{cases} -5\pi/4, & \tau < \tau_h^\infty, \\ 3\pi/4, & \tau > \tau_h^\infty. \end{cases}$$

The single boundary spike solution therefore undergoes a Hopf bifurcation as τ exceeds the Hopf bifurcation threshold τ_h^∞. Using the shadow limit threshold as an initial guess, we numerically continue the Hopf bifurcation threshold for finite values of $D > 0$ to obtain the Hopf bifurcation threshold $\tau_h(D,A)$ and accompanying critical eigenvalue $\lambda = i\lambda_h(D,A)$ shown in Figure 4.3b and 4.3c respectively.

The above analysis, together with the plots of $\tau_h^\infty(A)$ and $\tau_h(D,A)$ in Figures 4.3a and 4.3b respectively, indicate that the single boundary spike solution is stabilized as $A > 0$ is increased. Additionally, if A exceeds the threshold q_{0c} given in (4.74), then the single boundary spike is stable independently of the parameters $\tau \geq 0$ and $D > 0$. We illustrate the onset of oscillatory instabilities when $D = 5$ for $\tau = 1, 2, 7$ and $A = 0, 0.2, 0.4, 0.6$ by numerically computing the solution of (4.2) using FlexPDE 6 [1] and plotting $u(0,t)$ in Figure 4.4. In particular we observe that the single spike pattern is stabilized by increasing the boundary flux A. Additionally, our numerical simulations show good qualitative agreement with the Hopf bifurcation thresholds plotted in Figure 4.3b.

4.4.2 Example 2: Two Boundary Spikes with $A = B \geq 0$

In this example we investigate the role of equal boundary fluxes on the structure and stability of a two-boundary-spike pattern. Using the method of §4.1.1, a two-boundary-spike pattern is found by letting $l_L = l$ and $l_R = 1 - l$ and solving (4.24b), which is explicitly given by

$$\frac{\tanh \omega_0 l}{\eta(y_L) \cosh \omega_0 l} - \frac{\tanh \omega_0 (1-l)}{\eta(y_R) \cosh \omega_0 (1-l)} = 0, \tag{4.76}$$

for $0 < l < 1$ where η is given by (4.8) and y_L and y_R are given by (4.23). Note that by (4.21) the algebraic equation (4.76) is equivalent to

$$\frac{\xi_L}{\xi_R} = \frac{\cosh \omega_0 l}{\cosh \omega_0 (1-l)}, \tag{4.77}$$

from which we deduce that $l \lesseqgtr 1/2$ implies $\xi_L \lesseqgtr \xi_R$. In particular $l = 1/2$ solves (4.76) for all $A \geq 0$ and since in this case $\xi_L = \xi_R$ we refer to it as the symmetric solution. For the remainder of this example we will construct asymmetric two-spike patterns for which $0 < l < 1/2$ (by symmetry the case $l > 1/2$ is identical) and then study the linear stability of both the symmetric and asymmetric patterns.

Before constructing asymmetric two-boundary-spike patterns for $A \geq 0$ we first recall the following existence result from [104] in the case $A = 0$. Specifically, we let $z = \omega_0 l_L$ and $\tilde{z} = \omega_0 l_R$ so that when $A = 0$ the system (4.24) (and hence also (4.76)) is equivalent to

$$z + \tilde{z} = \omega_0, \qquad b(z) = b(\tilde{z}), \qquad b(z) \equiv \frac{\tanh z}{\cosh z}. \tag{4.78}$$

It follows from Result 2.3 (with $k_1 = k_2 = 1$, $\mu = 1$, and $r = 1$) of [104] that (4.76) has a unique solution $0 < l < 1$ if and only if

$$0 < D < D_{c1} \equiv [2\log(1+\sqrt{2})]^{-2} \approx 0.322. \tag{4.79}$$

When $A > 0$ we solve (4.76) numerically and find that for given values of D and $A > 0$ it accepts zero, one, or two solutions in the range $0 < l < 1/2$. Rather than solving (4.76) numerically for l as a function of A and D, we found it more convenient to solve for $A = A(D,l)$. The results of our numerical calculations are shown in Figure 4.5a where we plot $A = A(D,l)$ as well as the curve $l = l_{\max}(D)$ along which $A(D,l)$ is maximized for a fixed value of D, and the curve $l = l_{c1}(D)$ along which $A(D, l_{c1}(D)) = A(D, 1/2)$ for $D_{c1} < D < D_{c2} \approx 0.660$ and $l_{c1}(D) = 0$ for $0 < D < D_{c1}$. Consequently, (4.76) has zero solutions in $0 < l < 1/2$ if $A > A_{\max}(D) \equiv A(D, l_{\max}(D))$, whereas it has two solutions, one with $l < l_{c1}(D)$ and the other with $l > l_{c1}(D)$, if $A_{\max}(D) > A > A_{c1}(D) \equiv A(D, l_{c1}(D))$ for $0 < D < D_{c2}$. For all other values of $D > 0$ and $A > 0$ equation (4.76) has exactly one solution

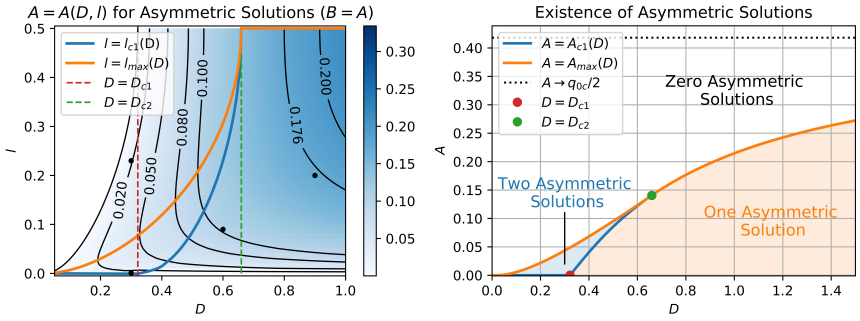

(a) **(b)**

Figure 4.5: Plots of (a) $A = A(D,l)$ and (b) thresholds for the existence of zero, one, or two asymmetric two-boundary-spike solutions in the presence of equal boundary fluxes considered in Example 2.

in $0 < l < 1/2$. We summarize these existence thresholds in Figure 4.5b where we note in particular that $A > 0$ greatly extends the range of D values over which asymmetric two-boundary-spike patterns exist.

We now consider the linear stability of both the symmetric and asymmetric two-boundary-spike patterns constructed above. Note that since $x_L = 0$ and $x_R = 1$ are fixed there are no slow drift dynamics and the linear stability of the two-spike patterns is completely determined by the $\mathcal{O}(1)$ eigenvalues calculated from the NLEP (4.30). Moreover, we assume that $\tau = 0$ so that no oscillatory instabilities arise (see Example 1) and for which we can exclusively focus on zero eigenvalue crossing, or competition, instabilities. We proceed by first using the rigorous results of §4.3 to determine the linear stability of the symmetric two-spike patterns constructed above, and we will then use the algebraic reduction outlined in §4.2.1 to determine the stability of the remaining asymmetric two-spike patterns.

Using (4.15b) and (4.21), the NLEP (4.30) for the symmetric two-spike pattern constructed above is explicitly given by

$$\mathcal{L}_{y_0}\boldsymbol{\phi} - 2\omega_0 \tanh\left(\tfrac{\omega_0}{2}\right)\frac{\int_0^\infty w_c(y+y_0)\mathcal{G}_{\omega_0}\boldsymbol{\phi}\,dy}{\int_0^\infty w_c(y+y_0)^2 dy} w_c(y+y_0)^2 = \lambda\boldsymbol{\phi}, \quad 0 < y < \infty,$$
$$\boldsymbol{\phi}'(0) = 0,$$

where

$$\boldsymbol{\phi} = \begin{pmatrix} \phi_1 \\ \phi_2 \end{pmatrix}, \quad \mathcal{G}_{\omega_0} = \frac{1}{\omega_0 \sinh \omega_0} \begin{pmatrix} \cosh \omega_0 & 1 \\ 1 & \cosh \omega_0 \end{pmatrix}. \tag{4.80}$$

The Green's matrix is symmetric and of constant row sum and therefore has eigenvectors $(1, \pm 1)^T$. Substituting $\boldsymbol{\phi} = (\phi, \pm\phi)^T$ into the NLEP therefore yields two uncoupled scalar NLEPs of the form (4.44) with $\mu = \mu_\pm$ where

$$\mu_+ \equiv 2, \qquad \mu_- \equiv 2\tanh^2\left(\tfrac{\omega_0}{2}\right). \tag{4.81}$$

From Theorem 4.3.3 and accompanying Figure 4.2b we immediately deduce that the $\boldsymbol{\phi}_+$ mode is linearly stable. On the other hand, by Theorem 4.3.2 the $\boldsymbol{\phi}_-$ mode is unstable if $\mu_- < \mu_c$, where μ_c is defined by (4.56). We therefore calculate the competition instability threshold by numerically solving $2\tanh^2 \frac{\omega_0}{2} = \mu_c(y_0)$ where $y_0 = y_L = y_R$ is the shift parameter given by (4.23) with $l = 1/2$. Our numerical calculations indicate that the resulting instability threshold coincides with the values

$$A(D, 1/2) = \begin{cases} A_{c1}(D), & D_{c1} < D < D_{c2}, \\ A_{\max}(D), & D > D_{c2}, \end{cases} \tag{4.82}$$

calculated above. In particular, the symmetric two-spike pattern is linearly unstable for all $A < A(D, 1/2)$ when $D > D_{c1}$. Furthermore, since $\mu_c(y_0) < 0$ for $y_0 > y_{0c}$ we determine from (4.24b) that there are no competition instabilities if

$$A > \omega_0^{-1} q_{0c} \tanh(\omega_0/2), \tag{4.83}$$

where q_{0c} is the threshold identified in Example 1 and is explicitly given by (4.74). Note that, analogous to the results in Example 1, in the shadow limit ($D \to \infty$) there are no competition instabilities for the symmetric pattern if $A > q_{0c}/2$ (see Figure 4.5b). As in §4.3 we conjecture and have numerically supported that the symmetric two-spike pattern is linearly stable for $\mu > \mu_c$ and hence for all $A > A(D, 1/2)$. Finally, as is clear from Figure 4.5b, increasing $A > 0$ expands the range of D values over which the symmetric two-boundary-spike pattern is linearly stable.

For the asymmetric two-boundary-spike solutions constructed above the NLEP (4.30) is not diagonalizable since $w_c(y + y_L) \not\equiv w_c(y + y_R)$. We therefore can't

directly apply the rigorous results of §4.3. To determine the competition instability we instead use the algebraic reduction outlined in §4.2.1 and seek parameter values such that

$$\det(\mathbb{I}_2 - 2\omega_0^2 \mathcal{G}_{\omega_0} \mathcal{D}_0) = 0 \tag{4.84}$$

where $\mathbb{I}_2$ is the 2×2 identity matrix, $\mathcal{G}_{\omega_0}$ is the 2×2 Green's matrix given in (4.80), and

$$\mathcal{D}_0 = \frac{1}{\omega_0}\begin{pmatrix} \tanh\omega_0 l \mathcal{F}_{y_L}(0) & 0 \\ 0 & \tanh\omega_0(1-l)\mathcal{F}_{y_R}(0) \end{pmatrix}. \tag{4.85}$$

Substituting the function $A = A(D,l)$ calculated above into (4.84) we can solve for l as a function of D using standard numerical methods (specifically we used a combination of Scipy's brentq and fsolve function in Python 3.6.8). Our computations indicate that the resulting competition instability threshold coincides with the curves $l_{\max}(D)$ for $D > 0$ and $l = 1/2$ for $D_{c1} < D < D_{c2}$. In fact, we can show that this is the case explicitly by first differentiating the quasi-equilibrium equation $\boldsymbol{B} = \mathbf{0}$ with respect to l to get

$$\nabla_{\boldsymbol{\xi}}\boldsymbol{B}\left(\frac{\partial \boldsymbol{\xi}}{\partial l} + \frac{\partial \boldsymbol{\xi}}{\partial A}\frac{\partial A}{\partial l}\right) + \frac{\partial \boldsymbol{B}}{\partial A}\frac{\partial A}{\partial l} = 0. \tag{4.86}$$

Along the curve $l_{\max}(D)$ for $D > 0$ the function $A(D,l)$ is maximized whereas, by symmetry, it is minimized along $l = 1/2$ for $D_{c1} < D < D_{c2}$. In both cases $\partial A/\partial l = 0$ along these curves so that (4.86) becomes $\nabla_{\boldsymbol{\xi}}\boldsymbol{B}\partial\boldsymbol{\xi}/\partial l = \mathbf{0}$. Differentiating (4.77) with respect to l implies that $\partial\boldsymbol{\xi}/\partial l \neq \mathbf{0}$ and therefore we deduce that $\nabla_{\boldsymbol{\xi}}\boldsymbol{B}$ is singular along $l = l_{\max}(D)$ and $l = 1/2$. By the discussion of §4.2.1 it follows that along these curves the algebraic equation (4.84) is satisfied and they therefore correspond to competition instability thresholds. Note in particular that the competition instability threshold along $l = 1/2$ corresponds to the competition instability threshold for the symmetric two-spike pattern. As an immediate consequence it follows that $A_{\max} \to q_{0c}/2$ as $D \to \infty$.

To determine in which of the regions demarcated by the competition instability thresholds the asymmetric two-boundary-spike patterns are linearly stable and unstable, we calculate the stability of the asymmetric patterns along the $A = 0$ curve. As outlined in Appendix D.3, the asymmetric two-boundary spike patterns when

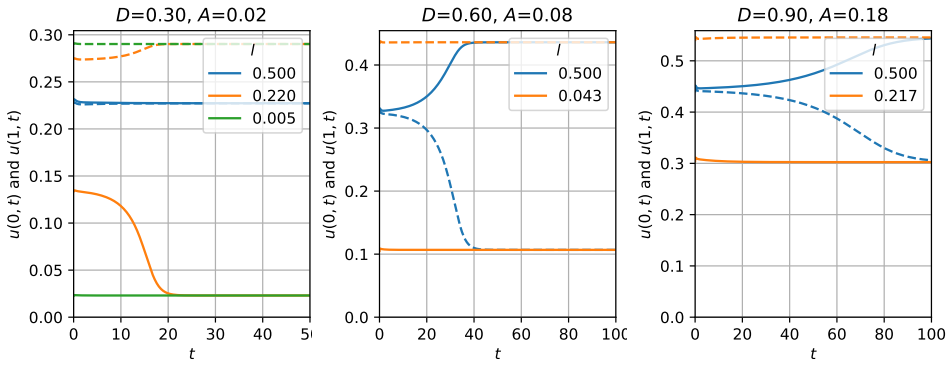

Figure 4.6: Results of numerical simulation of (4.2) using FlexPDE 6 [1] with $\varepsilon = 0.005$, $\tau = 0.1$, and select values of D and A. In each plot the solid (resp. dashed) lines correspond tot he spike height at $x = 0$ (resp. $x = 1$). Both the asymptotically constructed symmetric ($l = 1/2$) and asymmetric $0 < l < 1/2$ solutions were used as initial conditions. See Figure 4.5a for position of parameter values relative to existence and stability thresholds.

$A = 0$ are always linearly unstable, and therefore we deduce that the asymmetric two-boundary-spike patterns in the region bounded by $l = 1/2$ and $l = l_{\max}(D)$ for $0 < D < D_{c2}$ are linearly unstable. On the other hand, numerically calculating the dominant eigenvalue of the NLEP (4.30) (see Appendix D.2 for description of numerical method) for select parameter values with $l < l_{\max}(D)$ we find that such asymmetric two-boundary spike patterns are linearly stable. In particular, we note that in the region where there are two asymmetric patterns (i.e. for $A_{c1}(D) < A < A_{\max}(D)$), the pattern with $l > l_{\max}(D)$ is linearly unstable while that with $l < l_{\max}(D)$ is linearly stable. Moreover, the single asymmetric two-boundary-spike pattern that exists for $A < A_{\max}(D)$ and $D > D_{c1}$ is linearly stable.

Finally we support our asymptotic predictions by numerically solving (4.2) using FlexPDE 6 [1] with parameters $\varepsilon = 0.005$ and $\tau = 0.1$ for select values of D and A. Letting u_e and v_e be the any of the symmetric or asymmetric two-boundary-

spike patterns constructed above, we use

$$\begin{aligned} u(x,0) &= (1+0.025\cos(20x))u_e(x), \\ v(x,0) &= (1+0.025\cos(20x))v_e(x), \end{aligned} \tag{4.87}$$

as initial conditions and simulate (4.2) sufficiently long that the solution settles. The results of our numerical simulations indicate good agreement with the asymptotically calculated linear stability thresholds for both symmetric and asymmetric two-boundary-spike patterns. We include in Figure 4.6 the results of our numerical calculations for select values of D, l, and A indicated by black markers in Figure 4.5a. In particular, in Figure 4.6a we plot the spike heights at $x_L = 0$ (solid) and $x_R = 1$ (dashed) for $D = 0.30$ and $A = 0.02$ with initial conditions given by the two-boundary-spike pattern constructed with $l = 0.5$ which is symmetric and predicted to be stable, as well as $l = 0.220$ and $l = 0.005$ which are both asymmetric but predicted to be linearly unstable and stable respectively. It is clear from the resulting plots that our asymptotic predictions hold in this numerical simulations. Additionally, we observe that the unstable asymmetric two-spike pattern tends toward the linearly stable pattern. We observed this trend for all our numerical simulations in which $l_{\max} < l < 1/2$ though predicting this long-time behaviour analytically is beyond the scope of this chapter. Similarly we numerically simulate the dynamics of a symmetric and asymmetric two-boundary-spike pattern when $D = 0.60$ and $A = 0.08$ (Figure 4.6b) and when $D = 0.90$ and $A = 0.18$ (Figure 4.6c). In both cases the symmetric and asymmetric patterns are predicted to be linearly unstable and stable respectively, which agrees with the outcomes observed in our numerical simulations.

4.4.3 Example 3: Two Boundary Spikes with a One Sided Flux ($A \geq 0$ and $B = 0$)

In this example we investigate the effect of a one sided boundary flux ($A \geq 0$ and $B = 0$) on the structure and linear stability of a two-boundary-spike pattern. Letting

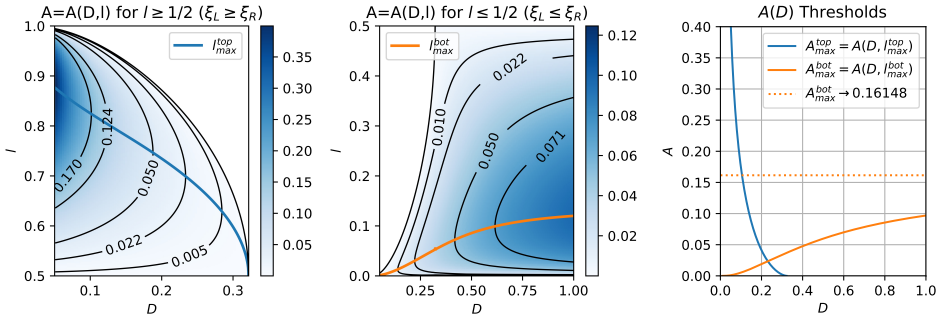

Figure 4.7: Plot of $A = A(D,l)$ for Example 3 obtained by solving (4.88) when (a) $0 < l < 1/2$ and (b) $1/2 < l < 1$. The solid curves $l = l^{\text{top}}_{\text{max}}(D)$ and $l^{\text{bot}}_{\text{max}}(D)$ indicate the values of l at which $A(D,l)$ is maximized as well as the competition instability threshold in the $l > 1/2$ and $l < 1/2$ regions respectively. The corresponding existence thresholds of A versus D are plotted against D in (c).

$l_L = l$ and $l_R = 1-l$, the gluing equation (4.24b) of §4.1.1 becomes

$$\frac{\tanh \omega_0 l}{\eta(y_L)\cosh \omega_0 l} - \frac{\tanh \omega_0 (1-l)}{3\cosh \omega_0 (1-l)} = 0, \tag{4.88}$$

which is to be solved for $0 < l < 1$ where $\eta(y_L)$ and $y_L = y_0(\frac{\omega_0 A}{\tanh \omega_0})$ are given by (4.8) and (4.23) respectively. Note that since $\eta(y_L) < 3$ for all $A > 0$ it follows that $l = 1/2$ is a solution of (4.88) if and only if $A = 0$. In particular $\xi_L \neq \xi_R$ for all $A > 0$ and by the asymmetry of the boundary fluxes the cases $l \lessgtr 1/2$, for which $\xi_L \lessgtr \xi_R$, must be considered separately. On the other hand, when $A = 0$ we apply the same results from [104] summarized in Example 2.

Proceeding as in Example 2 we numerically solve (4.88) for $A = A(D,l) > 0$ when $l < 1/2$ and $l > 1/2$. In addition we compute $l = l^{\text{bot}}_{\text{max}}(D)$ and $l = l^{\text{top}}_{\text{max}}(D)$ defined as the curves along which $A(D,l)$ is maximized in the regions $l < 1/2$ and $l > 1/2$ respectively. In Figures 4.7a and 4.7b we plot $A = A(D,l)$ together with $l^{\text{top}}_{\text{max}}$ and $l^{\text{bot}}_{\text{max}}$ in the regions $1/2 < l < 1$ and $0 < l < 1/2$ respectively. In each region the maximum value of A given by $A^{\text{top}}_{\text{max}}(D) \equiv A(D, l^{\text{top}}_{\text{max}}(D))$ and $A^{\text{bot}}_{\text{max}}(D) \equiv A(D, l^{\text{bot}}_{\text{max}}(D)$ and plotted in Figure 4.7c gives an existence threshold for the bound-

ary flux beyond which no two-boundary-spike with $\xi_L > \xi_R$ and $\xi_L < \xi_R$ exists respectively. In particular, a two-boundary-spike pattern with $\xi_L > \xi_R$ only exists if $A < A^{\text{top}}_{\text{max}}(D)$ and D satisfies (4.79), whereas a two-boundary-spike pattern with $\xi_L < \xi_R$ exists for all $D > 0$ provided that $A < A^{\text{bot}}_{\text{max}}(D)$. Furthermore, by letting $D \to \infty$ in (4.88) we numerically calculate $l^{\text{bot}}_{\text{max}} \to 0.13772$ and $A^{\text{bot}}_{\text{max}}(D) \to 0.16148$ as $D \to \infty$ and this horizontal asymptote is indicated in Figure 4.7c.

Next we consider the linear stability of the two-boundary-spike patterns constructed above when $\tau = 0$. In particular we restrict our attention to competition instabilities which arise through a zero eigenvalue crossing. Proceeding as in Example 2 we first deduce that both $l = l^{\text{top}}_{\text{max}}(D)$ and $l = l^{\text{bot}}_{\text{max}}(D)$ yield a competition instability threshold. Furthermore, we verify that these are the only competition instability thresholds by numerically computing the algebraic equation (4.38) where $\mathscr{G}_{\omega_0}$ and $\mathscr{D}_0$ are given by (4.80) and (4.85) respectively. Since all asymmetric two-boundary-spike patterns when $A = 0$ are unstable with respect to competition instabilities (see Example 2 and Appendix D.3), we immediately deduce that all asymmetric two-boundary spike patterns with $\xi_L > \xi_R$ and $\xi_L < \xi_R$ are linearly unstable when $l > l^{\text{top}}_{\text{max}}(D)$ and $l > l^{\text{bot}}_{\text{max}}(D)$ respectively, and are linearly stable otherwise. In particular, the non-zero boundary flux $A > 0$ both extends the range of parameter values for which asymmetric patterns exists and are linearly stable.

To support our asymptotic predictions we numerically calculate solutions to (4.2) when $\varepsilon = 0.005$ and $\tau = 0.1$ for select values of D and $A < \max\{A^{\text{top}}_{\text{max}}(D), A^{\text{bot}}_{\text{max}}(D)\}$. For each pair (D,A) we let $0 < l < 1$ be any of the values for which $A(D,l) = A$ and then let $(u_e(x), v_e(x))$ be the corresponding equilibrium pattern constructed above. Using (4.87) as an initial condition we then solve (4.2) numerically using FlexPDE 6 [1]. The results of our numerical simulations are illustrated in Figures 4.8 and 4.9 when l is chosen to be in $1/2 < l < 1$ and $0 < l < 1/2$ respectively. Specifically, in Figure 4.8a (resp. 4.9a) we indicate with a blue or orange marker respectively whether the solution settles (after simulating for $0 < t < 200$) to the asymptotically predicted stable equilibrium with $l < l^{\text{top}}_{\text{max}}(D)$ (resp. $l < l^{\text{bot}}_{\text{max}}(D)$) or to a one-boundary spike solution in which the spike at $x = 1$ collapses respectively. In Figures 4.8b and 4.8c (resp. 4.9b and 4.9c) we show the spike heights as func-

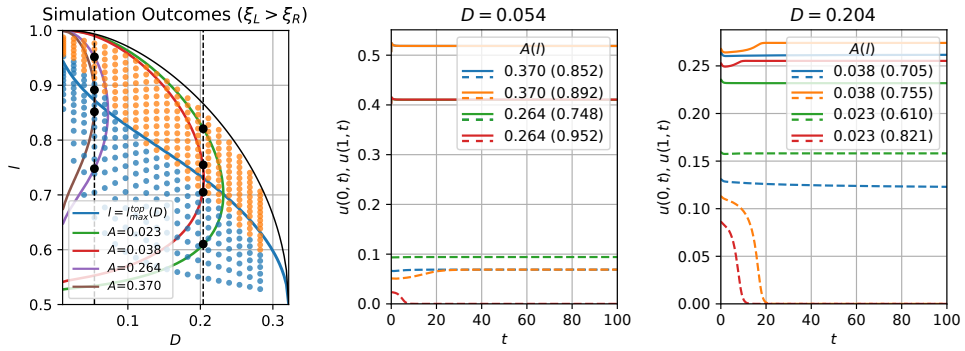

(a) **(b)** **(c)**

Figure 4.8: Numerical simulations for Example 2 when $\xi_L > \xi_R$. (a) Outcome of numerical simulation of (4.2) starting from the asymmetric two-boundary-spike pattern constructed using the indicated values of D, l, and A. Blue and orange markers indicate the two-boundary spike pattern settled to the stable two-spike pattern (i.e. with $l < l^{\text{top}}_{\text{max}}(D)$) or collapsed to a single spike pattern respectively. Black dots indicate values of D, A, and l for which the spike heights are plotted over time in Figures (b) and (c). The left and right dashed vertical lines indicate $D = 0.054$ and $D = 0.204$ respectively. In (b) and (c) we plot spike heights at $x = 0$ (solid) and $x = 1$ (dashed) at given values of D and A and with initial condition specified by indicated value of l.

tions of time at select values of A and D using an unstable and stable value of l in $1/2 < l < 1$ (resp. $0 < l < 1/2$) to construct the initial condition (see captions for more details). The results of these numerical simulations are in good agreement with our asymptotic predictions. However, we comment that in the numerical outcomes shown in Figure 4.8a some of the asymmetric patterns which are predicted to be stable collapse. We expect that this error due to a combination of small errors from the asymptotic theory, numerical errors from the time integration of (4.2), as well as the close proximity to the fold point $A = A^{\text{top}}_{\text{max}}(D)$ for these values of l.

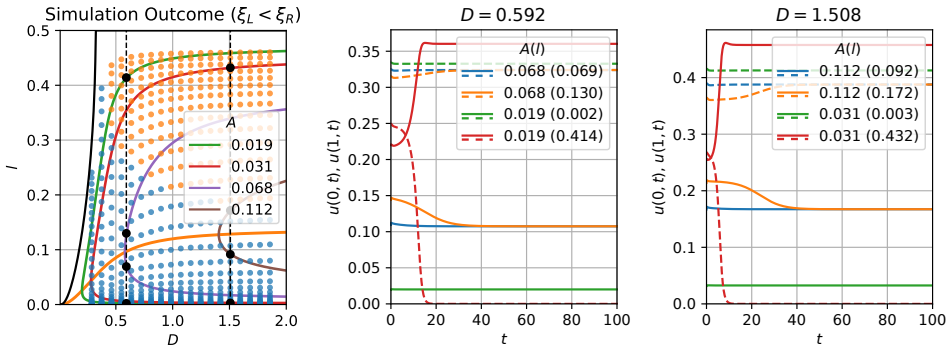

(a) **(b)** **(c)**

Figure 4.9: Numerical simulations for Example 2 when $\xi_L < \xi_R$. (a) Outcome of numerical simulation of (4.2) starting from the asymmetric two-boundary-spike pattern constructed using the indicated values of D, l, and A. Blue and orange markers indicate the two-boundary spike pattern settled to the stable two-spike pattern (i.e. with $l < l_{\max}^{\text{bot}}(D)$) or collapsed to a single spike pattern respectively. Black dots indicate values of D, A, and l for which the spike heights are plotted over time in Figures (b) and (c). The left and right dashed vertical lines indicate $D = 0.592$ and $D = 1.508$ respectively. In (b) and (c) we plot spike heights at $x = 0$ (solid) and $x = 1$ (dashed) at given values of D and A and with initial condition specified by indicated value of l.

4.4.4 Example 4: One Boundary and Interior Spike with One-Sided Feed ($A \geq 0$, $B = 0$)

In this final example we extend the results of Example 3 to the case where there is one boundary spike at $x_L = 0$ and one interior spike at $0 < x_1 < 1$. The asymptotic construction of the resulting two spike patterns, as well as the analysis of their linear stability on an $\mathcal{O}(1)$ timescale proceeds as in the previous example. However, since x_1 is an equilibrium of the slow dynamics equation (4.18), we must now also determine the stability of the two-spike pattern on an $\mathcal{O}(\varepsilon^{-2})$ timescale by analyzing the linearization of (4.18). We remark that an alternative approach to determine the stability of multi-spike patterns on an $\mathcal{O}(\varepsilon^{-2})$ timescale is to calculate the $\mathcal{O}(\varepsilon^2)$ eigenvalues of the linearization (4.25) though we do not pursue this approach further (see for example [41] for the analysis of $\mathcal{O}(\varepsilon^2)$ eigenvalues).

Using the method of §4.1.1, with $l_L = l$ and $l_1 = (1-l)/2$ equation (4.24b) becomes

$$\frac{\tanh \omega_0 l}{\eta(y_L)\cosh \omega_0 l} - \frac{\tanh \omega_0 \frac{1-l}{2}}{3\cosh \omega_0 \frac{1-l}{2}} = 0, \tag{4.89}$$

which is to be solved for $0 < l < 1$ where $\eta(y_L)$ and $y_L = y_0(\omega_0 A/\tanh \omega_0 l)$ are given by (4.8) and (4.23) respectively. As in the previous examples we observe that $\xi_L = \xi_1$ if and only if $l = 1/3$ which is a solution to (4.89) if and only if $A = 0$. In particular, together with the discussion in Example 3 we deduce that there are no symmetric two-spike patterns when there is a one-sided positive boundary flux $A > 0$. As in the previous examples we also note that $\xi_L \lessgtr \xi_1$ if $l \lessgtr 1/3$. Next we note that since $l_1 = (1-l)/2$ the relevant asymmetric equilibrium results for $A = 0$ from [104] summarized in Example 2 must be modified. In particular, letting $z = \omega_0 l_L$ and $\tilde{z} = \omega_0 l_1$, equations (4.24a) and (4.24b) when $A = 0$ become

$$z + 2\tilde{z} = \omega_0, \qquad b(z) = b(\tilde{z}), \tag{4.90}$$

where $b(z)$ is given in (4.78). Then Result 2.3 of [104] (with $k_1 = 1$ and $k_2 = 2$) implies that a unique asymmetric two-spike solution with $z \leq \tilde{z}$ exists if and only if

$$D < D_m \equiv [3\log(1+\sqrt{2})]^{-2} \approx 0.143, \tag{4.91}$$

whereas Result 2.4 of [104] (with $k_1 = 2$ and $k_2 = 1$) implies that there are either exactly one or two asymmetric two-spike solutions with $z > \tilde{z}$ if and only if

$$D < D_m \text{ or } D_m < D < D_{m1} \equiv [2\sinh^{-1}(1/2) + \sinh^{-1}(2)]^{-2} \approx 0.17274, \tag{4.92}$$

respectively. Proceeding as in Examples 2 and 3 we can then numerically calculate $A = A(D,l)$ from (4.89) in the appropriate regions with $0 < l < 1/3$ and $1/3 < l < 1$. In Figures 4.10a and 4.10b we plot $A = A(D,l)$ together with the curves $l = l^{\text{top}}_{\text{max}}(D)$ and $l = l^{\text{bot}}_{\text{max}}(D)$ along which $A(D,l)$ is maximized. The resulting existence thresholds $A^{\text{top}}_{\text{max}}(D) \equiv A(D, l^{\text{top}}_{\text{max}}(D))$ and $A^{\text{bot}}_{\text{max}}(D) \equiv A(D, l^{\text{bot}}_{\text{max}}(D))$ are plotted in Figure 4.10c. In particular a two spike pattern with a two-spike pattern consisting of one boundary and one interior spike with $\xi_L > \xi_1$ only exists for $D < D_{m1}$ when $A < A^{\text{top}}_{\text{max}}(D)$, whereas such a two-spike pattern with $\xi_L < \xi_1$ exists

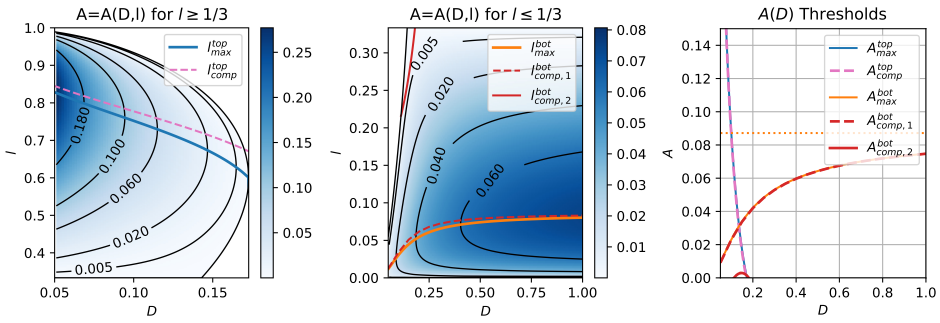

Figure 4.10: Plot of $A = A(D,l)$ obtained by solving (4.88) when (a) $0 < l < 1/3$ and (b) $1/3 < l < 1$. The curves $l = l^{\text{top}}_{\text{max}}(D)$ and $l^{\text{bot}}_{\text{max}}(D)$ indicate the values of l at which $A(D,l)$ is maximized while the curves $l^{\text{top}}_{\text{comp}}(D)$, $l^{\text{bot}}_{\text{comp},1}(D)$, and $l^{\text{bot}}_{\text{comp},2}(D)$ indicate the competition instability thresholds. The corresponding existence thresholds, $A^{\text{top}}_{\text{max}}(D)$ and $A^{\text{bot}}_{\text{max}}(D)$ are plotted in (c).

for all $D > 0$ provided that $A < A^{\text{bot}}_{\text{max}}(D)$. Finally, by taking the limit $D \to \infty$ in (4.89) we numerically obtain the limiting values $l^{\text{bot}}_{\text{max}}(D) \to 0.0857$ and $A^{\text{bot}}_{\text{max}}(D) \to 0.087174$ as $D \to \infty$.

Next we consider the linear stability of the two-spike patterns constructed above on an $\mathcal{O}(1)$ timescale. As in Examples 2 and 3 we focus exclusively on competition instabilities by assuming that $\tau = 0$ and seeking a zero eigenvalue crossing of the NLEP (4.30). In contrast to Examples 2 and 3 above the relevant competition instability threshold does not necessarily coincide with the curves $l = l^{\text{top}}_{\text{max}}(D)$ and $l = l^{\text{bot}}_{\text{max}}$. Indeed, fixing $D > 0$ and differentiating the quasi-equilibrium equation $\boldsymbol{B} = 0$ with respect to l gives

$$\nabla_{\boldsymbol{\xi}} \boldsymbol{B}\left(\frac{\partial \boldsymbol{\xi}}{\partial l} + \frac{\partial \boldsymbol{\xi}}{\partial A}\frac{\partial A}{\partial l}\right) + \frac{\partial \boldsymbol{B}}{\partial A}\frac{\partial A}{\partial l} + \frac{\partial \boldsymbol{B}}{\partial x_1}\frac{dx_1}{dl} = 0, \tag{4.93}$$

which along either $l = l^{\text{top}}_{\text{max}}(D)$ or $l = l^{\text{bot}}_{\text{max}}(D)$ reduces to

$$\nabla_{\boldsymbol{\xi}} \boldsymbol{B}\frac{\partial \boldsymbol{\xi}}{\partial l} = -\frac{1}{2}\frac{\partial \boldsymbol{B}}{\partial x_1}.$$

Since $\partial \boldsymbol{B}/\partial x_1 \neq \mathbf{0}$ it follows that $\nabla_{\boldsymbol{\xi}} \boldsymbol{B}$ is not necessarily singular along $l^{\text{top}}_{\text{max}}(D)$ or $l^{\text{bot}}_{\text{max}}(D)$ and in particular these curves need not coincide with the competition instability thresholds. Note however that $\partial \boldsymbol{B}/\partial x_1 \to 0$ as $D \to \infty$ and therefore the competition instability threshold will coincide with $l^{\text{bot}}_{\text{max}}(D)$ but only in the limit $D \to \infty$. Thus, to calculate the appropriate competition instability thresholds we use the algebraic reduction of §4.2.1 and numerically solve (4.38) when $\lambda = 0$ and where the matrices $\mathscr{G}_{\omega_0}$ and $\mathscr{D}_{\omega_0}$ are respectively given by

$$\mathscr{G}_{\omega_0} = \frac{1}{\omega_0 \sinh \omega_0} \begin{pmatrix} \cosh \omega_0 & \cosh \omega_0 (1-x_1) \\ \cosh \omega_0 (1-x_1) & \cosh \omega_0 x_1 \cosh \omega_0 (1-x_1) \end{pmatrix}, \tag{4.94a}$$

and

$$\mathscr{D}_0 = \frac{1}{\omega_0} \begin{pmatrix} \tanh(\omega_0 l) \mathscr{F}_{y_L}(0) & 0 \\ 0 & 2\tanh\left(\omega_0 \frac{1-l}{2}\right) \mathscr{F}_0(0) \end{pmatrix}. \tag{4.94b}$$

The resulting competition instability threshold $l^{\text{top}}_{\text{comp}}(D)$ when $\xi_L > \xi_1$ as well as $l^{\text{bot}}_{\text{comp},i}(D)$ $(i = 1,2)$ when $\xi_L < \xi_1$ are indicated in Figures 4.10a and 4.10b respectively. Additionally, in Figure 4.10c we have plotted $A^{\text{top}}_{\text{comp}}(D) \equiv A(D, l^{\text{top}}_{\text{comp}}(D))$ and $A^{\text{top}}_{\text{comp},i}(D) \equiv A(D, l^{\text{top}}_{\text{comp},i}(D))$ $(i = 1,2)$. Finally, the stability result along the $A = 0$ curve calculated in Appendix D.3 implies that the two-spike pattern with $\xi_L > \xi_1$ is linearly unstable on an $\mathscr{O}(1)$ timescale when $l > l^{\text{top}}_{\text{comp}}(D)$, and similarly when $\xi_L < \xi_1$ the two-spike pattern is linearly unstable in the region bounded by the curves $l = l^{\text{bot}}_{\text{comp},1}(D)$ and $l = l^{\text{bot}}_{\text{comp},2}(D)$.

Next we consider the linear stability of the two-spike patterns on an $\mathscr{O}(\varepsilon^{-2})$ timescale. We explicitly calculate the right-hand-side of (4.18) by first calculating

$$\left\langle \partial_x G_{\omega_0}(x, x_1) \right\rangle_{x_1} = \frac{\sinh \omega_0 (2x_1 - 1)}{\sinh \omega_0}, \quad \partial_x G_{\omega_0}(x,0)\big|_{x_1} = -\frac{\sinh \omega_0 (1-x_1)}{\sinh \omega_0},$$

and rearranging the quasi-equilibrium equation (4.17a) as

$$\frac{\omega_0^2 \xi_L^2 \eta(y_L)}{\xi_1} = \frac{1 - 6\omega_0^2 \xi_1 G_{\omega_0}(x_1, x_1)}{G_{\omega_0}(x_1, 0)}.$$

so that (4.18) becomes

$$\frac{1}{\varepsilon^2}\frac{dx_1}{dt} = -6\omega_0^2 f(x_1), \qquad f(x_1,\xi_1) = \xi_1 - \frac{\tanh\omega_0(1-x_1)}{3\omega_0}, \tag{4.95}$$

where ξ_1 together with ξ_L and y_L are functions of x_1 found by solving (4.17a) and (4.5). Note that the asymmetric two-spike equilibrium solutions constructed above using the method of §4.1.1 immediately satisfy $f(x_1) = 0$. The linear stability of these asymmetric two-spike patterns on an $\mathcal{O}(\varepsilon^{-2})$ timescale is determined by the sign of $f'(x_1)$; it is stable if $f'(x_1) > 0$ and unstable otherwise. We explicitly calculate

$$\frac{df}{dx_1} = \frac{\partial\xi_1}{\partial x_1} + \frac{1}{3}\operatorname{sech}^2\omega_0(1-x_1), \tag{4.96}$$

where $\partial\xi_1/\partial x_1$ is calculated by first differentiating the quasi-equilibrium equation $\boldsymbol{B} = 0$ with respect to x_1

$$\nabla_{\boldsymbol{\xi}}\boldsymbol{B}\frac{\partial\boldsymbol{\xi}}{\partial x_1} = -\frac{\partial\boldsymbol{B}}{\partial x_1}, \tag{4.97}$$

and then solving for $\partial\boldsymbol{\xi}/\partial x_1$ which we can do since we are assuming the two-spike pattern is stable on an $\mathcal{O}(1)$ timescale and the matrix $\nabla_{\boldsymbol{\xi}}\boldsymbol{B}$ is therefore invertible. Numerically evaluating $f'(x_1)$ we find that the drift instability thresholds for which $f'(x_1) = 0$ coincide with the curves $l_{\max}^{\text{top}}(D)$ and $l_{\max}^{\text{bot}}(D)$. In fact, we can show that this is the case analytically by first evaluating (4.93) along either $l_{\max}^{\text{top}}(D)$ or $l_{\max}^{\text{bot}}(D)$ to get

$$\nabla_{\boldsymbol{\xi}}\boldsymbol{B}\frac{\partial\boldsymbol{\xi}}{\partial l} = -\frac{1}{2}\frac{\partial\boldsymbol{B}}{\partial x_1}. \tag{4.98}$$

Since the competition instability thresholds do not coincide with the curves $l_{\max}^{\text{top}}(D)$ and $l_{\max}^{\text{bot}}(D)$, the matrix $\nabla_{\boldsymbol{\xi}}\boldsymbol{B}$ is invertible along these curves and comparing (4.97) with (4.98) we obtain

$$\frac{\partial\xi_1}{\partial x_1} = 2\frac{\partial\xi}{\partial l} = -\frac{1}{3}\operatorname{sech}^2\omega_0\frac{1-l}{2} = -\frac{1}{3}\operatorname{sech}^2\omega_0(1-x_1). \tag{4.99}$$

In particular $f'(x_1) = 0$ along the curves $l = l_{\max}^{\text{top}}(D)$ and $l_{\max}^{\text{bot}}(D)$. Numerically evaluating $f'(x_1)$ at select values of l above and below these thresholds we determine that the two-spike patterns constructed above with $\xi_L > \xi_1$ or $\xi_L < \xi_1$ are

linearly stable on an $\mathcal{O}(\varepsilon^{-2})$ timescale if and only if $l < l_{\max}^{\text{top}}(D)$ or $l < l_{\max}^{\text{bot}}(D)$ respectively.

As in the previous examples we performed full numerical simulations of (4.2) with FlexPDE 6 [1] to support our asymptotic predictions. Our numerical simulations were found to strongly agree with the predicted stability thresholds. In particular, we observed the following dynamics. For values of l that are stable with respect to both competition and drift instabilities, that is when $l < l_{\max}^{\text{top}}$ (resp. $l < l_{\max}^{\text{bot}}$) for $l > 1/3$ (resp. $l < 1/2$) the two-spike pattern was observed to be stable. In the remaining regions (both stable and unstable with respect to competition instabilities) we observed that the interior spike either collapses and the boundary spike collapses to the one-boundary-spike solution, or else the interior spike changes height to the height of the stable pattern and then slowly drifts toward the location of the interior spike in the stable two-spike solution. As in Example 3 we noticed sensitivity to the competition instability threshold which we believe to be primarily due to the flatness of A in this region

4.5 Discussion

We have extended the asymptotic theory developed for the singularly perturbed one-dimensional GM model to include the possibility of inhomogeneous Neumann boundary conditions for the activator. Additionally, we have rigorously established partial stability and instability results for a class of *shifted* NLEPs. While the shifted NLEPs we considered are closely related to those in [60] we highlight that the difference in sign of the shift parameter leads substantial differences in the stability properties of the NLEP. Finally we considered four examples to illustrate the asymptotic and rigorous theory as well as to explore the behaviour of the GM system with non-zero flux boundary conditions. For a one-boundary spike solution we found that the non-zero Neumann boundary condition improves the stability with respect to oscillatory instabilities arising through a Hopf bifurcation. Moreover, by considering a two-boundary-spike pattern with equal inhomogeneous boundary fluxes we illustrated that the non-zero boundary flux improves the stability of symmetric two-spike patterns and also extends the region of $D > 0$ values for which asymmetric patterns exist provided that $A = B > 0$ is not larger than a computed

threshold. Similar results were obtained when considering a one-sided boundary flux for which we considered patterns where both spikes concentrate on the boundary and where one concentrates on the boundary and the other in the interior. In each of our two-spike pattern examples we observed that there are two asymmetric patterns, where one is always linearly unstable and the other is always linearly stable. In a sense, the stable asymmetric pattern can be considered a *boundary layer* solution that is a direct consequence of the inhomogeneous Neumann boundary condition. In particular its existence is mandated by the inhomogeneous boundary condition which makes a direct comparison with asymmetric spike patterns in the absence of boundary flux conditions difficult. However, our results illustrate that inhomogeneities at the boundaries predispose the GM to forming patterns concentrating at the boundaries in both symmetric and asymmetric configurations. We believe the distinction between interior and boundary-layer like localized pattern will play a key role in understanding more complicated mathematical models such as those incorporating bulk-surface coupling (see Figure 3 in [58] for an example of a boundary-layer type pattern in a bulk-surface model).

There are several key open problems and directions for future research. First, our rigorous results for the shifted NLEP do not provide tight bounds for regions of stability and instability. Specifically, in the small shift-case we have determined that the NLEP is unstable if $\mu < \mu_c(y_0)$, and stable if $\mu_1(y_0) < \mu < \mu_2(y_0)$ where we have highlighted that $\mu_c(y_0) < \mu_1(y_0)$. As indicated in §4.3 we conjecture that in fact the shifted NLEP is stable for all $\mu > \mu_c$ and in Appendix D.2 we provide numerical support for this conjecture. Proving this conjecture is our first open problem. In addition, to calculate the stability of asymmetric patterns for which the shift parameters are different we could not directly use the rigorous results established in §4.3 since the NLEP (4.30) could not be diagonalized. The development of a rigorous stability theory for NLEP systems of this form is an additional direction for future research.

One of the key insights from our investigation of a two-boundary spike configuration is that the presence of equal or one sided boundary fluxes for the activator greatly extends the range of diffusivity values for which asymmetric patterns exist and are linearly stable. This expanded region of existence and stability parallels that found when spatially inhomogeneous precursors are included in the GM

model. However, it can be argued that introducing inhomogeneous flux conditions provides a simpler alternative for generating asymmetric patterns. This warrants further research into the role of inhomogeneous boundary conditions for the activator in both activator-inhibitor and activator-substrate models in one-, two-, and three-dimensional domains.

Chapter 5

Localized Patterns in the 3D GM Model

In this chapter we analyze the existence, linear stability, and slow dynamics of localized N-spot patterns for the singularly perturbed dimensionless Gierer-Meinhardt (GM) reaction-diffusion (RD) model (cf. [23])

$$\begin{gathered} v_t = \varepsilon^2 \Delta v - v + \frac{v^2}{u}, \quad \tau u_t = D\Delta u - u + \varepsilon^{-2} v^2, \quad x \in \Omega; \\ \partial_n v = \partial_n u = 0, \quad x \in \partial\Omega, \end{gathered} \tag{5.1}$$

where $\Omega \subset \mathbb{R}^3$ is a bounded domain, $\varepsilon \ll 1$, and v and u denote the activator and inhibitor fields, respectively. While the shadow limit in which $D \to \infty$ has been extensively studied (cf. [108], [112], [105]), there have relatively few studies of localized RD patterns in 3-D with a finite inhibitor diffusivity D (see [11], [22], [53], [98] and some references therein). For 3-D spot patterns, the existence, stability, and slow-dynamics of multi-spot quasi-equilibrium solutions for the singularly perturbed Schnakenberg RD model was analyzed using asymptotic methods in [98]. Although our current study is heavily influenced by [98], our results for the GM model offer some new insights into the structure of localized spot solutions for RD systems in three-dimensions. In particular, one of our key findings is the existence of two regimes, the $D = \mathcal{O}(1)$ and $D = \mathcal{O}(\varepsilon^{-1})$ regimes, for which localized patterns can be constructed in the GM-model, in contrast to the single

$D = \mathcal{O}(\varepsilon^{-1})$ regime where such patterns occur for the Schnakenberg model. Furthermore, our analysis traces this distinction back to the specific far-field behaviour of the appropriate core problem, characterizing the local behaviour of a spot, for the GM-model. By numerically solving the core problem, we formulate a conjecture regarding the far-field limiting behaviour of the solution to the core problem. With the numerically established properties of the core problem, strong localized perturbation theory (cf. [103]) is used to construct N-spot quasi-equilibrium solutions to (5.1), to study their linear stability, and to determine their slow-dynamics. We now give a more detailed outline of this chapter.

In the limit $\varepsilon \to 0$, in §5.1 we construct N-spot quasi-equilibrium solutions to (5.1). To do so, we first formulate an appropriate core problem for a localized spot, from which we numerically compute certain key properties of its far field behaviour. Using the method of matched asymptotic expansions, we then establish two distinguished regimes for the inhibitor diffusivity D, the $D = \mathcal{O}(1)$ and $D = \mathcal{O}(\varepsilon^{-1})$ regimes, for which N-spot quasi-equilibrium solutions exist. By formulating and analyzing a nonlinear algebraic system, we then demonstrate that only symmetric patterns can be constructed in the $D = \mathcal{O}(1)$ regime, whereas both symmetric and asymmetric patterns can be constructed in the $D = \mathcal{O}(\varepsilon^{-1})$ regime.

In §5.2 we study the linear stability on an $\mathcal{O}(1)$ time scale of the N-spot quasi-equilibrium solutions constructed in §5.1. More specifically, we use the method of matched asymptotic expansions to reduce a linearized eigenvalue problem to a single globally coupled eigenvalue problem. We determine that the symmetric quasi-equilibrium patterns analyzed in §5.1 are always linearly stable in the $D = \mathcal{O}(1)$ regime but that they may undergo both oscillatory and competition instabilities in the $D = \mathcal{O}(\varepsilon^{-1})$ regime. Furthermore, we demonstrate that the asymmetric patterns studied in §5.1 for the $D = \mathcal{O}(\varepsilon^{-1})$ regime are always unstable. Our stability predictions are then illustrated in §5.4 where the finite element software FlexPDE6 [1] is used to perform full numerical simulations of (5.1) for select parameter values.

In §5.5 we consider the weak interaction limit, defined by $D = \mathcal{O}(\varepsilon^2)$, where localized spots interact weakly through exponentially small terms. In this regime, (5.1) can be reduced to a modified core problem from which we numerically calculate quasi-equilibrium solutions and determine their linear stability properties.

Unlike in the $D = \mathcal{O}(1)$ and $D = \mathcal{O}(\varepsilon^{-1})$ regimes, we establish that spot solutions in the $D = \mathcal{O}(\varepsilon^2)$ regime can undergo *peanut-splitting* instabilities. By performing full numerical simulations using FlexPDE6 [1], we demonstrate that these instabilities lead to a cascade of spot self-replication events in 3-D. Although spike self-replication for the 1-D GM model have been studied previously in the weak interaction regime $D = \mathcal{O}(\varepsilon^2)$ (cf. [19], [46], [72]), spot self-replication for the 3-D GM model has not previously been reported.

In §5.6 we briefly consider the generalized GM system characterized by different exponent sets for the nonlinear kinetics. We numerically verify that the far-field behaviour associated with the new core problem for the generalized GM system has the same qualitative properties as for the classical GM model (5.1) This directly implies that many of the qualitative results derived for (5.1) in §5.1–5.3 still hold in this more general setting. Finally, in §5.7 we summarize our findings and highlight some key open problems for future research.

5.1 Asymptotic Construction of an N-Spot Quasi-Equilibrium Solution

In this section we asymptotically construct an N-spot quasi-equilibrium solution where the activator is concentrated at N specified points that are well-separated in the sense that $x_1, \ldots, x_N \in \Omega$, $|x_i - x_j| = \mathcal{O}(1)$ for $i \neq j$, and $\text{dist}(x_i, \partial\Omega) = \mathcal{O}(1)$ for $i = 1, \ldots, N$. In particular, we first outline the relevant core problem and describe some of its properties using asymptotic and numerical calculations. Then, the method of matched asymptotic expansions is used to derive a nonlinear algebraic system whose solution determines the quasi-equilibrium pattern. A key feature of this nonlinear system, in contrast to that derived in [98] for the 3-D Schnakenberg model, is is that it supports different solutions depending on whether $D = \mathcal{O}(1)$ or $D = \mathcal{O}(\varepsilon^{-1})$. More specifically, we will show that the $D = \mathcal{O}(1)$ regime admits only N-spot quasi-equilibrium solutions that are symmetric to leading order, whereas the $D = \mathcal{O}(\varepsilon^{-1})$ regime admits both symmetric and asymmetric N-spot quasi-equilibrium solutions.

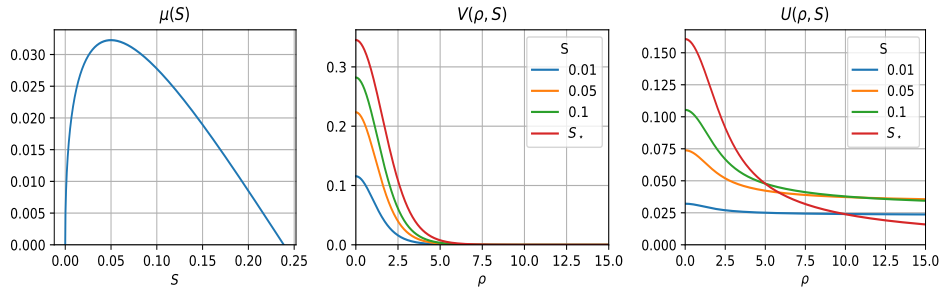

Figure 5.1: Plots of numerical solutions of the core problem (5.2): (a) $\mu(S)$ versus S, as well as the (b) activator V and (c) inhibitor U, at a few select values of S. The value $S = S_\star \approx 0.23865$ corresponds to the root of $\mu(S) = 0$.

5.1.1 The Core Problem

A key step in the application of the method of matched asymptotic expansions to construct localized spot patterns is the study of the core problem

$$\Delta_\rho V - V + U^{-1}V^2 = 0\,, \qquad \Delta_\rho U = -V^2\,, \qquad \rho > 0\,, \tag{5.2a}$$

$$\partial_\rho V(0) = \partial_\rho U(0) = 0\,; \quad V \longrightarrow 0 \quad \text{and} \quad U \sim \mu(S) + S/\rho\,, \quad \rho \to \infty\,, \tag{5.2b}$$

where $\Delta_\rho \equiv \rho^{-2}\partial_\rho\left[\rho^2\partial_\rho\right]$. For a given value of the spot strength $S > 0$, the system (5.2) is solved for $V = V(\rho;S)$, $U = U(\rho;S)$, and $\mu = \mu(S)$. Specifying the value of $S > 0$ is equivalent to specifying the $L^2(\mathbb{R}^3)$ norm of V, as can be verified by applying the divergence theorem to the second equation in (5.2a) over an infinitely large ball, which yields the identity $S = \int_0^\infty \rho^2\left[V(\rho)\right]^2 d\rho$. Specifying the value of the spot strength therefore yields a unique solution to (5.2) and in the context of constructing multi-spot solutions by using the method of matched asymptotic expansions the spot strengths completely determine the local profile of each spot.

When $S \ll 1$ we deduce from this identity that $V = \mathcal{O}(\sqrt{S})$. By applying the divergence theorem to the first equation in (5.2a) we get $U = \mathcal{O}(\sqrt{S})$, while from (5.2b) we conclude that $\mu = \mathcal{O}(\sqrt{S})$. It is then straightforward to compute the

leading order asymptotics

$$V(\rho;S) \sim \sqrt{\frac{S}{b}} w_c(\rho)\,, \quad U(\rho;S) \sim \sqrt{\frac{S}{b}}\,, \quad \mu(S) \sim \sqrt{\frac{S}{b}}\,, \quad \text{for} \quad S \ll 1\,, \quad (5.3)$$

where $b \equiv \int_0^\infty \rho^2 \left[w_c(\rho)\right]^2 d\rho \approx 10.423$ and $w_c > 0$ is the unique nontrivial solution to

$$\Delta_\rho w_c - w_c + w_c^2 = 0\,, \quad \rho > 0\,; \qquad \partial_\rho w_c(0) = 0\,, \qquad w_c \to 0 \quad \text{as } \rho \to \infty\,. \quad (5.4)$$

We remark that (5.4) has been well studied, with existence being proved using a constrained variational method, while its symmetry and decay properties are established by a maximum principle (see for example Appendix 13.2 of [112]). The limit case $S \ll 1$ is related to the *shadow limit* obtained by taking $D \to \infty$, for which numerous rigorous and asymptotic results have previously been obtained (cf. [108], [112], [105]).

Although the existence of solutions to (5.2) have not been rigorously established, we can use the small S asymptotics given in (5.3) as an initial guess to numerically path-follow solutions to (5.2) as S is increased. The results of our numerical computations are shown in Figure 5.1 where we have plotted $\mu(S)$, $V(\rho;S)$, and $U(\rho;S)$ for select values of $S > 0$. A key feature of the plot of $\mu(S)$ is that it has a zero crossing at $S = 0$ and $S = S_\star \approx 0.23865$, while it attains a unique maximum on the interval $0 \le S \le S_\star$ at $S = S_{\text{crit}} \approx 0.04993$. Moreover, our numerical calculations indicate that $\mu''(S) < 0$ on $0 < S \le S_\star$. The majority of our subsequent analysis hinges on these numerically determined properties of $\mu(S)$. We leave the task of rigorously proving the existence of solutions to (5.2) and establishing the numerically verified properties of $\mu(S)$ as an open problem, which we summarize in the following conjecture:

Conjecture 5.1.1. *There exists a unique value of $S_\star > 0$ such that* (5.2) *admits a ground state solution with the properties that $V, U > 0$ in $\rho > 0$ and for which $\mu(S_\star) = 0$. Moreover, $\mu(S)$ satisfies $\mu(S) > 0$ and $\mu''(S) < 0$ for all $0 < S < S_\star$.*

5.1.2 Derivation of the Nonlinear Algebraic System (NAS)

We now proceed with the method of matched asymptotic expansions to construct quasi-equilibrium solutions to (5.1). First we seek an inner solution by introducing local coordinates $y = \varepsilon^{-1}(x - x_i)$ near the i^{th} spot and letting $v \sim DV_i(y)$ and $u \sim DU_i(y)$ so that the local steady-state problem for (5.1) becomes

$$\Delta_y V_i - V_i + U_i^{-1} V_i^2 = 0\,, \qquad \Delta_y U_i - \varepsilon^2 D^{-1} U_i + V_i^2 = 0\,, \qquad y \in \mathbb{R}^3\,. \tag{5.5}$$

In terms of the solution to the core problem (5.2) we determine that

$$V_i \sim V(\rho, S_{i\varepsilon}) + \mathcal{O}(D^{-1}\varepsilon^2)\,, \quad U_i \sim U(\rho, S_{i\varepsilon}) + \mathcal{O}(D^{-1}\varepsilon^2), \tag{5.6}$$

where $\rho \equiv |y| = \varepsilon^{-1}|x - x_i|$ and $S_{i\varepsilon}$ is an unknown constant that depends weakly on ε. We remark that the derivation of the next order term requires that $x_1, \ldots, x_N$ be allowed to vary on a slow time scale. This higher order analysis is done in §5.3 where we derive a system of ODE's for the spot locations.

To determine $S_{1\varepsilon}, \ldots, S_{N\varepsilon}$ we now derive a nonlinear algebraic system (NAS) by matching inner and outer solutions for the inhibitor field. As a first step, we calculate in the sense of distributions that $\varepsilon^{-3} v^2 \longrightarrow 4\pi D^2 \sum_{j=1}^N S_{j\varepsilon}\, \delta(x - x_j) + \mathcal{O}(\varepsilon^2)$ as $\varepsilon \to 0^+$. Therefore, in the outer region the inhibitor satisfies

$$\begin{aligned} \Delta u - D^{-1} u &= -4\pi\varepsilon D \sum_{j=1}^N S_{j\varepsilon}\, \delta(x - x_j) + \mathcal{O}(\varepsilon^3)\,, \quad x \in \Omega\,; \\ \partial_n u &= 0\,, \quad x \in \partial\Omega\,. \end{aligned} \tag{5.7}$$

To solve (5.7), we let $G(x;\xi)$ denote the reduced-wave Green's function satisfying

$$\begin{aligned} &\Delta G - D^{-1} G = -\delta(x - \xi)\,, \quad x \in \Omega\,; \qquad \partial_n G = 0\,, \quad x \in \partial\Omega\,, \\ &G(x;\xi) \sim \frac{1}{4\pi|x - \xi|} + R(\xi) + \nabla_x R(x;\xi)\cdot(x - \xi)\,, \qquad \text{as} \quad x \to \xi\,, \end{aligned} \tag{5.8}$$

where $R(\xi)$ is the regular part of G. The solution to (5.7) can be written as

$$u \sim 4\pi\varepsilon D \sum_{j=1}^N S_{j\varepsilon} G(x; x_j) + \mathcal{O}(\varepsilon^3)\,. \tag{5.9}$$

Before we begin matching inner and outer expansions to determine $S_{1\varepsilon},\ldots,S_{N\varepsilon}$ we first motivate two distinguished limits for the relative size of D with respect to ε. To do so, we note that when $D \gg 1$ the Green's function satisfying (5.8) has the regular asymptotic expansion

$$G(x,\xi) \sim D|\Omega|^{-1} + G_0(x,\xi) + \mathscr{O}(D^{-1}), \tag{5.10}$$

where $G_0(x,\xi)$ is the Neumann Green's function satisfying

$$\Delta G_0 = \frac{1}{|\Omega|} - \delta(x-\xi), \quad x \in \Omega; \qquad \partial_n G_0 = 0, \quad x \in \partial\Omega; \tag{5.11a}$$

$$\int_\Omega G_0\, dx = 0, \tag{5.11b}$$

with asymptotics

$$G_0(x,\xi) \sim \frac{1}{4\pi|x-\xi|} + R_0(\xi) + \nabla_x R_0(x;\xi)\cdot(x-\xi), \qquad \text{as} \quad x \to \xi, \tag{5.11c}$$

and where $R_0(\xi)$ is the regular part of G_0. In summary, for the two ranges of D we have

$$G(x,\xi) \sim \frac{1}{4\pi|x-\xi|} + \begin{cases} R(\xi) + o(1), & D = \mathscr{O}(1), \\ D|\Omega|^{-1} + R_0(\xi) + o(1), & D \gg 1, \end{cases} \quad \text{as } |x-\xi| \to 0, \tag{5.12}$$

where $R(\xi)$ is the regular part of $G(x,\xi)$. By matching the $\rho \to \infty$ behaviour of $U_i(\rho)$ given by (5.6) with the behaviour of u given by (5.9) as $|x-x_i| \to 0$, we obtain in the two regimes of D that

$$\mu(S_{i\varepsilon}) = 4\pi\varepsilon \begin{cases} S_{i\varepsilon}R(x_i) + \sum_{j\neq i} S_{j\varepsilon}G(x_i,x_j), & D = \mathscr{O}(1), \\ S_{i\varepsilon}R_0(x_i) + \sum_{j\neq i} S_{j\varepsilon}G_0(x_i,x_j) + D|\Omega|^{-1}\sum_{j=1}^N S_{j\varepsilon}, & D \gg 1. \end{cases} \tag{5.13}$$

From the $D \gg 1$ case we see that $D = \mathscr{O}(\varepsilon^{-1})$ is a distinguished regime for which the right-hand side has an $\mathscr{O}(1)$ contribution. Defining the vectors $\boldsymbol{S}_\varepsilon \equiv (S_{1\varepsilon},\ldots,S_{N\varepsilon})^T$, $\mu(\boldsymbol{S}_\varepsilon) \equiv (\mu(S_{1\varepsilon}),\ldots,\mu(S_{N\varepsilon}))^T$, and $\boldsymbol{e} \equiv (1,\ldots,1)^T$, as well as the

matrices $\mathscr{E}_N$, $\mathscr{G}$, and $\mathscr{G}_0$ by

$$\mathscr{E}_N \equiv \frac{1}{N}\boldsymbol{e}\boldsymbol{e}^T\,, \quad (\mathscr{G})_{ij} = \begin{cases} R(x_i)\,, & i=j \\ G(x_i,x_j)\,, & i\neq j \end{cases}, \quad (\mathscr{G}_0)_{ij} = \begin{cases} R_0(x_i)\,, & i=j \\ G_0(x_i,x_j)\,, & i\neq j \end{cases}, \tag{5.14}$$

we obtain from (5.13) that the unknowns $S_{1\varepsilon},\ldots,S_{N\varepsilon}$ must satisfy the NAS

$$\mu(\boldsymbol{S}_\varepsilon) = 4\pi\varepsilon\mathscr{G}\boldsymbol{S}_\varepsilon\,, \tag{5.15a}$$

for $D=\mathscr{O}(1)$ and

$$\mu(\boldsymbol{S}_\varepsilon) = \kappa\mathscr{E}_N\boldsymbol{S}_\varepsilon + 4\pi\varepsilon\mathscr{G}_0\boldsymbol{S}_\varepsilon\,, \qquad \kappa \equiv \frac{4\pi N D_0}{|\Omega|}\,, \tag{5.15b}$$

for $D=\varepsilon^{-1}D_0$.

5.1.3 Symmetric and Asymmetric N-Spot Quasi-Equilibrium

We now determine solutions to the NAS (5.15) in both the $D=\mathscr{O}(1)$ and the $D=\mathscr{O}(\varepsilon^{-1})$ regimes. In particular, we show that it is possible to construct *symmetric* N-spot solutions to (5.1) by finding a solution to the NAS (5.15) with $\boldsymbol{S}_\varepsilon = S_{c\varepsilon}\boldsymbol{e}$ in both the $D=\mathscr{O}(1)$ and $D=\mathscr{O}(\varepsilon^{-1})$ regimes. Moreover, when $D=\mathscr{O}(\varepsilon^{-1})$ we will show that it is possible to construct *asymmetric* quasi-equilibrium solutions to (5.1) characterized by spots each having one of two strengths.

When $D=\mathscr{O}(1)$ the NAS (5.15a) implies that to leading order $\mu(S_{i\varepsilon})=0$ for all $i=1,\ldots,N$. From the properties of $\mu(S)$ outlined in §5.1.1 and in particular the plot of $\mu(S)$ in Figure 5.1a, we deduce that $S_{i\varepsilon}\sim S_\star$ for all $i=1,\ldots,N$. Thus, to leading order, N-spot quasi-equilibrium solutions in the $D=\mathscr{O}(1)$ regime have spots with a common height, which we refer to as a *symmetric* pattern. By calculating the next order term using (5.15a) we readily obtain the two term result

$$\boldsymbol{S}_\varepsilon \sim S_\star\boldsymbol{e} + \frac{4\pi\varepsilon S_\star}{\mu'(S_\star)}\mathscr{G}\boldsymbol{e}\,. \tag{5.16}$$

We conclude that the configuration $x_1,\ldots,x_N$ of spots only affects the spot strengths at $\mathscr{O}(\varepsilon)$ through the Green's matrix $\mathscr{G}$. Note that if $\boldsymbol{e}$ is an eigenvector of $\mathscr{G}$ with eigenvalue g_0 then the solution to (5.15a) is $\boldsymbol{S}_{i\varepsilon}=S_{c\varepsilon}\boldsymbol{e}$ where $S_{c\varepsilon}$ satisfies the scalar

equation $\mu(S_{c\varepsilon}) = 4\pi\varepsilon g_0 S_{c\varepsilon}$.

Next, we consider solutions to the NAS (5.15b) in the $D = \varepsilon^{-1}D_0$ regime. Seeking a solution $\boldsymbol{S}_\varepsilon \sim \boldsymbol{S}_0 + \varepsilon\boldsymbol{S}_1 + \cdots$ we obtain the leading order problem

$$\mu(\boldsymbol{S}_0) = \kappa\mathscr{E}_N\boldsymbol{S}_0. \tag{5.17}$$

Note that the concavity of $\mu(S)$ (see Figure 5.1a) implies the existence of two values $0 < S_l < S_r < S_\star$ such that $\mu(S_l) = \mu(S_r)$. Thus, in addition to the symmetric solutions already encountered in the $D = \mathscr{O}(1)$ regime, we also have the possibility of *asymmetric* solutions, where the spots can have two different heights. We first consider symmetric solutions, where to leading order $\boldsymbol{S}_0 = S_c\boldsymbol{e}$ in which S_c satisfies

$$\mu(S_c) = \kappa S_c\,. \tag{5.18}$$

The plot of $\mu(S)$ in Figure 5.1a, together with the $S \ll 1$ asymptotics given in (5.3), imply that a solution to (5.18) can be found in the interval $0 < S_c \le S_\star$ for all $\kappa > 0$. In Figure 5.3a we illustrate graphically that the common spot strength S_c is obtained by the intersection of $\mu(S)$ with the line κS. We refer to Figure 5.4 for plots of the symmetric solution strengths as a function of κ. In addition, we readily calculate that

$$\begin{aligned} S_c &\sim S_\star\left(1 + \frac{\kappa}{\mu'(S_\star)}\right) + \mathscr{O}(\kappa^2)\,, \quad \text{for } \kappa \ll 1\,, \\ S_c &\sim \frac{1}{b\kappa^2} + \mathscr{O}(\kappa^{-3}), \quad \text{for } \kappa \gg 1\,, \end{aligned} \tag{5.19}$$

which provides a connection between the $D = \mathscr{O}(1)$ and $D \to \infty$ (shadow limit) regimes, respectively. From (5.15b), the next order correction $\boldsymbol{S}_1$ satisfies $\mu'(S_c)\boldsymbol{S}_1 - \kappa\mathscr{E}_N\boldsymbol{S}_1 = 4\pi S_c\mathscr{G}_0\boldsymbol{e}$. Upon left-multiplying this expression by $\boldsymbol{e}^T$ we can determine $\boldsymbol{e}^T\boldsymbol{S}_1$. Then, by recalling the definition of $\mathscr{E}_N \equiv N^{-1}\boldsymbol{e}\boldsymbol{e}^T$ we can calculate $\boldsymbol{S}_1$. Summarizing, a two term asymptotic expansion for the symmetric solution to (5.15b) is

$$\boldsymbol{S}_\varepsilon \sim S_c\boldsymbol{e} + \frac{4\pi\varepsilon}{\mu'(S_c)}\left(S_c\mathscr{I}_N + \frac{\mu(S_c)}{\mu'(S_c) - \kappa}\mathscr{E}_N\right)\mathscr{G}_0\boldsymbol{e}\,, \tag{5.20}$$

provided that $\mu'(S_c) \neq 0$ (i.e. $S_c \neq S_{\text{crit}}$). Note that $\mu'(S_c) - \kappa = 0$ is impossible

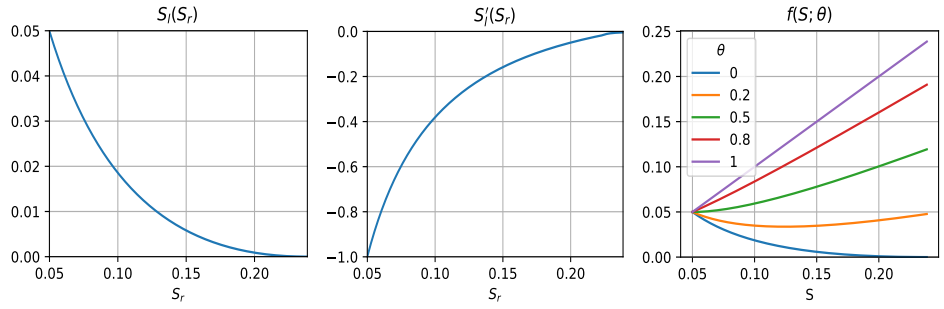

(a) **(b)** **(c)**

Figure 5.2: Plots of (a) $S_l(S_r)$ and (b) $S_l'(S_r)$ for the construction of asymmetric N-spot patterns. (c) Plots of $f(S,\theta)$ for select values of $\theta \equiv n/N$. For $0 < \theta < 0.5$ the function $f(S,\theta)$ attains an interior minimum in $S_{\text{crit}} < S < S_\star$.

by the following simple argument. First, for this equality to hold we require that $0 < S < S_{\text{crit}}$ since otherwise $\mu'(S_c) < 0$. Moreover, we can solve (5.18) for κ to get $\mu'(S_c) - \kappa = S_c^{-1} g(S_c)$ where $g(S) \equiv S\mu'(S) - \mu(S)$. However, we calculate $g'(S) = S\mu''(S) < 0$ and moreover, using the small S asymptotics found in (5.3) we determine that $g(S) \sim -\sqrt{S/(4b)} < 0$ as $S \to 0^+$. Therefore, $g(S_c) < 0$ for all $0 < S_c < S_{\text{crit}}$ so that $\mu'(S_c) < \kappa$ holds. Finally, as for the $D = \mathcal{O}(1)$ case, if $\mathscr{G}_0 \boldsymbol{e} = g_{00}\boldsymbol{e}$ then the common source values extends to higher order and we have $\boldsymbol{S}_\varepsilon = S_{c\varepsilon}\boldsymbol{e}$ where $S_{c\varepsilon}$ is the unique solution to the scalar problem

$$\mu(S_{c\varepsilon}) = (\kappa + 4\pi\varepsilon g_{00}) S_{c\varepsilon}\,. \tag{5.21}$$

Next, we construct of *asymmetric* N-spot configurations. The plot of $\mu(S)$ indicates that for any value of $S_r \in (S_{\text{crit}}, S_\star]$ there exists a unique value $S_l = S_l(S_r) \in [0, S_{\text{crit}})$ satisfying $\mu(S_l) = \mu(S_r)$. A plot of $S_l(S_r)$ is shown in Figure 5.2a. Clearly $S_l(S_{\text{crit}}) = S_{\text{crit}}$ and $S_l(S_\star) = 0$. We suppose that to leading order the N-spot configuration has n *large* spots of strength S_r and $N-n$ *small* spots of strengths S_l. More specifically, we seek a solution of the form

$$\boldsymbol{S}_\varepsilon \sim (S_r, \ldots, S_r, S_l(S_r), \ldots, S_l(S_r))^T\,, \tag{5.22}$$

so that (5.17) reduces to the single scalar nonlinear equation

$$\mu(S_r) = \kappa f(S_r; n/N), \quad f(S;\theta) \equiv \theta S + (1-\theta) S_l(S), \tag{5.23}$$

for $S_{\text{crit}} < S_r < S_\star$. Since $\mu(S_{\text{crit}}) - \kappa f(S_{\text{crit}}; n/N) = \mu(S_{\text{crit}}) - \kappa S_{\text{crit}}$ and $\mu(S_\star) - \kappa f(S_\star; n/N) = -\kappa n S_\star / N < 0$, we obtain by the intermediate value theorem that there exists at least one solution to (5.23) for any $0 < n \leq N$ when

$$0 < \kappa < \kappa_{c1} \equiv \mu(S_{\text{crit}})/S_{\text{crit}} \approx 0.64619.$$

Next, we calculate

$$f'(S;\theta) = (1-\theta)\left(\frac{\theta}{1-\theta} + S_l'(S)\right),$$

where $S_l'(S)$ is computed numerically (see Figure 5.2b). We observe that $-1 \leq S_l'(S_r) \leq 0$ with $S_l'(S_{\text{crit}}) = -1$ and $S_l'(S_\star) = 0$. In particular, $f(S; n/N)$ is monotone increasing if $\theta/(1-\theta) = n/(N-n) > 1$, while it attains a local minimum in $(S_{\text{crit}}, S_\star)$ if $n/(N-n) < 1$. A plot of $f(S;\theta)$ is shown in Figure 5.2c. In either case, we deduce that the solution to (5.23) when $0 < \kappa < \kappa_{c1}$ is unique (see Figure 5.3a). On the other hand, when $n/(N-n) < 1$ we anticipate an additional range of values $\kappa_{c1} < \kappa < \kappa_{c2}$ for which (5.23) has *two* distinct solutions $S_{\text{crit}} < \tilde{S}_r < S_r < S_\star$. Indeed, this threshold can be found by demanding that $\mu(S)$ and $\kappa f(S; n/N)$ intersect tangentially. In this way, we find that the threshold κ_{c2} can be written as

$$\kappa_{c2} = \kappa_{c2}(n/N) \equiv \frac{\mu(S_r^\star)}{f(S_r^\star; n/N)}, \tag{5.24a}$$

where $S_r^\star$ is the unique solution to

$$f(S_r^\star; n/N)\mu'(S_r^\star) = f'(S_r^\star; n/N)\mu(S_r^\star). \tag{5.24b}$$

In Figure 5.3c we plot $\kappa_{c2} - \kappa_{c1}$ as a functions of n/N where we observe that $\kappa_{c2} > \kappa_{c1}$ with $\kappa_{c2} - \kappa_{c1} \to 0^+$ and $\kappa_{c2} - \kappa_{c1} \to \infty$ as $n/N \to 0.5^-$ and $n/N \to 0^+$ respectively. Furthermore, in Figure 5.3b we graphically illustrate how multiple solutions to (5.23) arise as $\theta = n/N$ and κ are varied. We remark that the condi-

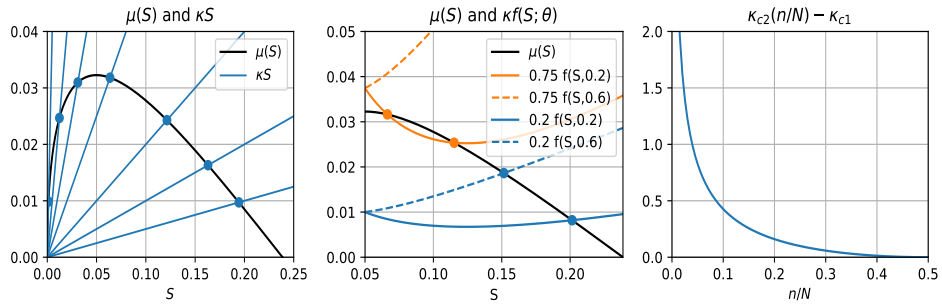

(a) **(b)** **(c)**

Figure 5.3: (a) Illustration of solutions to (5.18) as the intersection between $\mu(S)$ and κS. There is a unique solution if $\kappa < \kappa_{c1} \equiv \mu(S_{\rm crit})/S_{\rm crit}$. (b) Illustration of solutions to (5.23) as the intersection between $\mu(S)$ and $\kappa f(S,\theta)$ where $\theta = n/N$ denotes the fraction of *large* spots in an asymmetric pattern. Note that when $\theta = 0.2 < 0.5$ and $\kappa > \kappa_{c1} \approx 0.64619$ there exist two solutions. (c) Plot of $\kappa_{c2} - \kappa_{c1}$ versus n/N. Observe that $\kappa_{c2} - \kappa_{c1}$ increases as the fraction of large spots decreases.

tion $n/(N-n) < 1$ implies that $n < N/2$, so that there are more small than large spots. The appearance of two distinct asymmetric patterns in this regime has a direct analogy to results obtained for the 1-D and 2-D GM model in [104] and [109], respectively. The resulting bifurcation diagrams are shown in Figure 5.4 for $n/N = 0.2, 0.4, 0.6$. We summarize our results for quasi-equilibrium solutions in the following proposition.

Proposition 5.1.1. *(Quasi-Equilibrium Solutions): Let $\varepsilon \to 0$ and $x_1, \ldots, x_N \in \Omega$ be well-separated. Then, the 3-D GM model* (5.1) *admits an N-spot quasi-equilibrium solution with inner asymptotics*

$$v \sim DV_i(\varepsilon^{-1}|x - x_i|), \qquad u \sim DU_i(\varepsilon^{-1}|x - x_i|), \tag{5.25}$$

as $x \to x_i$ for each $i = 1, \ldots, N$ where V_i and U_i are given by (5.6)*. When $|x - x_i| = \mathcal{O}(1)$, the activator is exponentially small while the inhibitor is given by* (5.9)*. The spot strengths $S_{i\varepsilon}$ for $i = 1, \ldots, N$ completely determine the asymptotic solution and there are two distinguished limits. When $D = \mathcal{O}(1)$ the spot strengths satisfy*

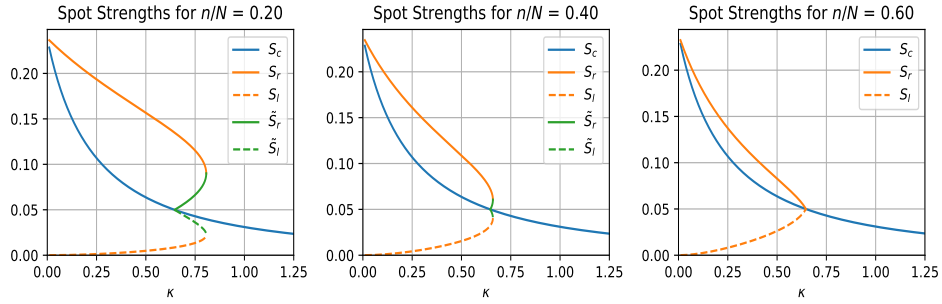

(a) **(b)** **(c)**

Figure 5.4: Bifurcation diagram illustrating the dependence on κ of the common spot strength S_c as well as the asymmetric spot strengths S_r and S_l or $\tilde{S}_r$ and $\tilde{S}_l$. In (a) and (b) we have $n/N < 0.5$ so that there are more small spots than large spots in an asymmetric pattern. As a result, we observe that there can be two types of asymmetric patterns with strengths S_r and S_l or $\tilde{S}_r$ and $\tilde{S}_l$. In (c) the number of large spots exceeds that of small spots and only one type of asymmetric pattern is possible.

the NAS (5.15a)*, which has the leading order asymptotics* (5.16)*. In particular,* $S_{i\varepsilon} \sim S_\star$ *so all N-spot patterns are symmetric to leading order. When* $D = \varepsilon^{-1} D_0$ *the spot strengths satisfy the NAS* (5.15b)*. A symmetric solution with asymptotics* (5.20) *where* S_c *satisfies* (5.18) *always exists. Moreover, if*

$$0 < \frac{4\pi N D_0}{|\Omega|} < \kappa_{c1} \approx 0.64619\,,$$

then an asymmetric pattern with n large spots of strength $S_r \in (S_{crit}, S_\star)$ *and* $N-n$ *small spots of strength* $S_l \in (0, S_{crit})$ *can be found by solving* (5.23) *for* S_r *and calculating* S_l *from* $\mu(S_l) = \mu(S_r)$*. If, in addition we have* $n/(N-n) < 1$*, then* (5.23) *admits two solutions on the range*

$$0.64619 \approx \kappa_{c1} < \frac{4\pi N D_0}{|\Omega|} < \kappa_{c2}(n/N)\,,$$

where $\kappa_{c2}(n/N)$ *is found by solving the system* (5.24)*.*

As we have already remarked, in the $D = D_0/\varepsilon$ regime, if $D_0 \ll 1$ then the

symmetric N-spot solution (5.20) coincides with the symmetric solution for the $D = \mathcal{O}(1)$ regime given by (5.16). The asymmetric solutions predicted for the $D = D_0/\varepsilon$ regime persist as D_0 decreases and it is, therefore, natural to ask what these solutions correspond to in the $D = \mathcal{O}(1)$ regime. From the small S asymptotics (5.3) we note that the NAS (5.15a) does admit an asymmetric solution, albeit one in which the spot strengths of the small spots are of $\mathcal{O}(\varepsilon^2)$. Specifically, for a given integer n in $1 < n \leq N$ we can construct a solution where

$$\boldsymbol{S}_\varepsilon \sim (S_\star, \ldots, S_\star, \varepsilon^2 S_{n+1,0}, \ldots, \varepsilon^2 S_{N,0})^T . \tag{5.26}$$

By using the small S asymptotic expansion for $\mu(S)$ given in (5.3), we obtain from (5.15a) that

$$S_{i,0} = b\left(4\pi S_\star \sum_{j=1}^{n} G(x_i, x_j)\right)^2, \qquad i = n+1, \ldots, N. \tag{5.27}$$

We observe that in order to support $N-n$ spots of strength $\mathcal{O}(\varepsilon^2)$, we require at least one spot of strength $\mathcal{O}(1)$. Setting $D = D_0/\varepsilon$, we use the large D asymptotics for $G(x,\xi)$ in (5.10) to reduce (5.27) to

$$S_{i,0} \sim b\varepsilon^{-2}\left(\frac{4\pi D_0 n S_\star}{|\Omega|}\right)^2, \qquad i = n+1, \ldots, N. \tag{5.28}$$

Alternatively, by taking $\kappa \ll 1$ in the NAS (5.15b) for the $D = D_0/\varepsilon$ regime, we conclude that $S_r \sim S_\star$ and $S_l \sim b\,(\kappa n S_\star/N)^2$. Since $\kappa n/N = 4\pi D_0 n/|\Omega|$, as obtained from (5.15b), we confirm that the asymmetric patterns in the $D = D_0/\varepsilon$ regime lead to an asymmetric pattern consisting of spots of strength $\mathcal{O}(1)$ and $\mathcal{O}(\varepsilon^2)$ in the $D = \mathcal{O}(1)$ regime.

5.2 Linear Stability

Let (v_{qe}, u_{qe}) be an N-spot quasi-equilibrium solution as constructed in §5.1. We will analyze instabilities for quasi-equilibrium solutions that occur on $\mathcal{O}(1)$ time-

scales. To do so, we substitute

$$v = v_{qe} + e^{\lambda t}\phi\,, \qquad u = u_{qe} + e^{\lambda t}\psi\,, \tag{5.29}$$

into (5.1) and, upon linearizing, we obtain the eigenvalue problem

$$\begin{aligned} \varepsilon^2\Delta\phi - \phi + \frac{2v_{qe}}{u_{qe}}\phi - \frac{v_{qe}^2}{u_{qe}^2}\psi = \lambda\phi\,, \\ D\Delta\psi - \psi + 2\varepsilon^{-2}v_{qe}\phi = \tau\lambda\psi\,, \end{aligned} \tag{5.30}$$

where $\partial_n\phi = \partial_n\psi = 0$ on $\partial\Omega$. In the inner region near the j^{th} spot, we introduce a local expansion in terms of the associated Legendre polynomials $P_l^m(\cos\theta)$ of degree $l = 0,2,3,\ldots$, and order $m = 0,1,\ldots,l$

$$\phi \sim c_j D P_l^m(\cos\theta)e^{im\varphi}\Phi_j(\rho)\,, \qquad \psi \sim c_j D P_l^m(\cos\theta)e^{im\varphi}\Psi_j(\rho)\,, \tag{5.31}$$

where $\rho = \varepsilon^{-1}|x - x_j|$, and $(\theta,\varphi) \in (0,\pi)\times[0,2\pi)$. Suppressing subscripts for the moment, and assuming that $\varepsilon^2\tau\lambda/D \ll 1$, we obtain the leading order inner problem

$$\begin{aligned} \Delta_\rho\Phi - \frac{l(l+1)}{\rho^2}\Phi - \Phi + \frac{2V}{U}\Phi - \frac{V^2}{U^2}\Psi = \lambda\Phi, \quad \rho > 0\,, \\ \Delta_\rho\Psi - \frac{l(l+1)}{\rho^2}\Psi + 2V\Phi = 0\,, \quad \rho > 0\,, \end{aligned} \tag{5.32a}$$

with the boundary conditions $\Phi'(0) = \Psi'(0) = 0$, and $\Phi \to 0$ as $\rho \to \infty$. Here (V,U) satisfy the core problem (5.2). The behaviour of Ψ as $\rho \to \infty$ depends on the parameter l. More specifically, we have that

$$\Psi \sim \begin{cases} B(\lambda,S) + \rho^{-1}\,, & \text{for } l = 0\,, \\ \rho^{-(1/2+\gamma_l)}\,, & \text{for } l > 0\,, \end{cases} \qquad \text{as} \quad \rho \to \infty\,, \tag{5.32b}$$

where $\gamma_l \equiv \sqrt{\frac{1}{4} + l(l+1)}$ and $B(\lambda,S)$ is a constant. Here we have normalized Ψ by fixing to unity the multiplicative factor in the decay rate in (5.32b). Next, we

introduce the Green's function $G_l(\rho,\tilde{\rho})$ solving

$$\Delta_\rho G_l - \frac{l(l+1)}{\rho^2} G_l = -\rho^{-2}\delta(\rho-\tilde{\rho}), \quad \rho,\tilde{\rho} > 0, \tag{5.33a}$$

and explicitly given by

$$G_l(\rho,\tilde{\rho}) = \frac{1}{2\gamma_l\sqrt{\rho\tilde{\rho}}} \begin{cases} (\rho/\tilde{\rho})^{\gamma_l}, & 0<\rho<\tilde{\rho}, \\ (\tilde{\rho}/\rho)^{\gamma_l}, & \rho>\tilde{\rho}, \end{cases} \tag{5.33b}$$

when $l > 0$. For $l = 0$ the same expression applies, but an arbitrary constant may be added. For convenience we fix this constant to be zero. In terms of this Green's function we can solve for Ψ explicitly in (5.32a) as

$$\Psi = 2\int_0^\infty G_l(\rho,\tilde{\rho})V(\tilde{\rho})\Phi(\tilde{\rho})\tilde{\rho}^2\,d\tilde{\rho} + \begin{cases} B(\lambda,S), & \text{for } l=0, \\ 0, & \text{for } l>0. \end{cases} \tag{5.34}$$

Upon substituting this expression into (5.32a) we obtain the nonlocal spectral problems

$$\mathscr{M}_0\Phi = \lambda\Phi + B(\lambda,S)\frac{V^2}{U^2}, \quad \text{for} \quad l=0; \qquad \mathscr{M}_l\Phi = \lambda\Phi, \quad \text{for} \quad l>0. \tag{5.35a}$$

Here the integro-differential operator $\mathscr{M}_l$ is defined for every $l \geq 0$ by

$$\mathscr{M}_l\Phi \equiv \Delta_\rho\Phi - \frac{l(l+1)}{\rho^2}\Phi - \Phi + \frac{2V}{U}\Phi - \frac{2V^2}{U^2}\int_0^\infty G_l(\rho,\tilde{\rho})V(\tilde{\rho})\Phi(\tilde{\rho})\tilde{\rho}^2\,d\tilde{\rho}. \tag{5.35b}$$

A key difference between the $l = 0$ and $l > 0$ linear stability problems is the appearance of an unknown constant $B(\lambda,S)$ in the $l = 0$ equation. This unknown constant is determined by matching the far-field behaviour of the inner inhibitor expansion with the outer solution. In this sense, we expect that $B(\lambda,S)$ will encapsulate global contributions from all spots, so that instabilities for the mode $l = 0$ are due to the interactions between spots. In contrast, the absence of an unknown constant for instabilities for the $l > 0$ modes indicates that these instabilities are localized, and that the weak effect of any interactions between spots occurs only

through higher order terms. In this way, instabilities for modes with $l > 0$ are determined solely by the spectrum of the operator $\mathscr{M}_l$. In Figure 5.5a we plot the numerically-computed dominant eigenvalue of $\mathscr{M}_l$ for $l = 0, 2, 3$ as well as the sub dominant eigenvalue for $l = 0$ for $0 < S < S_\star$. This spectrum is calculated from the discretization of $\mathscr{M}_l$ obtained by truncating the infinite domain to $0 < \rho < L$, with $L \gg 1$, and using a finite difference approximation for spatial derivatives combined with a trapezoidal rule discretization of the integral terms. The $l = 1$ mode always admits a zero eigenvalue, as this simply reflects the translation invariance of the inner problem. Indeed, these instabilities will be briefly considered in §5.3 where we consider the slow dynamics of quasi-equilibrium spot patterns. From Figure 5.5a we observe that the dominant eigenvalues of $\mathscr{M}_l$ for $l = 2, 3$ satisfy $\mathrm{Re}(\lambda) < 0$ (numerically we observe the same for larger values of l). Therefore, since the modes $l > 1$ are always *linearly stable*, for the 3-D GM model there will be no *peanut-splitting* or spot self-replication instabilities such as observed for the 3-D Schnakenberg model in [98]. In the next subsection we will focus on analyzing instabilities associated with $l = 0$ mode, which involves a global coupling between localized spots.

5.2.1 Competition and Synchronous Instabilities for the $l = 0$ Mode

From (5.35a) we observe that λ is in the spectrum of $\mathscr{M}_0$ if and only if $B(\lambda, S) = 0$. Assuming that $B(\lambda, S) \neq 0$ we can then solve for Φ in (5.35a) as

$$\Phi = B(\lambda, S)(\mathscr{M}_0 - \lambda)^{-1}(V^2/U^2)\,. \tag{5.36}$$

Upon substituting (5.36) into the expression (5.34) for Ψ when $l = 0$, we let $\rho \to \infty$ and use $G_0(\rho, \tilde{\rho}) \sim 1/\rho$ as $\rho \to \infty$, as obtained from (5.33), to deduce the far-field behaviour

$$\Psi \sim B + \frac{2B}{\rho}\int_0^\infty V(\mathscr{M}_0 - \lambda)^{-1}(V^2/U^2)\rho^2 d\rho\,, \qquad \text{as} \quad \rho \to \infty\,. \tag{5.37}$$

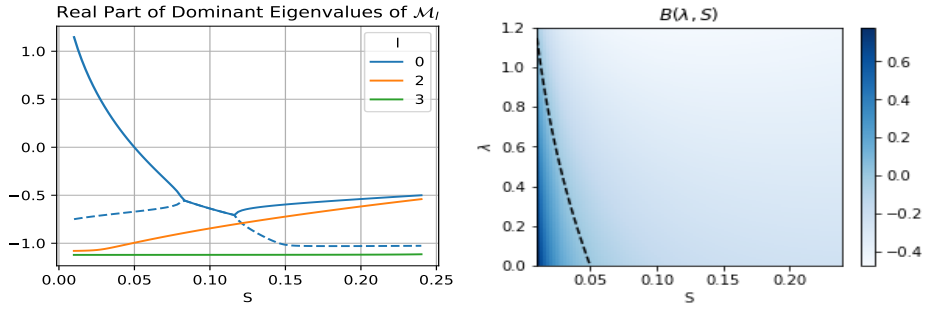

(a) **(b)**

Figure 5.5: (a) Spectrum of the operator $\mathscr{M}_l$ defined in (5.35b). The dashed blue line indicates the eigenvalue with second largest real part for $l = 0$. Notice that the dominant eigenvalue of $\mathscr{M}_0$ is zero when $S = S_{\text{crit}} \approx 0.04993$, corresponding to the maximum of $\mu(S)$ (see Figure 5.1a). (b) Plot of $B(\lambda, S)$. The dashed line black indicates the largest positive eigenvalue of $\mathscr{M}_0(S)$ and also corresponds to the contour $B(\lambda, S) = 0$. We observe that $B(\lambda, S)$ is both continuous and negative for $S > S_{\text{crit}} \approx 0.04993$.

We compare this expression with the normalized decay condition on Ψ in (5.32b) for $l = 0$ to conclude that

$$B(\lambda, S) = \frac{1}{2\int_0^\infty V(\mathscr{M}_0 - \lambda)^{-1}(V^2/U^2)\rho^2\, d\rho}\,. \tag{5.38}$$

We now solve the outer problem and through a matching condition derive an algebraic equation for the eigenvalue λ. Since the interaction of spots will be important for analyzing instabilities for the $l = 0$ mode, we re-introduce the subscript j to label the spot. First, since $\partial_\rho \Psi_j \sim -\rho^{-2}$ as $\rho \to \infty$, as obtained from (5.32b) for $l = 0$, an application of the divergence theorem to $\Delta_\rho \Psi_j = -2V_j\Phi_j$ yields that $\int_0^\infty V_j \Phi_j \rho^2\, d\rho = 1/2$. Next, by using $v_{qe} \sim DV_j(\rho)$ and $\phi \sim c_j D\Phi_j(\rho)$ for $|x - x_j| = \mathscr{O}(\varepsilon)$ as obtained from (5.25) and (5.31), respectively, we calculate in the sense of distributions for $\varepsilon \to 0$ that

$$2\varepsilon^{-2} v_{qe}\phi \to 8\pi\varepsilon D^2 \sum_{j=1}^N c_j \left(\int_0^\infty V_j \Phi_j \rho^2\, d\rho \right) \delta(x - x_j) = 4\pi\varepsilon D^2 \sum_{j=1}^N c_j \delta(x - x_j)\,.$$

Therefore, by using this distributional limit in the equation for ψ in (5.30), the outer problem for ψ is

$$\Delta\psi - \frac{(1+\tau\lambda)}{D}\psi = -4\pi\varepsilon D\sum_{j=1}^{N} c_j\delta(x-x_j)\,, \quad x\in\Omega; \qquad \partial_n\psi = 0\,, \quad x\in\partial\Omega\,. \tag{5.39}$$

The solution to (5.39) is represented as

$$\psi = 4\pi\varepsilon D\sum_{j=1}^{N} c_j G^{\lambda}(x,x_j)\,, \tag{5.40}$$

where $G^{\lambda}(x,\xi)$ is the eigenvalue-dependent Green's function satisfying

$$\begin{aligned} &\Delta G^{\lambda} - \frac{(1+\tau\lambda)}{D}G^{\lambda} = -\delta(x-\xi)\,, \quad x\in\Omega; \qquad \partial_n G^{\lambda} = 0\,, \quad x\in\partial\Omega\,, \\ &\qquad G^{\lambda}(x,\xi) \sim \frac{1}{4\pi|x-\xi|} + R^{\lambda}(\xi) + o(1)\,, \qquad \text{as} \quad x\to\xi\,. \end{aligned} \tag{5.41}$$

By matching the limit as $x\to x_i$ of ψ in (5.40) with the far-field behaviour $\psi\sim Dc_iB(\lambda,S_i)$ of the inner solution, as obtained from (5.37) and (5.31), we obtain the matching condition

$$B(\lambda,S_i)c_i = 4\pi\varepsilon\left(c_iR^{\lambda}(x_i) + \sum_{j\neq i}^{N} c_jG^{\lambda}(x_i,x_j)\right). \tag{5.42}$$

As similar to the construction of quasi-equilibrium solutions in §5.1, there are two distinguished limits $D=\mathcal{O}(1)$ and $D=D_0/\varepsilon$ to consider. The stability properties are shown to be significantly different in these two regimes.

In the $D=\mathcal{O}(1)$ regime, we recall that $S_i\sim S_\star$ for $i=1,\ldots,N$ where $\mu(S_\star)=0$. From (5.42), we conclude to leading order that $B(\lambda,S_\star)=0$, so that λ must be an eigenvalue of $\mathcal{M}_0$ when $S=S_\star$. However, from Figure 5.5a we find that all eigenvalues of $\mathcal{M}_0$ when $S=S_\star$ satisfy $\mathrm{Re}(\lambda)<0$. As such, from our leading order calculation we conclude that N-spot quasi-equilibrium solutions in the $D=\mathcal{O}(1)$ regime are all linearly stable.

For the remainder of this section we focus exclusively on the $D=D_0/\varepsilon$ regime. Assuming that $\varepsilon|1+\tau\lambda|/D_0\ll 1$ we calculate $G^{\lambda}(x,\xi)\sim\varepsilon^{-1}D_0/\left[(1+\tau\lambda)|\Omega|\right]+G_0(x,\xi)$, where G_0 is the Neumann Green's function satisfying (5.11). We substi-

tute this limiting behaviour into (5.42) and, after rewriting the the resulting homogeneous linear system for $\boldsymbol{c} \equiv (c_1, \ldots, c_N)^T$ in matrix form, we obtain

$$\mathscr{B}\boldsymbol{c} = \frac{\kappa}{1+\tau\lambda}\mathscr{E}_N\boldsymbol{c} + 4\pi\varepsilon\mathscr{G}_0\boldsymbol{c}\,, \tag{5.43a}$$

where

$$\mathscr{B} \equiv \mathrm{diag}(B(\lambda, S_1), \ldots, B(\lambda, S_N))\,, \quad \mathscr{E}_N \equiv N^{-1}\boldsymbol{e}\boldsymbol{e}^T\,. \tag{5.43b}$$

Here $\mathscr{G}_0$ is the Neumann Green's matrix and $\kappa \equiv 4\pi N D_0/|\Omega|$ (see (5.15b)). Next, we separate the proceeding analysis into the two cases: symmetric quasi-equilibrium patterns and asymmetric quasi-equilibrium solutions.

Stability of Symmetric Patterns in the $D = D_0/\varepsilon$ Regime

We suppose that the quasi-equilibrium solution is symmetric so that to leading order $S_1 = \ldots = S_N = S_c$ where S_c is found by solving the nonlinear algebraic equation (5.18). Then, from (5.43), the leading order stability problem is

$$B(\lambda, S_c)\boldsymbol{c} = \frac{\kappa}{1+\tau\lambda}\mathscr{E}_N\boldsymbol{c}\,. \tag{5.44}$$

We first consider *competition* instabilities for $N \geq 2$ characterized by $\boldsymbol{c}^T\boldsymbol{e} = 0$ so that $\mathscr{E}_N\boldsymbol{c} = 0$. Since $B(\lambda, S_c) = 0$ from (5.44), it follows that λ must be an eigenvalue of $\mathscr{M}_0$, defined in (5.35b), at $S = S_c$. From Figure 5.5a we deduce that the pattern is unstable for S below some threshold where the dominant eigenvalue of $\mathscr{M}_0$ equals zero. In fact, this threshold is easily determined to correspond to $S_c = S_{\mathrm{crit}}$, where $\mu'(S_{\mathrm{crit}}) = 0$, since by differentiating the core problem (5.2) with respect to S and comparing the resulting system with (5.32) when $l = 0$, we conclude that $B(0, S_c) = \mu'(S_c)$. The dotted curve in Figure 5.5b shows that the zero level curve $B(\lambda, S_c) = 0$ is such that $\lambda > 0$ for $S_c < S_{\mathrm{crit}}$. As such, we conclude from (5.18) that symmetric N-spot quasi-equilibrium solutions are unstable to competition instabilities when $\kappa > \kappa_{c1} \equiv \mu(S_{\mathrm{crit}})/S_{\mathrm{crit}}$.

For special spot configurations $\{x_1, \ldots, x_N\}$ where $\boldsymbol{e}$ is an eigenvector of $\mathscr{G}_0$ we can easily calculate a higher order correction to this instability threshold. Since $\mathscr{G}_0$ is symmetric, there are $N-1$ mutually orthogonal eigenvectors $\boldsymbol{q}_2, \ldots, \boldsymbol{q}_N$ such that $\mathscr{G}_0\boldsymbol{q}_k = g_k\boldsymbol{q}_k$ with $\boldsymbol{q}_k^T\boldsymbol{e} = 0$. Setting $\boldsymbol{c} = \boldsymbol{q}_k$ in (5.43), and using $B(0, S) \sim \varepsilon\mu''(S_{\mathrm{crit}})\delta$

for $S = S_{\text{crit}} + \varepsilon\delta$, we can determine the perturbed stability threshold where $\lambda = 0$ associated with each eigenvector $\boldsymbol{q}_k$. By taking the minimum of such values, and by recalling the refined approximation (5.21), we obtain that N-spot symmetric quasi-equilibrium solutions are all unstable on the range

$$S_{c\varepsilon} < S_{\text{crit}} + \frac{4\pi\varepsilon}{\mu''(S_{\text{crit}})} \min_{k=2,\ldots,N} g_k \,. \tag{5.45}$$

Next we consider the case $\boldsymbol{c} = \boldsymbol{e}$ for which we find from (5.43) that, to leading order, λ satisfies

$$B(\lambda, S_c) - \frac{\kappa}{1+\tau\lambda} = 0 \,. \tag{5.46}$$

First, we note that $\lambda = 0$ is not a solution of (5.46) since, by using $B(0,S) = \mu'(S)$, this would require that $\mu'(S_c) = \kappa$, which the short argument following (5.20) demonstrates is impossible. Therefore, the $\boldsymbol{c} = \boldsymbol{e}$ mode does not admit a zero-eigenvalue crossing and any instability that arises must occur through a Hopf bifurcation. We will seek a leading order threshold $\tau = \tau_h(\kappa)$ beyond which a Hopf bifurcation is triggered. To motivate the existence of such a threshold we consider first the $\kappa \to \infty$ limit for which the asymptotics (5.19) implies that $S_c = 1/(b\kappa^2) \ll 1$ so that from the small S expansion (5.3) of the core solution we calculate from (5.35b) that $\mathscr{M}_0\Phi \sim \Delta_\rho\Phi - \Phi + 2w_c\Phi + \mathscr{O}(\kappa^{-1})$. Then, by substituting this expression, together with the small S asymptotics (5.3) where $S_c \sim 1/b\kappa^2 \ll 1$, into (5.38) we can determine $B(\lambda, S_c)$ when $\kappa \gg 1$. Then, by using the resulting expression for B in (5.46), we obtain the following well-known nonlocal eigenvalue problem (NLEP) corresponding to the shadow limit $\kappa = 4\pi N D_0/|\Omega| \to \infty$:

$$1 + \tau\lambda - \frac{2\int_0^\infty w_c(\Delta_\rho - 1 + 2w_c - \lambda)^{-1} w_c^2 \rho^2 \, d\rho}{\int_0^\infty w_c^2 \rho^2 \, d\rho} = 0 \,. \tag{5.47}$$

From Table 1 in [105], this NLEP has a Hopf bifurcation at $\tau = \tau_h^\infty \approx 0.373$ with corresponding critical eigenvalue $\lambda = i\lambda_h^\infty$ with $\lambda_h^\infty \approx 2.174$. To determine $\tau_h(\kappa)$ for $\kappa = \mathscr{O}(1)$, we set $\lambda = i\lambda_h$ in (5.46) and separate the resulting expression into real and imaginary parts to obtain

$$\tau_h = -\frac{\text{Im}\left(B(i\lambda_h, S_c)\right)}{\lambda_h \text{Re}\left(B(i\lambda_h, S_c)\right)} \,, \qquad \frac{|B(i\lambda_h, S_c)|^2}{\text{Re}\left(B(i\lambda_h, S_c)\right)} - \kappa = 0 \,, \tag{5.48}$$

where S_c depends on κ from (5.18). Starting with $\kappa = 50$ we solve the second equation for λ_h using Newton's method with $\lambda_h = \lambda_h^\infty$ as an initial guess. We then use the first equation to calculate τ_h. Decreasing κ and using the previous solution as an initial guess we obtain the curves $\tau_h(\kappa)$ and $\lambda_h(\kappa)$ as shown in Figure 5.6.

We conclude this section by noting that as seen in Figures 5.6a and 5.6c the leading order Hopf bifurcation threshold diverges as $\kappa \to \kappa_{c1}^+$, where $\kappa_{c1} = \mu(S_{\rm crit})/S_{\rm crit}$. This is a direct consequence of the assumption that $\varepsilon|1+\tau\lambda|/D_0 \ll 1$ which fails to hold as τ gets increasingly large. Indeed, by using the series expansion in (3.12)–(3.14) of [89] for the reduced wave Green's function in the sphere, we can solve (5.42) directly using Newton's method for an $N = 1$ spot configuration centred at the origin of the unit ball. Fixing $\varepsilon = 0.001$, this yields the higher order asymptotic approximation for the Hopf bifurcation threshold indicated by the dashed lines in Figure 5.6. This shows that to higher order the bifurcation threshold is large but finite in the region $\kappa \le \kappa_{c1}$. Moreover, it hints at an ε dependent rescaling of τ in the region $\kappa \le \kappa_{c1}$ for which a counterpart to (5.44) may be derived. While we do not undertake this rescaling in this chapter we remark that for 2-D spot patterns this rescaling led to the discovery in [99] of an *anomalous* scaling law for the Hopf bifurcation threshold.

Stability of Asymmetric Patterns in the $D = D_0/\varepsilon$ Regime

When the N-spot pattern consists of n *large* spots of strength $S_1 = \ldots = S_n = S_r$ and $N-n$ *small* spots of strength $S_{n+1} = \ldots = S_N = S_l$, the leading order linear stability is characterized by the blocked matrix system

$$\begin{pmatrix} B(\lambda, S_r)\mathscr{I}_n & 0 \\ 0 & B(\lambda, S_l)\mathscr{I}_{N-n} \end{pmatrix} \boldsymbol{c} = \frac{\kappa}{1+\tau\lambda}\mathscr{E}_N \boldsymbol{c}\,, \tag{5.49}$$

where $\mathscr{I}_m$ denotes the $m \times m$ identity matrix. In particular, an asymmetric quasi-equilibrium solution is linearly unstable if this system admits any nontrivial modes, $\boldsymbol{c}$, for which λ has a positive real part. We will show that asymmetric patterns are always unstable by explicitly constructing unstable modes.

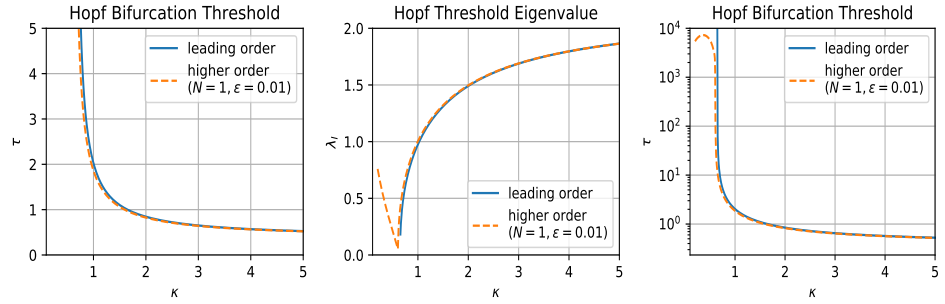

(a) **(b)** **(c)**

Figure 5.6: Leading order (a) Hopf bifurcation threshold $\tau_h(\kappa)$ and (b) critical eigenvalue $\lambda = i\lambda_h$ for a symmetric N-spot pattern as calculated by solving (5.48) numerically. The leading order theory assumes $\varepsilon|1+\tau\lambda|/D_0 \ll 1$ and is independent of the spot locations. We calculate the higher order Hopf bifurcation threshold for an $N = 1$ spot pattern centred at the origin of the unit ball with $\varepsilon = 0.01$ by solving (5.42) directly (note $\kappa = 3D_0$). In (c) we see that although the leading order Hopf bifurcation threshold diverges as $\kappa \to \kappa_{c1}$, going to higher order demonstrates that a large but finite threshold persists.

First, we assume that $1 \le n < N-1$ and we choose $\boldsymbol{c}$ to be a mode satisfying

$$c_1 = \cdots = c_n = 0\,, \qquad c_{n+1} + \cdots + c_N = 0\,. \tag{5.50}$$

Note that this mode describes *competition* among the $N-n$ small spots of strength S_l. For such a mode, (5.49) reduces to the single equation $B(\lambda, S_l) = 0$, which implies that λ must be an eigenvalue of $\mathcal{M}_0$ at $S = S_l$. However, since $S_l < S_{\rm crit}$, we deduce from Figure 5.5a that there exists a real and positive λ for $\mathcal{M}_0$ at $S = S_l$. As such, any mode $\boldsymbol{c}$ satisfying (5.50) is linearly unstable.

We must consider the $n = N-1$ case separately since (5.50) fails to yield non-trivial modes. Instead of considering competition between the small spots, we instead consider competition between large and small spots collectively. We assume that $n \ge N-n$, for which $n = N-1$ is a special case, and we try to exhibit an unstable mode $\boldsymbol{c}$ of the form

$$c_1 = \ldots = c_n = c_r\,, \qquad c_{n+1} = \ldots = c_N = c_l\,. \tag{5.51}$$

Then, (5.49) reduces to the system of two equations

$$\begin{aligned}\left(B(\lambda,S_r)-\tfrac{\kappa}{1+\tau\lambda}\tfrac{n}{N}\right)c_r-\tfrac{\kappa}{1+\tau\lambda}\tfrac{(N-n)}{N}c_l=0\,,\\ -\tfrac{\kappa}{1+\tau\lambda}\tfrac{n}{N}c_r+\left(B(\lambda,S_l)-\tfrac{\kappa}{1+\tau\lambda}\tfrac{(N-n)}{N}\right)c_l=0\,,\end{aligned}$$

which admits a nontrivial solution if and only if the determinant of this 2×2 system vanishes. Therefore, to show that this mode is unstable it suffices to prove that the zero-determinant condition, written as

$$F(\lambda)\equiv B(\lambda,S_l)B(\lambda,S_r)-\frac{\kappa}{1+\tau\lambda}\left(\frac{n}{N}B(\lambda,S_l)+\frac{(N-n)}{N}B(\lambda,S_r)\right)=0\,, \quad (5.52)$$

has a solution $\lambda>0$. To establish this, we first differentiate $\mu(S_r)=\mu(S_l)$ with respect to S_r to obtain the identity $\mu'(S_l)S_l'(S_r)=\mu'(S_r)$. Combining this result with $B(0,S)=\mu'(S)$ we calculate that

$$F(0)=\mu'(S_l)\left[\mu'(S_r)-\kappa\frac{(N-n)}{N}\left(\frac{n}{(N-n)}+\frac{dS_l}{dS_r}\right)\right]. \quad (5.53)$$

Using $\mu'(S_l)>0$ and $\mu'(S_r)<0$ together with $S_l'(S_r)>-1$ (see Figure 5.2b) and the assumption $n/(N-n)\geq 1$, we immediately deduce that $F(0)<0$. Next, we let $\lambda_0>0$ be the dominant eigenvalue of $\mathscr{M}_0$ when $S=S_l$ (see Figure 5.5a) so that $B(\lambda_0,S_l)=0$. Then, from (5.52) we obtain

$$F(\lambda_0)=-\frac{\kappa}{1+\tau\lambda_0}\frac{(N-n)}{N}B(\lambda_0,S_r)\,. \quad (5.54)$$

However, since $\mathscr{M}_0$ at $S=S_r>S_{\rm crit}$ has no positive eigenvalues (see Figure 5.5a), we deduce that $B(\lambda,S_r)$ is of one sign for $\lambda\geq 0$ and, furthermore, it must be negative since $B(0,S_r)=\mu'(S_r)<0$ (see Figure 5.5b for a plot of B showing both its continuity and negativity for all $\lambda>0$ when $S>S_{\rm crit}$). Therefore, we have $F(\lambda_0)>0$ and so, combined with (5.53), by the intermediate value theorem it follows that $F(\lambda)=0$ has a positive solution. We summarize our leading order linear stability results in the following proposition:

Proposition 5.2.1. *(Linear Stability): Let $\varepsilon\ll 1$ and assume that $t\ll\mathscr{O}(\varepsilon^{-3})$. When $D=\mathscr{O}(1)$, the N-spot symmetric pattern from Proposition 5.1.1 is linearly*

stable. If $D = \varepsilon^{-1} D_0$ then the symmetric N-spot pattern from Proposition 5.1.1 is linearly stable with respect to zero-eigenvalue crossing instabilities if $\kappa < \kappa_{c1} \equiv \mu(S_{crit})/S_{crit} \approx 0.64619$ and is unstable otherwise. Moreover, it is stable with respect to oscillatory instabilities on the range $\kappa > \kappa_{c1}$ if $\tau < \tau_h(\kappa)$ where $\tau_h(\kappa)$ is plotted in Figure 5.6a. Finally, every asymmetric N-spot pattern in the $D = \varepsilon^{-1} D_0$ regime is always linearly unstable.

5.3 Slow Spot Dynamics

A wide variety of singularly perturbed RD systems are known to exhibit slow dynamics of multi-spot solutions in 2-D domains (cf. [48], [12], [91], [103]). In this section we derive a system of ODE's which characterize the motion of the spot locations $x_1, \ldots, x_N$ for the 3-D GM model on a slow time scale. Since the only N-spot patterns that may be stable on an $\mathcal{O}(1)$ time scale are (to leading order) symmetric we find that the ODE system reduces to a gradient flow. We remark that both the derivation and final ODE system are closely related to those in [98] for the 3-D Schnakenberg model.

The derivation of slow spot dynamics hinges on establishing a solvability condition for higher order terms in the asymptotic expansion in the inner region near each spot. As a result, we begin by collecting higher order expansions of the limiting behaviour as $|x - x_i| \to 0$ of the Green's functions $G(x, x_j)$ and $G_0(x, x_j)$ that satisfy (5.8) and (5.11), respectively. In particular, we calculate that

$$G(x_i + \varepsilon y, x_j) \sim \begin{cases} G(x_i, x_j) + \varepsilon y \cdot \nabla_1 G(x_i, x_j), & i \neq j, \\ \frac{1}{4\pi\varepsilon\rho} + R(x_i) + \varepsilon y \cdot \nabla_1 R(x_i; x_i), & i = j, \end{cases} \tag{5.55a}$$

as $|x - x_i| \to 0$ where $\rho = |y|$ and $\nabla_1 R(x_i; x_i) \equiv \nabla_x R(x; x_1)|_{x=x_1}$. Likewise, for the Neumann Green's function, we have

$$G_0(x_i + \varepsilon y, x_j) \sim \frac{D_0}{\varepsilon|\Omega|} + \begin{cases} G_0(x_i, x_j) + \varepsilon y \cdot \nabla_1 G_0(x_i, x_j), & i \neq j, \\ \frac{1}{4\pi\varepsilon\rho} + R_0(x_i) + \varepsilon y \cdot \nabla_1 R_0(x_i; x_i), & i = j, \end{cases} \tag{5.55b}$$

as $|x - x_i| \to 0$ where ∇_1 again denotes the gradient with respect to the first argument. We next extend the asymptotic construction of quasi-equilibrium patterns

in §5.1 by allowing the spot locations to vary on a slow time scale. In particular, a dominant balance in the asymptotic expansion requires that $x_i = x_i(\sigma)$ where $\sigma = \varepsilon^3 t$. For x near x_i we introduce the two term inner expansion

$$\begin{aligned} v &\sim DV_i \sim D(V_{i\varepsilon}(\rho) + \varepsilon^2 V_{i2}(y) + \cdots), \\ u &\sim DU_i \sim D\big(U_{i\varepsilon}(\rho) + \varepsilon^2 U_{i2}(y) + \cdots\big), \end{aligned} \tag{5.56}$$

where we note the leading order terms are $V_{i\varepsilon}(\rho) \equiv V(\rho, S_{i\varepsilon})$ and $U_{i\varepsilon}(\rho) \equiv U(\rho, S_{i\varepsilon})$. By using the chain rule we calculate $\partial_t V_i = -\varepsilon^2 x_i'(\sigma)\cdot\nabla_y V_i$ and $\partial_t U_i = -\varepsilon^2 x_i'(\sigma)\cdot \nabla_y U_i$. In this way, upon substituting (5.56) into (5.1) we collect the $\mathcal{O}(\varepsilon^2)$ terms to obtain that V_{i2} and U_{i2} satisfy

$$\mathscr{L}_{i\varepsilon}\boldsymbol{W}_{i2} \equiv \Delta_y \boldsymbol{W}_{i2} + \mathscr{Q}_{i\varepsilon}\boldsymbol{W}_{i2} = -\boldsymbol{f}_{i\varepsilon}\,, \qquad y \in \mathbb{R}^2\,, \tag{5.57a}$$

where

$$\begin{aligned} \boldsymbol{W}_{i2} \equiv \begin{pmatrix} V_{i2} \\ U_{i2} \end{pmatrix}, \qquad \boldsymbol{f}_{i\varepsilon} \equiv \begin{pmatrix} \rho^{-1} V_{i\varepsilon}'(\rho)\, x_i'(\sigma)\cdot y \\ -D^{-1} U_{i\varepsilon} \end{pmatrix}, \\ \mathscr{Q}_{i\varepsilon} \equiv \begin{pmatrix} -1 + 2U_{i\varepsilon}^{-1} V_{i\varepsilon} & -U_{i\varepsilon}^{-2} V_{i\varepsilon}^2 \\ 2V_{i\varepsilon} & 0 \end{pmatrix}. \end{aligned} \tag{5.57b}$$

It remains to determine the appropriate limiting behaviour as $\rho \to \infty$. From the first row of $\mathscr{Q}_{i\varepsilon}$, we conclude that $V_{i2} \to 0$ exponentially as $\rho \to \infty$. However, the limiting behaviour of U_{i2} must be established by matching with the outer solution. To perform this matching, we first use the distributional limit

$$\varepsilon^{-2} v^2 \longrightarrow 4\pi\varepsilon D^2 \sum_{j=1}^N S_{j\varepsilon}\delta(x-x_j) + 2\varepsilon^3 D^2 \sum_{j=1}^N \left(\int_{\mathbb{R}^3} V_{j\varepsilon} V_{j2}\, dy\right) \delta(x-x_j)\,,$$

as $\varepsilon \to 0$ where the localization at each $x_1, \ldots, x_N$ eliminates all cross terms. We then update (5.9) to include the $\mathcal{O}(\varepsilon^3)$ correction term. This leads to the refined approximation for the outer solution

$$u \sim 4\pi\varepsilon D \sum_{j=1}^N S_{j\varepsilon} G(x;x_j) + 2\varepsilon^3 D \sum_{j=1}^N \left(\int_{\mathbb{R}^3} V_{j\varepsilon} V_{j2}\, dy\right) G(x;x_j)\,. \tag{5.58}$$

We observe that the leading order matching condition is immediately satisfied in both the $D = \mathscr{O}(1)$ and the $D = D_0/\varepsilon$ regimes. To establish the higher order matching condition we distinguish between the $D = \mathscr{O}(1)$ and $D = \varepsilon^{-1}D_0$ regimes and use the higher order expansions of the Green's functions as given by (5.55a) and (5.55b). In this way, in the $D = \mathscr{O}(1)$ regime we obtain the far-field behaviour as $|y| \to \infty$ given by

$$U_{i2} \sim \frac{1}{2\pi\rho} \int_{\mathbb{R}^3} V_{i\varepsilon} V_{i2}\, dy + y \cdot b_{i\varepsilon}\,, \tag{5.59a}$$

where

$$\frac{b_{i\varepsilon}}{4\pi} \equiv S_{i\varepsilon} \nabla_1 R(x_i; x_i) + \sum_{j \neq i} S_{j\varepsilon} \nabla_1 G(x_i, x_j)\,. \tag{5.59b}$$

Similarly, in the $D = D_0/\varepsilon$ regime we obtain the following far-field matching condition as $|y| \to \infty$:

$$U_{i2} \sim \frac{1}{2\pi\rho} \int_{\mathbb{R}^3} V_{i\varepsilon} V_{i2}\, dy + \frac{2D_0}{|\Omega|} \sum_{j=1}^{N} \int_{\mathbb{R}^3} V_{j\varepsilon} V_{j2}\, dy + y \cdot b_{0i\varepsilon}\,, \tag{5.60a}$$

where

$$\frac{b_{0i\varepsilon}}{4\pi} \equiv S_{i\varepsilon} \nabla_1 R_0(x_i; x_i) + \sum_{j \neq i} S_{j\varepsilon} \nabla_1 G_0(x_i, x_j)\,. \tag{5.60b}$$

In both cases, our calculations below will show that only $b_{i\varepsilon}$ and $b_{0i\varepsilon}$ affect the slow spot dynamics.

To characterize slow spot dynamics we calculate $x_i'(\sigma)$ by formulating an appropriate solvability condition. We observe for each $k = 1, 2, 3$ that the functions $\partial_{y_k} \boldsymbol{W}_{i\varepsilon}$ where $\boldsymbol{W}_{i\varepsilon} \equiv (V_{i\varepsilon}, U_{i\varepsilon})^T$ satisfy the homogeneous problem $\mathscr{L}_{i\varepsilon} \partial_{y_k} \boldsymbol{W}_{i\varepsilon} = 0$. Therefore, the null-space of the adjoint operator $\mathscr{L}_{i\varepsilon}^{\star}$ is at least three-dimensional. Assuming it is exactly three dimensional we consider the three linearly independent solutions $\boldsymbol{\Psi}_{ik} \equiv y_k \boldsymbol{P}_i(\rho)/\rho$ to the homogeneous adjoint problem, where each $\boldsymbol{P}_i(\rho) = (P_{i1}(\rho), P_{i2}(\rho)^T$ solves

$$\Delta_\rho \boldsymbol{P}_i - \frac{2}{\rho^2} \boldsymbol{P}_i + \mathscr{Q}_{i\varepsilon}^T \boldsymbol{P}_i = 0\,, \quad \rho > 0\,; \quad \boldsymbol{P}_i'(0) = \begin{pmatrix} 0 \\ 0 \end{pmatrix}\,, \tag{5.61}$$

and for which we note

$$\mathscr{Q}_{i\varepsilon}^T \longrightarrow \begin{pmatrix} -1 & 0 \\ 0 & 0 \end{pmatrix} \quad \text{as } \rho \to \infty. \tag{5.62}$$

Owing to this limiting far-field behaviour of the matrix $\mathscr{Q}_{i\varepsilon}^T$, we immediately deduce that $P_{i2} = \mathscr{O}(\rho^{-2})$ and that P_{i1} decays exponentially to zero as $\rho \to \infty$. Enforcing, for convenience, the point normalization condition $P_{i2} \sim \rho^{-2}$ as $\rho \to \infty$, we find that (5.61) admits a unique solution. We use each $\boldsymbol{\Psi}_{ik}$ to impose a solvability condition by multiplying (5.57a) by $\boldsymbol{\Psi}_{ik}^T$ and integrating over the ball, B_{ρ_0}, centred at the origin and of radius ρ_0 with $\rho_0 \gg 1$. Then, by using the divergence theorem, we calculate

$$\begin{aligned} \lim_{\rho_0\to\infty} \int_{B_{\rho_0}} \left(\boldsymbol{\Psi}_{ik}^T \mathscr{L}_i \boldsymbol{W}_{i2} - \boldsymbol{W}_{i2} \mathscr{L}_i^\star \boldsymbol{\Psi}_{ik} \right) dy \\ = \lim_{\rho_0\to\infty} \int_{\partial B_{\rho_0}} \left(\boldsymbol{\Psi}_{ik}^T \partial_\rho \boldsymbol{W}_{i2} - \boldsymbol{W}_{i2}^T \partial_\rho \boldsymbol{\Psi}_{ik} \right) \Big|_{\rho=\rho_0} \rho_0^2 \, d\Theta, \end{aligned} \tag{5.63}$$

where Θ denotes the solid angle for the unit sphere.

To proceed, we use the following simple identities given in terms of the Kronecker symbol δ_{kl}:

$$\int_{B_{\rho_0}} y_k f(\rho)\, dy = 0, \qquad \int_{B_{\rho_0}} y_k y_l f(\rho)\, dy = \delta_{kl} \frac{4\pi}{3} \int_0^{\rho_0} \rho^4 f(\rho)\, d\rho, \tag{5.64}$$

for $l,k = 1,2,3$. Since $\mathscr{L}_i^\star \boldsymbol{\Psi}_{ik} = 0$, we can use (5.57a) and (5.64) to calculate the left-hand side of (5.63) as

$$\begin{aligned} \lim_{\rho_0\to\infty} \int_{B_{\rho_0}} \boldsymbol{\Psi}_{ik}^T \mathscr{L}_i \boldsymbol{W}_{i2} dy = \lim_{\rho_0\to\infty} \Bigg(-\sum_{l=1}^{3} x_{il}'(\sigma) \int_{B_{\rho_0}} y_k y_l \frac{P_{i1}(\rho) V_{i\varepsilon}'(\rho)}{\rho^2}\, dy \\ + \frac{1}{D} \int_{B_{\rho_0}} y_k \frac{P_{i2}(\rho) U_{i\varepsilon}(\rho)}{\rho}\, dy \Bigg) \\ = -\frac{4\pi}{3} x_{ik}'(\sigma) \int_0^\infty P_{i1}(\rho) V_{i\varepsilon}'(\rho) \rho^2\, d\rho. \end{aligned} \tag{5.65}$$

Next, in calculating the right-hand side of (5.63) by using the far-field behaviour

(5.59) and (5.60), we observe that only $b_{i\varepsilon}$ and $b_{0i\varepsilon}$ terms play a role in the limit. In particular, in the $D = \mathcal{O}(1)$ regime we calculate in terms of the components of $b_{i\varepsilon l}$ of the vector $b_{i\varepsilon}$, as given in (5.59), that

$$\begin{aligned}
&\lim_{\rho_0\to\infty}\int_{\partial B_{\rho_0}} \boldsymbol{\Psi}_{ik}^T\partial_\rho \boldsymbol{W}_{i2}\big|_{\rho=\rho_0}\rho_0^2\,d\Theta = \lim_{\rho_0\to\infty}\sum_{l=1}^3 b_{i\varepsilon l}\int_{\partial B_{\rho_0}}\frac{y_k y_l}{\rho_0^2}\,d\Theta = \frac{4\pi}{3}b_{i\varepsilon k}\,,\\
&\lim_{\rho_0\to\infty}\int_{\partial B_{\rho_0}} \boldsymbol{W}_{i2}^T\partial_\rho \boldsymbol{\Psi}_{ik}\big|_{\rho=\rho_0}\rho_0^2\,d\Theta = -2\lim_{\rho_0\to\infty}\sum_{l=1}^3 b_{i\varepsilon l}\int_{\partial B_{\rho_0}}\frac{y_k y_l}{\rho_0^2}\,d\Theta = -\frac{8\pi}{3}b_{i\varepsilon k}\,.
\end{aligned} \tag{5.66}$$

From (5.63), (5.65), and (5.66), we conclude for the $D = \mathcal{O}(1)$ regime that

$$x_{ik}'(\sigma) = -\frac{3}{\gamma(S_{i\varepsilon})}\,b_{i\varepsilon k}\,, \qquad \gamma(S_{i\varepsilon}) \equiv \int_0^\infty P_{i1}(\rho)V_i'(\rho,S_{i\varepsilon})\rho^2\,d\rho\,, \tag{5.67}$$

which holds for each component $k = 1,2,3$ and each spot $i = 1,\ldots,N$. From symmetry considerations we see that the constant contribution to the far-field behaviour, as given by the first term in (5.59), is eliminated when integrated over the boundary. In an identical way, we can determine x_{ik}' for the $D = D_0/\varepsilon$ regime. In summary, in terms of the gradients of the Green's functions and $\gamma_{i\varepsilon} \equiv \gamma(S_{i\varepsilon})$, as defined in (5.67), we obtain the following vector-valued ODE systems for the two distinguished ranges of D:

$$\frac{dx_i}{d\sigma} = -\frac{12\pi}{\gamma_{i\varepsilon}}\begin{cases}\Big(S_{i\varepsilon}\nabla_1 R(x_i;x_i) + \sum_{j\neq i} S_{j\varepsilon}\nabla_1 G(x_i,x_j)\Big)\,, & \text{for } D = \mathcal{O}(1)\,,\\ \Big(S_{i\varepsilon}\nabla_1 R_0(x_i;x_i) + \sum_{j\neq i} S_{j\varepsilon}\nabla_1 G_0(x_i,x_j)\Big)\,, & \text{for } D = D_0/\varepsilon\,.\end{cases} \tag{5.68}$$

Since only the symmetric N-spot configurations can be stable on an $\mathcal{O}(1)$ time scale (see Proposition 5.2.1), it suffices to consider the ODE systems in (5.68) when $S_{i\varepsilon} = S_\star + \mathcal{O}(\varepsilon)$ in the $D = \mathcal{O}(1)$ regime and when $S_{i\varepsilon} = S_c + \mathcal{O}(\varepsilon)$, where S_c solves (5.18), in the $D = \varepsilon^{-1}D_0$ regime. In particular, we find that to leading order, where the $\mathcal{O}(\varepsilon)$ corrections to the spot strengths are neglected, the ODE systems in (5.68) can be reduced to the gradient flow dynamics

$$\frac{dx_i}{d\sigma} = -\frac{6\pi S}{\gamma(S)}\nabla_{x_i}\mathcal{H}(x_1,\ldots,x_N)\,, \quad \gamma(S) = \int_0^\infty P_1(\rho)V_1(\rho,S)\rho^2\,d\rho\,, \tag{5.69a}$$

where $S = S_\star$ or $S = S_c$ depending on whether $D = \mathcal{O}(1)$ or $D = \varepsilon^{-1}D_0$, respectively. In (5.69) the discrete energy $\mathcal{H}$, which depends on the instantaneous spot locations, is

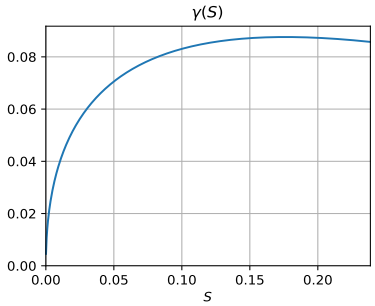

Figure 5.7: Plot of the numerically-computed multiplier $\gamma(S)$ as defined in the slow gradient flow dynamics (5.69).

defined by

$$\mathscr{H}(x_1,\ldots,x_N) \equiv \begin{cases} \sum_{i=1}^N R(x_i) + 2\sum_{i=1}^N \sum_{j>i} G(x_i,x_j)\,, & \text{for} \quad D = \mathscr{O}(1)\,, \\ \sum_{i=1}^N R_0(x_i) + 2\sum_{i=1}^N \sum_{j>i} G_0(x_i,x_j)\,, & \text{for} \quad D = \varepsilon^{-1} D_0\,. \end{cases} \tag{5.69b}$$

In accounting for the factor of two between (5.69) and (5.68), we used the reciprocity relations for the Green's functions. In this leading order ODE system, the integral $\gamma(S)$ is the same for each spot, since $P_1(\rho)$ is computed numerically from the homogeneous adjoint problem (5.61) using the core solution $V_1(\rho,S)$ and $U_1(\rho,S)$ to calculate the matrix $\mathscr{Q}_{i\varepsilon}^T$ in (5.61). In Figure 5.7 we plot the numerically-computed $\gamma(S)$, where we note that $\gamma(S) > 0$. Since $\gamma(S) > 0$, local minima of $\mathscr{H}$ are linearly stable equilibrium solutions to (5.69).

We remark that this gradient flow system (5.69) differs from that derived in [98] for the 3-D Schnakenberg model only through the constant $\gamma(S)$. Since this parameter affects only the time-scale of the slow dynamics we deduce that the equilibrium configurations and stability properties for the ODE dynamics will be identical to those of the Schnakenberg model. As such, we do not analyze (5.69) further and instead refer to [98] for more detailed numerical investigations. Finally we note that the methods employed here and in [98] should be applicable to other 3-D RD systems yielding similar limiting ODE systems for slow spot dynamics. The similarity between slow dynamics for a variety of RD systems in 2-D has been previously observed and a general asymptotic framework has been pursued in [91] for the dynamics on the sphere.

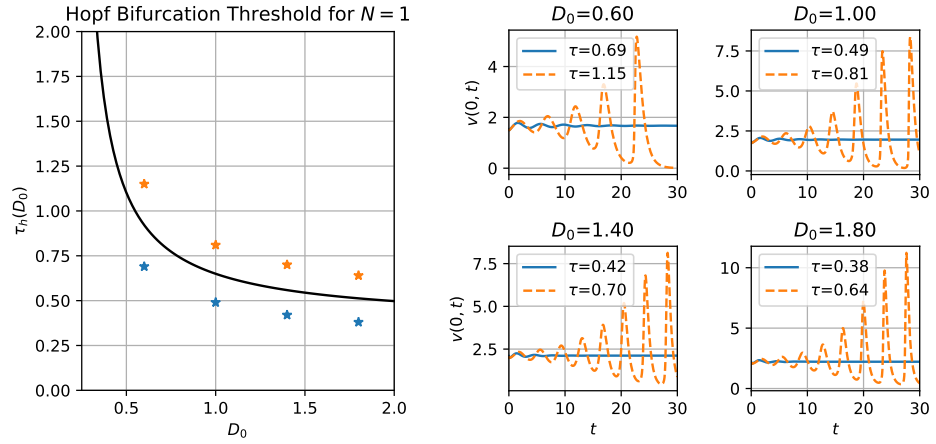

Figure 5.8: (a) Leading order Hopf bifurcation threshold for a one-spot pattern. (b) Plots of the spot height $v(0,t)$ from numerically solving (5.1) using FlexPDE6 [1] in the unit ball with $\varepsilon = 0.05$ at the indicated τ and D_0 values.

5.4 Numerical Examples

In this section we use FlexPDE6 [1] to numerically solve (5.1) when Ω is the unit ball. In particular, we illustrate the emergence of oscillatory and competition instabilities, as predicted in §5.2 for symmetric spot patterns in the $D = D_0/\varepsilon$ regimes.

We begin by considering a single spot centred at the origin in the unit ball, for the $D = \varepsilon^{-1}D_0$ regime. Since no competition instabilities occur for a single spot solution, we focus exclusively on the onset of oscillatory instabilities as τ is increased. In Figure 5.8a we plot the Hopf bifurcation threshold obtained from our linear stability theory, and indicate several sample points below and above the threshold. Using FlexPDE6 [1], we performed full numerical simulations of (5.1) in the unit ball with $\varepsilon = 0.05$ and parameters D_0 and τ corresponding to the labelled points in Figure 5.8a. The resulting activator height at the origin, $v(0,t)$, computed from FlexPDE6 is shown in Figure 5.8b for these indicated parameter values. We observe that there is good agreement with the onset of Hopf bifurcations as predicted by our linear stability theory.

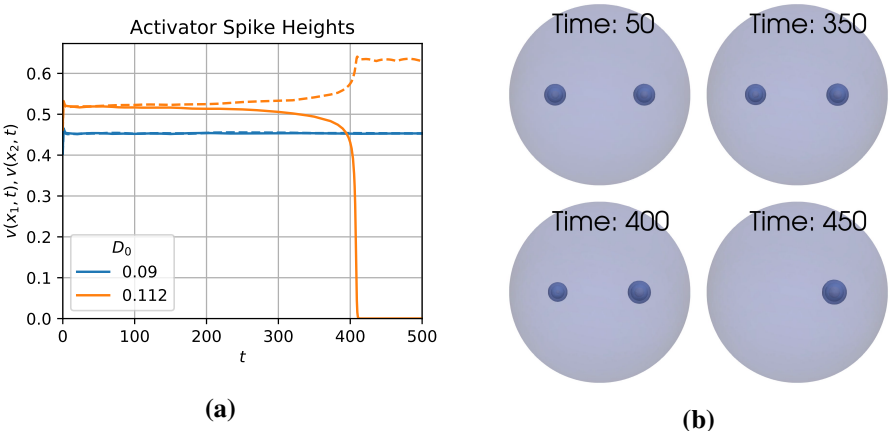

(a) **(b)**

Figure 5.9: (a) Plots of the spot heights (solid and dashed lines) in a two-spot symmetric pattern at the indicated values of D_0. Results were obtained by using FlexPDE6 [1] to solve (5.1) in the unit ball with $\varepsilon = 0.05$ and $\tau = 0.2$. (b) plot of three-dimensional contours of $v(x,t)$ for $D_0 = 0.112$, with contours chosen at $v = 0.1, 0.2, 0.4$.

Next, we illustrate the onset of a competition instability by considering a symmetric two-spot configurations with spots centred at $(\pm 0.51565, 0, 0)$ in the unit ball and with $\tau = 0.2$ (chosen small enough to avoid Hopf bifurcations) and $\varepsilon = 0.05$. The critical value of $\kappa_{c1} \approx 0.64619$ then implies that the leading order competition instability threshold for the unit ball with $|\Omega| = 4\pi/3$ is $D_0 \approx 0.64619/(3N) = 0.108$. We performed full numerical simulations of (5.1) using FlexPDE6 [1] with values of $D_0 = 0.09$ and $D_0 = 0.112$. The results of our numerical simulations are shown in Figure 5.9, where we observe that a competition instability occurs for $D_0 = 0.112$, as predicted by the linear stability theory. Moreover, in agreement with previous studies of competition instabilities (cf. [98], [12]), we observe that a competition instability triggers a nonlinear event leading to the annihilation of one spot.

5.5 The Weak Interaction Limit $D = \mathcal{O}(\varepsilon^2)$

In §5.2 we have shown in both the $D = \mathcal{O}(1)$ and $D = \mathcal{O}(\varepsilon^{-1})$ regimes that N-spot quasi-equilibrium solutions are not susceptible to locally non-radially symmetric instabilities. Here we consider the weak-interaction regime $D = D_0\varepsilon^2$, where we

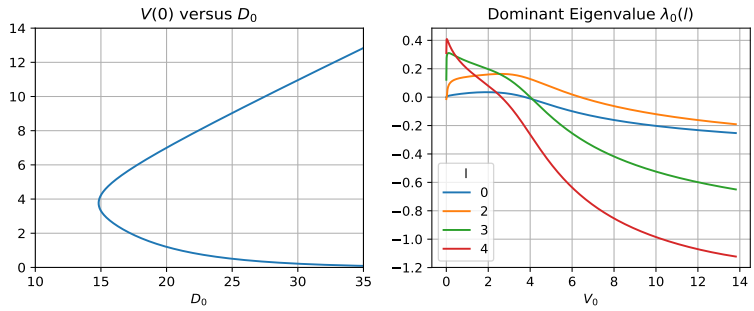

(a) **(b)**

Figure 5.10: (a) Bifurcation diagram for solutions to the core problem (5.70) in the $D = \varepsilon^2 D_0$ regime. (b) Dominant eigenvalue of the linearization of the core problem for each mode $l = 0, 2, 3, 4$, as computed numerically from (5.74).

numerically determine that locally non-radially symmetric instabilities of a localized spot are possible. First, we let $\xi \in \Omega$ satisfy $\text{dist}(\xi, \partial\Omega) \gg \mathcal{O}(\varepsilon^2)$ and we introduce the local coordinates $x = \xi + \varepsilon y$ and the inner variables $v \sim \varepsilon^2 V(\rho)$ and $u \sim \varepsilon^2 U(\rho)$. With this scaling, and with $D = D_0\varepsilon^2$, the steady-state problem for (5.1) becomes

$$\Delta_\rho V - V + U^{-1}V^2 = 0\,, \qquad D_0\Delta_\rho U - U + V^2 = 0\,, \qquad \rho = |y| > 0\,. \tag{5.70}$$

For this core problem, we impose the boundary conditions $V_\rho(0) = U_\rho(0) = 0$ and $(V,U) \to 0$ exponentially as $\rho \to \infty$. Unlike the $D = \mathcal{O}(1)$ and $D = \mathcal{O}(\varepsilon^{-1})$ regimes, u and v are both exponentially small in the outer region. Therefore, for any well-separated configuration $x_1, \ldots, x_N$, the inner problems near each spot centre are essentially identical and independent. In Figure 5.10a we plot $V(0)$ versus D_0 obtained by numerically solving (5.70). From this figure, we observe that for all $D_0 \gtrapprox 14.825$, corresponding to a saddle-node point, the core problem (5.70) admits two distinct radially-symmetric solutions.

Since both the activator V and inhibitor U decay exponentially there are only exponentially weak interactions between individual spots. As a result, it suffices to consider only the linear stability of the core problem (5.70). Upon linearizing (5.1)

about the core solution we obtain the eigenvalue problem

$$\begin{aligned} \Delta_\rho \Phi - \frac{l(l+1)}{\rho^2}\Phi - \Phi + \frac{2V}{U}\Phi - \frac{V^2}{U^2}\Psi = \lambda\Phi, \\ D_0\Delta_\rho \Psi - \frac{l(l+1)}{\rho^2}\Psi - \Psi + 2V\Phi = 0, \end{aligned} \tag{5.71}$$

for each $l \geq 0$ and for which we impose that $\Phi'(0) = \Psi'(0) = 0$ and $(\Phi, \Psi) \to 0$ exponentially as $\rho \to \infty$. We reduce (5.71) to a single nonlocal equation by noting that the Green's function $G_l(\rho, \rho_0)$ satisfying

$$D_0\Delta_\rho G_l - \frac{l(l+1)}{\rho^2}G_l - G_l = -\frac{\delta(\rho-\rho_0)}{\rho^2}, \tag{5.72}$$

is given explicitly by

$$G_l(\rho,\rho_0) = \frac{1}{D_0\sqrt{\rho_0\rho}} \begin{cases} I_{l+1/2}(\rho/\sqrt{D_0})K_{l+1/2}(\rho_0/\sqrt{D_0}), & \rho < \rho_0, \\ I_{l+1/2}(\rho_0/\sqrt{D_0})K_{l+1/2}(\rho/\sqrt{D_0}), & \rho > \rho_0, \end{cases} \tag{5.73}$$

where $I_n(\cdot)$ and $K_n(\cdot)$ are the n^{th} order modified Bessel Functions of the first and second kind, respectively. As a result, by proceeding as in §5.2 we reduce (5.71) to the nonlocal spectral problem $\mathscr{M}_l\Phi = \lambda\Phi$ where

$$\begin{aligned} \mathscr{M}_l\Phi \equiv \Delta_\rho\Phi - \frac{l(l+1)}{\rho^2}\Phi - \Phi + \frac{2V}{U}\Phi \\ - \frac{2V^2}{U^2}\int_0^\infty G_l(\rho,\tilde{\rho})\,V(\tilde{\rho})\,\Phi(\tilde{\rho})\tilde{\rho}^2\,d\tilde{\rho}\,. \end{aligned} \tag{5.74}$$

In Figure 5.10b we plot the real part of the largest numerically-computed eigenvalue of $\mathscr{M}_l$ as a function of $V(0)$ for $l = 0,2,3,4$. From this figure, we observe that the entire lower solution branch in the $V(0)$ versus D_0 bifurcation diagram in Figure 5.10a is unstable. However, in contrast to the $D = \mathscr{O}(1)$ and $D = \mathscr{O}(\varepsilon^{-1})$ regimes, we observe from the orange curve in Figure 5.10b for the $l = 2$ mode that when $D = \varepsilon^2 D_0$ there is a range of D_0 values for which a peanut-splitting instability is the only unstable mode.

In previous studies of singularly perturbed RD systems supporting peanut-

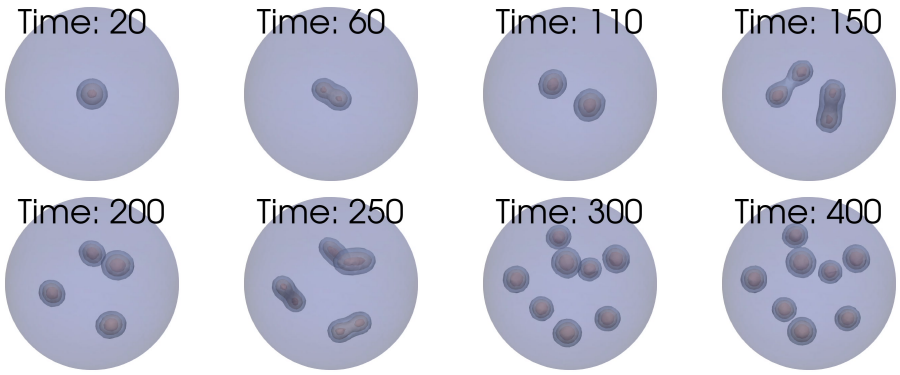

Figure 5.11: Snapshots of FlexPDE6 [1] simulation of (5.1) in the unit ball with $\varepsilon = 0.05$, $D = 16\varepsilon^2$, and $\tau = 1$ and with initial condition given by a single spot solution in the weak interaction limit calculated from (5.70) with $V(0) = 5$. The snapshots show contour plots of the activator $v(x,t)$ at different times where for each spot the outermost, middle, and innermost contours correspond to values of 0.006, 0.009, and 0.012 respectively. Note that the asymptotic theory predicts a maximum peak height of $v \sim \varepsilon^2 V(0) \approx 0.0125$.

splitting instabilities it has typically been observed that such linear instabilities trigger nonlinear spot self-replication events (cf. [98], [48], [91], and [12]). Recently, in [113] it has been shown using a hybrid analytical-numerical approach that peanut-splitting instabilities are subcritical for the 2-D Schnakenberg, Gray-Scott, and Brusselator models, although the corresponding issue in a 3-D setting is still an open problem. Our numerical computations below suggest that peanut-splitting instabilities for the 3-D GM model in the $D = \varepsilon^2 D_0$ regime are also subcritical. Moreover, due to the exponentially small interaction between spots, we also hypothesize that a peanut-splitting instability triggers a cascade of spot self-replication events that will eventually pack the domain with identical spots. To explore this proposed behaviour we use FlexPDE6 [1] to numerically solve (5.1) in the unit ball with parameters $\tau = 1$, $\varepsilon = 0.05$ and $D_0 = 16\varepsilon^2$, where the initial condition is a single spot pattern given asymptotically by the solution to (5.70) with $V(0) = 5$. From the bifurcation and stability plots of Figure 5.10 our parameter values and initial conditions are in the range where a peanut-splitting instability occurs. In Figure 5.11 we plot contours of the solution $v(x,t)$ at various times. We

observe that the peanut-splitting instability triggered between $t = 20$ and $t = 60$ leads to a self-replication process resulting in two identical spots at $t = 110$. The peanut-splitting instability is triggered for each of these two spots and this process repeats, leading to a packing of the domain with $N = 8$ identical spots.

5.6 General Gierer-Meinhardt Exponents

Next, we briefly consider the generalized GM model

$$\begin{gathered} v_t = \varepsilon^2 \Delta v - v + u^{-q} v^p \,, \quad \tau u_t = D\Delta u - u + \varepsilon^{-2} u^{-s} v^m \,, \quad x \in \Omega \,; \\ \partial_n v = \partial_n u = 0 \,, \quad x \in \partial\Omega \,, \end{gathered} \tag{5.75}$$

where the GM exponents (p,q,m,s) satisfy the usual conditions $p > 1$, $q > 0$, $m > 1$, $s \geq 0$, and $\zeta \equiv mq/(p-1) - (s+1) > 0$ (cf. [105]). Although this general exponent set leads to some quantitative differences as compared to the prototypical set $(p,q,m,s) = (2,1,2,0)$ considered in this chapter, many of the qualitative properties resulting from the properties of $\mu(S)$ in Conjecture 5.1.1, such as the existence of symmetric quasi-equilibrium spot patterns in the $D = \mathcal{O}(1)$ regime, remain unchanged.

Suppose that (5.75) has an N-spot quasi-equilibrium solution with well-separated spots. Near the i^{th} spot we introduce the inner expansion $v \sim D^{\alpha} V_i(y)$, $u \sim D^{\beta} U_i(y)$, and $y = \varepsilon^{-1}(x - x_i)$, where

$$\begin{aligned} \Delta V_i - V_i + D^{(p-1)\alpha - q\beta} U_i^{-q} V_i^p = 0 \,, \qquad & y \in \mathbb{R}^3 \\ \Delta U_i - \varepsilon^2 D^{-1} U_i = -D^{m\alpha - (s+1)\beta - 1} U_i^{-s} V_i^m \,, \qquad & y \in \mathbb{R}^3 \,. \end{aligned}$$

Choosing α and β such that $(p-1)\alpha - q\beta = 0$ and $m\alpha - (s+1)\beta = 1$ we obtain

$$\alpha = \nu/\zeta \,, \qquad \beta = 1/\zeta \,, \qquad \nu = q/(p-1) \,,$$

with which the inner expansion takes the form $v \sim D^{\nu/\zeta} V(\rho; S_{i\varepsilon})$ and $u \sim D^{1/\zeta} U(\rho; S_{i\varepsilon})$, where $V(\rho;S)$ and $U(\rho;S)$ are radially-symmetric solutions to the *D-independent*

core problem

$$\Delta_\rho V - V + U^{-q}V^p = 0\,, \quad \Delta_\rho U = -U^{-s}V^m\,, \qquad \rho > 0\,, \tag{5.76a}$$

$$\partial_\rho V(0) = \partial_\rho U(0) = 0\,, \quad V \to 0 \quad \text{and} \quad U \sim \mu(S) + S/\rho\,, \qquad \rho \to \infty\,. \tag{5.76b}$$

By using the divergence theorem, we obtain the identity $S = \int_0^\infty U^{-s}V^m\rho^2\,d\rho > 0$.

By solving the core problem (5.76) numerically, we now illustrate that the function $\mu(S)$ retains several of the key qualitative properties of the exponent set $(p,q,m,s) = (2,1,2,0)$ observed in §5.1.1, which were central to the analysis in §5.1 and §5.2. To path-follow solutions, we proceed as in §5.1.1 by first approximating solutions to (5.76) for $S \ll 1$. For $S \ll 1$, we use the identity $S = \int_0^\infty U^{-s}V^m\rho^2\,d\rho > 0$ to motivate a small S scaling law, and from this we readily calculate that

$$V(\rho;S) \sim \left(\frac{S}{b}\right)^{\frac{v}{\zeta+1}} w_c(\rho)\,, \quad U(\rho;S) \sim \left(\frac{S}{b}\right)^{\frac{1}{\zeta+1}}\,, \quad \mu(S) \sim \left(\frac{S}{b}\right)^{\frac{1}{\zeta+1}}\,, \tag{5.77}$$

where

$$b \equiv \int_0^\infty w_c^m\rho^2 d\rho\,,$$

and $w_c > 0$ is the radially-symmetric solution of

$$\Delta_\rho w_c - w_c + w_c^p = 0\,, \quad \rho > 0\,; \quad \partial_\rho w_c(0) = 0, \qquad w_c \to 0, \quad \rho \to \infty\,. \tag{5.78}$$

With this approximate solution for $S \ll 1$, we proceed as in §5.1.1 to calculate $\mu(S)$ in (5.76) for different GM exponent sets by path-following in S. In Figure 5.12b we plot $\mu(S)$ when $(p,q,m,s) = (p,1,p,0)$ with $p = 2,3,4$, while a similar plot is shown in Figure 5.12a for other typical exponent sets in [105]. For each set considered, we find that $\mu(S)$ satisfies the properties in Conjecture 5.1.1. Finally, to obtain the NAS for the spot strengths we proceed as in §5.1.2 to obtain that the outer solution for the inhibitor field is given by simply replacing D with $D^{1/\zeta}$ in (5.9). Then, by using the matching condition $u \sim D^{1/\zeta}\left(\mu(S_{j\varepsilon}) + S_{j\varepsilon}\varepsilon/|x - x_j|\right)$ as $x \to x_j$, for each $j = 1,\ldots,N$, we conclude that the NAS (5.15) still holds for a general GM exponent set provided that $\mu(S)$ is now defined by the generalized

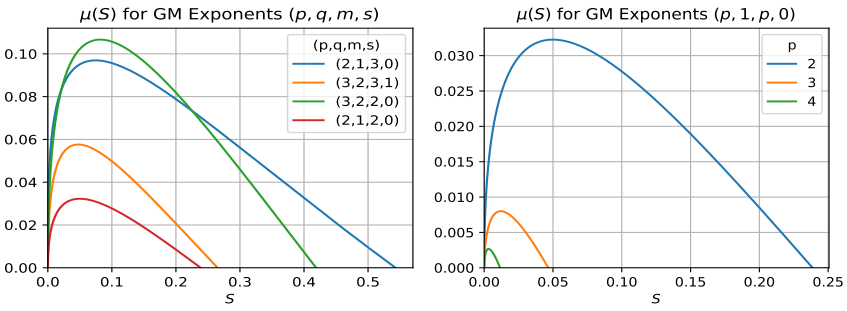

(a) **(b)**

Figure 5.12: Left panel: Plot of $\mu(S)$, computed from the generalized GM core problem (5.76), for the indicated exponent sets (p,q,m,s). Right panel: $\mu(S)$ for exponent sets $(p,1,p,0)$ with $p=2,3,4$. For each set, there is a unique $S=S_\star$ for which $\mu(S_\star)=0$. The properties of $\mu(S)$ in Conjecture 5.1.1 for the prototypical set $(2,1,2,0)$ still hold.

core problem (5.76).

5.7 Discussion

We have used the method of matched asymptotic expansions to construct and study the linear stability of N-spot quasi-equilibrium solutions to the 3-D GM model (5.1) in the limit of an asymptotically small activator diffusivity $\varepsilon \ll 1$. Our key contribution has been the identification of two distinguished regimes for the inhibitor diffusivity, the $D=\mathcal{O}(1)$ and $D=\mathcal{O}(\varepsilon^{-1})$ regimes, for which we constructed N-spot quasi-equilibrium patterns, analyzed their linear stability, and derived an ODE system governing their slow spot dynamics. We determined that in the $D=\mathcal{O}(1)$ regime all N-spot patterns are, to leading order in ε, symmetric and linearly stable on an $\mathcal{O}(1)$ time scale. On the other hand, in the $D=\mathcal{O}(\varepsilon^{-1})$ regime we found the existence of both symmetric and asymmetric N-spot patterns. However, we demonstrated that all asymmetric patterns are unstable on an $\mathcal{O}(1)$ time scale, while for the symmetric patterns we calculated synchronous and competition instability thresholds. These GM results are related to those in [98] for the

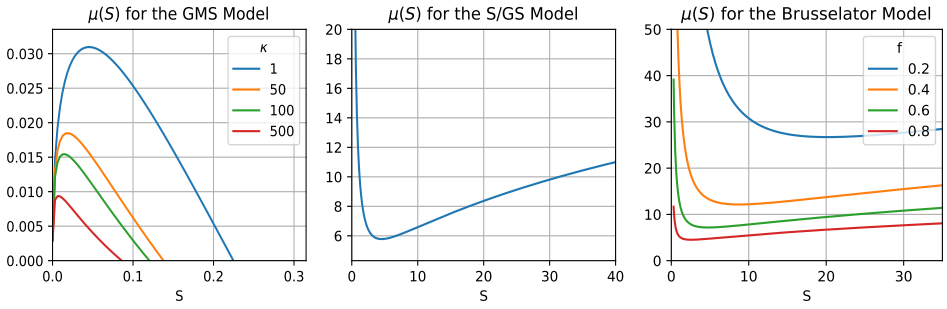

(a) **(b)** **(c)**

Figure 5.13: Plots of the far-field constant behaviour for the (a) Gierer-Meinhardt with saturation, (b) Schnakenberg or Gray-Scott, and (c) Brusselator models. See Table 5.1 for the explicit form of the kinetics $F(v,u)$ and $G(v,u)$ for each model. A zero-crossing of $\mu(S)$ at some $S > 0$ occurs only for the GMS model.

3-D singularly perturbed Schnakenberg model, with one of the key new features being the emergence of *two* distinguished limits, and in particular the existence of localized solutions in the $D = \mathcal{O}(1)$ regime for the GM model. For $D = \mathcal{O}(1)$, concentration behaviour for the Schnakenberg model as $\varepsilon \to 0$ is no longer at discrete points typical of spot patterns, but instead appears to occur on higher co-dimension structures such as thin sheets and tubes in 3-D (cf. [94]). For the GM model, we illustrated the onset of both oscillatory and competition instabilities by numerically solving the full GM PDE system using the finite element software FlexPDE6 [1]. We have also considered the weak-interaction regime $D = \mathcal{O}(\varepsilon^2)$, where we used a hybrid analytical-numerical approach to calculate steady-state solutions and determine their linear stability properties. In this small D regime we found that spot patterns are susceptible to peanut-splitting instabilities. Finally, using FlexPDE6 we illustrated how the weak-interaction between spots together with the peanut-splitting instability leads to a cascade of spot self-replication events.

We conclude by highlighting directions for future work and open problems. First, although we have provided numerical evidence for the properties of $\mu(S)$ highlighted in Conjecture 5.1.1, a rigorous proof remains to be found. In partic-

RD Model	$F(V,U)$	$G(V,U)$	Decay behaviour
Gierer-Meinhardt w/ Saturation (GMS)	$-V+\frac{V^2}{U(1+\kappa U^2)}$	V^2	$U\sim\mu(S)+S/\rho$
Schnakenberg or Gray-Scott (S/GS)	$-V+V^2U$	$-V^2U$	$U\sim\mu(S)-S/\rho$
Brusselator (B)	$-V+fV^2U$	$V-V^2U$	$U\sim\mu(S)-S/\rho$

Table 5.1: Core problems and inhibitor decay behaviour for some RD systems. In each case the activator decays exponentially.

ular, we believe that it would be significant contribution to rigorously prove the existence and uniqueness of the *ground state* solution to the core problem (5.2), which we numerically calculated when $S = S_\star$. A broader and more ambitious future direction is to characterize the reaction kinetics $F(V,U)$ and $G(V,U)$ for which the core problem

$$\Delta_\rho V + F(V,U) = 0, \qquad \Delta_\rho U + G(V,U) = 0, \qquad \text{in } \rho > 0\,, \tag{5.79}$$

admits a radially-symmetric ground state solution for which $V \to 0$ exponentially and $U = \mathcal{O}(1)$ as $\rho \to \infty$. The existence of such a ground state plays a key role in determining the regimes of D for which localized solutions can be constructed. For example, in the study of the 3-D singularly perturbed Schnakenberg model it was found that the core problem does not admit such a solution and as a result localized spot solutions could not be constructed in the $D = \mathcal{O}(1)$ regime (cf. [98]). To further motivate such an investigation of (5.79) we extend our numerical method from §5.1.1 to calculate and plot in Figure 5.13 the far-field constant $\mu(S)$ for the core problems associated with the GM model with saturation (GMS), the Schnakenberg/Gray-Scott (S/GS) model, and the Brusselator (B) model (see Table 5.1 for more details). Note that for the GMS model we can find values of $S_\star$ such that $\mu(S_\star) = 0$, but such a zero-crossing does not appear to occur for the (S/GS) and (B) models. As a consequence, for these three specific RD systems, localized spot patterns in the $D = \mathcal{O}(1)$ regime should only occur for the GMS model. Additionally, understanding how properties of $\mu(S)$, such as convexity and positiveness, are inherited from the reaction kinetics would be a significant contri-

bution. In this direction, it would be interesting to try extend the rigorous numerics methodology of [3] to try to establish Conjecture 5.1.1.

Bibliography

[1] Flexpde 6. 2019. URL http://www.pdesolutions.com. → pages xvii, xx, xxi, 19, 126, 130, 135, 138, 145, 149, 150, 178, 179, 182, 186

[2] U. M. Ascher, S. J. Ruuth, and B. T. R. Wetton. Implicit-explicit methods for time-dependent partial differential equations. *SIAM J. Numer. Anal.*, 32 (3):797–823, 1995. ISSN 0036-1429. doi:10.1137/0732037. URL https://doi-org.ezproxy.library.ubc.ca/10.1137/0732037. → page 48

[3] I. Balázs, J. van den Berg, J. Courtois, J. Dudás, J. P. Lessard, A. Vörös-Kiss, J. F. Williams, and X. Y. Yin. Computer-assisted proofs for radially symmetric solutions of PDEs. *J. Comput. Dynamics*, 5(1 & 2): 61–80, 2018. → page 188

[4] H. Berestycki and J. Wei. On singular perturbation problems with robin boundary condition. *Annali della Scuola Normale Superiore di Pisa-Classe di Scienze*, 2(1):199–230, 2003. → pages 104, 105, 115

[5] M. Bonny, E. Fischer-Friedrich, M. Loose, P. Schwille, and K. Kruse. Membrane binding of mine allows for a comprehensive description of min-protein pattern formation. *PLoS computational biology*, 9(12): e1003347, 2013. ISSN 1553-734X. doi:10.1371/journal.pcbi.1003347. URL https://europepmc.org/articles/PMC3854456. → page 9

[6] F. Brauns, G. Pawlik, J. Halatek, J. Kerssemakers, E. Frey, and C. Dekker. Bulk-surface coupling reconciles min-protein pattern formation in vitro and in vivo, 2020. URL https://doi.org/10.1101/2020.03.01.971952. → page 9

[7] F. Brinkmann, M. Mercker, T. Richter, and A. Marciniak-Czochra. Post-turing tissue pattern formation: Advent of mechanochemistry. *PLOS Computational Biology*, 14(7):1–21, 07 2018. doi:10.1371/journal.pcbi.1006259. URL https://doi.org/10.1371/journal.pcbi.1006259. → page 3

[8] A. Buttenschon, T. Kolokolnikov, M. Ward, and J. Wei. Cops-on-the-dots: The linear stability of crime hotspots for a 1-d reaction-diffusion model of urban crime. *European Journal of Applied Mathematics*, pages 1–47, 11 2019. doi:10.1017/S0956792519000305. → page 2

[9] T. K. Callahan. Turing patterns with o(3) symmetry. *Phys. D*, 188(1-2): 65–91, 2004. ISSN 0167-2789. doi:10.1016/S0167-2789(03)00286-0. URL https://doi-org.ezproxy.library.ubc.ca/10.1016/S0167-2789(03)00286-0. → page 3

[10] L. Charette, C. B. Macdonald, and W. Nagata. Pattern formation in a slowly flattening spherical cap: delayed bifurcation. *IMA Journal of Applied Mathematics*, 85(4):513–541, 05 2020. ISSN 0272-4960. doi:10.1093/imamat/hxaa016. URL https://doi.org/10.1093/imamat/hxaa016. → page 3

[11] C. N. Chen, Y. S. Choi, Y. Hu, and X. Ren. Higher dimensional bubble profiles in a sharp interface limit of the FitzHugh-Nagumo system. *SIAM J. Math. Anal.*, 50(5):5072–5095, 2018. → page 148

[12] W. Chen and M. J. Ward. The stability and dynamics of localized spot patterns in the two-dimensional gray–scott model. *SIAM Journal on Applied Dynamical Systems*, 10(2):582–666, 2011. doi:10.1137/09077357X. URL https://doi.org/10.1137/09077357X. → pages 13, 172, 179, 182

[13] A. F. Cheviakov, M. J. Ward, and R. Straube. An asymptotic analysis of the mean first passage time for narrow escape problems: Part ii: The sphere. *Multiscale Modeling & Simulation*, 8(3):836–870, 2010. → page 67

[14] E. J. Crampin, E. A. Gaffney, and P. K. Maini. Reaction and diffusion on growing domains: scenarios for robust pattern formation. *Bulletin of mathematical biology*, 61(6):1093–1120, 1999. → page 3

[15] M. C. Cross and P. C. Hohenberg. Pattern formation outside of equilibrium. *Reviews of Modern Physics*, 65(3):851–1112, July 1993. doi:10.1103/RevModPhys.65.851. → page 3

[16] D. Cusseddu, L. Edelstein-Keshet, J. A. Mackenzie, S. Portet, and A. Madzvamuse. A coupled bulk-surface model for cell polarisation. *J. Theoret. Biol.*, 481:119–135, 2019. ISSN 0022-5193.

doi:10.1016/j.jtbi.2018.09.008. URL https://doi.org/10.1016/j.jtbi.2018.09.008. → pages 9, 10, 11

[17] R. Diegmiller, H. Montanelli, C. B. Muratov, and S. Y. Shvartsman. Spherical caps in cell polarization. *Biophysical Journal*, 115(1):26 – 30, 2018. ISSN 0006-3495. doi:https://doi.org/10.1016/j.bpj.2018.05.033. URL http://www.sciencedirect.com/science/article/pii/S0006349518306726. → pages 9, 10, 11

[18] R. Dillon, P. Maini, and H. Othmer. Pattern formation in generalized turing systems. i: Steady-state patterns in systems with mixed boundary conditions. *Journal of Mathematical Biology*, 32, 04 1994. doi:10.1007/BF00160165. → page 103

[19] A. Doelman and H. Van der Ploeg. Homoclinic stripe patterns. *SIAM J. Appl. Dyn. Sys.*, 1(1):65–104, 2002. → page 150

[20] A. Doelman, R. A. Gardner, and T. Kaper. Large stable pulse solutions in reaction-diffusion equations. *Indiana U. Math. Journ.*, 50(1):443–507, 2001. → pages 13, 21

[21] A. Doelman, R. A. Gardner, and T. Kaper. Stability of spatially periodic pulse patterns in a class of singularly perturbed reaction-diffusion equations. *Indiana U. Math. Journ.*, 54(5):1219–1301, 2005. → page 21

[22] S. I. Ei and S. Y. Tzeng. Spike solutions for a mass conservation reaction-diffusion system. *DCDS Series A*, 40(6):3357–3374, 2020. → page 148

[23] A. Gierer and H. Meinhardt. A theory of biological pattern formation. *Kybernetik*, 12(1):30–39, Dec 1972. ISSN 1432-0770. doi:10.1007/BF00289234. URL https://doi.org/10.1007/BF00289234. → pages 2, 148

[24] W. Giese, M. Eigel, S. Westerheide, C. Engwer, and E. Klipp. Influence of cell shape, inhomogeneities and diffusion barriers in cell polarization models. *Physical Biology*, 12, 11 2015. doi:10.1088/1478-3975/12/6/066014. → page 11

[25] J. Gjorgjieva and J. Jacobsen. Turing patterns on growing spheres: the exponential case. *Discrete Contin. Dyn. Syst.*, (Dynamical systems and differential equations. Proceedings of the 6th AIMS International Conference, suppl.):436–445, 2007. ISSN 1078-0947. → page 3

[26] D. Gomez, L. Mei, and J. Wei. Stable and unstable periodic spiky solutions for the gray–scott system and the schnakenberg system. *Journal of Dynamics and Differential Equations*, 02 2019. doi:10.1007/s10884-019-09736-3. → page 15

[27] D. Gomez, M. J. Ward, and J. Wei. The linear stability of symmetric spike patterns for a bulk-membrane coupled Gierer-Meinhardt model. *SIAM J. Appl. Dyn. Syst.*, 18(2):729–768, 2019. ISSN 1536-0040. doi:10.1137/18M1222338. URL https://doi.org/10.1137/18M1222338. → page 104

[28] D. Gomez, L. Mei, and J. Wei. Hopf bifurcation from spike solutions for the weak coupling gierer–meinhardt system. *European Journal of Applied Mathematics*, page 1–33, 2020. doi:10.1017/S0956792520000066. → page 15

[29] A. B. Goryachev and A. V. Pokhilko. Dynamics of cdc42 network embodies a turing-type mechanism of yeast cell polarity. *FEBS Letters*, 582(10):1437–1443, 2008. doi:10.1016/j.febslet.2008.03.029. URL https://febs.onlinelibrary.wiley.com/doi/abs/10.1016/j.febslet.2008.03.029. → pages 9, 11

[30] P. Gray and S. Scott. Autocatalytic reactions in the isothermal, continuous stirred tank reactor: Isolas and other forms of multistability. *Chemical Engineering Science*, 38(1):29 – 43, 1983. ISSN 0009-2509. doi:https://doi.org/10.1016/0009-2509(83)80132-8. URL http://www.sciencedirect.com/science/article/pii/0009250983801328. → page 2

[31] P. Gray and S. Scott. Autocatalytic reactions in the isothermal, continuous stirred tank reactor: Oscillations and instabilities in the system a + 2b → 3b; b → c. *Chemical Engineering Science*, 39(6):1087 – 1097, 1984. ISSN 0009-2509. doi:https://doi.org/10.1016/0009-2509(84)87017-7. URL http://www.sciencedirect.com/science/article/pii/0009250984870177. → page 2

[32] C. Gui and J. Wei. Multiple interior peak solutions for some singularly perturbed Neumann problems. *J. Differential Equations*, 158(1):1–27, 1999. ISSN 0022-0396. doi:10.1016/S0022-0396(99)80016-3. URL https://doi-org.ezproxy.library.ubc.ca/10.1016/S0022-0396(99)80016-3. → page 13

[33] J. Halatek and E. Frey. Highly canalized mind transfer and mine sequestration explain the origin of robust mincde-protein dynamics. *Cell reports*, 1:741–52, 06 2012. doi:10.1016/j.celrep.2012.04.005. → page 9

[34] J. Halatek, F. Brauns, and E. Frey. Self-organization principles of intracellular pattern formation. *Philosophical Transactions of the Royal Society B: Biological Sciences*, 373(1747):20170107, 2018. doi:10.1098/rstb.2017.0107. URL https://royalsocietypublishing.org/doi/abs/10.1098/rstb.2017.0107. → page 9

[35] D. M. Holloway and L. G. Harrison. Pattern selection in plants: coupling chemical dynamics to surface growth in three dimensions. *Annals of botany*, 101(3):361–374, 2008. → pages 2, 64

[36] D. M. Holloway, I. Rozada, and J. J. H. Bray. Two-stage patterning dynamics in conifer cotyledon whorl morphogenesis. *Annals of Botany*, 121(3):525–534, 01 2018. ISSN 0305-7364. doi:10.1093/aob/mcx185. URL https://doi.org/10.1093/aob/mcx185. → pages 2, 64

[37] M. Howard, A. D. Rutenberg, and S. de Vet. Dynamic compartmentalization of bacteria: Accurate division in e. coli. *Phys. Rev. Lett.*, 87:278102, Dec 2001. doi:10.1103/PhysRevLett.87.278102. URL https://link.aps.org/doi/10.1103/PhysRevLett.87.278102. → pages 8, 9

[38] K. C. Huang, Y. Meir, and N. S. Wingreen. Dynamic structures in escherichia coli: Spontaneous formation of mine rings and mind polar zones. *Proceedings of the National Academy of Sciences*, 100(22): 12724–12728, 2003. ISSN 0027-8424. doi:10.1073/pnas.2135445100. URL https://www.pnas.org/content/100/22/12724. → page 9

[39] D. Iron and M. J. Ward. A metastable spike solution for a nonlocal reaction-diffusion model. *SIAM J. Appl. Math.*, 60(3):778–802, 2000. ISSN 0036-1399. doi:10.1137/S0036139998338340. URL https://doi-org.ezproxy.library.ubc.ca/10.1137/S0036139998338340. → pages 13, 18

[40] D. Iron and M. J. Ward. The dynamics of boundary spikes for a nonlocal reaction-diffusion model. *European J. Appl. Math.*, 11(5):491–514, 2000. ISSN 0956-7925. doi:10.1017/S0956792500004253. URL https://doi-org.ezproxy.library.ubc.ca/10.1017/S0956792500004253. → page 13

[41] D. Iron, M. J. Ward, and J. Wei. The stability of spike solutions to the one-dimensional Gierer-Meinhardt model. *Phys. D*, 150(1-2):25–62, 2001. ISSN 0167-2789. doi:10.1016/S0167-2789(00)00206-2. URL https://doi-org.ezproxy.library.ubc.ca/10.1016/S0167-2789(00)00206-2. → pages 13, 16, 21, 25, 66, 85, 115, 140

[42] H.-S. Jung, V. Oropeza, and I. Thesleff. Shh, bmp-2, bmp-4 and fgf-8 are associated with initiation and patterning of mouse tongue papillae. *Mechanisms of Development*, 81(1):179 – 182, 1999. ISSN 0925-4773. doi:https://doi.org/10.1016/S0925-4773(98)00234-2. URL http://www.sciencedirect.com/science/article/pii/S0925477398002342. → page 2

[43] J. Keller. An outlook on biothermodynamics. ii. adsorption of proteins. *Journal of Non Equilibrium Thermodynamics*, 34:1–33, 03 2009. doi:10.1515/JNETDY.2009.001. → pages 10, 63

[44] E. Knobloch. Spatial Localization in Dissipative Systems. *Annual Review of Condensed Matter Physics*, 6:325–359, Mar. 2015. doi:10.1146/annurev-conmatphys-031214-014514. → page 3

[45] T. Kolokolnikov and M. J. Ward. Reduced wave green's functions and their effect on the dynamics of a spike for the gierer-meinhardt model. *European J. Appl. Math.*, 14(5):513–545, 2003. ISSN 0956-7925. doi:10.1017/S0956792503005254. URL https://doi-org.ezproxy.library.ubc.ca/10.1017/S0956792503005254. → page 13

[46] T. Kolokolnikov, M. Ward, and J. Wei. Pulse-splitting for some reaction-diffusion systems in one-space dimension. *Studies in Applied Mathematics*, 114:115 – 165, 02 2005. doi:10.1111/j.0022-2526.2005.01542.x. → pages 15, 150

[47] T. Kolokolnikov, M. J. Ward, and J. Wei. The existence and stability of spike equilibria in the one-dimensional Gray-Scott model on a finite domain. *Appl. Math. Lett.*, 18(8):951–956, 2005. ISSN 0893-9659. doi:10.1016/j.aml.2004.06.024. URL https://doi-org.ezproxy.library.ubc.ca/10.1016/j.aml.2004.06.024. → page 13

[48] T. Kolokolnikov, M. J. Ward, and J. Wei. Spot self-replication and dynamics for the schnakenberg model in a two-dimensional domain. *J. Nonlinear Sci.*, 19(1):1–56, 2009. → pages 66, 80, 172, 182

[49] T. Kolokolnikov, F. Paquin-Lefebvre, and M. J. Ward. Stable asymmetric spike equilibria for the gierer-meinhardt model with a precursor field. *arXiv preprint arXiv:2002.01608*, 2020. → page 105

[50] S. Kondo and R. Asai. A reaction–diffusion wave on the skin of the marine angelfish pomacanthus. *Nature*, 376(6543):765–768, 1995. → page 2

[51] M. Kowalczyk. Multiple spike layers in the shadow Gierer-Meinhardt system: existence of equilibria and the quasi-invariant manifold. *Duke Math. J.*, 98(1):59–111, 1999. ISSN 0012-7094. doi:10.1215/S0012-7094-99-09802-2. URL https://doi-org.ezproxy.library.ubc.ca/10.1215/S0012-7094-99-09802-2. → page 13

[52] A. L. Krause, M. A. Ellis, and R. A. Van Gorder. Influence of curvature, growth, and anisotropy on the evolution of Turing patterns on growing manifolds. *Bull. Math. Biol.*, 81(3):759–799, 2019. ISSN 0092-8240. doi:10.1007/s11538-018-0535-y. URL https://doi-org.ezproxy.library.ubc.ca/10.1007/s11538-018-0535-y. → page 3

[53] M. Leda, V. K. Vanag, and I. R. Epstein. Instabilities of a three-dimensional localized spot. *Phys. Rev. E*, 80:066204, 2009. → page 148

[54] H. Levine and W.-J. Rappel. Membrane-bound Turing patterns. *Phys. Rev. E (3)*, 72(6):061912, 5, 2005. ISSN 1539-3755. doi:10.1103/PhysRevE.72.061912. URL https://doi-org.ezproxy.library.ubc.ca/10.1103/PhysRevE.72.061912. → pages 3, 9, 10, 104

[55] J. Lippincott-Schwartz, E. Snapp, and A. Kenworthy. Studying protein dynamics in living cells. *Nature reviews. Molecular cell biology*, 2:444–56, 07 2001. doi:10.1038/35073068. → page 10

[56] C. B. Macdonald, B. Merriman, and S. J. Ruuth. Simple computation of reaction-diffusion processes on point clouds. *Proc. Natl. Acad. Sci. USA*, 110(23):9209–9214, 2013. → page 20

[57] A. Madzvamuse and A. H. Chung. The bulk-surface finite element method for reaction diffusion systems on stationary volumes. *Finite Elements in Analysis and Design*, 108:9–21, 2016. ISSN 0168-874X. doi:https://doi.org/10.1016/j.finel.2015.09.002. URL

http://www.sciencedirect.com/science/article/pii/S0168874X15001377. → pages 11, 61

[58] A. Madzvamuse, A. H. W. Chung, and C. Venkataraman. Stability analysis and simulations of coupled bulk-surface reaction-diffusion systems. *Proc. A.*, 471(2175):20140546, 18, 2015. ISSN 1364-5021. doi:10.1098/rspa.2014.0546. URL https://doi-org.ezproxy.library.ubc.ca/10.1098/rspa.2014.0546. → pages 3, 9, 11, 20, 61, 104, 146

[59] P. Maini, K. Painter, and H. P. Chau. Spatial pattern formation in chemical and biological systems. *Journal of the Chemical Society, Faraday Transactions*, 93(20):3601–3610, 1997. → pages 2, 103

[60] P. K. Maini, J. Wei, and M. Winter. Stability of spikes in the shadow gierer-meinhardt system with robin boundary conditions. *Chaos: An Interdisciplinary Journal of Nonlinear Science*, 17(3):037106, 2007. → pages 16, 104, 105, 106, 115, 145

[61] P. K. Maini, T. E. Woolley, R. E. Baker, E. A. Gaffney, and S. S. Lee. Turing's model for biological pattern formation and the robustness problem. *Interface Focus*, 2(4):487–496, 2012. doi:10.1098/rsfs.2011.0113. URL https://royalsocietypublishing.org/doi/abs/10.1098/rsfs.2011.0113. → pages 2, 3

[62] H. Meinhardt and A. Gierer. Pattern formation by local self-activation and lateral inhibition. *BioEssays*, 22:753–760, 08 2000. doi:10.1002/1521-1878(200008)22:8<753::AID-BIES9>3.3.CO;2-Q. → page 2

[63] M. Mercker, D. Hartmann, and A. Marciniak-Czochra. A mechanochemical model for embryonic pattern formation: Coupling tissue mechanics and morphogen expression. *PLOS ONE*, 8(12):1–6, 12 2013. doi:10.1371/journal.pone.0082617. URL https://doi.org/10.1371/journal.pone.0082617. → page 3

[64] T. Miura, K. Shiota, G. Morriss-Kay, and P. Maini. Mixed-mode pattern in doublefoot mutant mouse limb - turing reaction-diffusion model on a growing domain during limb development. *Journal of theoretical biology*, 240:562–73, 07 2006. doi:10.1016/j.jtbi.2005.10.016. → page 2

[65] Y. Mori, A. Jilkine, and L. Edelstein-Keshet. Wave-pinning and cell polarity from a bistable reaction-diffusion system. *Biophysical journal*, 94 (9):3684—3697, May 2008. ISSN 0006-3495. doi:10.1529/biophysj.107.120824. URL https://europepmc.org/articles/PMC2292363. → pages 9, 11

[66] I. Moyles, W. H. Tse, and M. J. Ward. Explicitly solvable nonlocal eigenvalue problems and the stability of localized stripes in reaction-diffusion systems. *Studies in Applied Mathematics*, 136(1): 89–136, 2016. doi:10.1111/sapm.12093. URL https://onlinelibrary.wiley.com/doi/abs/10.1111/sapm.12093. → page 15

[67] J. Murray. A pre-pattern formation mechanism for animal coat markings. *Journal of Theoretical Biology*, 88(1):161 – 199, 1981. ISSN 0022-5193. doi:https://doi.org/10.1016/0022-5193(81)90334-9. URL http://www.sciencedirect.com/science/article/pii/0022519381903349. → page 2

[68] J. D. Murray. *Mathematical biology. II*, volume 18 of *Interdisciplinary Applied Mathematics*. Springer-Verlag, New York, third edition, 2003. ISBN 0-387-95228-4. Spatial models and biomedical applications. → page 2

[69] W. Nagata, L. G. Harrison, and S. Wehner. Reaction-diffusion models of growing plant tips: Bifurcations on hemispheres. *Bulletin of Mathematical Biology*, 65(4):571 – 607, 2003. ISSN 0092-8240. doi:https://doi.org/10.1016/S0092-8240(03)00025-9. URL http://www.sciencedirect.com/science/article/pii/S0092824003000259. → page 2

[70] Y. Nec and M. J. Ward. An explicitly solvable nonlocal eigenvalue problem and the stability of a spike for a class of reaction-diffusion system. *Math. Mod. Nat. Phen.*, 8(2):55–87, 2013. → pages 15, 32

[71] W.-M. Ni. Diffusion, cross-diffusion, and their spike-layer steady states. *Notices Amer. Math. Soc.*, 45(1):9–18, 1998. ISSN 0002-9920. → page 13

[72] Y. Nishiura. *Far-from Equilibrium dynamics: Translations of mathematical monographs*, volume 209. AMS Publications, Providence, Rhode Island, 2002. → pages 3, 20, 150

[73] F. Paquin-Lefebvre, W. Nagata, and M. J. Ward. Pattern formation and oscillatory dynamics in a two-dimensional coupled bulk-surface

reaction-diffusion system. *SIAM Journal on Applied Dynamical Systems*, 18(3):1334–1390, 2019. doi:10.1137/18M1213737. URL https://doi.org/10.1137/18M1213737. → page 11

[74] F. Paquin-Lefebvre, W. Nagata, and M. J. Ward. Weakly nonlinear theory for oscillatory dynamics in a one-dimensional pde-ode model of membrane dynamics coupled by a bulk diffusion field. *SIAM Journal on Applied Mathematics*, 80(3):1520–1545, 2020. doi:10.1137/19M1304908. URL https://doi.org/10.1137/19M1304908. → page 11

[75] F. Paquin-Lefebvre, B. Xu, K. L. DiPietro, A. E. Lindsay, and A. Jilkine. Pattern formation in a coupled membrane-bulk reaction-diffusion model for intracellular polarization and oscillations. *Journal of Theoretical Biology*, 497:110242, 2020. ISSN 0022-5193. doi:https://doi.org/10.1016/j.jtbi.2020.110242. URL http://www.sciencedirect.com/science/article/pii/S0022519320300977. → page 9

[76] B. Peña and C. Pérez-García. Stability of Turing patterns in the Brusselator model. *Phys. Rev. E (3)*, 64(5, part 2):056213, 9, 2001. ISSN 1539-3755. doi:10.1103/PhysRevE.64.056213. URL https://doi-org.ezproxy.library.ubc.ca/10.1103/PhysRevE.64.056213. → page 3

[77] J. E. Pearson. Complex patterns in a simple system. *Science*, 261(5118): 189–192, 1993. ISSN 0036-8075. doi:10.1126/science.261.5118.189. URL https://science.sciencemag.org/content/261/5118/189. → page 3

[78] R. G. Plaza, F. Sánchez-Garduño, P. Padilla, R. A. Barrio, and P. K. Maini. The effect of growth and curvature on pattern formation. *J. Dynam. Differential Equations*, 16(4):1093–1121, 2004. ISSN 1040-7294. doi:10.1007/s10884-004-7834-8. URL https://doi-org.ezproxy.library.ubc.ca/10.1007/s10884-004-7834-8. → page 3

[79] I. Prigogine and R. Lefever. Symmetry breaking instabilities in dissipative systems. ii. *The Journal of Chemical Physics*, 48(4):1695–1700, 1968. doi:10.1063/1.1668896. URL https://doi.org/10.1063/1.1668896. → pages 2, 62

[80] P. Prusinkiewicz, H. Meinhardt, and D. Fowler. *The Algorithmic Beauty of Sea Shells*. The Virtual Laboratory. Springer Berlin Heidelberg, 2003.

ISBN 9783540440109. URL https://books.google.ca/books?id=wD2k1aMeeu4C. → page 2

[81] A. Rätz and M. Röger. Turing instabilities in a mathematical model for signaling networks. *J. Math. Biol.*, 65(6-7):1215–1244, 2012. → pages 3, 9, 11, 20, 61

[82] A. Rätz and M. Röger. Erratum to: Turing instabilities in a mathematical model for signaling networks [mr2993944]. *J. Math. Biol.*, 66(1-2): 421–422, 2013. ISSN 0303-6812. doi:10.1007/s00285-012-0630-x. URL https://doi-org.ezproxy.library.ubc.ca/10.1007/s00285-012-0630-x. → page 20

[83] A. Rätz and M. Röger. Symmetry breaking in a bulk-surface reaction-diffusion model for signalling networks. *Nonlinearity*, 27(8): 1805–1827, 2014. ISSN 0951-7715. doi:10.1088/0951-7715/27/8/1805. URL https://doi-org.ezproxy.library.ubc.ca/10.1088/0951-7715/27/8/1805. → pages 11, 20, 61, 104

[84] I. Rozada, S. J. Ruuth, and M. J. Ward. The stability of localized spot patterns for the Brusselator on the sphere. *SIAM J. Appl. Dyn. Syst.*, 13(1): 564–627, 2014. ISSN 1536-0040. doi:10.1137/130934696. URL https://doi.org/10.1137/130934696. → pages 13, 18, 64, 66, 67, 70, 71, 74, 80, 84, 92, 101

[85] S. J. Ruuth. Implicit-explicit methods for reaction-diffusion problems in pattern formation. *J. Math. Biol.*, 34(2):148–176, 1995. ISSN 0303-6812. doi:10.1007/BF00178771. URL https://doi-org.ezproxy.library.ubc.ca/10.1007/BF00178771. → page 48

[86] L. A. Segel and J. L. Jackson. Dissipative structure: An explanation and an ecological example. *Journal of Theoretical Biology*, 37(3):545 – 559, 1972. ISSN 0022-5193. doi:https://doi.org/10.1016/0022-5193(72)90090-2. URL http://www.sciencedirect.com/science/article/pii/0022519372900902. → page 2

[87] M. B. SHORT, M. R. D'ORSOGNA, V. B. PASOUR, G. E. TITA, P. J. BRANTINGHAM, A. L. BERTOZZI, and L. B. CHAYES. A statistical model of criminal behavior. *Mathematical Models and Methods in Applied Sciences*, 18(supp01):1249–1267, 2008. doi:10.1142/S0218202508003029. URL https://doi.org/10.1142/S0218202508003029. → page 2

[88] A. Stathopoulos and D. Iber. Studies of morphogens: keep calm and carry on. *Development*, 140(20):4119–4124, 2013. ISSN 0950-1991. doi:10.1242/dev.095141. URL https://dev.biologists.org/content/140/20/4119. → page 2

[89] R. Straube and M. J. Ward. Intraceulluar signalling gradients arising from multiple compartments: A matched asymptotic expansion approach. *SIAM J. Appl. Math.*, 70(1):248–269, 2009. → page 169

[90] I. Takagi. Point-condensation for a reaction-diffusion system. *J. Differential Equations*, 61(2):208–249, 1986. ISSN 0022-0396. doi:10.1016/0022-0396(86)90119-1. URL https://doi-org.ezproxy.library.ubc.ca/10.1016/0022-0396(86)90119-1. → page 13

[91] P. H. Trinh and M. J. Ward. The dynamics of localized spot patterns for reaction-diffusion systems on the sphere. *Nonlinearity*, 29(3):766–806, 2016. ISSN 0951-7715. doi:10.1088/0951-7715/29/3/766. URL https://doi.org/10.1088/0951-7715/29/3/766. → pages 13, 18, 64, 66, 67, 70, 78, 80, 84, 85, 88, 94, 102, 172, 177, 182

[92] W. H. Tse, J. Wei, and M. Winter. The Gierer-Meinhardt system on a compact two-dimensional Riemannian manifold: interaction of Gaussian curvature and Green's function. *J. Math. Pures Appl. (9)*, 94(4):366–397, 2010. ISSN 0021-7824. doi:10.1016/j.matpur.2010.03.003. URL https://doi.org/10.1016/j.matpur.2010.03.003. → pages 67, 68, 69, 102

[93] A. M. Turing. The chemical basis of morphogenesis. *Philos. Trans. Roy. Soc. London Ser. B*, 237(641):37–72, 1952. ISSN 0080-4622. → page 1

[94] J. Tzou. private communication. → page 186

[95] J. C. Tzou and L. Tzou. Spot patterns of the Schnakenberg reaction-diffusion system on a curved torus. *Nonlinearity*, 33(2):643–674, 2020. ISSN 0951-7715. doi:10.1088/1361-6544/ab5161. URL https://doi-org.ezproxy.library.ubc.ca/10.1088/1361-6544/ab5161. → pages 13, 66, 67, 85, 102

[96] J. C. Tzou and M. J. Ward. The stability and slow dynamics of spot patterns in the 2D Brusselator model: the effect of open systems and heterogeneities. *Phys. D*, 373:13–37, 2018. ISSN 0167-2789. doi:10.1016/j.physd.2018.02.002. URL

https://doi-org.ezproxy.library.ubc.ca/10.1016/j.physd.2018.02.002. → pages 13, 16, 18, 66, 73, 80, 85, 88, 101, 104

[97] J. C. Tzou, Y. Nec, and M. J. Ward. The stability of localized spikes for the 1-d brusselator reaction–diffusion model. *European Journal of Applied Mathematics*, 24(4):515–564, 2013. doi:10.1017/S0956792513000089. → pages 13, 66

[98] J. C. Tzou, S. Xie, T. Kolokolnikov, and M. J. Ward. The stability and slow dynamics of localized spot patterns for the 3-D Schnakenberg reaction-diffusion model. *SIAM J. Appl. Dyn. Syst.*, 16(1):294–336, 2017. doi:10.1137/16M108121X. URL https://doi-org.ezproxy.library.ubc.ca/10.1137/16M108121X. → pages 13, 16, 66, 80, 85, 148, 150, 164, 172, 177, 179, 182, 185, 187

[99] J. C. Tzou, M. J. Ward, and J. C. Wei. Anomalous scaling of Hopf bifurcation thresholds for the stability of localized spot patterns for reaction-diffusion systems in two dimensions. *SIAM J. Appl. Dyn. Syst.*, 17 (1):982–1022, 2018. doi:10.1137/17M1137759. URL https://doi-org.ezproxy.library.ubc.ca/10.1137/17M1137759. → pages 15, 169

[100] V. K. Vanag and I. R. Epstein. Localized patterns in reaction-diffusion systems. *Chaos: An Interdisciplinary Journal of Nonlinear Science*, 17(3): 037110, 2007. doi:10.1063/1.2752494. URL https://doi.org/10.1063/1.2752494. → page 3

[101] F. Veerman. Breathing pulses in singularly perturbed reaction-diffusion systems. *Nonlinearity*, 28(7):2211–2246, 2015. ISSN 0951-7715. doi:10.1088/0951-7715/28/7/2211. URL https://doi-org.ezproxy.library.ubc.ca/10.1088/0951-7715/28/7/2211. → page 15

[102] M. J. Ward. An asymptotic analysis of localized solutions for some reaction-diffusion models in multidimensional domains. *Stud. Appl. Math.*, 97(2):103–126, 1996. ISSN 0022-2526. doi:10.1002/sapm1996972103. URL https://doi-org.ezproxy.library.ubc.ca/10.1002/sapm1996972103. → page 13

[103] M. J. Ward. Spots, traps, and patches: asymptotic analysis of localized solutions to some linear and nonlinear diffusive systems. *Nonlinearity*, 31 (8):R189–R239, 2018. ISSN 0951-7715. doi:10.1088/1361-6544/aabe4b.

URL https://doi-org.ezproxy.library.ubc.ca/10.1088/1361-6544/aabe4b. → pages 149, 172

[104] M. J. Ward and J. Wei. Asymmetric spike patterns for the one-dimensional Gierer-Meinhardt model: equilibria and stability. *European J. Appl. Math.*, 13(3):283–320, 2002. ISSN 0956-7925. doi:10.1017/S0956792501004442. URL https://doi-org.ezproxy.library.ubc.ca/10.1017/S0956792501004442. → pages 13, 18, 105, 111, 115, 131, 137, 141, 159, 231

[105] M. J. Ward and J. Wei. Hopf bifurcation and oscillatory instabilities of spike solutions for the one-dimensional gierer-meinhardt model. *J. Nonlinear Science*, 13(2):209–264, 2003. → pages 15, 16, 21, 32, 38, 39, 148, 152, 168, 183, 184

[106] M. J. Ward and J. Wei. Hopf bifurcation of spike solutions for the shadow Gierer-Meinhardt model. *European J. Appl. Math.*, 14(6):677–711, 2003. ISSN 0956-7925. doi:10.1017/S0956792503005278. URL https://doi-org.ezproxy.library.ubc.ca/10.1017/S0956792503005278. → pages 38, 39, 42

[107] J. Wei. On single interior spike solutions of the Gierer-Meinhardt system: uniqueness and spectrum estimates. *European J. Appl. Math.*, 10(4): 353–378, 1999. ISSN 0956-7925. doi:10.1017/S0956792599003770. URL https://doi-org.ezproxy.library.ubc.ca/10.1017/S0956792599003770. → pages 13, 15, 21, 43, 115, 118, 124, 233

[108] J. Wei. Existence and stability of spikes for the gierer-meinhardt system. In *Handbook of differential equations: stationary partial differential equations. Vol. V*, Handb. Differ. Equ., pages 487–585. Elsevier/North-Holland, Amsterdam, 2008. doi:10.1016/S1874-5733(08)80013-7. URL https://doi-org.ezproxy.library.ubc.ca/10.1016/S1874-5733(08)80013-7. → pages 13, 148, 152

[109] J. Wei and M. Winter. Spikes for the two-dimensional gierer-meinhardt system: the weak coupling case. *J. Nonlinear Sci.*, 11(6):415–458, 2001. ISSN 0938-8974. doi:10.1007/s00332-001-0380-1. URL https://doi-org.ezproxy.library.ubc.ca/10.1007/s00332-001-0380-1. → page 159

[110] J. Wei and M. Winter. Spikes for the Gierer-Meinhardt system in two dimensions: the strong coupling case. *J. Differential Equations*, 178(2):

478–518, 2002. ISSN 0022-0396. doi:10.1006/jdeq.2001.4019. URL https://doi-org.ezproxy.library.ubc.ca/10.1006/jdeq.2001.4019. → page 13

[111] J. Wei and M. Winter. Existence, classification and stability analysis of multiple-peaked solutions for the Gierer-Meinhardt system in $\mathbf{R}^1$. *Methods Appl. Anal.*, 14(2):119–163, 2007. ISSN 1073-2772. doi:10.4310/MAA.2007.v14.n2.a2. URL https://doi-org.ezproxy.library.ubc.ca/10.4310/MAA.2007.v14.n2.a2. → pages 13, 113, 115, 117

[112] J. Wei and M. Winter. *Mathematical aspects of pattern formation in biological systems*, volume 189. Applied Mathematical Sciences Series, Springer, 2014. → pages 13, 15, 148, 152

[113] T. Wong and M. J. Ward. Weakly nonlinear analysis of peanut-shaped deformations for localized spots of singularly perturbed reaction-diffusion systems. *arXiv preprint arXiv:2002.01453*, 2020. → pages 15, 80, 182

Appendix A

Bulk-Membrane-Coupled Reaction-Diffusion-Systems are a Leading Order Approximation

In this appendix we demonstrate the sense in which bulk-membrane coupled reaction-diffusion systems of the form (1.8) are to be understood as a leading order approximation in the limit of a thin membrane.

A.1 Geometric Preliminaries

We first derive a three-term approximation to the Laplacian near a smooth and compact $(N-1)$-dimensional manifold $S \subset \mathbb{R}^N$ for $N = 2, 3$. Let $X(s_1, ..., s_{N-1}) \in S$ be a parametrization of S where $(s_1, ..., s_{N-1}) \in U \subset \mathbb{R}^{N-1}$ and $X : U \to S$ is smooth. When $N = 2$ we will assume that the curve S is parameterized by arc-length so that the tangent vector $|dX/ds_1| = 1$. The unit normal to S at X is defined by

$$\nu(s) = \kappa^{-1} \frac{d^2X}{ds_1^2} \quad (N = 2), \qquad \nu(s_1, s_2) = \frac{\partial_1 X \times \partial_2 X}{|\partial_1 X \times \partial_2 X|} \quad (N = 3), \qquad \text{(A.1)}$$

where κ is the curvature of the curve S when $N = 2$, and where we use the notation $\partial_i \equiv \partial/\partial s_i$ $(i = 1,2)$. Next we define the tensors g, b, and c with entires

$$g_{ij} \equiv \partial_i X \cdot \partial_j X, \qquad b_{ij} \equiv \partial_i \partial_j X \cdot \nu = -\partial_i X \cdot \partial_j \nu, \qquad c_{ij} = \partial_i \nu \cdot \partial_j \nu \tag{A.2}$$

where the second equality in the definition of b_{ij} follows from differentiating the orthogonality relation $\partial_i X \cdot \nu = 0$. Note that g corresponds to the metric tensor, while b corresponds to the second fundamental form when $N = 3$. Explicitly we calculate

$$g = 1, \qquad b = \kappa, \tag{A.3a}$$

for $N = 2$, and

$$g = \begin{pmatrix} \partial_1 X \cdot \partial_1 X & \partial_1 X \cdot \partial_2 X \\ \partial_2 X \cdot \partial_1 X & \partial_2 X \cdot \partial_2 X \end{pmatrix}, \quad b = -\begin{pmatrix} \partial_1 X \cdot \partial_1 \nu & \partial_1 X \cdot \partial_2 \nu \\ \partial_2 X \cdot \partial_1 \nu & \partial_2 X \cdot \partial_2 \nu \end{pmatrix} \tag{A.3b}$$

for $N = 3$. Note that both g and b are symmetric.

Next we derive a useful formula for c in terms of b and g. Throughout the next calculations we use the Einstein summation convention in which we sum over all repeated indices. Since $|\nu| = 1$ it follows that $\partial_i \nu \cdot \nu = 0$ and we can therefore write $\partial_i \nu$ in terms of the tangent vectors $\partial_i X$ as $\partial_j \nu = a_{jk} \partial_k X$ for some unknown coefficients a_{ij}. Taking the inner product with $\partial_i X$ and recalling the definition of g_{ij} and b_{ij} in (A.2) we obtain $-b_{ij} = a_{jk} g_{ki}$ and therefore $a_{ij} = -b_{ik} g^{kj}$, where g^{ij} are the entries of g^{-1}. Calculating $c_{ij} = a_{ik} a_{jq} g_{kq} = b_{il} g^{lk} b_{jr} g^{rq} g_{qk} = b_{il} g^{lk} b_{kj}$ we deduce that

$$c = \kappa^2 \quad (N = 2), \qquad c = b g^{-1} b \quad (N = 3). \tag{A.4}$$

We now consider the parametrization of a region near S in $\mathbb{R}^N$ given by

$$\tilde{X}(s_1, ..., s_N) = X(s_1, ..., s_{N-1}) + s_N \nu(s_1, ..., s_N), \tag{A.5}$$

where s_N is assumed to be sufficiently small so that $\tilde{X}(s_1, ..., s_N)$ is well defined and in particular $1 + \kappa s_2 > 0$ when $N = 2$ and $(I + s_N g^{-1} b)$ is positive definite when $N = 3$ where I is the 2×2 identity matrix Using (A.2) and (A.4) we readily determine that the metric tensor $\tilde{g}$ with entries $\tilde{g}_{ij} = \partial_i \tilde{X} \cdot \partial_j \tilde{X}$ is block diagonal and

explicitly given by

$$\tilde{g} = \begin{pmatrix} (1+s_2\kappa)^2 & 0 \\ 0 & 1 \end{pmatrix} \quad (N=2), \quad \tilde{g} = \begin{pmatrix} g(I+s_N g^{-1}b)^2 & 0 \\ 0 & 1 \end{pmatrix} \quad (N=3). \tag{A.6}$$

Since $\tilde{g}$ is block diagonal, the Laplacian in this parametrization is given by

$$\begin{aligned} \Delta\phi &= \frac{1}{\sqrt{\det\tilde{g}}} \sum_{i,j=1}^{N} \frac{\partial}{\partial s_i}\left(\sqrt{\det\tilde{g}}\tilde{g}^{ij}\frac{\partial\phi}{\partial s_j}\right) \\ &= \partial_N^2\phi + \frac{\partial_N \det\tilde{g}}{2\det\tilde{g}}\partial_N\phi + \frac{1}{\sqrt{\det\tilde{g}}}\sum_{i,j=1}^{N-1}\partial_i\big(\sqrt{\det\tilde{g}}\tilde{g}^{ij}\partial_j\phi\big). \end{aligned} \tag{A.7}$$

When $N=2$ we use (A.6) to easily calculate the exact formula

$$\Delta\phi = \frac{\partial^2\phi}{\partial s_2^2} + \frac{\kappa}{1+\kappa s_2}\frac{\partial\phi}{\partial s_2} + \frac{1}{1+\kappa s_2}\frac{\partial}{\partial s_1}\left(\frac{1}{1+\kappa s_2}\frac{\partial\phi}{\partial s_1}\right). \tag{A.8}$$

For $N=3$ an exact formula is more involved and we instead focus on retaining the first three terms in an expansion of the Laplacian when $s_N \ll 1$. First we calculate

$$\det\tilde{g} = \det g \det^2(I+s_N g^{-1}b). \tag{A.9}$$

Next we use Jacobi's formula for the derivative of a determinant to calculate

$$\begin{aligned} \left.\frac{\partial\det(I+s_N g^{-1}b)}{\partial s_N}\right|_{s_N=0} &= \mathrm{tr}(g^{-1}b) = 2H, \\ \left.\frac{\partial^2\det(I+s_N g^{-1}b)}{\partial s_N^2}\right|_{s_N=0} &= \mathrm{tr}^2(g^{-1}b) - \mathrm{tr}(g^{-1}b)^2 = 4H^2 - (\kappa_1^2+\kappa_2^2). \end{aligned}$$

where we have used that the principal curvatures, κ_1 and κ_2 are the eigenvalues of $g^{-1}b$ and the mean curvature H is

$$H = \frac{\kappa_1+\kappa_2}{2}. \tag{A.10}$$

Therefore

$$\begin{aligned}\det\tilde{g} &= \det g\big(1+2Hs_N+\tfrac{1}{2}(4H^2-\kappa_1^2-\kappa_2^2)s_N^2+O(s_N^3)\big)^2\\ &= \det g\big(1+4Hs_N+(8H^2-\kappa_1^2-\kappa_2^2)s_N^2+O(s_N^3)\big),\end{aligned}$$

and

$$\begin{aligned}\frac{\partial_N \det\tilde{g}}{2\det\tilde{g}} &= \frac{2H+(8H^2-\kappa_1^2-\kappa_2^2)s_N+O(s_N^2)}{1+4Hs_N+(8H^2-\kappa_1^2-\kappa_2^2)s_N^2+O(s_N^3)}\\ &= 2H-(\kappa_1^2+\kappa_2^2)s_N+O(s_N^2).\end{aligned}$$

Retaining leading order terms in s_N and letting Δ_S be the Laplace-Beltrami operator on S we obtain

$$\Delta\phi = \frac{\partial^2\phi}{\partial s_N^2}+2H\frac{\partial\phi}{\partial s_N}-(\kappa_1^2+\kappa_2^2)s_N\frac{\partial\phi}{\partial s_N}+\Delta_S\phi+O(s_N). \tag{A.11}$$

Summarizing, we let $s_N=\delta\eta$ where $\delta\ll 1$ and $\eta=O(1)$ to obtain

$$\Delta\phi = \delta^{-2}\frac{\partial^2\phi}{\partial\eta^2}+\delta^{-1}\kappa\frac{\partial\phi}{\partial\eta}-\kappa^2\eta\frac{\partial\phi}{\partial\eta}+\frac{\partial^2\phi}{\partial s^2}+O(\delta), \tag{A.12}$$

$$\Delta\phi = \delta^{-2}\frac{\partial^2\phi}{\partial\eta^2}+2\delta^{-1}H\frac{\partial\phi}{\partial\eta}-(\kappa_1^2+\kappa_2^2)\eta\frac{\partial\phi}{\partial\eta}+\Delta_S\phi+O(\delta). \tag{A.13}$$

for $N=2$ and $N=3$ respectively, and where we have used s to denote the arc-length along S in $N=2$.

A.2 Derivation of Bulk-Membrane-Coupled Reaction-Diffusion System

We begin by assuming that the cell bulk is given by a bounded domain $\Omega\subset\mathbb{R}^N$ ($N=2,3$) with smooth boundary $\partial\Omega$. Next we let $\nu(x)$ be the outward unit normal to $\partial\Omega$ at $s\in\partial\Omega$ and let the cell membrane be given by

$$\Omega_\delta \equiv \{x+\delta\eta\,\nu(x)\,|x\in\partial\Omega,\,0<\eta<1\}, \tag{A.14}$$

where $\delta > 0$ is the membrane thickness and is assumed to be sufficiently small so that Ω_δ is well defined. Furthermore, we separate $\partial\Omega_\delta$ into two disjoint $(N-1)$-dimensional surfaces $\partial\Omega_\delta = \partial\Omega_\delta^i \cup \partial\Omega_\delta^e$ where $\partial\Omega_\delta^i = \partial\Omega$ denotes the interface between the bulk and membrane and corresponds to setting $\eta = 0$ in (A.14) while $\partial\Omega_\delta^e$ denotes the interface between the membrane and the extracellular space and corresponds to setting $\eta = 1$ in (A.14).

Next we suppose that there are n and m chemical species in the bulk and in the membrane with concentrations respectively given by

$$\boldsymbol{U} = (U_1, ..., U_n)^T, \qquad \boldsymbol{u} = (u_1, ..., u_m)^T.$$

In both the bulk and the membrane we further assume that these chemical species undergo isotropic diffusion and reaction kinetics so that the spatio-temporal evolution of their concentrations is governed by the system of reaction-diffusion equations

$$\tau_B \partial_t \boldsymbol{U} = D_B \Delta \boldsymbol{U} + \boldsymbol{F}(\boldsymbol{U}), \qquad x \in \Omega, \tag{A.15a}$$

$$D_B \partial_n \boldsymbol{U} = \gamma q_\delta(\boldsymbol{u}, \boldsymbol{U}), \qquad x \in \partial\Omega, \tag{A.15b}$$

and

$$\tau_M \partial_t \boldsymbol{u} = D_M \Delta \boldsymbol{u} + \boldsymbol{f}_\delta(\boldsymbol{u}), \qquad x \in \Omega_\delta, \tag{A.16a}$$

$$D_M \partial_n \boldsymbol{u} = -q_\delta(\boldsymbol{u}, \boldsymbol{U}), \qquad x \in \partial\Omega_\delta^i, \tag{A.16b}$$

$$D_M \partial_n \boldsymbol{u} = 0, \qquad x \in \partial\Omega_\delta^e. \tag{A.16c}$$

where $D_B = \text{diag}(D_{B1}, ..., D_{Bn})$ and $D_M = \text{diag}(D_{M1}, ..., D_{Mm})$ are the diffusion coefficients of each species, $\tau_B = \text{diag}(\tau_{B1}, ..., \tau_{Bn})$ and $\tau_M = \text{diag}(\tau_{M1}, ..., \tau_{Mm})$ are the time constants of each species, $\boldsymbol{F}$ and $\boldsymbol{f}_\delta$ describe the bulk- and membrane-bound reaction kinetics, and $\boldsymbol{q}_\delta$ describes the interchange between bulk- and membrane-bound species across the bulk-membrane interface $\partial\Omega$. The constant γ in (A.15b) is included to reflect possible asymmetries in the interchange between bulk- and membrane-bound species. While we may anticipate that the bulk-bound reaction kinetics $\boldsymbol{F}(\cdot)$ are independent of the membrane-thickness, the same cannot be said

of the membrane-bound kinetics $\boldsymbol{f}_\delta(\cdot)$ and boundary interchange $\boldsymbol{q}_\delta(\cdot,\cdot)$. Indeed, integrating (A.16a) over Ω_δ and using the divergence theorem gives

$$\tau_M \frac{d}{dt}\int_{\Omega_\delta} \boldsymbol{u} = \int_{\partial\Omega_\delta^i} \boldsymbol{q}_\delta(\boldsymbol{u},\boldsymbol{U}) + \int_{\Omega_\delta} \boldsymbol{f}_\delta(\boldsymbol{u}).$$

Since $\mathrm{vol}(\Omega_\delta) = O(\delta)$ and $\mathrm{area}(\partial\Omega) = O(1)$, the three terms are balanced for $\delta \ll 1$ provided that they satisfy $O(\delta)O(\boldsymbol{u}) = O(\boldsymbol{q}_\delta) = O(\delta)O(\boldsymbol{f}_\delta)$. Anticipating that $\boldsymbol{U} = O(1)$, (A.15) and (A.16) imply that

$$\boldsymbol{q}_\delta = O(1), \quad \boldsymbol{u} = O(\delta^{-1}), \quad \boldsymbol{f}_\delta = O(\delta^{-1}). \tag{A.17}$$

We now derive a leading order approximation to the bulk-membrane coupled reaction-diffusion system (A.15) and (A.16) in the $\delta \ll 1$ limit. We let $X(s) \in \partial\Omega$ parametrize $\partial\Omega$ where $s \in B \subset \mathbb{R}^{N-1}$. In particular we assume that s is the arc-length along $\partial\Omega$ when $N = 2$ and $s = (s_1, s_2)$ when $N = 3$. Next we choose the sign of the curvature $\kappa(s)$ of $X(s)$ when $N = 2$ and the orientation of the local basis (X_1, X_2) when $N = 3$ such that the unit normal at $X(s) \in \partial\Omega$ given by

$$\nu(s) = \kappa(s)^{-1}\frac{d^2X}{ds_1^2} \quad (N=2), \qquad \nu(s_1,s_2) = \frac{\partial_1 X \times \partial_2 X}{|\partial_1 X \times \partial_2 X|} \quad (N=3), \tag{A.18}$$

points away from the interior of Ω. Parameterizing Ω_δ in terms of the boundary fitted coordinates $(s,\eta) \in U \times (0,1)$ as

$$X(s) + \delta\eta\,\nu(s) \in \Omega_\delta, \tag{A.19}$$

the results from Appendix A.1 we imply the following approximations for the Laplacian in Ω_δ

$$\Delta = \delta^{-2}\partial_\eta^2 + \delta^{-1}\kappa\partial_\eta - \kappa^2\eta\,\partial_\eta + \partial_s^2 + O(\delta), \qquad (N=2) \tag{A.20}$$

$$\Delta = \delta^{-2}\partial_\eta^2 + 2\delta^{-1}H_{\partial\Omega}\partial_\eta - (\kappa_1^2+\kappa_2^2)\eta\,\partial_\eta + \Delta_{\partial\Omega} + O(\delta), \quad (N=3) \tag{A.21}$$

where κ_i $(i = 1,2)$ are the principal curvatures of $\partial\Omega$, $H = (\kappa_1+\kappa_2)/2$ is the mean curvature, and $\Delta_{\partial\Omega}$ is the Laplace-Beltrami operator on $\partial\Omega$. Throughout this

section we will use $\Delta_{\partial\Omega} = \partial_s^2$ when $N = 2$. Based on the scaling (A.17) we suppose that $\boldsymbol{f}_\delta(\boldsymbol{u}) = \delta^{-1}\boldsymbol{f}(\delta\boldsymbol{u})$ and $\boldsymbol{q}_\delta(\boldsymbol{u},\boldsymbol{U}) = \boldsymbol{q}(\delta\boldsymbol{u},\boldsymbol{U})$ and let

$$\boldsymbol{u} = \delta^{-1}\boldsymbol{u}_0 + \boldsymbol{u}_1 + \delta\boldsymbol{u}_2 + O(\delta^2), \qquad \boldsymbol{U} = \boldsymbol{U}_0 + O(\delta), \tag{A.22}$$

where each $\boldsymbol{u}_i = O(1)$ and $\boldsymbol{U}_0 = O(1)$. Note that whereas $\boldsymbol{u}$ denotes a volume concentration, $\boldsymbol{u}_0$ denotes a surface concentration. Substituting both $\partial_n = -\delta^{-1}\partial_\eta$ and (A.20) into the membrane-bound system (A.16) and collecting powers of δ, we find that the leading order, $O(\delta^{-3})$, equation is given by

$$D_M\partial_{\eta\eta}\boldsymbol{u}_0 = 0, (s,\eta) \in \partial\Omega \times (0,1), \qquad D_M\partial_\eta\boldsymbol{u}_0 = 0, \quad \eta = 0,1$$

which implies $\boldsymbol{u}_0 = \boldsymbol{u}_0(s)$. Similarly, from the $O(\delta^{-2})$ equation we find that the first order correction is independent of η, $\boldsymbol{u}_1 = \boldsymbol{u}_1(s)$. The $O(\delta^{-1})$ problem is then given by

$$\begin{aligned}
&\partial_t\boldsymbol{u}_0 = D_M\partial_{\eta\eta}\boldsymbol{u}_2 + D_M\Delta_{\partial\Omega}\boldsymbol{u}_0 + \boldsymbol{f}(\boldsymbol{u}_0), \quad (s,\eta) \in \partial\Omega \times (0,1),\\
&D_M\partial_\eta\boldsymbol{u}_2 = \boldsymbol{q}(\boldsymbol{u}_0,\boldsymbol{U}_0), \quad \eta = 0, \qquad D_M\partial_\eta\boldsymbol{u}_2 = 0, \quad \eta = 1.
\end{aligned}$$

Integrating over $0 < \eta < 1$ and using both the boundary conditions of $\boldsymbol{u}_2$ and the η-independence of $\boldsymbol{u}_0$ we obtain

$$\partial_t\boldsymbol{u}_0 = D_M\Delta_{\partial\Omega}\boldsymbol{u}_0 + \boldsymbol{f}(\boldsymbol{u}_0) - \boldsymbol{q}(\boldsymbol{u}_0,\boldsymbol{U}_0), \qquad \text{in} \quad \partial\Omega.$$

Summarizing, in the limit of a thin membrane, $\delta \ll 1$, the bulk-membrane coupled reaction-diffusion system (A.15) and (A.16) is approximated by

$$\tau\partial_t\boldsymbol{U}_0 = D_B\Delta\boldsymbol{U}_0 + \boldsymbol{F}(\boldsymbol{U}_0), \qquad \text{in} \quad \Omega, \tag{A.23a}$$

$$D_B\partial_n\boldsymbol{U}_0 = \gamma q(\boldsymbol{u}_0,\boldsymbol{U}_0), \qquad \text{on} \quad \partial\Omega, \tag{A.23b}$$

$$\partial_t\boldsymbol{u}_0 = D_M\Delta_{\partial\Omega}\boldsymbol{u}_0 + \boldsymbol{f}(\boldsymbol{u}_0) - \boldsymbol{q}(\boldsymbol{u}_0,\boldsymbol{U}_0), \qquad \text{in} \quad \partial\Omega, \tag{A.23c}$$

where $\boldsymbol{U}_0 = O(1)$ and $\boldsymbol{u}_0 = O(1)$ are the leading order terms in the expansion (A.22) and where we assume that $\boldsymbol{f}(\boldsymbol{u}_0) = O(1)$ and $\boldsymbol{q}(\boldsymbol{u}_0,\boldsymbol{U}_0) = O(1)$. Note that we have assumed no interaction between the extracellular space and the cell membrane. It

is clear from the above derivation that including such an interaction would add an additional term to (A.23c). Additionally we have assumed that the membrane thickness is constant and equal to $\delta > 0$. It is a straightforward extension to include a non-constant thickness by letting $0 < \eta < \delta h(s)$ for $s \in \partial\Omega$.

Appendix B

Appendix for Chapter 2

B.1 Green's Functions in the Well-Mixed Limit and for the Disk

In this appendix we collect all the relevant Green's functions and indicate some of their key properties. We focus specifically on the uncoupled ($K = 0$) Green's function, the well-mixed Green's function ($D_b \to \infty$), and the disk Green's function ($\Omega = B_R(0)$). For the first two cases explicit formulae can be derived, while for the final case we must rely on a Fourier series expansion representation.

B.1.1 Uncoupled Membrane Green's Function

When the bulk and membrane are uncoupled there is no direct dependence on the bulk Green's function. Indeed the only relevant geometric dependent parameter becomes the perimeter of the domain $L = |\partial\Omega|$. Thus, Ω may be an arbitrary bounded and simply connected subset of $\mathbb{R}^2$ with C^2 boundary. We define the uncoupled Green's function Γ^λ as the solution to

$$D_v\partial_\sigma^2\Gamma - \mu^2\Gamma = -\delta(\sigma-\zeta), \qquad 0<\sigma<L, \qquad \Gamma \quad \text{is } L\text{-periodic.} \tag{B.1}$$

The solution to (B.1) is readily calculated as

$$\Gamma(\sigma,\zeta) = \frac{\coth\left(\frac{\mu L}{2\sqrt{D_v}}\right)\cosh\left(\frac{\mu}{\sqrt{D_v}}|\sigma-\zeta|\right)}{2\sqrt{D_v}\mu} - \frac{\sinh\left(\frac{\mu}{\sqrt{D_v}}|\sigma-\zeta|\right)}{2\sqrt{D_v}\mu}. \tag{B.2}$$

B.1.2 Bulk and Membrane Green's functions in the Well-Mixed Limit

We now derive the leading order expression for the membrane Green's function, defined by (2.22), when $D_b \to \infty$. To leading order G^λ_Ω, defined by (2.19), is constant and from the divergence theorem we find

$$G^\lambda_\Omega(\sigma,\tilde{\sigma}) \sim G^\lambda_{\Omega 0} = \frac{1}{KL+\mu^2_{b\lambda}A} = \frac{\beta/K}{\mu^2_{b\lambda}+\beta}\frac{1}{L}, \qquad \text{where} \quad \beta \equiv K\frac{L}{A}. \tag{B.3}$$

Here $L \equiv |\partial\Omega|$ and $A \equiv |\Omega|$. The leading order problem for the membrane Green's function in (2.22) is then

$$D_v\partial^2_\sigma G^\lambda_{\partial\Omega} - \mu^2_{s\lambda}G^\lambda_{\partial\Omega} + K^2 G^\lambda_{\Omega 0}\int_0^L G^\lambda_{\partial\Omega}(\tilde{\sigma};\zeta)\,d\tilde{\sigma} = -\delta(\sigma-\zeta). \tag{B.4}$$

Upon integrating this equation and using the periodic boundary conditions we get

$$\int_0^L G^\lambda_{\partial\Omega}(\tilde{\sigma};\zeta)\,d\tilde{\sigma} = \frac{1}{\mu^2_{s\lambda} - K^2 L G^\lambda_{\Omega 0}} = \left(\frac{1}{\mu^2_{s\lambda}(\mu^2_{b\lambda}+\beta) - K\beta}\right)\frac{1}{AG^\lambda_{\Omega 0}},$$

where $G^\lambda_{\Omega 0}$ is defined in (B.3). Therefore, from (B.4), we find that $G^\lambda_{\partial\Omega}$ satisfies

$$D_v\partial^2_\sigma G^\lambda_{\partial\Omega} - \mu^2_{s\lambda}G^\lambda_{\partial\Omega} = -\delta(\sigma-\zeta) - \frac{K^2/A}{\mu^2_{s\lambda}(\mu^2_{b\lambda}+\beta) - K\beta}.$$

This problem is readily solved in terms of the uncoupled Green's function of (B.2) by defining

$$\Gamma^\lambda(\sigma,\zeta) := \Gamma(\sigma,\zeta)\big|_{\mu=\mu_{s\lambda}},$$

and then using the decomposition

$$G^{\lambda}_{\partial\Omega}(\sigma,\zeta) = \Gamma^{\lambda}(\sigma,\zeta) + \frac{\gamma_{\lambda}}{\mu^2_{s\lambda}}, \qquad \gamma_{\lambda} \equiv \frac{K^2/A}{\mu^2_{s\lambda}(\mu^2_{b\lambda}+\beta) - K\beta}. \tag{B.5}$$

B.1.3 Bulk and Membrane Green's functions in the Disk

Here we consider the bulk Green's function defined by (2.19). By using separation of variables (in polar coordinates), and applying the boundary condition in (2.19), we can write this Green's function as a Fourier series

$$\begin{aligned} G^{\lambda}_{\Omega}(r,\sigma,\tilde{\sigma}) &= \frac{1}{2\pi R}\sum_{n=-\infty}^{\infty} a^{\lambda}_n P_n(r) e^{\frac{in}{R}(\sigma-\tilde{\sigma})}, \\ P_n(r) \equiv \frac{I_{|n|}(\omega_{b\lambda} r)}{I_{|n|}(\omega_{b\lambda} R)}, &\quad a^{\lambda}_n \equiv \frac{1}{D_b P_n'(R) + K}, \quad \omega_{b\lambda} \equiv \frac{\mu_{b\lambda}}{\sqrt{D_b}}. \end{aligned} \tag{B.6}$$

We remark that the singularity lies on the boundary and for this reason the radial dependence is given only in terms of the modified Bessel functions of the first kind $I_n(z)$. Similarly, we can represent the membrane Green's function in (2.22) for the disk in terms of the Fourier series

$$G^{\lambda}_{\partial\Omega}(\sigma,\sigma_0) = \frac{1}{2\pi R}\sum_{n=-\infty}^{\infty} g^{\lambda}_n e^{\frac{in}{R}(\sigma-\sigma_0)}, \qquad g^{\lambda}_n \equiv \frac{1}{D_v \frac{n^2}{R^2} + \mu^2_{s\lambda} - K^2 a^{\lambda}_n}. \tag{B.7}$$

B.1.4 A Useful Summation Formula for the Disk Green's Functions

We make note here of a useful summation formula for numerically evaluating the Green's function eigenvalues for the disk. By integrating the function $(\zeta^2 + z^2)^{-1}\cot\big(\frac{\pi}{N}(\zeta-k)\big)$ over the contour enclosing $[-R,R]\times[-R,R]$, and then taking the limit $R\to\infty$, we obtain

$$S(z;N,k) := \sum_{n=-\infty}^{\infty} \frac{1}{(nN+k)^2+z^2} = \frac{\pi}{2Nz}\left[\coth\left(\frac{\pi}{N}(z+ik)\right) + \coth\left(\frac{\pi}{N}(z-ik)\right)\right]. \tag{B.8}$$

B.2 Derivation of Membrane Green's Function for the Perturbed Disk

In this appendix we provide the details for calculating the leading-order correction to the perturbed disk Green's function given in (2.2). Recall that the bulk Green's function solves

$$\begin{aligned} D_b \Delta G^\lambda_\Omega - \mu^2_{b\lambda} G^\lambda_\Omega &= 0, \quad \text{in} \quad \Omega_\delta, \\ D_b \partial_n G^\lambda_\Omega + K G^\lambda_\Omega &= \delta_{\partial\Omega_\delta}(x-\tilde{x}), \quad \text{on} \quad \partial\Omega_\delta. \end{aligned} \tag{B.9}$$

On the boundary $r = R + \delta h(\theta)$ of the perturbed disk we calculate in terms of polar coordinates that

$$\hat{n}(\theta) = \left[1 + \left(\tfrac{\delta h'(\theta)}{R+\delta h(\theta)}\right)^2\right]^{-\frac{1}{2}} \left(\hat{e}_r - \tfrac{\delta h'(\theta)}{R+\delta h(\theta)} \hat{e}_\theta\right), \quad \nabla = \hat{e}_r \partial_r + \frac{1}{r} \hat{e}_\theta \partial_\theta,$$
$$\delta_{\partial\Omega_\delta}(x-\tilde{x}) = \left[1 + \left(\tfrac{\delta h'(\theta)}{R+\delta h(\theta)}\right)^2\right]^{-\frac{1}{2}} \frac{\delta(\theta-\tilde{\theta})}{R+\delta h(\theta)},$$

which yields the following asymptotic behaviour as $\delta \to 0$:

$$\hat{n}(\theta) \sim \hat{e}_r - \delta \frac{h'(\theta)}{R} \hat{e}_\theta + \mathscr{O}(\delta^2),$$
$$\delta_{\partial\Omega_\delta}(x-\tilde{x}) \sim \frac{1}{R}\delta(\theta-\tilde{\theta}) - \delta \frac{h(\theta)}{R^2}\delta(\theta-\tilde{\theta}) + \mathscr{O}(\delta^2).$$

Next, for $\delta \ll 1$, we seek a solution of the form

$$G^\lambda_\Omega(r,\theta,\tilde{\theta} \sim G^\lambda_{\Omega 0}(r,\theta,\tilde{\theta}) + G^\lambda_{\Omega 1}(r,\theta,\tilde{\theta})\delta + \mathscr{O}(\delta^2).$$

Upon substituting these expansions into (B.9), and collecting powers of δ, we obtain the following zeroth-order and first-order problems:

$$\begin{aligned} D_b \Delta G^\lambda_{\Omega 0} - \mu^2_{b\lambda} G^\lambda_{\Omega 0} &= 0, \quad \text{in } \Omega_0, \\ \mathscr{B}_0 G^\lambda_{\Omega 0} &= \frac{\delta(\theta-\tilde{\theta})}{R}, \quad \text{on } \partial\Omega_0, \end{aligned}$$

and

$$D_b\Delta G^\lambda_{\Omega 1} - \mu^2_{b\lambda} G^\lambda_{\Omega 1} = 0, \quad \text{in } \Omega_0,$$
$$\mathscr{B}_0 G^\lambda_{\Omega 1} = -\frac{h(\theta)}{R}\frac{\delta(\theta-\tilde\theta)}{R} - \mathscr{B}_1 G^\lambda_{\Omega 0}, \quad \text{on } \partial\Omega_0,$$

where the boundary operators $\mathscr{B}_0$ and $\mathscr{B}_1$ are defined by

$$\mathscr{B}_0 \equiv D_b\partial_r + K \qquad \mathscr{B}_1 \equiv D_b\left(h(\theta)\partial_r^2 - \frac{h'(\theta)}{R^2}\partial_\theta\right) + Kh(\theta)\partial_r.$$

The zeroth-order solution is the unperturbed disk bulk Green's function given in (B.6). For the problem for the leading order correction, we use linearity to decompose its solution in the form

$$\begin{aligned} G^\lambda_{\Omega 1}(r,\theta,\tilde\theta) &= -\frac{h(\tilde\theta)}{R} G^\lambda_{\Omega 0}(r,\theta,\tilde\theta) + \tilde G^\lambda_{\Omega 1}(r,\theta,\tilde\theta), \\ \tilde G^\lambda_{\Omega 1}(r,\theta,\tilde\theta) &= \frac{1}{2\pi R}\sum_{n=-\infty}^{\infty} \tilde a^\lambda_{1n}(\tilde\theta) P_n(r) e^{in\theta}, \end{aligned} \tag{B.10}$$

for some coefficients $\tilde a^\lambda_{1n}$ to be found. To determine an expression for these coefficients, we first multiply the boundary condition $\mathscr{B}_0\tilde G^\lambda_{\Omega 1} = -\mathscr{B}_1 G^\lambda_{\Omega 0}$ by $e^{-in\theta}$, and then integrate from 0 to 2π. This gives

$$\frac{1}{R}\left(D_b P_n'(R) + K\right)\tilde a^\lambda_{1n}(\tilde\theta) = -\int_0^{2\pi} e^{-in\theta}\mathscr{B}_1 G^\lambda_{\Omega 0}\, d\theta. \tag{B.11}$$

Then, by using the differential equation satisfied by $G^\lambda_{\Omega 0}$ we calculate the right-hand side of this expression as

$$\begin{aligned} \int_0^{2\pi} e^{-in\theta}\mathscr{B}_1 G^\lambda_{\Omega 0}(R,\theta,\tilde\theta)\, d\theta = & D_b\int_0^{2\pi} h(\theta) G^\lambda_{\Omega 0 rr}(R,\theta,\tilde\theta) e^{-in\theta}\, d\theta \\ & - \tfrac{D_b}{R^2}\int_0^{2\pi} h'(\theta) G^\lambda_{\Omega 0\theta}(R,\theta,\tilde\theta) e^{-in\theta}\, d\theta \\ & + K\int_0^{2\pi} h(\theta) G^\lambda_{\Omega 0 r}(R,\theta,\tilde\theta) e^{-in\theta}\, d\theta. \end{aligned} \tag{B.12}$$

Next, we assume that the boundary perturbation $h(\theta)$ is sufficiently smooth so that

each of the following hold:

$$h(\theta)=\sum_{n=-\infty}^{\infty}h_n e^{in\theta},\quad h'(\theta)=i\sum_{n=-\infty}^{\infty}nh_n e^{in\theta},\quad h''(\theta)=-\sum_{n=-\infty}^{\infty}n^2h_n e^{in\theta}. \tag{B.13}$$

This allows us to calculate the individual terms on the right-hand side of (B.12) as

$$\begin{aligned}
\int_0^{2\pi}h(\theta)G^{\lambda}_{\Omega 0rr}(R,\theta,\tilde{\theta})e^{-in\theta}d\theta &= \frac{1}{R}\sum_{k=-\infty}^{\infty}P_k''(R)a_k^{\lambda}h_{n-k}e^{-ik\tilde{\theta}},\\
\int_0^{2\pi}h'(\theta)G^{\lambda}_{\Omega 0\theta}(R,\theta,\tilde{\theta})e^{-in\theta}d\theta &= -\frac{1}{R}\sum_{k=-\infty}^{\infty}k(n-k)a_k^{\lambda}h_{n-k}e^{-ik\tilde{\theta}},\\
\int_0^{2\pi}h(\theta)G^{\lambda}_{\Omega 0r}(R,\theta,\tilde{\theta})e^{-in\theta}d\theta &= \frac{1}{R}\sum_{k=-\infty}^{\infty}P_k'(R)a_k^{\lambda}h_{n-k}e^{-ik\tilde{\theta}},
\end{aligned}$$

where a_k^{λ} are the Fourier coefficients of the leading-order Green's function, as defined in (B.6). By substituting these relations into (B.12), and then using (B.11), we determine the coefficients as

$$\tilde{a}_{1n}^{\lambda}(\tilde{\theta})=\sum_{k=-\infty}^{\infty}\hat{a}_{n,k}^{\lambda}a_k^{\lambda}h_{n-k}e^{-ik\tilde{\theta}},\quad \hat{a}_{n,k}^{\lambda}\equiv-\frac{D_bP_k''(R)+KP_k'(R)+\frac{D_b}{R^2}k(n-k)}{D_bP_n'(R)+K}. \tag{B.14}$$

In (B.14), to calculate various derivatives of $P_n(R)$, as defined in (B.6), we make repeated use of the identity

$$I_n'(z)=\frac{n}{z}I_n(z)+I_{n+1}(z),$$

to readily derive that

$$\begin{aligned}
P_n'(R)&=\frac{|n|}{R}+\omega_{b\lambda}\frac{I_{|n+1|}(\omega_{b\lambda}R)}{I_{|n|}(\omega_{b\lambda}R)},\\
P_n''(R)&=\frac{|n|(|n|-1)}{R^2}+\frac{2|n|+1}{R}\omega_{b\lambda}\frac{I_{|n+1|}(\omega_{b\lambda}R)}{I_{|n|}(\omega_{b\lambda}R)}+\omega_{b\lambda}^2\frac{I_{|n+2|}(\omega_{b\lambda}R)}{I_{|n|}(\omega_{b\lambda}R)}.
\end{aligned}$$

This completes the derivation of the leading-order correction for the bulk Green's function, defined in (B.10).

Next, we derive a two-term approximation for the membrane Green's function

problem on the perturbed disk. This Green's function satisfies

$$D_v\partial_\sigma^2 G^\lambda_{\partial\Omega}(\sigma,\sigma_0) - \mu_{s\lambda}^2 G^\lambda_{\partial\Omega}(\sigma,\sigma_0) + K^2\int_0^{|\partial\Omega_\delta|} G^\lambda_\Omega(\sigma,\tilde\sigma)G^\lambda_{\partial\Omega}(\tilde\sigma,\sigma_0)\,d\tilde\sigma = -\delta(\sigma-\sigma_0), \tag{B.15}$$

for $0 \le \sigma < |\partial\Omega_\delta|$. Repeated use of the chain rule to the arc-length formula

$$\sigma(\theta) = \int_0^\theta \big(R+\delta h(\vartheta)\big)\sqrt{1+\left(\frac{\delta h'(\vartheta)}{R+\delta h(\vartheta)}\right)^2}\,d\vartheta,$$

gives

$$\partial_\sigma^2 = \frac{1}{(R+\delta h(\theta))^2+(\delta h'(\theta))^2}\partial_\theta^2 - \delta h'(\theta)\frac{R+\delta h(\theta)+\delta h''(\theta)}{[(R+\delta h(\theta))^2+(\delta h'(\theta))^2]^2}\partial_\theta.$$

Multiplying the membrane equation through by $(R+\delta h(\theta))^2+(\delta h'(\theta))^2$, writing $D_v = D_{v0}\big(1+\frac{D_{v1}}{D_{v0}}\delta\big)$, and then dividing through by $R^2\big(1+\frac{D_{v1}}{D_{v0}}\delta\big)$, we obtain the perturbed problem

$$\begin{aligned}
&\tfrac{D_{v0}}{R^2}\partial_\theta^2 G^\lambda_{\partial\Omega}(\theta,\theta_0) - \tfrac{D_{v0}}{R^2}\delta h'(\theta)\tfrac{R+\delta[h(\theta)+h''(\theta)]}{(R+\delta h(\theta))^2+(\delta h'(\theta))^2}\partial_\theta G^\lambda_{\partial\Omega}(\theta,\theta_0) - \tfrac{\mu_{s\lambda}^2}{R^2}\tfrac{(R+\delta h(\theta))^2+(\delta h'(\theta))^2}{1+\frac{D_{v1}}{D_{v0}}\delta}G^\lambda_{\partial\Omega}(\theta,\theta_0)\\
&+\tfrac{K^2}{R^2}\tfrac{(R+\delta h(\theta))^2+(\delta h'(\theta))^2}{1+\frac{D_{v1}}{D_{v0}}\delta}\int_0^{2\pi}\big(G^\lambda_{\Omega 0}(R,\theta,\tilde\theta)+\delta G^\lambda_{\Omega 1}(R,\theta,\tilde\theta)+\delta h(\theta)G^\lambda_{\Omega 0r}(R,\theta,\tilde\theta)\big)\\
&\qquad\qquad\times G^\lambda_{\partial\Omega}(\tilde\theta,\theta_0)\sqrt{(R+\delta h(\tilde\theta))^2+(\delta h'(\tilde\theta))^2}\,d\tilde\theta\\
&\quad = -\tfrac{1}{R^2}\tfrac{\sqrt{(R+\delta h(\theta))^2+(\delta h'(\theta))^2}}{1+\frac{D_{v1}}{D_{v0}}\delta}\delta(\theta-\theta_0).
\end{aligned}$$

To determine a two-term asymptotic solution to this problem, we expand the membrane Green's function as

$$G^\lambda_{\partial\Omega}(\theta,\theta_0) \sim G^\lambda_{\partial\Omega 0}(\theta,\theta_0) + \delta G^\lambda_{\partial\Omega 1}(\theta,\theta_0) + \mathscr{O}(\delta^2).$$

Upon substituting this expansion into the perturbed problem, and collecting powers

of δ, we obtain the following zeroth-order and first-order problems:

$$\mathscr{M}_0 G^{\lambda}_{\partial\Omega 0}(\theta,\theta_0) = -\tfrac{1}{R}\delta(\theta-\theta_0),$$
$$\mathscr{M}_0 G^{\lambda}_{\partial\Omega 1}(\theta,\theta_0) = -\big(\tfrac{h(\theta)}{R} - \tfrac{D_{v1}}{D_{v0}}\big)\tfrac{1}{R}\delta(\theta-\theta_0) - \mathscr{M}_1 G^{\lambda}_{\partial\Omega 0}(\theta,\theta_0).$$

Here we have defined the unperturbed membrane operator $\mathscr{M}_0$ by

$$\mathscr{M}_0\psi(\theta,\theta_0) \equiv \tfrac{D_{v0}}{R^2}\partial_\theta^2\psi(\theta,\theta_0) - \mu_{s\lambda}^2\psi(\theta,\theta_0) + K^2\int_0^{2\pi} G^{\lambda}_{\Omega 0}(R,\theta,\tilde\theta)\psi(\tilde\theta,\theta_0)R\,d\tilde\theta,$$

and its leading-order correction $\mathscr{M}_1$ by

$$\begin{aligned}\mathscr{M}_1\psi(\theta,\theta_0) \equiv &-\tfrac{D_{v0}}{R^3}h'(\theta)\partial_\theta\psi(\theta,\theta_0) - \mu_{s\lambda}^2\big(\tfrac{2h(\theta)}{R} - \tfrac{D_{v1}}{D_{v0}}\big)\psi(\theta,\theta_0)\\ &+K^2\big(\tfrac{2h(\theta)}{R} - \tfrac{D_{v1}}{D_{v0}}\big)\int_0^{2\pi} G^{\lambda}_{\Omega 0}(R,\theta,\tilde\theta)\psi(\tilde\theta,\theta_0)R\,d\tilde\theta\\ &+K^2\int_0^{2\pi} G^{\lambda}_{\Omega 1}(R,\theta,\tilde\theta)\psi(\tilde\theta,\theta_0)R\,d\tilde\theta\\ &+K^2h(\theta)\int_0^{2\pi} G^{\lambda}_{\Omega 0r}(R,\theta,\tilde\theta)\psi(\tilde\theta,\theta_0)R\,d\tilde\theta\\ &+K^2\int_0^{2\pi} G^{\lambda}_{\Omega 0}(R,\theta,\tilde\theta)\psi(\tilde\theta,\theta_0)h(\tilde\theta)\,d\tilde\theta.\end{aligned} \tag{B.16}$$

The zeroth-order solution is that of the unperturbed disk and is given by (B.7). By linearity, we then seek the solution for the leading order correction in the form

$$G^{\lambda}_{\partial\Omega 1}(\theta,\theta_0) = \big(\tfrac{h(\theta_0)}{R} - \tfrac{D_{v1}}{D_{v0}}\big)G^{\lambda}_{\partial\Omega 0}(\theta,\theta_0) + \tilde G^{\lambda}_{\partial\Omega 1}(\theta,\theta_0), \tag{B.17}$$

where $\tilde G^{\lambda}_{\partial\Omega 1}(\theta,\phi)$ now satisfies

$$\mathscr{M}_0\tilde G^{\lambda}_{\partial\Omega 1}(\theta,\theta_0) = -\mathscr{M}_1 G^{\lambda}_{\partial\Omega 0}(\theta,\theta_0).$$

We will represent the solution $\tilde G^{\lambda}_{\partial\Omega 1}$ in terms of a Fourier series as

$$\tilde G^{\lambda}_{\partial\Omega 1}(\theta,\theta_0) = \frac{1}{2\pi R}\sum_{n=-\infty}^{\infty}\tilde g^{\lambda}_{1n}(\theta_0)e^{in\theta}, \tag{B.18}$$

for some coefficients $\tilde g^{\lambda}_{1n}(\theta_0)$ to be found. Similar to the calculation provided above

for the perturbed bulk Green's function, we obtain that

$$\tilde{g}^{\lambda}_{1n}(\theta_0) = R g^{\lambda}_{0n} \int_0^{2\pi} e^{-in\theta} \mathscr{M}_1 G^{\lambda}_{\partial\Omega 0}(\theta,\theta_0)\, d\theta. \tag{B.19}$$

By using (B.16) we calculate the right-hand side of this expression as

$$\int_0^{2\pi} e^{-in\theta} \mathscr{M}_1 G^{\lambda}_{\partial\Omega 0}(\theta,\theta_0) d\theta = -\tfrac{D_{v0}}{R^3} J_{1n}(\theta_0) - \tfrac{2\mu^2_{s\lambda}}{R} J_{2n}(\theta_0) + \tfrac{\mu^2_{s\lambda} D_{v1}}{D_{v0}} J_{3n}(\theta_0) \tag{B.20}$$

$$+ 2K^2 J_{4n}(\theta_0) - \tfrac{K^2 R D_{v1}}{D_{v0}} J_{5n}(\theta_0) + K^2 R J_{6n}(\theta_0) + K^2 R J_{7n}(\theta_0), \tag{B.21}$$

where the various integrals $J_{1n},\ldots,J_{7n}$ are defined by

$$\begin{aligned}
J_{1n}(\theta_0) &= \int_0^{2\pi} h'(\theta) G^{\lambda}_{\partial\Omega 0\theta}(\theta,\theta_0) e^{-in\theta} d\theta,\\
J_{2n}(\theta_0) &= \int_0^{2\pi} h(\theta) G_{\partial\Omega 0}(\theta,\theta_0) e^{-in\theta} d\theta,\\
J_{3n}(\theta_0) &= \int_0^{2\pi} G^{\lambda}_{\partial\Omega 0}(\theta,\theta_0) e^{-in\theta} d\theta,\\
J_{4n}(\theta_0) &= \int_0^{2\pi}\int_0^{2\pi} h(\theta) G^{\lambda}_{\Omega 0}(R,\theta,\tilde{\theta}) G^{\lambda}_{\partial\Omega 0}(\tilde{\theta},\theta_0) e^{-in\theta} d\tilde{\theta} d\theta,\\
J_{5n}(\theta_0) &= \int_0^{2\pi}\int_0^{2\pi} G^{\lambda}_{\Omega 0}(R,\theta,\tilde{\theta}) G^{\lambda}_{\partial\Omega 0}(\tilde{\theta},\theta_0) e^{-in\theta} d\tilde{\theta} d\theta,\\
J_{6n}(\theta_0) &= \int_0^{2\pi}\int_0^{2\pi} \tilde{G}^{\lambda}_{\Omega 1}(R,\theta,\tilde{\theta}) G^{\lambda}_{\partial\Omega 0}(\tilde{\theta},\theta_0) e^{-in\theta} d\tilde{\theta} d\theta,\\
J_{7n}(\theta_0) &= \int_0^{2\pi}\int_0^{2\pi} h(\theta) G^{\lambda}_{\Omega 0 r}(R,\theta,\tilde{\theta}) G^{\lambda}_{\partial\Omega 0}(\tilde{\theta},\theta_0) e^{-in\theta} d\tilde{\theta} d\theta.
\end{aligned}$$

By using the Fourier series representations for the leading-order bulk and membrane Green's functions given in (B.6) and (B.7), respectively, together with (B.13)

for $h(\theta)$, we calculate explicitly that

$$
\begin{aligned}
J_{1n}(\theta_0) &= -\frac{1}{R}\sum_{k=-\infty}^{\infty} k(n-k)h_{n-k}g_k^{\lambda}e^{-ik\theta_0},\\
J_{2n}(\theta_0) &= \frac{1}{R}\sum_{k=-\infty}^{\infty} h_{n-k}g_k^{\lambda}e^{-ik\theta_0},\\
J_{3n}(\theta_0) &= \frac{1}{R}g_n^{\lambda}e^{-in\theta_0},\\
J_{4n}(\theta_0) &= \frac{1}{R^2}\sum_{k=-\infty}^{\infty} h_{n-k}a_k^{\lambda}g_k^{\lambda}e^{-ik\theta_0},\\
J_{5n}(\theta_0) &= \frac{1}{R^2}a_n^{\lambda}g_n^{\lambda}e^{-in\theta_0},\\
J_{6n}(\theta_0) &= \frac{1}{R^2}\sum_{k=-\infty}^{\infty} h_{n-k}\hat{a}_{n,k}^{\lambda}a_k^{\lambda}g_k^{\lambda}e^{-ik\theta_0},\\
J_{7n}(\theta_0) &= \frac{1}{R^2}\sum_{k=-\infty}^{\infty} h_{n-k}P_k'(R)a_k^{\lambda}g_k^{\lambda}e^{-ik\theta_0}.
\end{aligned}
$$

Upon substituting these expressions into (B.20), and then recalling (B.19), we conclude that

$$
\begin{aligned}
\tilde{g}_{1n}^{\lambda}(\theta_0) =& g_n^{\lambda}\sum_{k=-\infty}^{\infty}\big\{\tfrac{D_{v0}}{R^3}k(n-k)-\tfrac{2\mu_{s\lambda}^2}{R}+\tfrac{2K^2}{R}a_k^{\lambda}+K^2\hat{a}_{n,k}^{\lambda}a_k^{\lambda}+K^2P_k'(R)a_k^{\lambda}\big\}h_{n-k}g_k^{\lambda}e^{-ik\theta_0}\\
&+\tfrac{D_{v1}}{D_{v0}}g_n^{\lambda}\big(\mu_{s\lambda}^2-2\pi K^2Ra_n^{\lambda}\big)g_n^{\lambda}e^{-in\theta_0},
\end{aligned}
$$

where the coefficients a_k^{λ} are defined in (B.6). We can use the definition of the coefficients g_n^{λ}, as given in (B.7), to write $\mu_{s\lambda}^2-K^2a_n^{\lambda}=\frac{1}{g_n^{\lambda}}-\frac{D_{v0}}{R^2}n^2$. In this way, we get

$$
\tilde{g}_{1n}^{\lambda}(\theta_0)=\sum_{k=-\infty}^{\infty}\hat{g}_{n,k}^{\lambda}h_{n-k}g_k^{\lambda}e^{-ik\theta_0}g_n^{\lambda}+\big(\tfrac{D_{v1}}{D_{v0}}-\tfrac{2h(\theta_0)}{R}\big)g_n^{\lambda}e^{-in\theta_0}-\tfrac{D_{v1}}{R^2}n^2(g_n^{\lambda})^2e^{-in\theta_0},
$$

where

$$
\hat{g}_{n,k}^{\lambda}=\tfrac{D_{v0}}{R^3}k(n+k)+K^2a_k^{\lambda}\big(\hat{a}_{n,k}^{\lambda}+P_k'(R)\big).
$$

Finally, from (B.17) and (B.18), we conclude that the first order correction for the

membrane Green's function is

$$G^{\lambda}_{\partial\Omega 1}(\theta,\theta_0) = -\frac{h(\theta_0)}{R} G^{\lambda}_{\partial\Omega 0}(\theta,\theta_0) + \frac{1}{2\pi R} \sum_{n=-\infty}^{\infty} \sum_{k=-\infty}^{\infty} \hat{g}^{\lambda}_{n,k} h_{n-k} g^{\lambda}_{k} g^{\lambda}_{n} e^{in\theta - ik\theta_0} - \frac{D_{v1}}{2\pi R^3} \sum_{n=-\infty}^{\infty} n^2 (g^{\lambda}_{n})^2 e^{in(\theta-\theta_0)}.$$

Appendix C

Appendix for Chapter 3

C.1 Derivation of Lemma 3.3.1

Denote by $\boldsymbol{I}$ the left hand side of (3.66) and let $\mathscr{R}_{\boldsymbol{y}}$ be any rotation matrix such that $\mathscr{R}_{\boldsymbol{y}}\boldsymbol{y} = \boldsymbol{e}_z \equiv (0,0,1)^T$. Since $f(\boldsymbol{x},\boldsymbol{z}) = f(\mathscr{R}_{\boldsymbol{y}}\boldsymbol{x},\mathscr{R}_{\boldsymbol{y}}\boldsymbol{z})$ and $|\boldsymbol{y}-\boldsymbol{x}| = |\mathscr{R}_{\boldsymbol{y}}\boldsymbol{y}-\mathscr{R}_{\boldsymbol{y}}\boldsymbol{x}|$ we immediately get

$$\mathscr{R}_{\boldsymbol{y}}\boldsymbol{I} = \int_{\partial\Omega} \frac{\boldsymbol{e}_z - \mathscr{R}_{\boldsymbol{y}}\boldsymbol{x}}{|\mathscr{R}_{\boldsymbol{y}}\boldsymbol{y}-\mathscr{R}_{\boldsymbol{y}}\boldsymbol{x}|^2} f(\mathscr{R}_{\boldsymbol{y}}\boldsymbol{x},\mathscr{R}_{\boldsymbol{y}}z)dA_{\boldsymbol{x}} = \int_{\partial\Omega} \frac{\boldsymbol{e}_z - \boldsymbol{x}}{|\boldsymbol{e}_z-\boldsymbol{x}|^2} f(\boldsymbol{x},\mathscr{R}_{\boldsymbol{y}}\boldsymbol{z})dA_{\boldsymbol{x}}.$$

Since $|\boldsymbol{e}_z-\boldsymbol{x}|^2 = 2(1-\boldsymbol{e}_z^T\boldsymbol{x})$ for all $\boldsymbol{x}\in\partial\Omega$ the z-component of the left-hand side above is given by

$$\boldsymbol{e}_z^T(\mathscr{R}_{\boldsymbol{y}}\boldsymbol{I}) = \frac{1}{2}\int_{\partial\Omega} f(\boldsymbol{x},\mathscr{R}_{\boldsymbol{y}}\boldsymbol{z})dA_{\boldsymbol{x}} = \frac{1}{2} f_0(|\boldsymbol{z}|) \tag{C.1}$$

To compute the x and y components of the left-hand-side we use spherical coordinates and find that

$$\boldsymbol{e}_x^T(\mathscr{R}_{\boldsymbol{y}}\boldsymbol{I}) = \mathrm{Re}J, \quad \boldsymbol{e}_y^T(\mathscr{R}_{\boldsymbol{y}}\boldsymbol{I}) = -\mathrm{Im}J, \tag{C.2a}$$

where

$$J = -\frac{1}{2}\int_0^{\pi}\int_0^{2\pi} \frac{e^{-i\varphi}\sin\theta}{1-\cos\theta} f(\boldsymbol{x},\mathscr{R}_{\boldsymbol{y}}\boldsymbol{z})\sin\theta d\theta d\varphi \tag{C.2b}$$

and $\boldsymbol{e}_x = (1,0,0)^T$, $\boldsymbol{e}_y = (0,1,0)^T$, and we have used the notation

$$\boldsymbol{x} = (\sin\theta\cos\varphi, \sin\theta\sin\varphi, \cos\theta)^T, \quad \mathscr{R}_{\boldsymbol{y}}\boldsymbol{z} = |\boldsymbol{z}|(\sin\tilde{\theta}\cos\tilde{\varphi}, \sin\tilde{\theta}\sin\tilde{\varphi}, \cos\tilde{\theta})^T.$$

The summation formula

$$P_l(x_i^T x_j) = \sum_{m=-l}^{l} \frac{(l-m)!}{(l+m)!} P_l^m(\cos\theta_i) P_l^m(\cos\theta_j) e^{im(\varphi_i - \varphi_j)}, \tag{C.3}$$

then implies that

$$J = -\frac{1}{8\pi} \sum_{l=0}^{\infty} \sum_{m=-l}^{l} \frac{(l-m)!}{(l+m)!} f_l P_l^m(\cos\tilde{\theta}) e^{-im\tilde{\varphi}} \times \int_0^{\pi} \int_0^{2\pi} \frac{\sin^2\theta}{1-\cos\theta} P_l^m(\cos\theta) e^{i(m-1)\varphi} d\theta d\varphi,$$

of which only the $m = 1$ term is nonzero. The identity

$$\int_{-1}^{1} \sqrt{\frac{1+x}{1-x}} P_l^1(x) dx = -2,$$

obtained using integration by parts as well as $P_l^1(x) = -\sqrt{1-x^2} P_l'(x)$ and $P_l(1) = 1$ then gives the series

$$J = \frac{1}{2} \sum_{l=1}^{\infty} \frac{(l-m)!}{(l+m)!} f_l P_l^1(\cos\tilde{\theta}) e^{-i\tilde{\varphi}}. \tag{C.4}$$

Combining (C.1), (C.2), and (C.4), together with

$$\cos\tilde{\theta} = \boldsymbol{e}_z^T \frac{\mathscr{R}_{\boldsymbol{y}}\boldsymbol{z}}{|\boldsymbol{z}|} = (\mathscr{R}_{\boldsymbol{y}}^T \boldsymbol{e}_z)^T \frac{\boldsymbol{z}}{|\boldsymbol{z}|} = \boldsymbol{y}^T \frac{\boldsymbol{z}}{|\boldsymbol{z}|}.$$

and

$$\mathscr{R}_{\boldsymbol{y}}^T \begin{pmatrix} \cos\tilde{\varphi} \\ \sin\tilde{\varphi} \\ 0 \end{pmatrix} = \frac{1}{\sin\tilde{\theta}} \mathscr{R}_{\boldsymbol{y}}^T \left(\mathscr{R}_{\boldsymbol{y}} \frac{\boldsymbol{z}}{|\boldsymbol{z}|} - \cos\tilde{\theta} \boldsymbol{e}_z \right) = \frac{\mathscr{I}_3 - \boldsymbol{y}\boldsymbol{y}^T}{\sqrt{1 - (\boldsymbol{y}^T \boldsymbol{z}/|\boldsymbol{z}|)^2}} \frac{\boldsymbol{z}}{|\boldsymbol{z}|},$$

then gives (3.66).

C.2 Sign of Dynamic Terms

In this appendix we derive the inequalities (3.68) and (3.69b). To prove (3.68) we first calculate

$$\frac{d}{dz}\left(\sqrt{1-z^2}\sum_{l=1}^{\infty}\frac{g_l}{l(l+1)}P_l^1(z)\right)=\sum_{l=1}^{\infty}g_lP_l(z)=4\pi\left(g_{mr}(z)-\frac{1}{4\pi}g_0\right), \tag{C.5}$$

where

$$g_{mr}(z)\equiv G_{mr}((\sqrt{1-z^2},0,z)^T,\boldsymbol{e}_z) \tag{C.6}$$

and where the first equality was obtained using

$$P_l^1(z)=-\sqrt{1-z^2}P_l'(z), \tag{C.7}$$

and

$$\frac{d}{dz}\left[(1-z^2)\frac{dP_l}{dz}\right]+l(l+1)P_l(z)=0, \tag{C.8}$$

while the second equality was obtained using (3.27b). Integrating (C.5) from -1 to z and using $P_l^1(-1)=0$ for all $l\geq 1$ we obtain

$$\sum_{l=1}^{\infty}\frac{g_l}{l(l+1)}P_l^1(z)=\frac{4\pi}{\sqrt{1-z^2}}\int_{-1}^{z}\left(g_{mr}(\xi)-\frac{1}{2}\int_{-1}^{1}g_{mr}(\zeta)d\zeta\right)d\xi,$$

from which the inequality (3.68) follows by noting that $g_{mr}(z)$ is positive and monotone increasing in $-1<z<1$. The sign of $C(z)$ is similarly found by calculating

$$\frac{d}{dz}\left(\sqrt{1-z^2}C(z)\right)=1-\frac{f}{1-f}\frac{K}{D_w}g_0+\frac{4\pi f}{1-f}\frac{K}{D_w}g_{mr}(z)>0,$$

where the inequality follows by noting that $g_{mr}>0$ together with $g_0=D_w/(1-K)$ and the constraint (3.7) on f and K. The inequality (3.69b) then follows by noting that $\sqrt{1-z^2}C(z)=0$ at $z=-1$. Note in addition that $C(-1)=0$ since $P_l^1(-1)=0$ for all $l\geq 1$.

C.3 Linear Stability of the Common Angle Solution

In this appendix we consider the linear stability with respect to the slow dynamics of the common angle solution in Section 3.4.2 when the fuel source is given by (3.71). When $N = 2$ the 2×2 Green's matrix $\mathscr{G}$ is symmetric and of constant row-sum. It therefore admits the eigenvectors $\boldsymbol{p}_\pm = (1, \pm 1)^T$ with corresponding eigenvalues $\mu_\pm$ respectively. Additionally the Green's matrix $\mathscr{G}$ depends on the spot locations $\boldsymbol{x}_1$ and $\boldsymbol{x}_2$ only through the quantity

$$\xi \equiv \boldsymbol{x}_1^T \boldsymbol{x}_2 = \sin\theta_1 \sin\theta_2 \cos(\varphi_1 - \varphi_2) + \cos\theta_1 \cos\theta_2, \tag{C.9}$$

for which we note that when $\varphi_2 - \varphi_1 = \pi$ and $\theta_1 = \theta_2 = \theta_c$

$$\frac{\partial \xi}{\partial \varphi_1} = -\frac{\partial \xi}{\partial \varphi_2} = 0, \qquad \frac{\partial \xi}{\partial \theta_1} = \frac{\partial \xi}{\partial \theta_2} = -\sin 2\theta_c. \tag{C.10}$$

Substituting

$$\boldsymbol{S} = \frac{S_1 + S_2}{2} \boldsymbol{p}_1 + \frac{S_1 - S_2}{2} \boldsymbol{p}_2, \tag{C.11}$$

into the NAS (3.43b) and left-multiplying by $\boldsymbol{p}_1^T$ and $\boldsymbol{p}_2^T$ gives

$$S_1 + S_2 - 2S_c = 0, \tag{C.12}$$

$$(\nu^{-1} + 2\pi\mu_-)(S_1 - S_2) + \chi(S_1, f) - \chi(S_2, f) - \frac{v_E(\boldsymbol{x}_1) - v_E(\boldsymbol{x}_2)}{D_w \sqrt{D_v}} = 0. \tag{C.13}$$

Differentiating the first equation with respect to any parameter $z \in \{\varphi_1, \varphi_2, \theta_1, \theta_2\}$ we find that

$$\frac{\partial S_2}{\partial z} = -\frac{\partial S_1}{\partial z}.$$

On the other hand, differentiating the second equation with respect to z and assuming that

$$\mathscr{A}_2(S_1, S_2) \equiv \nu^{-1} + 2\pi\mu_- + \frac{\chi'(S_1, f) + \chi'(S_2, f)}{2} \neq 0, \tag{C.14}$$

we obtain

$$\frac{\partial S_1}{\partial z} = \frac{\frac{\partial v_E(\boldsymbol{x}_1)}{\partial z} - \frac{\partial v_E(\boldsymbol{x}_2)}{\partial z}}{2 D_w \sqrt{D_v} \mathscr{A}_2(S_1, S_2)} - \pi \frac{S_1 - S_2}{\mathscr{A}_2(S_1, S_2)} \frac{\partial \mu_-}{\partial z}. \tag{C.15}$$

Equation (3.73a) implies that $v_E(\boldsymbol{x}_1)$ and $v_E(\boldsymbol{x}_2)$ are functions only of $\cos\theta_1$ and $\cos\theta_2$ respectively. Therefore when $\varphi_2 - \varphi_1 = \pi$, $\theta_1 = \theta_2 = \theta_c$, and $S_1 = S_2 = S_c$ we obtain

$$\frac{\partial S_i}{\partial \varphi_j} = 0, \tag{C.16a}$$

for all $i, j \in \{1,2\}$, and

$$\begin{aligned}\frac{\partial S_1}{\partial \theta_1} &= -\frac{\partial S_2}{\partial \theta_1} = \frac{1}{2D_w\sqrt{D_v}\mathscr{A}_\star(S_c)}\frac{\partial v_E(\boldsymbol{x}_1)}{\partial \theta_1}\\ \frac{\partial S_2}{\partial \theta_2} &= -\frac{\partial S_1}{\partial \theta_2} = \frac{1}{2D_w\sqrt{D_v}\mathscr{A}_\star(S_c)}\frac{\partial v_E(\boldsymbol{x}_2)}{\partial \theta_2},\end{aligned}$$

where $\mathscr{A}_\star(S_c)$ is given by (3.56) and for which we note $\mu_\star = \mu_-$ when $N = 2$. Note that from (3.73a), (C.7), and (3.73d) we calculate

$$\frac{\partial v_E(\boldsymbol{x})}{\partial \theta} = \frac{E_0}{4\pi}\sum_{l=1}^{\infty}\frac{g_l\eta^l}{l(l+1)}(-\sin\theta P_l'(\cos\theta)) = \frac{E_0}{4\pi}C_E(\cos\theta), \tag{C.17}$$

which vanishes at $\theta = 0, \pi$ and is strictly negative otherwise. In particular we deduce that

$$\frac{\partial S_1}{\partial \theta_1} = -\frac{\partial S_2}{\partial \theta_1} = \frac{\partial S_2}{\partial \theta_2} = -\frac{\partial S_1}{\partial \theta_2} = \frac{E_0 C_E(\cos\theta_c)}{8\pi D_w\sqrt{D_v}\mathscr{A}_\star(S_c)}. \tag{C.18}$$

Using (C.16a) and (C.18) together with (3.81) we calculate the Jacobian matrices of the dynamics (3.77) evaluated at the common angle solution

$$\frac{\partial(F_1,F_2)}{\partial(\theta_1,\theta_2)} = \begin{pmatrix}0 & 0\\ 0 & 0\end{pmatrix}, \quad \frac{\partial(G_1,G_2)}{\partial(\varphi_1,\varphi_2)}\boldsymbol{G} = \begin{pmatrix}0 & 0\\ 0 & 0\end{pmatrix}, \tag{C.19}$$

as well as

$$\frac{\partial(F_1,F_2)}{\partial(\varphi_1,\varphi_1)} = \frac{S_c C(\cos(2\theta_c))\sin\theta_c}{2\sin(2\theta_c)}\begin{pmatrix}-1 & 1\\ 1 & -1\end{pmatrix}, \tag{C.20}$$

and

$$\begin{aligned}\frac{\partial(G_1,G_2)}{\partial(\theta_1,\theta_2)} =& \frac{(1-\frac{K}{1-f})S_cC_E(\cos\theta_c)C(\cos 2\theta_c)}{4D_w\mathscr{A}_\star(S_c)}\begin{pmatrix}-1 & 1\\ 1 & -1\end{pmatrix}\\ &-\frac{S_cC'(\cos 2\theta_c)\sin 2\theta_c}{2}\begin{pmatrix}1 & 1\\ 1 & 1\end{pmatrix}\\ &-\frac{(1-\frac{K}{1-f})S_cC'_E(\cos\theta_c)\sin\theta_c}{D_w}\begin{pmatrix}1 & 0\\ 0 & 1\end{pmatrix}.\end{aligned} \tag{C.21}$$

In particular the Jacobian $\partial(\boldsymbol{F},\boldsymbol{G})/\partial(\boldsymbol{\varphi},\boldsymbol{\theta})$ is block diagonal and it therefore suffices to consider the stability with respect to $\boldsymbol{\varphi}$ and $\boldsymbol{\theta}$ separately. Since

$$\det\left(\frac{\partial(F_1,F_2)}{\partial(\varphi_1,\varphi_1)}\right)=0, \qquad \operatorname{tr}\left(\frac{\partial(F_1,F_2)}{\partial(\varphi_1,\varphi_1)}\right)=-\frac{S_cC(\cos(2\theta_c))\sin\theta_c}{\sin(2\theta_c)}<0, \tag{C.22}$$

we deduce that $\partial(F_1,F_2)/\partial(\varphi_1,\varphi_1)$ has one neutral zero eigenvalue corresponding to rotational invariance and one negative eigenvalue. In particular the stability of the common angle solution is determined solely by the eigenvalues of $\partial(G_1,G_2)/\partial(\theta_1,\theta_1)$ which we calculate explicitly by noting that $(1,1)^T$ and $(1,-1)^T$ are its eigenvectors with corresponding eigenvalues

$$d_+ = -\frac{E_0}{4\pi\sqrt{D_v}}\left(\frac{C'(\cos 2\theta_c)\sin 2\theta_c}{1-\frac{K}{1-f}}+\frac{C'_E(\cos\theta_c)\sin\theta_c}{D_w}\right), \tag{C.23a}$$

$$d_- = -\frac{E_0}{4\pi D_w\sqrt{D_v}}\left(\frac{C(\cos 2\theta_c)C_E(\cos\theta_c)}{2\mathscr{A}_\star(S_c)}+C'_E(\cos\theta_c)\sin\theta_c\right), \tag{C.23b}$$

where we have used (3.75) for S_c. Note that d_+ corresponds to perturbations where θ_1 and θ_2 both increase or decrease synchronously. As a result the numerically supported observation that $G_i(\theta,\theta)\lessgtr 0$ when $\theta\gtrless\theta_c$ for $i=1,2$ implies that $d_+<0$. Therefore the common angle solution can only be destabilized by increasing one polar angle and decreasing the other. Specifically, the common angle solution is linearly unstable with respect to a *tilt instability* when $d_->0$ and is stable otherwise. The corresponding tilt instability threshold is obtained by setting $d_-=0$ which we note is equivalent to (3.88).

Appendix D

Appendix for Chapter 4

D.1 Large λ_I Asymptotics of $\mathscr{F}_{y_0}(i\lambda_I)$

In this appendix we determine some key properties of $\mathscr{F}_{y_0}(\lambda)$ defined in (4.36). Recalling (4.37), in Figure D.1a we plot $\mathscr{F}_{y_0}(0)$ versus $y_0 \geq 0$. Next we calculate the limiting behaviour of $\mathscr{F}_{y_0}(i\lambda_I)$ as $\lambda_I \to \infty$. First, we let $(\mathscr{L}_{y_0} - i\lambda_I)^{-1} w_c(y+y_0)^2 = \Phi_R + i\Phi_I$ where Φ_R and Φ_I solve

$$\mathscr{L}_{y_0}\Phi_R + \lambda_I\Phi_I = w_c(y+y_0)^2, \qquad \mathscr{L}_{y_0}\Phi_I - \lambda_I\Phi_R = 0, \tag{D.1}$$

with the boundary conditions $\Phi_R'(0) = \Phi_I'(0)$ and $\Phi_R, \Phi_L \to 0$ as $y \to \infty$. Taking $\lambda_I \gg 1$ and assuming that $y = \mathscr{O}(1)$ we obtain

$$\Phi_I(y) \sim \frac{1}{\lambda_I} w_c(y+y_0)^2, \qquad \Phi_R(y) \sim \frac{1}{\lambda_I}\mathscr{L}_{y_0}\Phi_I = \frac{1}{\lambda_I^2}\big(2w_c'(y+y_0)^2 + w_c(y+y_0)^2\big).$$

If $y_0 > 0$ then $\Phi_R'(0) = 0$ and $\Phi_I'(0) = 0$ are not satisfied and we must therefore consider the boundary layer at $y = 0$. Setting $z = \lambda_I^{1/2} y$ we consider the inner expansion $\Phi_R \sim \tilde{\Phi}_R(z)$ and $\Phi_I \sim \tilde{\Phi}_I(z)$ where $\tilde{\Phi}_I$ satisfies

$$\frac{d^4\tilde{\Phi}_I}{dz^4} + \tilde{\Phi}_I = \frac{1}{\lambda_I} w_c(y_0)^2 \quad z > 0; \qquad \frac{d\tilde{\Phi}_I}{dz} = \frac{d^3\tilde{\Phi}_I}{dz^3} = 0, \quad z = 0,$$

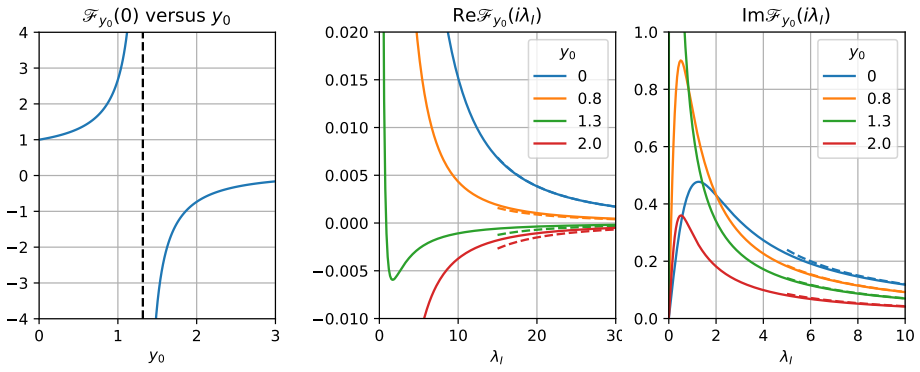

(a) **(b)** **(c)**

Figure D.1: (a) Plot of $\mathscr{F}_{y_0}(0)$ versus the shift parameter y_0. (b) and (c) Real and imaginary parts of $\mathscr{F}_{y_0}(i\lambda_I)$ for select values of $y_0 \geq 0$. The dashed lines indicate the $\lambda_I \gg 1$ asymptotics.

and must be matched to the outer, $y = \mathscr{O}(1)$, solution through the far-field behaviour

$$\tilde{\Phi}_I \sim \frac{1}{\lambda_I} w_c(y_0)^2, \quad \frac{d^2\tilde{\Phi}_I}{dz^2} \sim \frac{1}{\lambda_I^2}\left(2w_c'(y+y_0)^2 + w_c(y+y_0)^2\right), \qquad z \to \infty.$$

It is clear that the leading order solution is $\tilde{\Phi}_I(z) \sim \lambda_I^{-1} w_c(y_0)^2$. The constant behaviour of Φ_I at the boundary layer therefore does not contribute to the leading order behaviour of the integral

$$\int_0^\infty w_c(y+y_0)\Phi_I(y)dy \sim \lambda_I^{-1}\int_0^\infty w_c(y+y_0)^3 dy, \qquad \lambda_I \gg 1.$$

Moreover, multiplying the right equation in (D.1) by $w_c(y+y_0)$ and integrating we calculate

$$\begin{aligned}\int_0^\infty w_c(y+y_0)\Phi_R(y)dy &= \frac{1}{\lambda_I}\left(w_c'(y_0)\Phi_I(0) + \int_0^\infty \Phi_I \mathscr{L}_{y_0} w_c(y+y_0)dy\right) \\ &\sim \frac{1}{\lambda_I^2}\left(w_c'(y_0)w_c(y_0)^2 + \int_0^\infty w_c(y+y_0)^4 dy\right),\end{aligned}$$

for $\lambda_I \gg 1$ where we have used $\mathscr{L}_{y_0} w_c(y+y_0) = w_c(y+y_0)^2$. In summary, we have the large λ_I asymptotics

$$\mathscr{F}_{y_0}(i\lambda_I) \sim \frac{1}{\lambda_I^2} \frac{w_c'(y_0) w_c(y_0)^2 + \int_0^\infty w_c(y+y_0)^4 dy}{\int_0^\infty w_c(y+y_0)^2 dy} + \frac{i}{\lambda_I} \frac{\int_0^\infty w_c(y+y_0)^3 dy}{\int_0^\infty w_c(y+y_0)^2 dy}, \qquad \lambda_I \gg 1. \tag{D.2}$$

Note that the real part changes from positive to negative as y_0 exceeds $y_0 \approx 1.0487$. In Figures D.1b and D.1c we plot the real and imaginary parts of $\mathscr{F}_{y_0}(i\lambda_I)$ respectively for select values of y_0. In addition, we have included the large λ_I asymptotics which indicate close agreement for moderately large values of λ_I.

D.2 Numerical Support for Stability Conjecture

In this appendix we provide numerical support for the conjecture that the shifted NLEP (4.44) has a stable spectrum when $\mu > \mu_c(y_0)$ by numerically calculating the dominant eigenvalue of the NLEP for $0 \le y_0 \le 1.5$ and $0 \le \mu \le 10$. The numerical calculation of the spectrum was performed by truncating the domain $0 < y < \infty$ to $0 < y < 20$ and discretizing it with 600 uniformly distributed points. Then, we used a finite difference approximation for the second derivatives and a trapezoidal rule discretization for the integral term to approximate the NLEP (4.44) with a discrete matrix eigenvalue problem. We then numerically calculated the dominant eigenvalue of matrix by using the eig function in the Python scipy.linalg library for our numerical computation of the dominant eigenvalue. In Figure D.2a we plot $\mathrm{Re}\lambda_0$ versus y_0 and μ. We observe the real part of the dominant eigenvalue is negative when μ exceeds the threshold $\mu_c(y_0)$. Additionally, in Figure D.2b we plot $\Lambda_0 - \mathrm{Re}(\lambda_0)$ for the same range of y_0 and μ values. We observe that this difference is non-negative which suggest that $\mathrm{Re}\lambda_0 \le \Lambda_0$.

D.3 Stability of Asymmetric Two-Boundary Spike Pattern when $A = 0$

Previous results on the stability of asymmetric two spike equilibrium solutions of (4.2) when $A = 0$ have focused exclusively on interior multi-spike solutions [104]. To compare the $A = B = 0$ theory with our results obtained in Examples 2-4 we

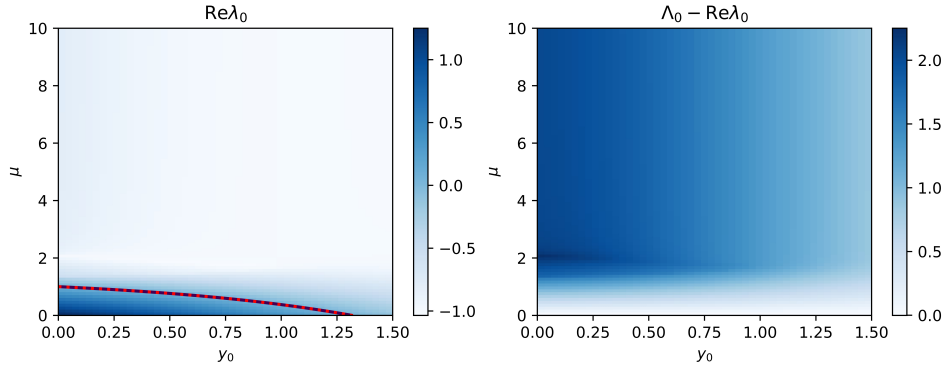

Figure D.2: (a) Plot of the real part of the dominant eigenvalue of the shifted NLEP (4.44) versus shift parameter y_0 and multiplier μ. The dotted red line corresponds to the critical threshold μ_c defined in (4.56) and the solid dark line is the zero-contour of $\mathrm{Re}\lambda_0$. (b) Plot of the difference between dominant eigenvalues of $\mathscr{L}_{y_0}$ and the NLEP (4.44).

include here a summary of the stability of an asymmetric two-spike solution where one spike concentrates at $x = 0$ and the other concentrates at either $x = 1$ or in the interior $0 < x < 1$. In both cases the NLEP (4.30) with $A = 0$ can be written as

$$\mathscr{L}_0\boldsymbol{\phi} - 2w_c(y)^2 \frac{\int_0^\infty w_c(y)\mathscr{E}\boldsymbol{\phi}\,dy}{\int_0^\infty w_c(y)^2 dy} = \lambda\boldsymbol{\phi}, \tag{D.3}$$

where for two boundary spikes we let

$$\mathscr{E} = \mathscr{E}_{bb} \equiv \begin{pmatrix} \coth\omega_0 \tanh\omega_0 l & \operatorname{csch}\omega_0 \tanh\omega_0(1-l) \\ \operatorname{csch}\omega_0 \tanh\omega_0 l & \coth\omega_0 \tanh\omega_0(1-l) \end{pmatrix}, \tag{D.4}$$

and in the case of one boundary and one interior spike we let

$$\mathscr{E} = \mathscr{E}_{bi} \equiv \begin{pmatrix} \coth\omega_0 \tanh\omega_0 l & 2\operatorname{csch}\omega_0 \sinh\omega_0 \frac{1-l}{2} \\ \operatorname{csch}\omega_0 \tanh\omega_0 l \cosh\omega_0 \frac{1-l}{2} & 2\operatorname{csch}\omega_0 \cosh\omega_0 \frac{1+l}{2} \sinh\omega_0 \frac{1-l}{2} \end{pmatrix}. \tag{D.5}$$

It is then straightforward to verify that $\sigma = 1$ is an eigenvalue of both matrices $\mathscr{E}_{bb}$

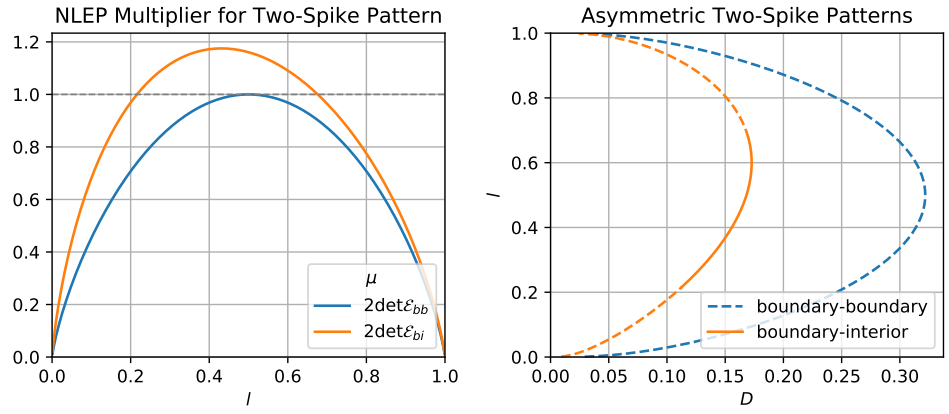

(a) **(b)**

Figure D.3: (a) NLEP multipliers for a boundary-boundary and boundary-interior configuration. (b) Plot of l versus D determining asymmetric boundary-boundary and boundary-interior spike patterns. Solid (resp.) dashed lines indicate the two-spike pattern is linearly stable (resp. unstable) with respect to competition instabilities.

and $\mathscr{E}_{bi}$. The remaining eigenvalue in each case is then given by the determinant. By diagonalizing $\mathscr{E}$ the NLEP (D.3) can therefore be written as (4.44) with $\mu = 2$ as well as with $\mu = 2\det\mathscr{E}_{bb}$ and $\mu = 2\det\mathscr{E}_{bi}$ for the boundary-boundary and boundary-interior cases respectively. Since the $A = B = 0$ stability theory implies that the NLEP (4.44) is stable if and only if $\mu > 1$ [107] we immediately deduce that the $\mu = 2$ modes are stable in both the boundary-boundary and boundary-interior cases. To determine the stability of the remaining modes we explicitly calculate

$$\det\mathscr{E}_{bb} = \tanh\omega_0 l \tanh\omega_0(1-l), \qquad \det\mathscr{E}_{bi} = 2\frac{\tanh\omega_0 l \sinh\omega_0\frac{1-l}{2}\sinh\omega_0\frac{1+l}{2}}{\sinh\omega_0}. \tag{D.6}$$

Finally, for the boundary-boundary and boundary-interior cases we solve (4.76) and (4.89) for $D = D(l)$ respectively and the resulting values of $2\det\mathscr{E}_{bb}$ and $2\det\mathscr{E}_{bi}$ for $0 < l < 1$ are shown in Figure D.3a. In particular the asymmetric pattern with two boundary spikes is always linearly unstable, while the pattern with one boundary and one interior spike has a region of stability (with respect to

the $\mathcal{O}(1)$ eigenvalues). In Figure D.3b we plot $l = l(D)$ (cf. Figures 4.7 and 4.10) for both two-spike configurations, indicating where the pattern is stable (solid line) and unstable (dashed line).